Synthesis and Characterisation of New Inorganic Silicate Luminescent Materials

MELISSA MONZERRAT RODRIGUEZ-GARCIA

How to cite:

RODRIGUEZ-GARCIA, MELISSA MONZERRAT (2021) Synthesis and Characterisation of New Inorganic Silicate Luminescent Materials. Doctoral thesis, Durham University.

Abstract

Solid-state lighting devices outshine the alternatives due to their unique properties such as high energy efficiency, brightness, longer lifetimes, excellent low temperature performance, reliability and added benefits like maintenance savings and environmental friendliness. Developing novel phosphors for solid-state white lighting based on inorganic luminescent materials has become highly important. Another important application area of luminescent materials is bioimaging with the NIR-emissive particles functioning as reporters of lifetime multiplexing, barcoding in cells and forensics, where long-lived NIR emitters are suitable to be used.

Chapter 1 Literature review details the strategies and requirements for solid-state white lighting, the mechanisms behind luminescence properties and luminescence quenching processes, the specific rare earth activators used in this project and the Jahn-Teller effect observed in the Cu(II)-containing compounds.

Chapter 2 Experimental methods reviews the different techniques used to characterise the structural and optical properties of the new inorganic silicate luminescent materials studied in this project. These include: single crystal and powder X-ray diffraction and fluorescence spectroscopy.

Each subsequent chapter is organised in manuscript-like format, with an introduction, the experimental details, the results and discussion and conclusions sections.

Chapter 3 New warm white-emitting Dy^{3+}-containing phosphors based on apatite-type $Gd_{9.33}(SiO_4)_6O_2$. Synthesis and characterisation of a $Gd_{9.33-x}(SiO_4)_6O_2$: x% La (x = 0, 10, 20, 30, 40 and 50) host series and a warm white-emitting $Gd_{4.67-\frac{x}{2}}La_{4.67-\frac{x}{2}}(SiO_4)_6O_2$:x% Dy and $Gd_{9.33-x}(SiO_4)_6O_2$:x% Dy (x = 0.5, 1.0 and 2.0%) series are reported. Dy^{3+}-doped phosphors showed a warm-white emission with colour coordinates that range from (0.413, 0.419) to (0.432, 0.421), ideal for residential applications.

Chapter 4 Green-emitting phosphors: Tb^{3+}-doped $Gd_{9.33}(SiO_4)_6O_2$. Tb^{3+}-doped $Gd_{9.33-x}(SiO_4)_6O_2$ single-phase phosphors are synthesised and characterised. Blue- to green-emitting tuneable phosphors are developed with chromaticity coordinates that ranged from (0.3120, 0.4623) to (0.3269, 0.5218). These phosphors are identified as light green emitters shifting towards almost deep green when the doping level increases.

Chapter 5 Single-phase white-emitting phosphors based on apatite-type gadolinium silicate, $Gd_{9.33}(SiO_4)_6O_2$ doped with Dy^{3+}, Eu^{3+} and Tb^{3+}. Single-phase phosphors based on the apatite-type silicate $Gd_{9.33}(SiO_4)_6O_2$ doped with combinations of Dy^{3+} and Eu^{3+} or Eu^{3+} and Tb^{3+} are developed and characterised. Eight novel white-emitting phosphor were synthesised, where the 0.5% Tb, 0.03% Eu co-doped phosphor shows better properties than any other apatite-based silicate phosphor in the literature, with colour coordinates of (0.340 0.341).

Chapter 6 Narrow-band red-emitting phosphors based on Eu^{3+}-doped $Gd_{9.33}(SiO_4)_6O_2$. A series of new narrow-band red phosphors based on apatite-type gadolinium silicate are synthesised. $Gd_{9.33-x}(SiO_4)_6O_2$:x% Eu^{3+} (x = 0.3, 0.5, 0.7, 1.0, 2.0, 3.0, 5.0, 7.0, 10.0, 15.0 and 20.0) materials with outstanding chemical and thermal stability are characterised and analysed. Eu^{3+} phosphors show emission with FWHM of 7 nm for the 614 nm emission peak. These phosphors show outstanding thermal properties, losing only 10% of emission intensity at 150 °C (working LED temperature).

Chapter 7 Cu(II)-containing silicate near infrared (NIR) emitters: the relationship between the structural distortion within the CuO_4 chromophore and luminescence properties. Four Cu(II)-containing silicate NIR emitters, $CaCuSi_4O_{10}$, $BaCuSi_4O_{10}$, $K_2CuSi_4O_{10}$ and $BaCuSi_2O_7$, are synthesised and their structural and optical properties studied. A strong relationship between the distortion of the CuO_4^{6-} chromophore environment and the optical properties was established.

Chapter 8 Overall conclusions summarise the work discussed in the previous chapters.

Graphical abstract

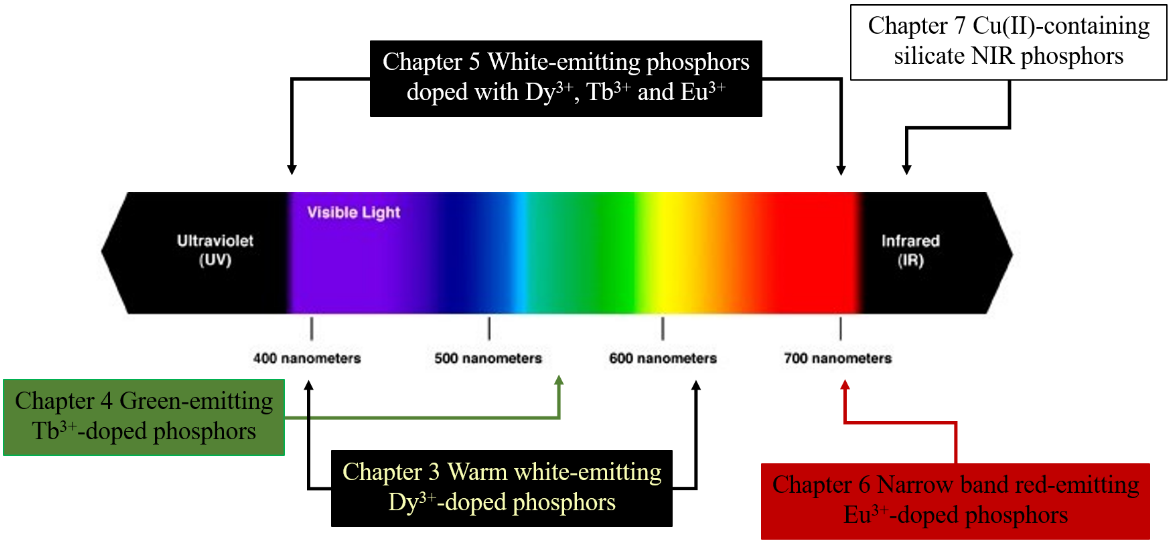

SYNTHESIS AND CHARACTERISATION OF NEW INORGANIC SILICATE LUMINESCENT MATERIALS

Melissa Monzerrat Rodríguez García

PhD Thesis

Supervisor

Prof. Ivana R Evans

Department of Chemistry
University of Durham

October 2020

Contents

Abstract **I**

List of Tables **V**

List of Figures **VI**

Abbreviations **X**

Declaration **XII**

Acknowledgements **XIII**

Dedication **XIV**

1 Literature review **1**
- 1.1 Technological uses of luminescent materials . . . 1
  - 1.1.1 Solid-state white lighting (SSWL) . . . 1
    - 1.1.1.1 Quantification of SSWL quality . . . 1
    - 1.1.1.2 Light-emitting diodes (LEDs) . . . 2
    - 1.1.1.3 Strategies for SSWL . . . 3
      - 1.1.1.3.1 Phosphor-free/Tricolour LEDs . . . 4
      - 1.1.1.3.2 Phosphor-converted LEDs . . . 4
    - 1.1.1.4 History of high-energy LEDs suitable for SSWL . . . 5
  - 1.1.2 Near Infrared emitters . . . 6
    - 1.1.2.1 The Jahn-Teller effect . . . 7
- 1.2 Photoluminescence . . . 8
  - 1.2.1 Term symbols and selection rules . . . 9
  - 1.2.2 Concentration, thermal and lifetime effects . . . 10
- 1.3 Rare earth (RE) ions . . . 11
  - 1.3.1 Dysprosium . . . 14
  - 1.3.2 Terbium . . . 14
  - 1.3.3 Europium . . . 14
    - 1.3.3.1 Eu^{3+} site symmetry properties . . . 15
    - 1.3.3.2 Judd-Ofelt parametrisation of Eu^{3+} . . . 15
- 1.4 Important classes of phosphor materials . . . 15
  - 1.4.1 Garnets . . . 16
  - 1.4.2 Silicates . . . 17
  - 1.4.3 Phosphates . . . 18
  - 1.4.4 Nitrides and oxynitrides . . . 18
  - 1.4.5 Other phosphors . . . 19
  - 1.4.6 Apatite-type silicate . . . 21
- 1.5 Aims of the PhD project . . . 22
- 1.6 References . . . 22

2 Experimental methods **28**
- 2.1 Synthetic methods . . . 28
  - 2.1.1 Solid-state synthesis . . . 28
  - 2.1.2 Single crystal growth . . . 28
- 2.2 X-Ray crystallography . . . 29
  - 2.2.1 Diffraction . . . 29
  - 2.2.2 Single crystal and powder X-ray diffraction . . . 31
  - 2.2.3 Instrumentation . . . 32
  - 2.2.4 Powder diffraction data analysis . . . 33
- 2.3 Optical measurements . . . 33
  - 2.3.1 Fundamentals . . . 33
  - 2.3.2 Instrumentation . . . 35
  - 2.3.3 White-light characterisation . . . 35

2.4 Scanning Electron Microscopy 38
  2.4.1 Fundamentals 38
  2.4.2 Instrumentation 38
  2.4.3 Data Analysis 38
2.5 References 39

3 New warm white-emitting Dy^{3+}-containing phosphors based on apatite-type $Gd_{9.33}(SiO_4)_6O_2$ 40
3.1 Introduction 40
3.2 Experimental details 45
  3.2.1 Sample preparation 45
  3.2.2 X-ray diffraction. 46
  3.2.3 Photoluminescence spectroscopy 46
3.3 Results and discussion 46
  3.3.1 New phosphor host materials based on apatite-type gadolinium silicate, $Gd_{9.33-x}La_x(SiO_4)_6O_2$ 46
    3.3.1.1 Structural characterisation: Powder X-Ray Diffraction 46
  3.3.2 New warm white-emitting phosphors based on apatite-type $Gd_{4.67-x}La_{4.67-x}(SiO_4)_6O_2$ and $Gd_{9.33-x}Dy_x(SiO_4)_6O_2$ doped with Dy^{3+} . . . 49
    3.3.2.1 Structural characterisation: Powder X-Ray Diffraction 49
    3.3.2.2 Optical properties 51
    3.3.2.3 Dy^{3+} temporal decay 55
3.4 Conclusions and future work 57
3.5 References 58

4 Green-emitting phosphors: Tb^{3+}-doped $Gd_{9.33}(SiO_4)_6O_2$ 61
4.1 Introduction 61
4.2 Experimental details 65
  4.2.1 Sample preparation 65
  4.2.2 X-ray diffraction. 65
  4.2.3 Photoluminescence spectroscopy 65
4.3 Results and discussion 65
  4.3.1 Structural characterisation: Powder X-Ray Diffraction 65
  4.3.2 Optical properties 67
  4.3.3 Tb^{3+} temporal decay 71
4.4 Conclusions and future work 73
4.5 References 73

5 Single-phase white-emitting phosphors based on apatite-type gadolinium silicate, $Gd_{9.33}(SiO_4)_6O_2$ doped with Dy^{3+}, Eu^{3+} and Tb^{3+} 76
5.1 Introduction 76
  5.1.1 A brief survey of apatite-type silicate phosphors 77
5.2 Experimental details 78
  5.2.1 Sample preparation 78
  5.2.2 X-ray diffraction. 79
  5.2.3 Photoluminescence spectroscopy 79
5.3 Results and discussion 79
  5.3.1 Characterisation of the $Gd_{9.33}(SiO_4)_6O_2$ host 79
  5.3.2 Phosphors incorporating dysprosium and europium: $Gd_{9.33-x-y}Eu_xDy_y(SiO_4)_6O_2$ 80
    5.3.2.1 Structure characterisation 80
    5.3.2.2 Optical properties 82
    5.3.2.3 Energy transfer, quenching and temporal decay 87
  5.3.3 Phosphors incorporating terbium and europium: $Gd_{9.33}(SiO_4)_6O_2$:Tb^{3+}, Eu^{3+} 90
    5.3.3.1 Structure characterisation 90
    5.3.3.2 Optical properties 91
    5.3.3.3 Energy transfer, quenching and temporal decay 96

5.4 Conclusions 98
5.5 Note 99
5.6 References 99

6 Narrow-band red-emitting phosphors based on Eu^{3+}-doped $Gd_{9.33}(SiO_4)_6O_2$ 101
6.1 Introduction 101
6.2 Experimental details 104
  6.2.1 Sample preparation 104
  6.2.2 X-ray diffraction. 105
  6.2.3 Photoluminescence spectroscopy 105
6.3 Results and discussion 105
  6.3.1 Structural characterisation and concentration quenching of $Gd_{9.33-x}$ $Eu_x(SiO_4)_6O_2$ phosphor 105
    6.3.1.1 Room temperature powder X-Ray diffraction 105
    6.3.1.2 Concentration quenching and luminescence analysis 109
    6.3.1.3 Room temperature Judd-Ofelt analysis 112
  6.3.2 Thermal stability of $Gd_{9.05}$ $Eu_{0.28}(SiO_4)_6O_2$ phosphor 114
    6.3.2.1 Variable-temperature powder X-Ray diffraction 114
    6.3.2.2 Thermal quenching of $Gd_{9.05}$ $Eu_{0.28}(SiO_4)_6O_2$ 116
    6.3.2.3 Maximum energy splitting of $^7F_1$ 118
    6.3.2.4 Variable-temperature Judd-Ofelt analysis 119
6.4 Conclusions and future work 121
6.5 Note 122
6.6 References 122

7 Cu(II)-containing silicate near infrared (NIR) emitters: the relationship between the structural distortion within the CuO_4 chromophore and luminescence properties 125
7.1 Introduction 125
7.2 Experimental details 126
  7.2.1 Sample preparation 126
  7.2.2 Exfoliation of $K_2CuSi_4O_{10}$ 126
  7.2.3 X-ray diffraction 126
  7.2.4 Photoluminescence spectroscopy 127
  7.2.5 Atomic Force Microscopy 127
  7.2.6 Scanning Electron Microscopy 127
7.3 Results and discussion 127
  7.3.1 Structure characterisation 127
  7.3.2 NIR luminescence 131
  7.3.3 $K_2CuSi_4O_{10}$ nanoparticles 135
    7.3.3.1 Size and shape of $K_2CuSi_4O_{10}$ nanoparticles 135
    7.3.3.2 NIR fluorescence properties of $K_2CuSi_4O_{10}$ nanoparticles 137
7.4 Conclusions 137
7.5 Note 137
7.6 References 138

8 Overall conclusions and future work 140

A Appendix 142
A.1 Publications 142
A.2 Laboratory PXRD refined parameters 142
A.3 Laboratory PXRD pattern refinement input file 142
A.4 Synchrotron PXRD pattern refinement input file 143
A.5 Detailed Rietveld fit of Eu^{3+}-doped phosphors 146
A.6 Crystallographic details for the NIR emitters 147
  A.6.1 $CaCuSi_4O_{10}$ 147
  A.6.2 $BaCuSi_4O_{10}$ 147
  A.6.3 $K_2CuSi_4O_{10}$ 148

A.6.4 $BaCu_2Si_2O_7$ 149

List of Tables

1.1 Persistent NIR emitters propierties. 6
3.1 Summary of Dy^{3+}-doped phosphors. 42
3.2 La^{3+} content in the $Gd_{9.33-x}La_x(SiO_4)_6O_2$ host material. 45
3.3 The different doping levels for the $Gd_{4.67-\frac{x}{2}}La_{4.67-\frac{x}{2}}Dy_x(SiO_4)_6O_2$ and $Gd_{9.33-x}Dy_x(SiO_4)_6O_2$ phosphor series. 45
3.4 Crystallographic data for $Gd_{9.33}(SiO_4)_6O_2$ apatite.[38] 45
3.5 Reagents used in these syntheses. 46
3.6 Unit cell parameters for $Gd_{9.33-x}La_x(SiO_4)_6O_2$ (x = 0, 0.93, 1.87, 2.8, 3.73 and 4.67) hosts. 48
3.7 Unit cell parameters for $Gd_{4.67-\frac{x}{2}}La_{4.67-\frac{x}{2}}Dy_x(SiO_4)_6O_2$ and $Gd_{9.33-x}Dy_x(SiO_4)_6O_2$ (x = 0.05, 0.09 and 0.19) phosphors. 50
3.8 The CIE coordinates and CCT values for the $Gd_{4.67-\frac{x}{2}}La_{4.67-\frac{x}{2}}Dy_x(SiO_4)_6O_2$ and $Gd_{9.33-x}Dy_x(SiO_4)_6O_2$ phosphors. 54
3.9 Lifetime values obtained for the $Gd_{4.67-\frac{x}{2}}La_{4.67-\frac{x}{2}}Dy_x(SiO_4)_6O_2$ and $Gd_{9.33-x}Dy_x(SiO_4)_6O_2$ phosphors recorded after excitation at 375 nm. 56
4.1 Summary of Tb^{3+}-doped phosphors. 62
4.2 Schematic representation of the different doping levels for the $Gd_{9.33-x}Tb_x(SiO_4)_6O_2$ phosphor series. 64
4.3 Reagents used in these syntheses. 65
4.4 Unit cell parameters for $Gd_{9.33-x}Tb_x(SiO_4)_6O_2$ phosphors. 66
4.5 Emission bands present in the $Gd_{9.33-x}Tb_x(SiO_4)_6O_2$ phosphor series. 68
4.6 CIE coordinates and CCT values for $Gd_{9.33-x}Tb_x(SiO_4)_6O_2$ phosphors. 70
4.7 Lifetime values obtained for $Gd_{9.33-x}Tb_x(SiO_4)_6O_2$ phosphors recorded after excitation at 375 nm. 72
5.1 Different doping levels of the $Gd_{9.33-x-y}Eu_xDy_y(SiO_4)_6O_2$ materials. 78
5.2 Different doping levels of the $Gd_{9.33-x-y}Eu_xTb_y(SiO_4)_6O_2$ materials. 78
5.3 Unit cell parameters of the best-performing $Gd_{9.33-x-y}Eu_xDy_y(SiO_4)_6O_2$ (x=0.002: y=0.093, 0.187 and 0.280, and x= 0.005: y=0.187 and 0.280) phosphors. 80
5.4 Emission bands present in the $Gd_{9.33-x-y}Eu_xB_y(SiO_4)_6O_2$ (B = Dy and Tb) phosphor series. 84
5.5 CIE coordinates and CCTs for the best-performing $Gd_{9.33-x-y}Eu_xDy_y(SiO_4)_6O_2$. . . 85
5.6 Lifetimes obtained for the best-performing $Gd_{9.33-x-y}Eu_xDy_y(SiO_4)_6O_2$ phosphors recorded after excitation at 375 nm. 87
5.7 Unit cell parameters of the best-performing $Gd_{9.33-x-y}Eu_xTb_y(SiO_4)_6O_2$ phosphors. . 91
5.8 The CIE coordinates and CCTs of the best-performing $Gd_{9.33-x-y}Eu_xTb_y(SiO_4)_6O_2$ phosphors. 94
5.9 Lifetime values obtained for the best-performing $Gd_{9.33-x-y}Eu_xTb_y(SiO_4)_6O_2$ phosphors recorded after excitation at 375 nm. 97
6.1 Summary of $^5D_0 \rightarrow {}^7F_J$ transitions observed in luminescence spectra of Eu^{3+}-doped phosphors. 101
6.2 Stark sublevels according to the site symmetry of the Eu^{3+} doping site. 102
6.3 Summary of narrow-band red phosphors. 103
6.4 Schematic representation of the different doping levels for the $Gd_{9.33-x}Eu_x(SiO_4)_6O_2$ phosphor series. 104
6.5 Reagents used in these syntheses. 104
6.6 Unit cell parameters for $Gd_{9.33-x}$ $Eu_x(SiO_4)_6O_2$ phosphors. 107
6.7 Quantum yield, η, for the $Gd_{9.33-x}Eu_x(SiO_4)_6O_2$ (x = 0.03, 0.05, 0.07, 0.09, 0.19, 0.28, 0.47, 0.65, 0.93, 1.40 and 1.87) phosphors. Refractive index = 1.8 114
6.8 Thermal expansion coefficients for $Gd_{9.05}Eu_{0.28}(SiO_4)_6O_2$ phosphors. 116
6.9 Judd-Ofelt parameters, radiative transition possibilities of $^5D_0 \rightarrow {}^7F_\lambda$ (λ = 1, 2, 4) transitions, branching ratios, radiative theoretical and experimental lifetime values for the $Gd_{9.05}Eu_{0.28}(SiO_4)_6O_2$ phosphors at different temperatures. 121
7.1 Unit cell parameters for $CaCuSi_4O_{10}$, $BaCuSi_4O_{10}$, $K_2CuSi_4O_{10}$ and $BaCu_2Si_2O_7$ obtained from the PXRD. 128
7.2 Bonds and angles of the different cuprosilicate pigments, from single crystals and high quality PXRD. *From powder data, obtained using high quality synchrotron PXRD. . 129

7.3 Key optical properties of the different cuprosilicate pigments, from powder samples. The error given on the values is the standard deviation from the fitting. 132
7.4 Fitted lifetime parameters of the different cuprosilicate pigments, from powder samples. The error given on the lifetime values is the standard deviation from the fitting. 135
7.5 Lifetime values and distortion analysis for the different cuprosilicate pigments. 135
I Unit cell parameters for $Gd_{9.33-x}La_x(SiO_4)_6O_2$ (x = 0, 0.93, 1.87, 2.8, 3.73 and 4.67) hosts from laboratory PXRD. 142

List of Figures

1.1 CIE 1931 photopic luminosity function, response to the light of a typical human eye. Adapted after eye sensitivity function.[2] . . . 2
1.2 The 1931 CIE standard observer diagram.[1] . . . 2
1.3 Production of light emission in LEDs.[6] . . . 3
1.4 Schematics of the different SSWL strategies: a) separate R, G and B-emitting LEDs (red, green and blue diode symbol), b) yellow down-converting phosphor with a blue LED (blue diode symbol), c) RGB phosphors excited by a UV LED (purple diode symbol), and d) single-phase phosphor with UV LED excitation. Grey line = substrate, yellow lines = yellow-emitting phosphor, red lines = red-emitting phosphor, green lines = green-emitting phosphor, blue lines = blue-emitting phosphor, pink lines = single-phase white-emitting phosphor. . . . 4
1.5 Schematic of the crystal field splittings for the different coordination geometries.[60] . . 7
1.6 Luminescence processes. a) Luminescent ion A. b) Energy transfer from a sensitiser S to an activator A.[64] . . . 8
1.7 Energy transfer mechanisms between ions.[65] a) Resonant radiative energy transfer. b)Resonant non-radiative energy transfer. c) Multiphonon-assisted energy transfer. d) Cross-relaxation between two identical ions. The red and blue arrows represent de-excitation and excitation. The black arrows represent the energy transfer. ϵ is energy mismatch. ΔE is the energy difference. . . . 9
1.8 Dy^{3+} electronic configuration. . . . 10
1.9 Configurational coordinate diagram showing the thermal quenching process.[75] . . . 11
1.10 Dieke diagram.[112] . . . 13
1.11 The garnet crystal structure of $Y_3Al_5O_{12}$ in the [010] direction. AlO_6 octahedra are illustrated in blue and AlO_4 tetrahedra in purple. YO_8 polyhedra have been excluded for clarity. Y atoms are shown in green and O atoms are in red.[127] . . . 16
1.12 Crystal structure of δ-$Gd_2Si_2O_7$ seen in the [010] direction. SiO_4 tetrahedra are illustrated in blue, 7-coordinate GdO_7 in purple and O atoms are shown in red.[134] . . . 17
1.13 Crystal structure of $KBaPO_4$ seen in the [100] direction. 11-coordinate $KO_{10}P$ is illustrated in purple, 9-coordinate BaO_9 in green, P atoms are shown in pink and O atoms in red.[138] . . . 18
1.14 Crystal structure of $Ca_2Si_5N_8$ seen in the [010] direction. SiN_4 tetrahedra are illustrated in blue, CaN_6 octahedra in green, CaN_5 trigonal bipyramidal in pink and N atoms are shown in grey.[141] . . . 19
1.15 The crystal structure of Ca_2SiS_4 in the [010] direction. CaS_6 octahedra are illustrated in purple, SiS_4 tetrahedra in blue and S atoms are shown in red.[65] . . . 20
1.16 The structure shown here is hexagonal $Gd_{9.33}(SiO_4)_6O_2$, space group $P6_3/m$. GdO_6 trigonal prisms are illustrated in pink, SiO_4 tetrahedra in blue. The latter share corners to form channels filled with Gd_6O_2 units (purple and red spheres inside the polyhedral framework). 7-coordinate GdO_7 polyhedra have been excluded for clarity. Gd atoms remain as purple spheres. a) View along the c axis, and b) view along the a axis.[104] . 21
2.1 The floating-zone method. . . . 29
2.2 Derivation of Bragg's law.[4] . . . 30
2.3 a) Single crystal and b) powder X-ray diffraction.[6] . . . 31
2.4 Diagram of a synchrotron, illustrating X-ray radiation output from bending magnets.[12] 32
2.5 Franck-Condon energy diagram. Red arrow represent absorption. Orange arrow represent the non-radiative transition. Yellow arrow represent emission.[18] . . . 35
2.6 Colour-matching functions.[21] . . . 36
2.7 The 1931 CIE standard observer diagram.[23] . . . 37
2.8 RGB components corresponding to the colour of a black body at different temperatures. 38
3.1 Energy-level diagram for Dy^{3+} ion showing the relevant transitions.[4] . . . 40
3.2 Energy-level diagrams for Gd^{3+} and Dy^{3+} ions showing the relevant transitions in the system.[4] . . . 44
3.3 Rietveld fits of the laboratory PXRD data for $Gd_{9.33-x}La_x(SiO_4)_6O_2$. a) x = 4.67, R_{wp} = 3.914%. b) x = 3.73, R_{wp} = 3.725%. c) x = 2.80, R_{wp} = 3.491%. d) x = 1.87, R_{wp} = 3.148%. e) x = 0.93, R_{wp} = 2.969%. f) x = 0, R_{wp} = 2.773%. . . . 47

3.4 Rietveld refinement of the synchrotron PXRD patterns for $Gd_{9.33-x}La_x(SiO_4)_6O_2$. a) x = 4.67, R_{wp} = 11.01%. b) x = 3.73, R_{wp} = 10.83%. c) x = 2.80, R_{wp} = 9.16%. d) x = 1.87, R_{wp} = 9.24%. e) x = 0.09, R_{wp} = 11.26%. f) x = 0, R_{wp} = 10.06%. ∇ indicates the Gd_2SiO_5 impurity peaks. 48

3.5 a) Lattice parameter *a*, b) lattice parameter *c* and c) unit cell volume *V* for $Gd_{9.33-x}La_x(SiO_4)_6O_2$ (x = 0, 0.93, 1.87, 2.8, 3.73 and 4.67) as a function of La^{3+} content (x). 49

3.6 Rietveld fit of the laboratory PXRD data. $Gd_{4.67-\frac{x}{2}}La_{4.67-\frac{x}{2}}Dy_x(SiO_4)_6O_2$ a) x = 0.05, R_{wp} = 3.62%, b) x = 0.09, R_{wp} = 3.56%, and c) x = 0.19, R_{wp} = 3.69%. $Gd_{9.33-x}Dy_x(SiO_4)_6O_2$ d) x = 0.05, R_{wp} = 2.71%, e) x = 0.09, R_{wp} = 2.51%, and f) x = 0.19, R_{wp} = 2.45%. 50

3.7 Lattice parameter a) *a*, b) *c* and c) unit cell volume *V* for $Gd_{4.67-\frac{x}{2}}La_{4.67-\frac{x}{2}}Dy_x(SiO_4)_6O_2$ and $Gd_{9.33-x}Dy_x(SiO_4)_6O_2$ (x = 0.05, 0.09 and 0.19) as a function of Dy^{3+} content (x). The error bars are smaller than the data points. 51

3.8 Excitation spectra of a) $Gd_{4.67-\frac{x}{2}}La_{4.67-\frac{x}{2}}Dy_x(SiO_4)_6O_2$, b) $Gd_{9.33-x}Dy_x(SiO_4)_6O_2$ materials, recorded at λ_{emi} =476 nm and normalised to the 273 nm peak. Red arrows show the Gd^{3+} excitation, indirectly populating the Dy^{3+}, and black arrows the direct Dy^{3+} excitation. 52

3.9 Emission spectra of a) $Gd_{4.67-\frac{x}{2}}La_{4.67-\frac{x}{2}}Dy_x(SiO_4)_6O_2$, b) $Gd_{9.33-x}Dy_x(SiO_4)_6O_2$, recorded at 273 nm. Green arrows show the Dy^{3+} emission. 53

3.10 Blue/yellow emission intensity ratio as a function of Dy^{3+} content (x) in $Gd_{4.67-\frac{x}{2}}La_{4.67-\frac{x}{2}}Dy_x(SiO_4)_6O_2$ and $Gd_{9.33-x}Dy_x(SiO_4)_6O_2$, from data collected at 273 nm. 54

3.11 a) 1931 CIE chromaticity diagram showing the chromaticity coordinates at λ_{exc} = 273 nm for the $ZnAl_2O_4:Dy^{3+}$,[45] $Y_2O_2S:Dy^{3+}$,[46] $Ca_2SnO_4:Dy^{3+}$,[47] $Gd_{4.67-\frac{x}{2}}La_{4.67-\frac{x}{2}}Dy_x(SiO_4)_6O_2$ and $Gd_{9.33-x}Dy_x(SiO_4)_6O_2$ series. b) Expansion of the pertinent CIE region for the hosts discussed. 55

3.12 Fitted decay curves (solid line) of the experimental data (dots) of the $^4F_{9/2} \rightarrow {}^6H_{15/2}$ transition at 485 nm and the $^4F_{9/2} \rightarrow {}^6H_{13/2}$ transition at 575 nm for $Gd_{4.67-\frac{x}{2}}La_{4.67-\frac{x}{2}}Dy_x(SiO_4)_6O_2$ a) x = 0.05, b) x = 0.09 and c) x = 0.19, and $Gd_{9.33-x}Dy_x(SiO_4)_6O_2$ d) x = 0.05, e) x = 0.09 and f) x = 0.19 phosphors recorded after excitation at 375 nm. 56

3.13 Lifetime values dependence Dy^{3+} content (x) for a) the $^4F_{9/2} \rightarrow {}^6H_{15/2}$ transition (485 nm) and b) the $^4F_{9/2} \rightarrow {}^6H_{13/2}$ transition (575 nm). Error given on the lifetime values is the standard deviation from the fitting. 57

4.1 Tb^{3+} ion energy-level diagram showing the relevant transitions in the system.[5] 61

4.2 Energy-level diagrams for Gd^{3+} and Tb^{3+} ions showing the relevant transitions in the system.[5] 64

4.3 Rietveld fit of the laboratory PXRD data. $Gd_{9.33-x}Tb_x(SiO_4)_6O_2$: a) x = 0.07, R_{wp} = 1.95%, b) x = 0.09, R_{wp} = 2.00% and c) x = 0.19, R_{wp} = 2.08%. 66

4.4 Lattice parameters of the a) *a*, b) *c* and c) unit cell volume *V* for $Gd_{9.33-x}Tb_x(SiO_4)_6O_2$ (x = 0.07, 0.09 and 0.19) as a function of Tb^{3+} content (x). The error bars are smaller than the data points. 67

4.5 Excitation spectra of $Gd_{9.33-x}Tb_x(SiO_4)_6O_2$ materials recorded at λ_{emi} = 476 nm and normalised to the highest peak. The red arrows show the Gd^{3+} excitation indirectly populating the Tb^{3+} and the black arrows the direct Tb^{3+} excitation. 68

4.6 Emission spectra of $Gd_{9.33-x}Tb_x(SiO_4)_6O_2$: recorded at λ_{exc} = 273 nm and normalised to the 545 nm peak. Green arrows show the Tb^{3+} emission. 69

4.7 Blue/green emission intensity ratio as a function of Tb^{3+} content (x) in $Gd_{9.33-x}Tb_x(SiO_4)_6O_2$, from data collected at 273 nm. 69

4.8 a) 1931 CIE chromaticity diagram showing the chromaticity coordinates at λ_{exc} = 273 nm for the $Gd_{9.33-x}Tb_x(SiO_4)_6O_2$ phosphor series. b) Expansion of the pertinent CIE region for the hosts discussed. 71

4.9 Fitted decay curves (solid line) of the experimental data (dots) of the $^5D_4 \rightarrow {}^7F_5$ transition at 545 nm for $Gd_{9.33-x}Tb_x(SiO_4)_6O_2$ phosphors recorded after excitation at 375 nm. 72

4.10 Lifetime values according to Tb^{3+} content (x) for the $^5D_4 \rightarrow ^7F_5$ transition (545 nm). The error given for the lifetime values is the standard deviation from the fitting. . . . 73
5.1 a) Rietveld fit of the synchrotron PXRD data for $Gd_{9.33}(SiO_4)_6O_2$. Rwp =9.94%. b) The corresponding PDF standard pattern.[11] 80
5.2 Rietveld fits of laboratory data for $Gd_{9.33-x-y}Eu_xDy_y(SiO_4)_6O_2$. x=0.002: a) y=0.093, b) y=0.187, c) y=0.280, and x= 0.005: d) y=0.187 and e) y=0.280. 81
5.3 Energy-level diagrams for Gd^{3+}, Dy^{3+} and Eu^{3+} ions showing the relevant transitions in the system. 82
5.4 Excitation spectra of $Gd_{9.33-x-y}Eu_xDy_y(SiO_4)_6O_2$ materials recorded at λ_{emi}=476 nm and normalised to the 273 nm peak. For a) x=0.002 and b) x=0.005. Red arrows show the Gd^{3+} excitation indirectly populating the Dy^{3+} and black arrows the direct Dy^{3+} excitation. 83
5.5 Emission spectra of $Gd_{9.33-x-y}Eu_xDy_y(SiO_4)_6O_2$ materials recorded at 273 nm and normalised in accordance with the Eu^{3+} peak in the 600 nm-640 nm range. For a) x=0.002 and b) x=0.005. Green arrows and red arrows show the Dy^{3+} emission and the Eu^{3+} emission respectively. 84
5.6 a) 1931 CIE chromaticity diagram showing the chromaticity coordinates at λ_{exc} = 273 nm for the Dy-doped host. b) Expansion of the pertinent CIE region for the hosts discussed. 86
5.7 Excitation spectra of $Gd_{9.325-y}Eu_{0.005}Dy_y(SiO_4)_6O_2$ materials recorded at λ_{emi} =615 nm and normalised to the 390 nm peak. Green arrows show the Dy^{3+} excitation bands. 87
5.8 Decay curves fitted (solid line) of the experimental data (dots) of $^4F_{9/2} \rightarrow ^6H_{15/2}$ transition at 485 nm, $^4F_{9/2} \rightarrow ^6H_{13/2}$ transition at 575 nm and $^5D_0 \rightarrow ^7F_2$ transition at 615 nm for $Gd_{9.33-x-y}Eu_xDy_y(SiO_4)_6O_2$ phosphors with x=0.002: a) y=0.093, b) y=0.187 and c) y=0.280, and x=0.005: d) y=0.187 and e) y=0.280, recorded after excitation at 375 nm. 88
5.9 Average lifetime values dependence Dy3+ content for a) $^4F_{9/2} \rightarrow ^6H_{15/2}$ transition (485 nm), b) $^4F_{9/2} \rightarrow ^6H_{13/2}$ transition (575 nm) and c) $^5D_0 \rightarrow ^7F_2$ transition (615 nm). . . 89
5.10 Rietveld refinements of laboratory data for $Gd_{9.33-x-y}Eu_yTb_y(SiO_4)_6O_2$. x=0.002: a) y=0.028, b) 0.037, c) 0.047, x=0.003: d) y=0.028, e) y=0.037, f) y=0.047, x=0.005: g) y=0.028, h) y=0.047. 90
5.11 Energy-level diagrams for Gd^{3+}, Tb^{3+} and Eu^{3+} ions showing the relevant transitions in the system. 91
5.12 Excitation spectra of $Gd_{9.33-x-y}Eu_xTb_y(SiO_4)_6O_2$ materials recorded at λ_{emi} = 476 nm and normalised to the 273 nm peak. a) x=0.002, b) x=0.003 and c) x=0.005. Red arrows show the Gd^{3+} energy transfer and the black arrow the Tb^{3+} direct excitation. 92
5.13 Emission spectra of $Gd_{9.33-x-y}Eu_xTb_y(SiO_4)_6O_2$ recorded at λ_{exc} = 273 nm and normalised to the Eu^{3+} $\Delta J = 2$ band. a) x=0.002, b) x=0.003 and c) x=0.005. Green and red arrows show the Tb^{3+} and Eu^{3+} emission bands respectively. 93
5.14 a) 1931 CIE chromaticity diagram showing the chromaticity coordinates at λ_{exc} = 273 nm of the Tb-doped host. b) Detailed diagram of the colour coordinates. 95
5.15 Excitation spectra of $Gd_{9.33-x-y}Eu_{0.003}Tb_y(SiO_4)_6O_2$ materials recorded at λ_{emi} =615 nm and normalised to the 390 nm peak. Green arrows show the Tb^{3+} excitation bands. 96
5.16 Fitted decay curves (solid line) of the experimental data (dots) of the $^5D_4 \rightarrow ^7F_5$ transition at 545 nm and the $^5D_0 \rightarrow ^7F_2$ transition at 615 nm for $Gd_{9.33-x-y}Eu_xTb_y(SiO_4)_6O_2$ recorded after excitation at 375 nm. For x=0.002: a) y=0.028, b) y=0.037 and c) y=0.047, x=0.003: d) y=0.028, e) y=0.037 and f) y=0.047, and x=0.005: g) y=0.028, h) y=0.047. 97
5.17 Variation in the lifetime values with the Tb^{3+} content for a) the $^5D_4 \rightarrow ^7F_5$ transition (545 nm), b) the $^5D_0 \rightarrow ^7F_2$ transition (615 nm). 98
6.1 Rietveld fit of the laboratory PXRD data. $Gd_{9.33-x}$ $Eu_x(SiO_4)_6O_2$ (x = 0.03, 0.05, 0.07, 0.09, 0.19, 0.28, 0.47, 0.65, 0.93, 1.40 and 1.87).∇ indicates the Gd_2SiO_5 impurity peaks. 106
6.2 Lattice parameters of the a)a, b)c and c)unit cell volume V for $Gd_{9.33-x}$ $Eu_x(SiO_4)_6O_2$ (x = 0.03, 0.05, 0.07, 0.09, 0.19, 0.28, 0.47, 0.65, 0.93, 1.40 and 1.87) as a function of Eu^{3+} content. The error bars are smaller than the data points. 108

6.3 a) View of the *ab* plane, b) schematic of the *ab* plane, c) c-direction for Gd1 sites and d) c-direction for Gd2 sites for the $Gd_{9.33}(SiO_4)_6O_2$ structure.[28] 109
6.4 Energy-level diagrams for Gd^{3+} and Eu^{3+} ions showing the relevant transitions in Eu^{3+}-doped $Gd_{9.34}(SiO_4)_6O_2$ phosphors. 110
6.5 Room temperature emission spectra of $Gd_{9.33-x}$ $Eu_x(SiO_4)_6O_2$ (x = 0.03, 0.05, 0.07, 0.09, 0.19, 0.28, 0.47, 0.65, 0.93, 1.40 and 1.87) under 275 nm excitation. Maximum energy splitting of $^7F_1$ ΔE is labelled. 111
6.6 Room temperature emission spectra of $Gd_{9.33-x}$ $Eu_x(SiO_4)_6O_2$ (x = 0.03, 0.05, 0.07, 0.09, 0.19, 0.28, 0.47, 0.65, 0.93, 1.40 and 1.87) as a function of the Eu^{3+} concentration. 112
6.7 Lifetime values according to Eu^{3+} content for the $^5D_0 \rightarrow {}^7F_5$ transition (614 nm) for $Gd_{9.33-x}$ $Eu_x(SiO_4)_6O_2$ (x = 0.03, 0.05, 0.07, 0.09, 0.19, 0.28, 0.47, 0.65, 0.93, 1.40 and 1.87) materials. 112
6.8 Judd-Ofelt intensity parameters estimated using Equation 6.2 from the emission spectra as a function of the Eu^{3+} concentration of the $Gd_{9.33-x}Eu_x(SiO_4)_6O_2$ (x = 0.03, 0.05, 0.07, 0.09, 0.19, 0.28, 0.47, 0.65, 0.93, 1.40 and 1.87) phosphors. Refractive index = 1.8. 113
6.9 Lifetime values - theoretical (blue diamond)and observed (green square) - as a function of the Eu $^{3+}$ doping level for the $Gd_{9.33-x}Eu_x(SiO_4)_6O_2$ (x = 0.03, 0.05, 0.07, 0.09, 0.19, 0.28, 0.47, 0.65, 0.93, 1.40 and 1.87) phosphors. 114
6.10 Variable-temperature laboratory PXRD patterns for the $Gd_{9.05}$ $Eu_{0.28}(SiO_4)_6O_2$ on warming and cooling between 18 °C and 527 °C. The artificial colour map shows intensity changes in the PXRD pattern. 115
6.11 Unit cell parameters as a function of temperature obtained from the Rietveld fit for laboratory PXRD data on warming (red) and cooling (blue) recorded for $Gd_{9.05}$ $Eu_{0.28}(SiO_4)_6O_2$. 116
6.12 Temperature-dependent luminescence of the $Gd_{9.05}$ $Eu_{0.28}(SiO_4)_6O_2$ phosphor at λ_{exc} = 275 nm. Colour scale marks the temperature from 25 °C (purple) to 475 °C (yellow). 117
6.13 Change transfer model fit (solid line) for temperature-dependent emission integrals of the experimental data (dots) for the $Gd_{9.05}Eu_{0.28}(SiO_4)_6O_2$ phosphor. 118
6.14 Maximum energy splitting of the $^7F_1$ manifold and lattice parameters as a function of temperature for the $Gd_{9.05}Eu_{0.28}(SiO_4)_6O_2$ phosphor. 119
6.15 Temperature-dependent Judd-Ofelt intensity parameters estimated from the emission spectra of the $Gd_{9.05}Eu_{0.28}(SiO_4)_6O_2$ phosphor. 120
6.16 Temperature-dependent lifetime values for the $Gd_{9.05}Eu_{0.28}(SiO_4)_6O_2$ phosphor. . . . 120
7.1 Rietveld fit of laboratory PXRD data for a) $CaCuSi_4O_{10}$, $R_{wp} = 6.49\%$, b) $BaCuSi_4O_{10}$, $R_{wp} = 4.20\%$, c) $K_2CuSi_4O_{10}$, $R_{wp} = 4.62\%$ and d) $BaCu_2Si_2O_7$, $R_{wp} = 4.26\%$. . . . 128
7.2 Image of the single crystals for a) $CaCuSi_4O_{10}$, b) $BaCuSi_4O_{10}$ and c) $BaCu_2Si_2O_7$. . 129
7.3 a) The tetragonal structure of $CaCuSi_4O_{10}$, space group *P*4/*ncc*. View along the *a* axis. b) View of CuO_4^{6-} in $CaCuSi_4O_{10}$, in a square planar environment. c) The tetragonal structure of $BaCuSi_4O_{10}$, space group *P*4/*ncc*. View along the *a* axis. d) View of CuO_4^{6-} in $BaCuSi_4O_{10}$, in a distorted square planar environment. e) The monoclinic structure of $K_2CuSi_4O_{10}$, space group $P2_1/m$. View along the *a* axis. f) View along the *b* axis of CuO_4^{6-} in $K_2CuSi_4O_{10}$, in a distorted square planar environment. g) The orthorhombic structure of $BaCu_2Si_2O_7$, space group *Pnma*. View along the *c* axis. h) View of CuO_4^{6-} in $BaCu_2Si_2O_7$, in a distorted square planar environment. Ca shown as light blue spheres, Ba as light green spheres, K as purple spheres, Cu as dark blue spheres, SiO_4^{4-} as grey tetrahedra and O as red spheres. CuO_4^{6-} in square plane corresponding to $CaCuSi_4O_{10}$ is shown in light pink and light blue for comparison of the distortion. 130
7.4 a) Diffuse reflectance, b) normalised absorption and c) emission spectra for $CaCuSi_4O_{10}$ (green), $BaCuSi_4O_{10}$ (blue), $K_2CuSi_4O_{10}$ (red) and $BaCuSi_2O_7$ (purple) powder samples. 131
7.5 Simplified energy level diagram of Cu^{2+} ions in a D_{4h} and C_{2v} crystal field environment in $CaCuSi_4O_{10}$, $BaCuSi_4O_{10}$, $K_2CuSi_4O_{10}$ and $BaCu_2Si_2O_7$ lattices. 132
7.6 Fitted decay curves (solid red line) of the luminescence decay experimental data (blue dots) for a) $CaCuSi_4O_{10}$, b) $BaCuSi_4O_{10}$ and c) $K_2CuSi_4O_{10}$, recorded after excitation at 658 nm. The residuals are offset for clarity. 134
7.7 Rietveld fit of laboratory PXRD data for $K_2CuSi_4O_{10}$, Rwp = 3.33%. 135

7.8 a) Topographic AFM image of $K_2CuSi_4O_{10}$ nanoparticles on two different sites (site 1 and site 2) and scales, and b) corresponding height profiles along the dotted lines in a). 136
7.9 EDS-SEM map images of $K_2CuSi_4O_{10}$ a) bulk and b) nanoparticles. Element colour mapping: potassium is purple, copper is red, silicon is green and oxygen is blue 136
7.10 Fitted lifetime parameters of the different cuprosilicate pigments, from powder samples. The error given on the lifetime values is the standard deviation from the fitting. The goodness of fit (χ^2_R) = 3.08. 137
A.1 Rietveld fit of the laboratory PXRD data. $Gd_{9.33-x}$ $Eu_x(SiO_4)_6O_2$ (x = 0.03, 0.05, 0.07, 0.09, 0.19, 0.28, 0.47, 0.65, 0.93, 1.40 and 1.87).∇ indicates the Gd_2SiO_5 impurity peaks. 146
A.2 Rietveld fit of synchrotron PXRD data for $K_2CuSi_4O_{10}$, R_{wp} = 11.42%. 148

Abbreviations

AFM: Atomic Force Microscopy
CRI: Colour-Rendering Index
CIE: Commission Internationale de l'Eclairage
CCT: Correlated Colour Temperature
CR: Cross-Relaxation
CFS: Crystal Field Splitting
ED: Electric dipole
EDX: Energy Dispersive X-Ray Spectroscopy
ET: Energy Transfer
FEG: Field Emission Gun
FWHM: Full Width at Half Maximum
LED: Light-Emitting Diode
LC: Luminescent Centre
MAC: Multi-Analysing Crystals
MD: Magnetic dipole
NP : Nanoparticle
PC: Phosphor-Converted
PXRD: Powder X-Ray Diffraction
QDs: Quantum Dots
QY: Quantum Yield
RE: Rare Earth
RGB: Red, Green, and Blue
SEM: Scanning Electron Microscopy
SSWL: Solid-State White Lighting
SXRD: Synchrotron X-Ray Diffraction
TM: Transition-Metal
UV: Ultraviolet
WLED: White LED

Declaration

The work presented in this thesis is entirely the work of the author, except where help is acknowledged from a named person, or a reference provided to a published source.

The research presented within was performed in the Department of Chemistry, Durham University, between October 2016 and September 2020. The results of this research have not been submitted for a degree in this or any other university. This thesis conforms to the word limit detailed in the Degree Regulation of the university.

Acknowledgement

This effort could not have been possible without the help of Prof. Ivana Radosavljevic Evans. I really appreciate her support and guidance during my PhD years. Under her supervision I got to be where I am today. Thanks to Prof. Gareth Williams, Prof. Andrew Beeby and Prof. Miroslav Dramicanin for the collaboration and help during this project.

Thanks and lots of love to my parents, Roberto and Irma, for shaping the person I am today and for still doing everything they can for me. Thank you to my sisters, Thalía and Ziomara, for the constant sibling rivalry that allowed us to build the best qualities in ourselves.

Thanks to my colleagues from the Evans group, it was very nice to share the office with every single one of them. Special thanks to Prof. John Evans that was a very good audience to all the rehearsals of my talks, to Luiza Araujo who joined me during the first half of my PhD and made me miss her for the other half, to Huiyu Liu for being my PhD sister, to Josie Auckett for all her help, to Chloe Fuller and Bettina Schwaighofer for always sharing tea time with me.

I also want to thank Alejandra Guillen, Eder Olivas, Henrike Philipp, Lioba Wendling, Rebecca Rutherford, Rodrigo Matus, Shitong Sun and all the friends I was fortunate to meet during my PhD student years. A special thanks to all of them that helped me survive both thesis writing and lockdown by cooking and baking delicious food.

I would like to also thank the financial support from the Mexican Secretary of Energy and CONACYT (SENER-CONACYT) through scholarship no. 447874. Thanks as well to the Durham University's Multidisciplinary Centre for Doctoral Training in Energy (Durham Energy Institute) where I was a member to expand my understanding to multidisciplinary topics.

This thesis is dedicated to my family, always to my family.

1 Literature review

Luminescent materials have a wide variety of applications including emissive displays, fluorescent lamps, light-emitting diodes (LEDs) and medical imaging. Based on the energy changes involved, there are two types of luminescent materials: upconversion (which can convert incident radiation into higher energy radiation) and downconversion (which can convert incident radiation into lower energy radiation) materials. The former do not experience Stokes shift but they tend to have lower efficiency than the downconversion materials as the probability of certain transitions decreases. For this reason, downconversion luminescent materials are the subject of intense research, primarily targeting their applications as phosphors for solid-state white lighting (SSWL) and NIR emitters for imaging.

The science of lighting devices has been changing over time and there has been an important effort to replace traditional lighting (incandescent, halogen, xenon and fluorescent light sources) with more energy-efficient, chemically more benign, dimmable and instantly-on devices with longer working lives. Hence, SSWL based on inorganic semiconductors has become a popular alternative. Solid-state lighting devices have the potential to surpass the limitations of the current technologies due to their unique properties such as small size, fast switching, high energy efficiency, controllable spectral power distribution, spatial distribution, colour temperature, temporal modulation and polarisation properties, brightness, longer lifetimes, excellent low temperature performance, robustness, reliability and added benefits like maintenance savings and environmental friendliness.

The wavelength of the light emitted by the LEDs is determined by the band gap of the semiconductor. This puts a limit to the colour of the light emitted, allowing only a single-colour light. Therefore, SSWL relies on phosphors to be able to emit in a broad visible spectrum. Different white-emitting phosphors have been researched in the last few years but there are still a few characteristics that can be improved such as higher quantum yield, chemical and thermal stability and colour coordinates near the white point.

Development of inorganic luminescent materials that emit in the near infrared (NIR) region is also important. The best known application for NIR emitters is fluorescence imaging (wavelength between 650 nm and 1700 nm), where the luminescence absorption and autofluorescence of biological tissue is minimal. The majority of NIR emitters used in this now traditional application are in the NIR region <900 nm, where the imaging resolution and penetration depths are limited.

This chapter reviews the strategies and requirements for inorganic phosphors for SSWL and the mechanisms behind luminescence properties and luminescence quenching processes. It then discusses the important activators used during this project and their properties. Finally, it provides a list of phosphors classified according to their different structure types. This chapter provides a general introduction to the subject to the particular materials studied are presented in chapter 3 to 7.

1.1 Technological uses of luminescent materials

1.1.1 Solid-state white lighting (SSWL)

1.1.1.1 Quantification of SSWL quality

The spectral sensitivity of visual perception of bright light is described by the luminosity function, shown in Figure 1.1. The Commission Internationale de l'Eclairage (CIE) standardised the colourimetry for photopic vision, represented in Figure 1.2. In this diagram any colour in the visible spectrum can be represented by coordinates (x,y), also known as chromaticity coordinates. In Figure 1.2, the locus outlining represents the monochromatic wavelengths. The standard equal energy white light coordinates are at $(\frac{1}{3},\frac{1}{3})$, which is the ideal for white light emission according to the 1931 CIE.[1]

The Planckian locus, curve found in the middle of the CIE diagram (Figure 1.2), denotes the colours of an ideal black body at certain temperatures. This is known as the colour correlated temperature (CCT), which ranges from 1000 K (a more red colour) to 25000 K (a more blue colour). Any light can be assigned a CCT value. It is worthwhile to mention that warm light corresponds to more yellow-red light (CCT=1000-3500 K) and cold light corresponds to more blue light (CCT=6000-25000 K), passing through neutral (CCT=3500–4500 K) and 'daylight' (CCT> 5500 K).

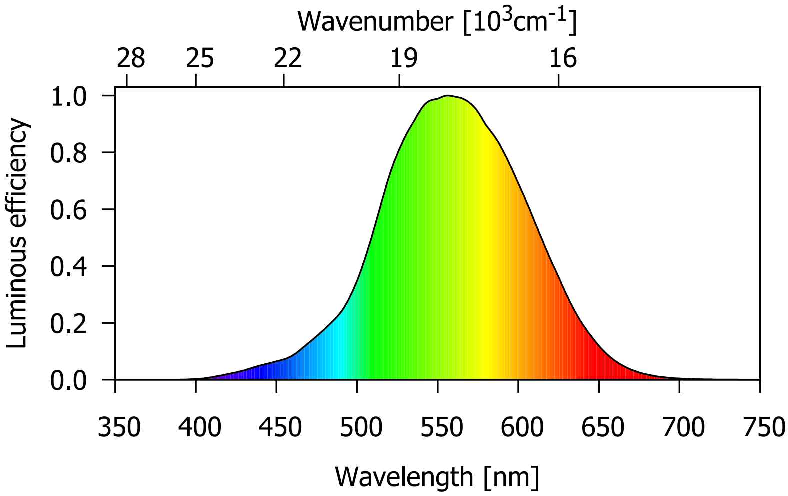

Figure 1.1: CIE 1931 photopic luminosity function, response to the light of a typical human eye. Adapted after eye sensitivity function.[2]

Another indicator to quantify the quality of light is the colour-rendering index (CRI). This parameter assesses the ability of certain light to illuminate an object and retain its true colours, in comparison to an ideal or natural light. It ranges from 0 to 100, where a black body radiator has a CRI of 100 by definition. A broadband emission in the visible spectral region (400-700 nm) provides a high CRI value.[3] The specifics of how to calculate the colour coordinates, CCT and CRI will be described in section 2.3.3.

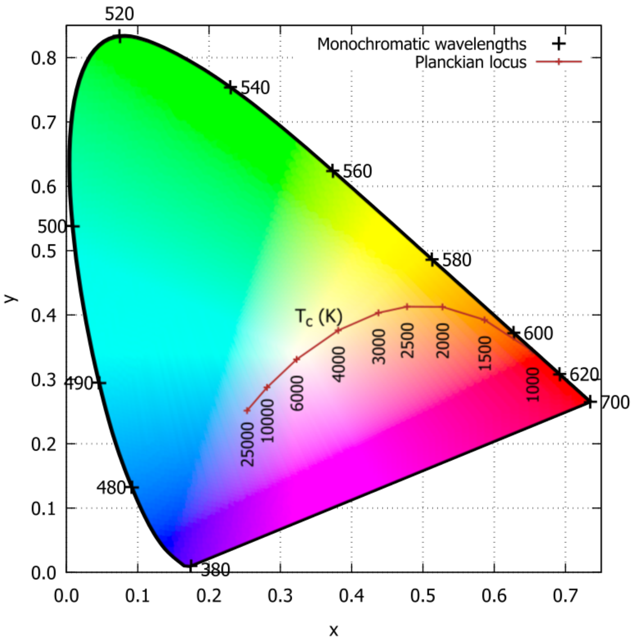

Figure 1.2: The 1931 CIE standard observer diagram.[1]

1.1.1.2 Light-emitting diodes (LEDs)

LEDs are the most important technology for the development of SSWL. LEDs are semiconductor devices that emit light due to the electroluminescence effect.[4] The most commonly used semiconductor is gallium nitride (GaN) with a binary III/V direct band gap.[5] LEDs consist of a p-type semiconductor and an n-type semiconductor of the same kind. Figure 1.3 shows the process of recombination of the electrons (from the conduction band) in the semiconductor with electron holes (from the valence band), which releases energy in the form of photons. The separation of these bands is known as the band gap. The energy of the photon, given by Equation 1.1, is directly related to the band gap size.

$$E = h\nu = hc/\lambda, \tag{1.1}$$

where E is the energy, h is the Planck constant, ν is the frequency of the light, c is the speed of light and λ is the wavelength of the light emitted. Hence, the colour of the light emitted is determined by the photon energy. The bandgap range for red LEDs is 1.8-2.0 eV, for green is 2.1-2.3 eV and for blue is 2.6-3.0 eV.[6] Modern high-energy LEDs are obtained by using multiple semiconductors or a layer of a light-emitting phosphor on the semiconductor device.[7, 8]

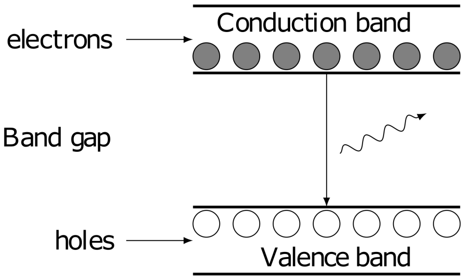

Figure 1.3: Production of light emission in LEDs.[6]

1.1.1.3 Strategies for SSWL

There are various strategies to create white light with a solid-state device (Figure 1.4):[3]

1) Phosphor free SSL (Figure 1.4a): red, green and blue (RGB) LEDs. This strategy employs three or more LED chips that emit at different wavelengths.
2) Phosphor-converted LEDs.
    a) Blue-emitting LEDs (InGaN) coated with a yellow phosphor (*i.e.* YAG: Ce^{3+} phosphor.[5]) (Figure 1.4b).
    b) Ultraviolet (UV) LEDs coated with RGB tricolour phosphors (*i.e.* red $CaAlSiN_3:Eu^{2+}$, green $Ba_2MgSi_2O_7:Eu^{2+}$ and blue $(Sr,Ba)_3MgSi_2O_8:Eu^{2+}$ phosphors[9]) (Figure 1.4c).
    c) Ultraviolet (UV) LEDs coated with a single-phase phosphor that emits at different wavelengths (*i.e.* single-phase $Li_2Gd_4(WO_4)_7:Dy^{3+}$, Tm^{3+}.[10]) (Figure 1.4d).

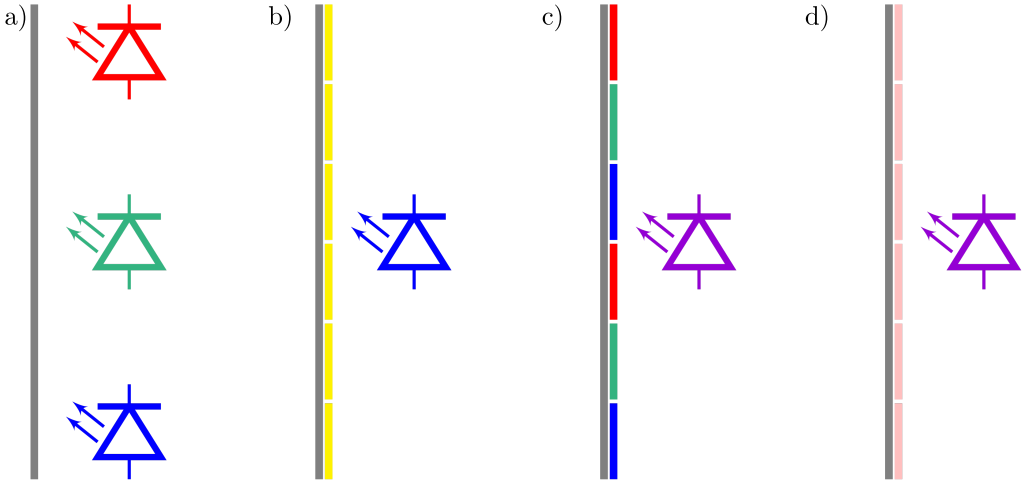

Figure 1.4: Schematics of the different SSWL strategies: a) separate R, G and B-emitting LEDs (red, green and blue diode symbol), b) yellow down-converting phosphor with a blue LED (blue diode symbol), c) RGB phosphors excited by a UV LED (purple diode symbol), and d) single-phase phosphor with UV LED excitation. Grey line = substrate, yellow lines = yellow-emitting phosphor, red lines = red-emitting phosphor, green lines = green-emitting phosphor, blue lines = blue-emitting phosphor, pink lines = single-phase white-emitting phosphor.

1.1.1.3.1 Phosphor-free/Tricolour LEDs

The most energy efficient strategy is to use multiple LED chips which emit at different wavelengths in a single device and give the optimum white-light output. These present an important advantage over phosphor-converted devices as the latter have an energy loss due to the Stokes shift (the energy difference when an emitted photon has less energy than the absorbed photon).

On the other hand, the different ageing rates and responses to temperature and to the changes of voltage of each LED component counteract the benefits of this strategy due to the need for complex electronics to provide the different currents needed. In these multiple LED chip devices, the colour temperature is tuneable by varying the power of the individual LED components, but this adds difficulty and cost. The yellow and green LEDs have low efficiencies, making them sub-optimal components of a tricolour LED device. The narrow radiation of the white light also leads to poor colour rendering.[11] Taking account of all of this, complex electronics to produce different currents are needed.

1.1.1.3.2 Phosphor-converted LEDs

Using a LED with downconverting phosphors is the other important strategy but, as previously mentioned, the Stokes shift problem is present. This shift occurs when the energy absorbed by the activator is higher than the energy of the photon emitted, causing an energy loss. To overcome this energy loss, also known as a quantum deficit,[12] an LED with a wavelength as long as possible must be used to minimise the difference between the absorbed and the emitted energy, hence minimising non-radiative transitions. Taking into account the desired colour rendering and colour temperature, in this kind of LEDs there is a trade-off between high colour rendition, low correlated colour temperatures and luminous efficacy.

In order to obtain phosphors for use in SSWL, certain requirements need to be met:[13]

- the excitation spectrum of the phosphor needs to be matched with the emission of the LED and an emission spectrum showing desirable visible light leading to an expected white emission must be obtained;
- efficient luminescence with a high fluorescence quantum efficiency, ratio of photons absorbed to photons emitted, at working temperatures needs to be obtained;

- high thermal quenching temperatures, for the emission and excitation spectra are required, avoiding materials that tend to present emission loss at LED working temperatures;
- excellent chemical, temperature and irradiation stability need to be obtained;
- uniform particle morphology, elimination of hazards and a reasonable production cost need be assessed.

An example of these phosphor-converted LEDs is the current commercially available white LED (WLED). It employs a combination of a blue LED chip with a yellow downconverting phosphor that allows some of the exciting blue radiation to bleed through, which is also known as partial downconversion. The drawback of this LED is that its white light has an intrinsic cold colour which is not ideal for residential applications. The LED device most commonly commercially used contains an InGaN blue LED, coated with YAG:Ce yellow-emitting phosphor. The lack of the red component and the instability of blue band emission from the blue LED chip[14] results in a poor colour rendering index and low stability of the colour temperature.[5]

Semiconducting nanocrystals, also known as quantum dots (QDs), can also be used as blue-absorbing phosphors as their optical properties can be finely and smoothly tuned by adjusting their size, surface to interfacial structure and chemical composition.[15] The colour to size relation has been studied in solid materials and a quantum-related particle size effect can tune semiconductor band gaps.[16]

Another approach uses a UV LED chip and a combination of RGB downconverting phosphors to cover a broad range of emission wavelengths. This gives good colour rendering and a stable emission colour, but each phosphor has a different degradation rate.[17] Efficiency degradation can happen gradually and be caused by the doping element having a change of valence through oxidation, the crystal lattice degrading, the activators diffusing through the material or a chemical reaction with the environment taking place at the surface. This degradation depends on the frequency of the driving current (which is also called 'brightness saturation'), the luminance level (the intensity of the light emitted from the surface per unit area in a certain direction), and the temperature (which is known as 'thermal quenching').[18] Hence, the best tactic to create a UV LED with RGB downconverting phosphors may be to use single-phase phosphors.

1.1.1.4 History of high-energy LEDs suitable for SSWL

Electroluminescence was discovered in 1907. Passing a current through SiC produced blue dim light but it was not until 1969, when the first blue LED, a SiC film with a p-n junction was fabricated. This LED was reported to emit at 590 nm with a total external efficiency of $\sim 0.0001\%$.[19] Over the next decades blue SiC LEDs were researched, a considerable improvement was achieved until 1993, when an LED with an emission peak at 470 nm with a power efficiency of $\sim 0.03\%$ was produced.[20, 21] These relatively low efficiencies were due to the indirect band gap of SiC. In an indirect band gap semiconductor, the valence band and the conduction band have different momentums. This shift in the momentum requires a phonon assisted transition to go from the valence band maximum to the conduction band minimum, this is also known as recombination process. Hence, there is low probability of these three entities interacting.

In 1960s, the visible light LED technology was boosted with the development of green GaP LEDs[22] and red Ga(P,As) LEDs[23] (which had enough brightness for use in indicator applications but not enough for white lighting). However, the development of high-energy (blue or UV) LEDs remained a challenge as the band gap needs to be considerably large. A clear candidate to produce blue light was GaN but this tends to be naturally n-type and at the time there was a difficulty in producing the necessary p-type. The development of the first p-type doping of GaN was reported in 1989.[24] This device was not very bright and further optimisation was needed. In 1994, the first InGaN/GaN double heterostructure blue LEDs with an active Zn-doped InGaN layer were fabricated. These novel blue LEDs presented the highest efficiency reported for a blue LED, with an emission at 450 nm and an external quantum efficiency of 2.7%.[5] In 1995, UV-stimulated emission from the AlGaN/GaN double heterostructure and violet-stimulated emission from the AlGaN/GaInN double heterostructure were achieved. UV/blue light emitting p-n homodiodes were developed in an AlGaN/GaN/GaInN stacked heterostructure diode.[25] Further work in this field was done by Nakamura, Akasaki and Amano, which led them to obtain the 2014 Nobel Prize in Physics. The highest internal quantum efficiency obtained for the best blue LED is at least 75%.[26]

Since the development of gallium nitride based LEDs (GaN/InGaN/AlGaN),[25] UV LEDs have been sought for use in various applications such as medical equipment, air cleaners, water purification, environmental sensors and for exciting phosphors.[27, 28] The development of efficient UV LEDs is particularly important as the majority of phosphors have a high downconversion quantum efficiency when excited at <370 nm (UV region). Furthermore, UV LEDs in combination with phosphors provide a better CRI value, as UV lies outside visible light, avoiding the unstable blue band emission from the blue LED chip. In 2002 a high-power InGaN-based UV LED was fabricated, emitting at 365 nm and with an external efficiency of 6.9%.[29] Development to increase the power and efficiency of UV LEDs has been observed in the last decade. In 2014, their external quantum efficiency was increased to 30% at a wavelength of 365 nm.[28] In 2015, for emission wavelengths between 250 nm and 300 nm inside the deep-UV region, their external energy efficiency still ranged below 5%.[30] In 2016, the external quantum efficiency was improved using direct bonding of the lens and the LED chip, obtaining 4.56% and 10.1% for 255 and 280 nm UV LEDs respectively.[31] In 2017, a transparent AlGaN:Mg contact layer, a Rh mirror electrode, a patterned sapphire substrate and encapsulating resin were introduced into UV-LEDs. These new features implemented increased their external quantum efficiency to 20%.[32] The highest external quantum efficiency for a deep UV LED has been reported to be 13.5% higher than previously reported. This was achieved by optimising the electron blocking layer in the LED.[33]

1.1.2 Near Infrared emitters

The near infrared (NIR) imaging window falls in the region of minimal tissue absorbance and autofluorescence between 650 nm and 1700 nm. Optical imaging using NIR fluorescence is a prospective approach to visible fluorescence imaging which can improve the imaging performance and signal-to-background ratio for *in vitro* and *in vivo* imaging. The NIR region has been divided into different channels, the NIR-I channel in the 700-900 nm range, the NIR-II channel in the 900-1300 nm range, the NIR-IIa channel in the 1300-1400 nm range and the NIR-IIb channel in the 1500-1700 nm range.[34] NIR-I has been under extensive study for clinical application in the last few years but its use is limited to detailed biological study for micrometric resolution and 0.2 mm depth analysis. The NIR-II channel has lower signal attenuation, a penetration depth of 1-3 mm and an even lower tissue autofluorescence.[35]

In addition, the use of NIR emitters spans a large group of applications. Among these are NIR-emitting codes, where quantum dots (QDs) exhibit significant advantages in fluorescent encoding owing to their excellent optical properties.[36] The fluorescence emission of QDs can be tuned by means of adjusting their structure and composition. There is a wide group of doped quantum dot NIR emitters, such as Cu-doped CdS[37] and Cu-doped InP[38] with emission at 722 nm and 950 nm respectively under UV irradiation. Mn-doped CdS are reported to emit at 820 nm with a quantum yield of 15%.[39] CdTeS:5.6% Fe has been reported to emit at 738 nm.[40] Monodispersed Ni-doped CdTeSe/CdS shows photoluminescence spectra tuneable from 750 to 820 nm.[41]

Long-lasting phosphors can be applied in *in vivo* bioimaging since the phosphors can be excited before administration into biological tissues and the NIR persistent luminescence can last up to several hours.[42] The advantage of this imaging process is that autofluorescence can be eliminated by removing the external excitation source. Selected illustrative examples of persistent NIR emitters are given in Table 1.1.

Material	λ_{emi} (nm)	λ_{exc} (nm)	Afterglow time
$Ca_{0.2}Zn_{0.9}Mg_{0.9}Si_2O_6:Eu^{2+},Dy^{3+},Mn^{2+}$[43, 44]	600-800, $\lambda_{max} \sim 690$ nm	340	100 s
$Zn_3Ga_2Ge_20_{12}:Cr^{3+}$[45]	650-1000, $\lambda_{max} \sim 696$ nm	400	5 min
$LaAlO_3:Mn^{4+}$[46]	$\lambda_{max} \sim 731$	336	10 min
$Y_3Al_2Ga_3O_{12}:Nd^{3+},Ce^{3+},Cr^{3+}$[47]	880, 1064 and 1335	460	60 min
$Y_3A_{l2}Ga_3O_{12}:Er^{3+},Ce^{3+},Cr^{3+}$[48]	1450-1670	442	5 min
$Zn_3Ga_2GeO_8:Cr^{3+},Yb^{3+},Er^{3+}$[49]	700	980	60 min

Table 1.1: Persistent NIR emitters propierties.

The vast majority of pigments are transparent to infrared radiation but there are a few exceptions, such as $xBaSO_4{\cdot}yBaMnO_4$, which is also known as manganese blue and which absorbs radiation in the visible and NIR regions between 500 and 1250 nm and emits at 1300 nm with a photoluminescence quantum yield of 0.5%.[50] The $SrCuSi_4O_{10}$ pigment has an emission at 956 nm under excitation at 620 nm. This pigment was developed based on two historical pigments, Egyptian blue $CaCuSi_4O_{10}$ and Han blue $BaCuSi_4O_{10}$, which emit at 910 nm under 637 nm excitation and 977 nm under 620 nm excitation respectively.[51, 52] Moreover, this optical property was first applied in non-destructive pigment identification technique for historical artefacts. The NIR luminescence in these pigments is attributed to the Cu^{2+} ions in the material, which are found in a square planar environment. Furthermore, Cu(II) is rarely found in a regular octahedral environment due to the geometrical distortion caused by the Jahn-Teller effect.[53] This geometrical behaviour is also observed in Fe(II)[54]- and Pt(II)[55]-containing compounds. Consequently, it has been suggested that the NIR emission of the Pt(II)[55] chromophore is also related to the square planar environment where the emission is related to the Jahn-Teller effect. Hence a complete study of the relationship between the Cu^{2+} square planar environment and the NIR luminescence is needed.

1.1.2.1 The Jahn-Teller effect

The Jahn-Teller effect concerns the distortions associated with degenerate energy states that cannot be stable due asymmetric electron ocuppancy.[56] Jahn-Teller distortions are commonly related to transition metal centres. These distortions strongly affect the electron distribution within the material and the position of their atoms.[57]

There are a few important considerations regarding the Jahn-Teller theorem:[58]

- A distortion can be predicted based on the degenerate state. There is no indication of the type of geometric distortion that will occur.
- To predict the magnitude of the distortion, detailed calculations of the energy of the entire complex must be made.
- If the undistorted configuration has a centre of symmetry, so also must the distorted equilibrium configuration, as the distortion is observed in the elongation of bonds.

As discussed before Cu^{2+} ions (d^9 configuration) are rarely found in a regular octahedral environment, as they are subject to Jahn-Teller distortion. The distortion in Cu(II)-containing compounds can be so extreme that the Cu(II) coordination number changes from six to four, forming a square planar coordination polyhedron.[59] Figure 1.5 shows the crystal field splittings for different possible distortions that the energy levels of Cu^{2+} can experience, from the octahedral (O_h) symmetry to the D_{4h} symmetry or even to the non-centrosymmetric C_{2v} symmetry.[60] The case of the distortion to the C_{2v} symmetry has been observed before, where the distortion goes from an environment with a centre of symmetry to one without, therefore the constant inversion centre theorem is not fulfilled.[61]

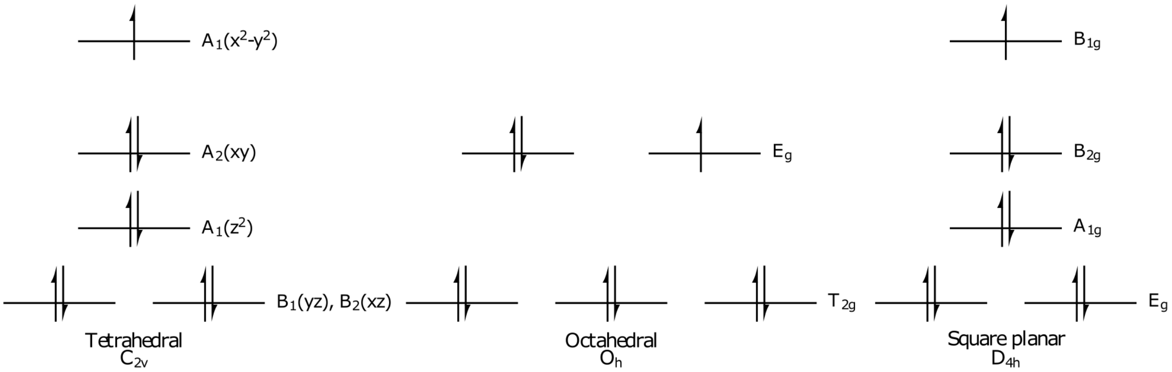

Figure 1.5: Schematic of the crystal field splittings for the different coordination geometries.[60]

1.2 Photoluminescence

In order to design and optimise phosphors it is necessary to understand the process of photoluminescence. The photoluminescence process occurs when a molecule excited by light of wavelength λ_1 decays to a lower energy-excited electronic state and then emits light of wavelength λ_2 as it radiatively decays to its ground electronic state.[62] Figure 1.6(a) shows a system consisting of a host lattice and a luminescent centre (activator A). In this scenario, the exciting radiation is absorbed by the activator, taking it to its excited state. The activator, known as the luminescent centre (LC), then returns to the ground state by emitting radiation, although a non-radiative return can also occur, which is indicated as 'heat' in Figure 1.6(a). The simplest way to understand a non-radiative process is as a transition from an excited level to a lower level, where part of the energy is dissipated into phonons instead of photons. Unlike a radiative transition (which depends of the emission intensity and the number of photons), the rate of the process depends on the energy of the phonons and the energy difference between the initial and final levels.[63]

In many cases, this process is a little more complicated as the exciting radiation is not absorbed by the activator but by another ion, a sensitiser S (*i.e.* Gd^{3+}), which absorbs the exciting radiation and transfers it to the activator A (*i.e.* Dy^{3+}, Tb^{3+}, Eu^{3+}). See Figure 1.6b).[64]

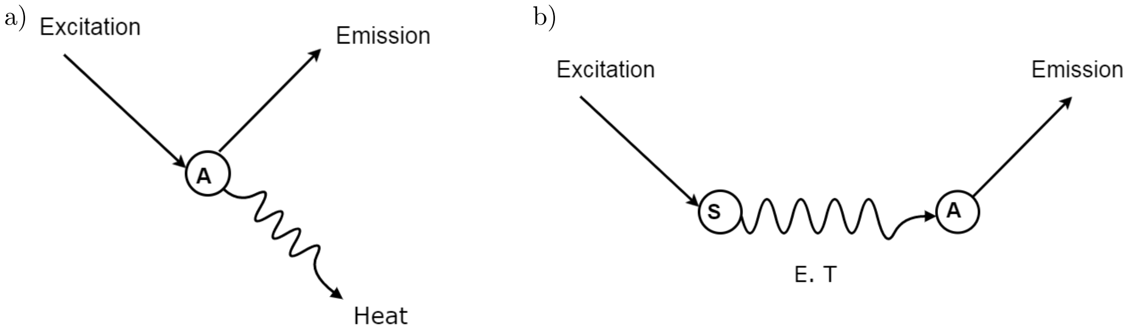

Figure 1.6: Luminescence processes. a) Luminescent ion A. b) Energy transfer from a sensitiser S to an activator A.[64]

The energy transfer mechanisms in phosphors can result from many competing interactions. The mechanisms involved in energy transfer processes between ions are (illustred in Figure 1.7):[65]

a. Resonant radiative transfer. This process occurs through emission from a sensitiser and reabsorption by an activator. The efficiency of this energy transfer depends on the overlap of the sensitiser emission and the activator absorption energies.

b. Resonant non-radiative transfer. Direct energy transfer between a sensitiser and an activator (with $\Delta E_s = \Delta E_a$). This process can occur through dipole-dipole (d-d), dipole-quadrupole (d-q) or quadrupole-quadrupole (q-q) interactions, depending on how the charge distribution interacts between these ions.[66]

c. Multiphonon-assisted energy transfer. This process occurs when an excited sensitiser passes energy to a lower energy activator via phonons.[67]

d. Cross-relaxation (CR). This process, also known as self-quenching, is an energy transfer between two identical ions. It occurs when the de-excitation of an ion causes the excitation of a low energy ion.

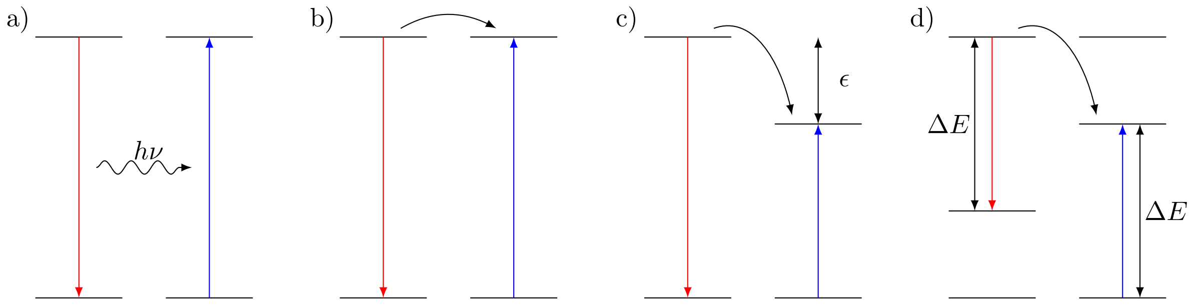

Figure 1.7: Energy transfer mechanisms between ions.[65] a) Resonant radiative energy transfer. b)Resonant non-radiative energy transfer. c) Multiphonon-assisted energy transfer. d) Cross-relaxation between two identical ions. The red and blue arrows represent de-excitation and excitation. The black arrows represent the energy transfer. ϵ is energy mismatch. ΔE is the energy difference.

The design of the energy transfer processes (together with doping concentration and reaction conditions) involved in the ion-ion interactions between multiple ions (activators and sensitisers) can tuned to control the photoluminescence of novel phosphors.[13] A vast group of ion-ion interaction couples have been reported, including Eu^{2+}-Mn^{2+}, Ce^{3+}-Mn^{2+}, Eu^{2+}-Ce^{3+}, Ce^{3+}-Tb^{3+}, Eu^{2+}-Tb^{3+}-Mn^{2+}, Dy^{3+}-Eu^{3+} and Tb^{3+}-Eu^{3+}. These ions commonly are rare earth (RE) ions as the excitation and emission energies can be predicted by the Dieke diagram. The characteristics of RE ions are described in more detail in section 1.3.

1.2.1 Term symbols and selection rules

The Russell-Saunders term symbol, $^{2S+1}\mathrm{L}_J$, is the most common way to designate electronic states. In this nomenclature, the orbital (L), spin (S) and total (J) angular momenta are specified for all the electrons. Capital letters S, P, D, F, G, H,... for L=0, 1, 2, 3, 4, 5, ... respectively are used in direct analogy to the atomic orbitals s, p, d, f, g, h... The electron spin multiplicity (2S+1) denotes the state as a 'singlet' when $S = 0$, a 'doublet' when $S = \frac{1}{2}$ and a 'triplet' when $S = 1$, etc.[68, 69]

'Allowed' and 'forbidden' transitions between these states are defined by selection rules.[70] Transitions between states with the same parity cannot occur, Δl = ±1, which is called the parity selection rule. Transitions can occur between states with the same spin, ΔS = 0, which is called the spin selection rule. However, certain forbidden transitions have a high probability of not occurring, but can be observed as weak bands.

To determine the ground state of an ion it is necessary to follow Hund's rules:[71, 72]

- the spin multiplicity has to be as large as possible, 2S + 1;
- if there is more the one term with the same spin multiplicity, the term with the highest total orbital angular momentum (L) is the ground state;
- for electronic shells that are less than half filled, the ground state has the lowest possible J value. For electronic shells that are more than half filled, the ground state has the highest possible J value.

In the case of the Dy^{3+} ions with a $4f^9$ configuration, the angular quantum momentum is l = 3, the magnetic quantum number is m_l=-3,-2,...,+2,+3, and the electrons occupy the orbitals shown in Figure 1.8. The spin angular momentum is S=5/2, the orbital angular momentum is L=5, hence the total angular momentum is J=5+5/2,...,—5-5/2—=15/2,13/2,...,7/2,5/2. Following Hund's rules, the spin multiplicity is 2S+1=6, the highest orbital angular momentum is L=5 so the term is H, and the 4f shell is greater than half filled so the highest J value is 15/2. The ground state for Dy^{3+} is $^6\mathrm{H}_{15/2}$.

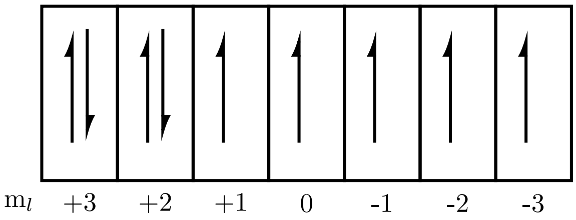

Figure 1.8: Dy^{3+} electronic configuration.

1.2.2 Concentration, thermal and lifetime effects

The concentration of excited activators is very relevant to the efficiency of phosphors in SSWL. The main effect responsible for this is 'Auger recombination', a non-radiative phenomenon where an electron transitions from an excited state to a lower energy state hole and the excess energy is passed to another electron instead of there being a photon emission. This effect is known to be responsible for concentration quenching in phosphors and is inversely proportional to the quantum efficiency. The 'droop' effect can be caused by a quenching emission interaction, which is also known as excited state absorption. It can be exhibited by red-emitting materials and it can happen to different extents. One way to avoid the droop is low doping, which reduces absorption but also reduces the concentration of excited centres. To study the cause of the droop it is necessary to obtain the balance of the excitation and relaxation rates of the activators (see Equation 1.2).[73]

$$G = (a + b)n + dn^2, \tag{1.2}$$

where G is the generation rate of excited activators per unit volume per second, n is the concentration of excited activators, a and b are the non-radiative and radiative relaxation rates and d scales a non-linear non-radiative process, or droop. The quantum efficiency for one-dimensional geometry is then given by Equation 1.3:

$$QE(x) = \frac{b}{a + b + dn(x)}. \tag{1.3}$$

The critical distance R$_C$ between excited activators can be used to understand the energy transfer mechanism between the activators. R$_C$ is given by Equation 1.4, which is also known as the Blasse equation:[74]

$$R_C \sim 2[\frac{3V}{4\pi X_C N}]^{1/3}, \tag{1.4}$$

where V is the volume of the unit cell, N is the number of host cations in the unit cell and X$_C$ is the critical concentration of doped ions.

Another important quantitative factor to considerate in the phosphors is heat. The heat generated by the LED chips while they function can be transferred to the phosphors, activating phonon modes and hence decreasing the efficiency and luminous intensity, and changing the colour rendering. Preservation of the phosphor emission intensity with an increase in temperature is known as thermal stability. The probability of photoionisation or of charge transfer is high if the excited state energy of the RE is near the conduction band of the host material, . This decreases the quantum efficiency. Because of this it is best to choose a host material with a band gap in the UV region far from the activator absorption energy.[3]

A quantitative method to describe the radiative and non-radiative relaxation is the quantum mechanical single configurational coordinate (QMSCC) model (Figure 1.9). In this model parabolas describe the potential energy wells of the ground and excited states. It can be used to study non-radiative relaxation at higher temperatures causing luminescence quenching. Thermal promotion of the 5d electron to the conduction band of the host crystal causing a 5d-4f crossover is one of the primary mechanisms in non-radiative transitions.[75]

Thermal quenching is an important phenomenon as it affects the efficiency and alters the colour of the phosphor at LED working temperatures (150 °C). The excited luminescent centre can be thermally activated through phonon interaction and then released at the crossing point between the excited and ground states (black dot in Figure 1.9). A rigid and thermally stable host structure is needed to minimise the emission loss with increasing temperature.[76] The thermal quenching temperature is defined as the temperature at which the phosphor photoluminescent emission intensity value becomes 50% of its value at room temperature.[77]

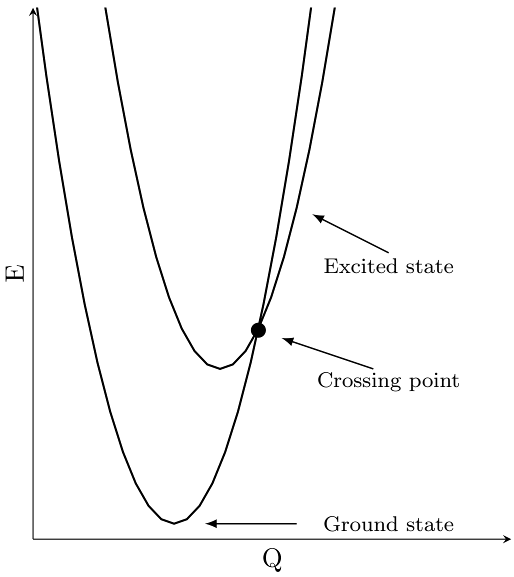

Figure 1.9: Configurational coordinate diagram showing the thermal quenching process.[75]

The human eye detects temporal changes in light down to ∼0.1 s, anything longer than this is phosphorescence. Therefore, a short decay time (ns) is desirable for lighting applications. Transitions between $4f$ levels have long decay times (μs and ms) due to their electric dipole forbidden nature. $4f$ and $5d$ transitions are shorter (∼ 10 ns), with the observed luminescence lifetimes for Ce^{3+} being in the order of 10 ns, which is 20-30 times shorter than for Eu^{3+}.[78]

In the luminescence process, radiative and non-radiative transfers have different rates (K) of occurrence. The lifetime is the inverse of the total decay rate, and is described by Equation 1.5

$$\tau = \frac{1}{K_{rad} + K_{nrad}}, \tag{1.5}$$

where K_{rad} and K_{nrad} are the decay rates of the radiative and non-radiative processes respectively.

Activator ion decay has an exponential behaviour, which is described by Equation 1.6:

$$I(t) = I_i exp(\frac{-t}{\tau_i}), \tag{1.6}$$

where I(t) is the luminescent intensity at time t, I_i is the ith component of the intensity and τ_i is the ith component of the decay time.

1.3 Rare earth (RE) ions

RE ions are important in the designing of phosphors, as the energy levels can be predicted using the Dieke diagram, and they are often used as luminescent centres. RE ions, also called lanthanides (or lanthanoids), have an incompletely filled $4f$ shell which is shielded by filled $5s^2$ and $5p^6$ orbitals. Hence, the influence of the host lattice on optical transitions in the $4f$ shell is minimal, although some is present. In lanthanide complexes, the splitting of the $4f$ orbitals by the crystal field is small not to impact the composition of the many-electron wave functions of the free ion.[109] The energy levels of the activator ions determine the excitation and emission properties and are directly related to the $4f$ and $5d$ energy levels. The $4f$ orbitals of the electrons of lanthanide ions are represented by the quantum number $n = 4$ and the orbital angular momentum number $l = 3$.

There are two types of optical transitions in RE ions: between $4f$ levels and between $4f^{n-1}5d^1$ and $4f^n5d^0$ levels. The majority of the interactions are by electric fields through electric dipole (ED) transitions. The intra-$4f^n$ optical transitions of lanthanides are known to include magnetic dipole (MD) transitions.[110] The emission of the $4f^n$ transitions tend to result in sharp narrow lines due the shielding by the $5d$ electrons. Therefore, the host does not play much role in the excitation and emission energies. Figure 1.10 shows the Dieke diagram, where the predicted energy levels are presented. The binding energy of the $4f$ electrons can be explained by Jørgensen theory,[111] which determines the excitation and emission energies of $4f^{n-1}5d^1 \rightarrow 4f^n5d^0$ transitions, as the lowest $5d$ level does not change much compared with the change in the $4f$ energy levels with the number of electrons in the atom.[64]

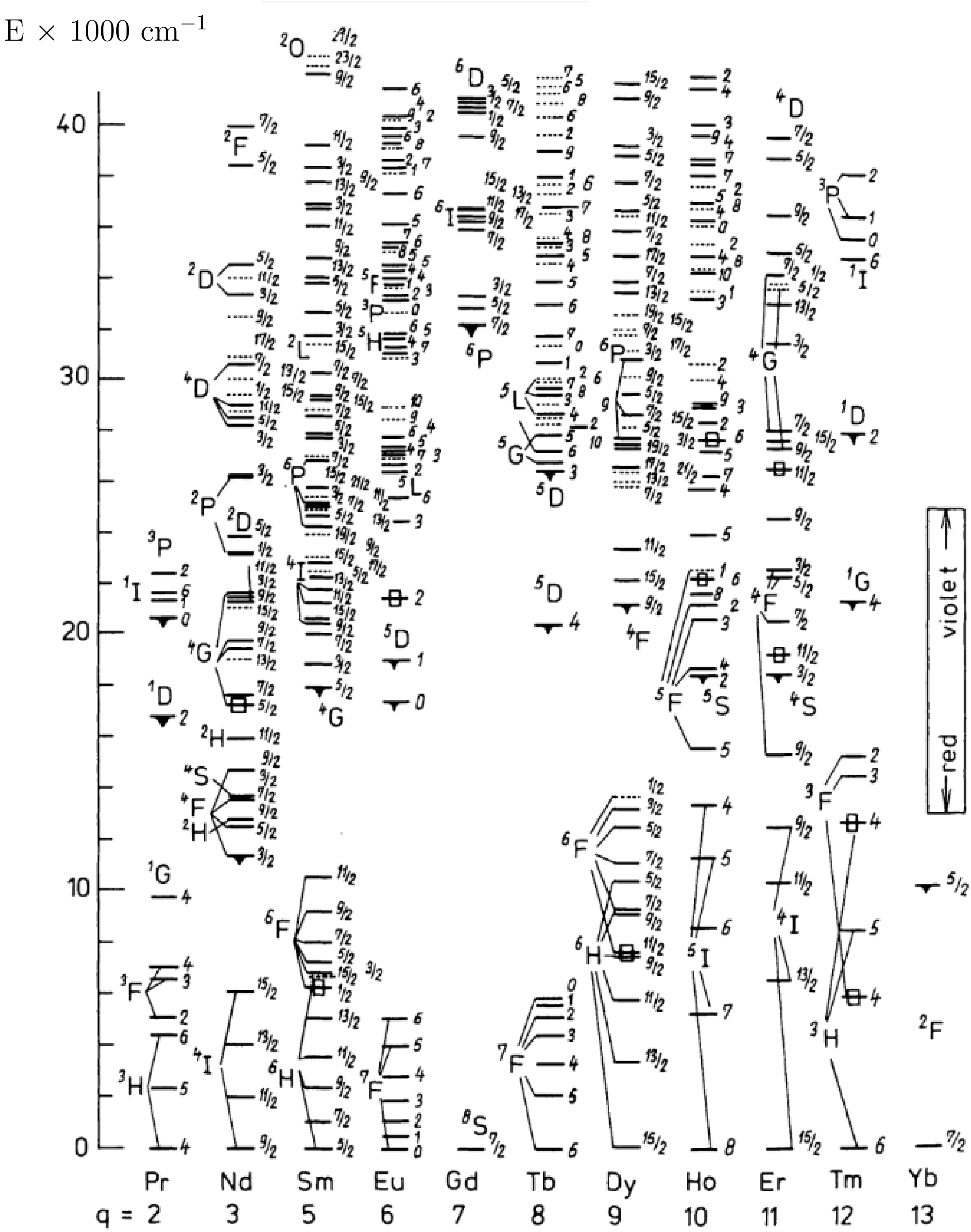

Figure 1.10: Dieke diagram.[112]

Activator ions have a large energy gap between the $4f$ ground state and the $5d$ excited state. This gap decreases by crystal field splitting (CFS) and a downward shift of the $5d$ centroid, known as redshift (lower energy).

The broad range of emission and excitation energies in $4f^{n-1}5d^{1} \rightarrow 4f^{n}5d^{0}$ transitions can be described by the Franck-Condon principle, which expresses different vibrational states of the $4f$ and

5*d* levels resulting in transitions with many different energies and breaking of the degeneracy of the 4*f* ground state, which itself is a result of a few effects, such as spin-orbit coupling of the 4*f* ground state into multiple levels.

Spin-allowed $f \leftrightarrow d$ transitions in trivalent lanthanides depend on two parameters: the type of lanthanide ion (Ln) and the type of host crystal (A). The host crystal causes a depression D(A), which is described in Equation 1.7.

$$D(Ln, A) = E(Ln, free) - E(Ln, A), \tag{1.7}$$

which can then be adapted for the Ce-doped materials, which has been more broadly studied, as in Equation 1.8.

$$D(A) = E(Ce, free) - E(Ln, A), \tag{1.8}$$

where E(Ce,free) (49.34×10^3 cm^{-1}) is the 4*f*-5*d* transition energy of the free Ce^{3+} ions. The influences of the host and the ion are additive, as they act independently from each other. Using this equation it is possible to predict *f*-*d* transition energies with an accuracy of ~ 600 cm^{-1} (equivalent to a wavelength of ± 5 nm).[113] Unlike other transitions, the hypersensitive transitions in RE ions are significantly dependent on the environment around them. The hypersensitive 4*f*-4*f* transitions occur when $\Delta J = \pm 2$. These transitions are forbidden when the lanthanide ion occupies a high symmetry site with an inversion centre.[114]

In this project, three different REs were used as activators such as Dysprosium (Dy^{3+}), Terbium ($^{3+}$) and Europium (Eu^{3+}). The specific properties of each RE ions are specified in each chapter and summarised briefly here.

1.3.1 Dysprosium

The Dy^{3+} ion ($4f^9$ configuration) shows emission in three regions: a blue band at 480 nm ($^4F_{9/2} \rightarrow {}^6H_{15/2}$), a yellow band at 575 nm ($^4F_{9/2} \rightarrow {}^6H_{13/2}$) and a red band at 670 nm ($^4F_{9/2} \rightarrow {}^6H_{11/2}$). The emission arising from the $^4F_{9/2} \rightarrow {}^6H_{11/2}$ transition is the weakest of these. The 5*d* level and the charge transfer state of Dy^{3+} ions are situated above 50000 cm^{-1}.[115] Therefore, a sensitiser is needed for it to be successfully excited by UV radiation. Dy^{3+}-activated phosphors have attracted some interest recently due to the balance between their blue and yellow integrated emission peaks that can make white light, making them favourable for application in near-white emitting materials.

1.3.2 Terbium

The Tb^{3+} ion ($4f^8$ configuration) shows green and blue emission respectively arising from transitions from the $^5D_4$ and $^5D_3$ levels to the ground state ^7F_J manifold (J = 6, 5, 4, 3, 2).[115] Tb^{3+} ions show low absorption efficiency in the n-UV region due to forbidden 4*f*-4*f* electric dipole transitions.[64]

1.3.3 Europium

Europium can be found in the +2 and +3 oxidation states and the trivalent ion is more often observed but the divalent ion is also common. Eu^{2+}-doped phosphors are subject of intense research to improve the already commercially available SiAlON: Eu^{2+} narrowest green-emitting phosphor.[116]

On the other hand, the Eu^{3+} ion ($4f^6$ configuration) shows red emission arising from $^5D_0 \rightarrow {}^7F_J$ transitions (J = 0-6). The transitions to the $^7F_5$ and $^7F_6$ levels are often not observed as they are outside the wavelength range of spectrofluorimeter detectors.[117] In Eu^{3+} ions, the distance between the J and the J + 1 level increases with increasing J value. This is due to the Landé interval rule "the interval between successive energy levels is proportional to the larger of their total angular momentum values J."[118]

The major influence of the apatite structure rigidity on the efficiency and thermal stability of the Eu^{3+}-activated phosphor can be calculated using the Judd-Ofelt analysis.

1.3.3.1 Eu^{3+} site symmetry properties

Eu^{3+} ions present seven $^5D_0 \rightarrow {}^7F_J$ transitions (J = 0-6), only one of which has an MD character: $^5D_0 \rightarrow {}^7F_1$. This transition is parity-allowed and is independent of the environment around the Eu^{3+} ion. The remaining six transitions have an ED character and are parity-forbidden.[119] Nevertheless, these ED transitions are observed via coupling with odd vibrations or mixing wavefunctions. These transitions are then called induced ED transitions. They are more probable than the MD transitions. When the Eu^{3+} occupies a centrosymmetric site, the parity rule applies and the MD transition becomes more probable.[110, 120] This unique behaviour allows the absorption and luminescence spectra of Eu^{3+} to be used to probe the local environment of the site occupied by the Eu^{3+} ion.[117]

1.3.3.2 Judd-Ofelt parametrisation of Eu^{3+}

The Judd-Ofelt theory[121, 122] can be used to predict oscillator strengths in absorption and luminescence, luminescence branching ratios, excited-state radiative lifetimes, energy-transfer probabilities, the stimulated emission cross section, the optical gain, the sensitisation efficiency and to estimate the quantum efficiencies of the *f*-*f* absorption spectra of trivalent lanthanides.[123, 124]

The intensity of the induced ED *f*-*f* transition in the absorption spectra can be expressed as the experimental dipole strength D, which is given by Equation 1.9:

$$D(exp) = \frac{10^{36}}{108.9X_A}\left((2J+1)\frac{9n}{(n^2+2)^2}\right)\int\frac{\epsilon(\tilde{\nu})}{\tilde{\nu}d\tilde{\nu}}, \tag{1.9}$$

where n is the refractive index, (2J + 1) is the degeneracy of the initial state, X_A is the fractional population of the initial state, $\epsilon(\tilde{\nu})$ is the absorption spectrum and $\tilde{\nu}$ is the average wavenumber in cm^{-1}. In the case of Eu^{3+}, the dipole strengths of the ED transitions are given by Equation 1.10:

$$D^{\lambda}_{ED} = e^2\Omega_\lambda U^\lambda, \tag{1.10}$$

where e = 4.803×10^{-10} esu (1 esu = $N^{-5/2}$cm) is the elementary charge. Furthermore, the reduced matrix U_λ is zero for transitions originating from the $^5D_0$ level, with the exception of the $^7F_\lambda$, which is described by U_λ, where λ = 2, 4, 6.[124]

In the case of Eu^{3+}, the dipole strength of its MD $^5D_0 \rightarrow {}^7F_1$ transition is independent of the environment. This allows the MD dipole strength given by Equation 1.11 to be a reference for the transitions arising from the $^5D_0$ level. For this reason the emission spectra can be used for these calculations.[125]

$$D_{MD} = 9.610^{-42}esu^2cm^2 = 9.610^{-6}Debye^2 \tag{1.11}$$

The Judd-Ofelt theory is expressed in terms of the parameters Ω_λ (λ = 2, 4, 6), which are given by Equation 1.12.

$$\Omega_\lambda = \frac{D_{MD}\tilde{\nu}_1^3}{e^2\tilde{\nu}_\lambda^3U^\lambda}\frac{9n_1^3}{n_\lambda(n_\lambda^2+2)^2}\frac{J_\lambda}{J_1}, \tag{1.12}$$

where J_λ is the integrated intensity of the $^5D_0 \rightarrow {}^7F_\lambda$ transition (λ =1, 2, 4, 6).[124]

The radiative transition probabilities, A_λ, can be estimated from the Judd-Ofelt parameters (Equation 1.13.

$$A_\lambda = \frac{64\pi^4\tilde{\nu}_\lambda^3}{3h}\frac{n_\lambda(n_\lambda^2+2)^2}{9}D^\lambda_{ED}, A_1 = \frac{64\pi^4\tilde{\nu}_1^3}{3h}n_1^3D_{MD}, \tag{1.13}$$

where h = 6.63×10^{-27} erg (1 erg = 10^{-5} N cm) is the Planck constant. In the Judd-Ofelt model for Eu^{3+}, A_λ = A($^5D_0 \rightarrow {}^7F_J$, J = 0, 3, 5) = 0, as these transitions are forbidden.

1.4 Important classes of phosphor materials

The latest techniques and research done in the interesting chemical and physical properties exhibited by inorganic solid state phosphors are presented in a few selected illustrative examples. These materials all show their good thermal and chemical stability, optical stability and environmental impact.

1.4.1 Garnets

The history of garnets goes back to ancient times when they were used as gemstones due to their colours or as abrasives because of their hardness. Structurally, garnets are described in space group $Ia\bar{3}d$, with a general formula of $A_3B_2C_3O_{12}$, where A denotes dodecahedral, B denotes octahedral, and C denotes tetrahedral coordination.[126]

The most common garnet used as a phosphor in lighting applications is Ce^{3+}-doped $Y_3Al_5O_{12}$ (also known as YAG, see Figure 1.11), which has a combination of qualities such as high luminescence efficiency, short luminescence lifetime and long wavelength emission (in the visible region). YAG:Ce shows good high-temperature thermal quenching, which is a very useful characteristic as in high-power LEDs increasing power consumption increases heat production due to the p-n junction.

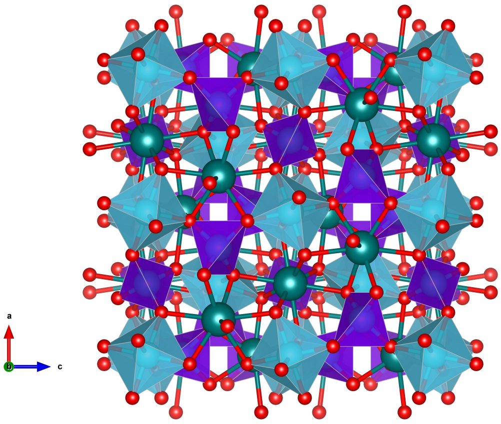

Figure 1.11: The garnet crystal structure of $Y_3Al_5O_{12}$ in the [010] direction. AlO_6 octahedra are illustrated in blue and AlO_4 tetrahedra in purple. YO_8 polyhedra have been excluded for clarity. Y atoms are shown in green and O atoms are in red.[127]

YAG:Ce^{3+} luminescence QYs with an excitation wavelength of 450 nm are $\sim$ 89 % for a 1 at.% Ce^{3+} and $\sim$ 81 % for 3 at.% Ce^{3+}, although for lower Ce^{3+}-doping levels the QY is less accurate due to its high reflectivity.[127]

Excitation of YAG:Ce^{3+} from the $^2F_{\frac{5}{2}}$ level to the lowest-energy $5d$ orbital occurs in a broad range with a maximum at ~460 nm, and emission occurs at ~540 nm from the transition of Ce^{3+} from the lowest-energy $5d$ orbital to the two $4f$ levels split by spin-orbit coupling.

The excitation wavelength is in the range of highly efficient blue LEDs, and the yellow emission produces a near white light with CRI = 70 (lower than that desired for general use), CCT = 4,000 K and quantum efficiency ~90% or even higher, with an acceptable but not spectacular quenching temperature (where the normalised emission integrals starts to decline at 400 K), where 20% of the emission intensity is lost at 300 K and 50% at 550 K. There have been attempts to improve the red component of the emission but there is a decrease in the thermal robustness of the quantum yield.[3]

Another well-known garnet-type phosphor is Ce^{3+}-doped $Ca_3Sc_2Si_3O_{12}$, which has a broad excitation centred at ~450 nm, a broad emission at a maximum of 505 nm and a quenching temperature below that of YAG:Ce. This garnet has been co-doped with Mn^{4+} to enhance its red emission, leading to peaks at approximately 574 and 680 nm.[128]

The $Ca_2YZr_2Al_3O_{12}$: Tb^{3+}, Eu^{3+} phosphor exhibits tuneable colour emission from green to yellow under n-UV excitation.[129] The $Y_2CaAl_2MgZr_2O_{12}$: Ce^{3+} phosphor emits in the greenish yellow region, peaking at 530 nm when excited with blue light of 420 to 460 nm wavelength. A WLED can be fabricated by coating a blue LED chip with a combination of $Y_2CaAl_2MgZr_2O_{12}$:0.03 Ce^{3+} and (Sr, Ca)$AlSiN_3$:Eu phosphors.[130] Dy^{3+} doped $(Lu,Gd)_3Al_5O_{12}$ garnet phosphors with spherical morphology can emit in the white region with colour coordinates (0.33,0.34) when they are excited at 275 nm via $Gd^{3+} \rightarrow Dy^{3+}$ energy transfer.[131]

1.4.2 Silicates

RE silicates are known for their high chemical and thermal stability, and are therefore potentially important candidates for new LED phosphor design. Orthosilicates have the general formula A_2SiO_4 (where A = Sr, Ba). When they are doped (on the A site) with Eu^{2+} ions and excited under NUV and blue light, these phosphors emit in the green (for Ba compounds) and yellow (for Sr compounds) regions with lifetimes of $\sim 0.7\ \mu s$ and $\sim 0.9\ \mu s$ respectively. $Sr_xBa_{2-x}SiO_4$:Eu^{2+} has an optimum doping level at 46 at.%, showing the highest resistance to thermal quenching luminescence, remaining stable from room temperature to 413 K, where maintains an emission efficiency of 75%.[132] There has been great interest in its potential use. As basic structural units, $[SiO_4]^{4-}$ groups can connect in different ways to form relatively complex crystal structures, which often contain a wide variety of structurally complex anion groups.[13]

$Gd_2Si_2O_7$ has two polymorphic forms: low-temperature α-$Gd_2Si_2O_7$, which has a single $[SiO_4]$ tetrahedra and linear edge-sharing $[Si_3O_{10}]$, and δ-$Gd_2Si_2O_7$ (see Figure 1.12), which contains (Si_2O_7) pyrosilicate groups. Gd^{3+} ions efficiently absorb UV radiation and can transfer it to active lanthanide ions (Dy^{3+}, Tb^{3+} and Eu^{3+}). There are several studies on optoelectronic applications of α-$Gd_2Si_2O_7$, such as on the possibility of Ce-doping this host.[133] The Gd-Ln^{3+} ($Ln^{3+} = Dy^{3+}$, Tb^{3+}, Eu^{3+}) energy transfer band has been used to excite δ-$Gd_2Si_2O_7$:Dy and δ-$Gd_2Si_2O_7$:Eu^{3+},Tb^{3+} phosphors, which intensifies the Ln^{3+} emissions. The δ-$Gd_2Si_2O_7$:x%Dy phosphor has chromatic coordinates (0.30, 0.33) and CCT values between 7077 and 6721 K. Its decay curves show a maximum lifetime value for δ-$Gd_2Si_2O_7$:0.5%Dy. δ-$Gd_2Si_2O_7$:0.3%Eu;0.8%Tb has been reported with CIE coordinates in the ideal white-light region and a CCT of 5828 K, althought due to the colour coordinates this phosphor should be considered the cold white light region, rather than ideal.[134]

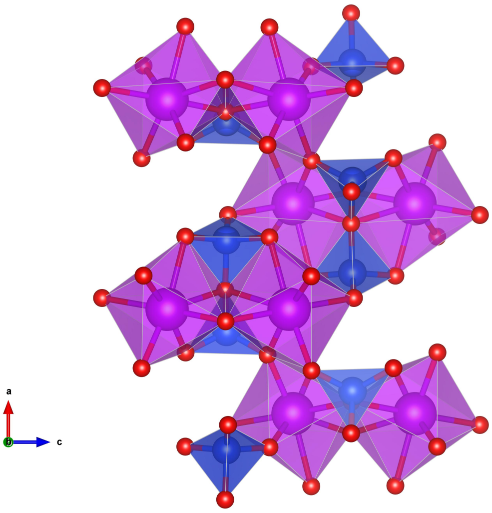

Figure 1.12: Crystal structure of δ-$Gd_2Si_2O_7$ seen in the [010] direction. SiO_4 tetrahedra are illustrated in blue, 7-coordinate GdO_7 in purple and O atoms are shown in red.[134]

Thiosilicates phosphors, such as Ca_2SiS_4 and Ba_2SiS_4, can be optimised by changing their synthesis conditions and compositions (levels of activator doping). However, the drawback of Ca_2SiS_4:Ce^{3+}, Eu^{3+} is that it presents a red afterglow.[135] Most of these thiosilicate phosphors experience thermal quenching. The $BaLa_2Si_2S_8$:Eu^{2+} phosphor has been reported to loose half its maximum emission intensity at 150 °C, with a quantum efficiency of $\sim$ 24% at room temperature. Another example are the disilicates such as Ba_3SiO_5:Eu^{2+}, which can be efficiently excited at 350 nm and 335 nm and emit in the yellow and green region, 504 nm and 566 nm respectively.[136137]

Another very important group of silicates are apatite silicates, which are known for their rigidity, high chemical and thermal stability.

1.4.3 Phosphates

Various phosphate phosphors with the general formula $ABPO_4$:RE (where A = Li, K; B = Sr, Ba; and RE = Eu^{2+}, Tb^{3+}, and Sm^{3+}, see Figure 1.13) have an excitation range in the NUV and UV region. The $KSr_{1-x}PO_4$:RE_x (RE = Eu^{2+}, Tb^{3+}, Sm^{3+}), Eu^{2+}-doped compound has a blue emission with a lifetime estimated at 530-470 ns. The Tb^{3+}-doped compound has a green emission with a lifetime estimated at 4-3 ms, and Sm^{3+} has a red emission with a lifetime estimated at 3-1 ms. It shows excellent thermally stable photoluminescence at high temperatures.[138]

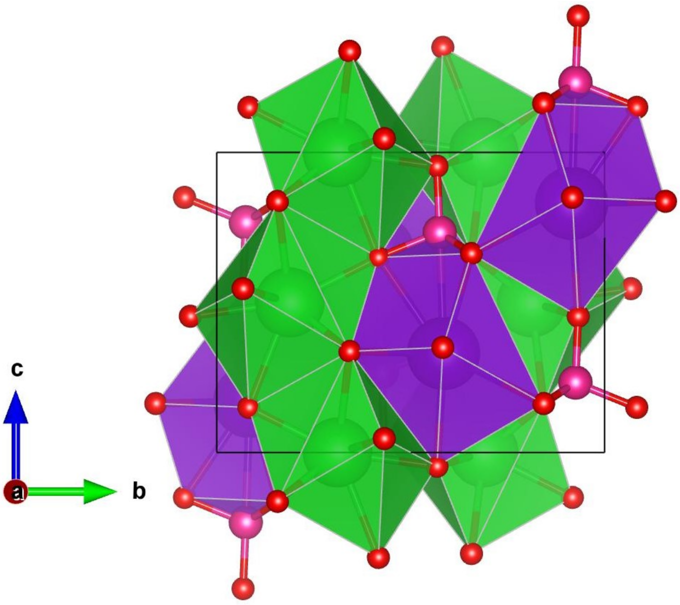

Figure 1.13: Crystal structure of $KBaPO_4$ seen in the [100] direction. 11-coordinate $KO_{10}P$ is illustrated in purple, 9-coordinate BaO_9 in green, P atoms are shown in pink and O atoms in red.[138]

Eulytite-type $M_3Ln(PO_4)_3$ phosphate compounds (where M = Sr, Ba and Ln = rare earth) acting as host materials for LED phosphors have drawn increasing attention. They are becoming important as they can incorporate different ions, which makes it possible to finely tune their physical and chemical properties. These blue-light-excited phosphate phosphors should be given more attention regarding their practical LED applications since they are chemically stable and some of them could show highly thermally stable photoluminescence.[13] An example of eulytite-type structure is $Ba_{3-x}Sr_xLu(PO_4)3$:Eu^{2+} phosphor, which can emit at 500 nm under 365 nm excitation.[139]

The Dy^{3+}-doped $Ca_3Bi(PO_4)_3$ phosphor exhibits white light emission under near-ultraviolet (n-UV) and blue excitation, retaining a 83.41% of the emission intensity at 373 K in comparison to room temperature and indicating a good thermal stability. The colour coordinates when excited at 451 nm are (0.329, 0.377), which fall inside the cool white light region.[140]

1.4.4 Nitrides and oxynitrides

Nitride and oxynitride phosphors typically have high mechanical strength, durability, physical and optical stability and excellent luminescence properties. They can be activated with Eu^{2+} and Ce^{3+}, have emission energies in the blue-to-yellow region of the visible-light spectrum, large CFS and a low centroid level of their $5d$ states, which causes a decrease in the energy difference between the $4f$ and $5d$ states. Broad emission bands in the red region create a problem in balancing high CRI and maximum achievable luminous efficacy.[13]

The increased covalency in nitride and oxynitride phosphors, due to the presence of the N_{3-} ion in the host crystal, induces large crystal field splitting resulting in long-wavelength emission. The $M_2Si_5N_8$ family of nitrides (where M = Ca, Sr, or Ba) is composed of well-known phosphor hosts (see Figure 1.14), some of which exhibit excellent thermal stability and a high quantum yield. When doped with Eu^{2+}, these $M_2Si_5N_8$ compounds exhibit a wide range of emission wavelengths from 570 to 680 nm and a broad excitation spectrum from blue and near-UV LEDs. The Ca compound has a maximum emission wavelength of 605 nm with a quantum yield of 55%, the Sr compound has a maximum emission wavelength of 620 nm, with a high quantum yield of 80%) and the Ba compound has a maximum emission wavelength of 580 nm with a relatively high quantum yield of 75%.[141]

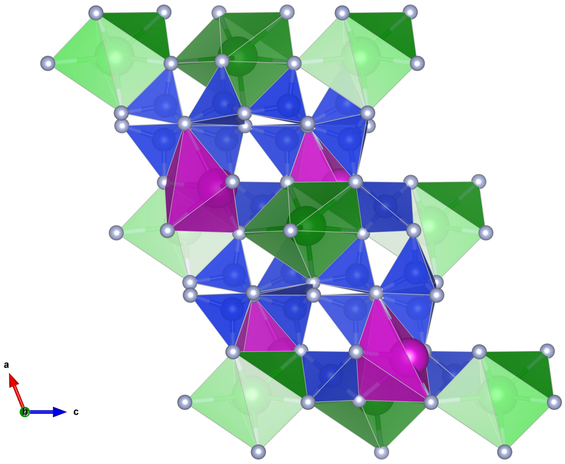

Figure 1.14: Crystal structure of $Ca_2Si_5N_8$ seen in the [010] direction. SiN_4 tetrahedra are illustrated in blue, CaN_6 octahedra in green, CaN_5 trigonal bipyramidal in pink and N atoms are shown in grey.[141]

The optimal Li-α-SiAlON: Eu^{3+} phosphor ($Li_{1.74}Si_9Al_3ON_{15}$:$Eu_{0.13}$) used with an InGaN-based blue LED chip reaches a quantum efficiency of $\sim$ 70% under 460 nm excitation. This pc-LED offers CCT = 6150 K and CRI = 72. The Ca-α-SiAlON: Eu^{3+} phosphor has CCT = 2830 K and CRI = 58.[142]

$Ca_8Mg_7Si_9N_{22}$:Ce^{3+} is a nitridomagnesosilicate yellow-emitting phosphor. It exhibits a broad band emission in the 475-675 nm spectral range under 445 nm excitation. In combination with the commercially available $SrLiAl_3N_4$:Eu^{2+}, it can be used with a blue LED chip for a warm WLED.[143] The $CaAlSi_4N_7$:Eu phosphor shows two main broad emission peaks at 498 nm and 614 nm under 400 nm n-UV excitation.[144]

Nitridosilicates, such as $(Ba,Sr)_2Si_5N_8$:Eu and $(Ca,Sr)AlSiN_3$:Eu, are non-oxide Si-containing phosphors. They are red-emitting materials with broad emission bands, which always result in a trade-off between a high CRI, good thermal quenching and the best luminous efficacy.[145] The small thermal quenching is due to the rigid network of $[SiN_4]$ and $[AlN_4]$ tetrahedra in its crystal structure.[146]

Even though nitride and oxynitride materials show excellent properties of long wavelength emission with high thermal stability, the drawbacks of these compounds are the high temperatures (1400 °C to 2000 °C) needed for their synthesis and their poor chemical stability.[65]

1.4.5 Other phosphors

Sulphide compounds can have a large nephelauxetic effect (low delocalization of two d electrons into the ligands) due to the very small electronegativity of S. An example of a sulphide phosphor is Ca_2SiS_4:Eu^{2+} (see Figure 1.15), which has a CCT of $\sim$ 3000 K and a CRI of $\sim$ 67.[65]

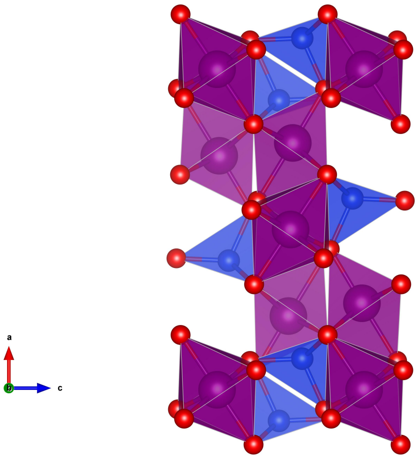

Figure 1.15: The crystal structure of Ca_2SiS_4 in the [010] direction. CaS_6 octahedra are illustrated in purple, SiS_4 tetrahedra in blue and S atoms are shown in red.[65]

Sulphide phosphors can be used for lighting applications but as they are relatively thermally and chemically unstable they have a rapid degradation of their luminescent intensity, they also have a low CRI due to their lack of green emission. To overcome this drawback, new sulphide phosphors with improved luminescent properties have been researched, such as RE fluorosulphide and thiosilicate-based phosphors, which in combination with Ce^{3+} and Eu^{3+} doping cover the whole visible spectrum and the emission colour can be changed from deep blue to red.

Therefore sulphides, especially thiosilicate phosphors, can be good candidates for WLEDs due to their low synthetic temperatures and various emission wavelengths with suitable excitation from UV to blue light. However, sulphide-based phosphors are not really friendly to the environment, which is the reason why instead there are developments in oxide-based phosphors instead with colour richness and good thermal and chemical stability.[147]

Aluminate phosphors, such as $LaSr_2AlO_5$:Ce^{3+} with quantum efficiency of ~ 42%, are earning prominence as they are strong competitors to YAG:Ce yellow phosphors.[148]

Fluoride and oxyfluoride hosts would normally be excluded from the development of LED phosphors due to their covalency and anion polarisability and the ionic nature of metal-F^- bonds, which limit feasible compositions. The ionisation-based quenching in these hosts can be reduced by increasing the band gap with a 'free' O^{2-} anion to charge compensate them.[149]

Mn^{4+}-doped fluoride phosphors can be classified into two groups: I_2–IV–F_6 and II–IV–F_6, with nominal compositions A_2MF_6:Mn^{4+} (A = Na, K, Cs, Rb and (NH_4); M = Si, Ge, Sn, Ti and Zr) or BMF_6:Mn^{4+} (B = Ba and Zn; M = Si, Ge, Sn and Ti). K_2SiF_6:Mn^{4+} and K_2TiF_6:Mn^{4+}, are known as narrow-line-emitting red phosphors for WLEDs with decay times of ~ 5.5 and 8 ms. Mn^{4+}-emission in oxides has $\lambda_{max} > 650$ nm, making these deep-red phosphors less useful for general lighting and display purposes. However, Mn^{4+} emission in fluoride hosts results in a 'blue-shift' of the $^2E \rightarrow {}^4A_2$ transition relative to oxide hosts. Mn^{4+}-doped fluorides need to be studied further to improve their absorption, quantum efficiency and stability under high humidity and high light flux.

Often a mix of phosphors makes an improvement to already known phosphors. A clear example of this is the combination of $Ca_{6-x-y}Mg_{x-z}(PO_4)_4$:$Eu^{2+}$ with $Ca_2MgSi_2O_7$:Eu^{3+} green-emitting phosphors using a NUV-LED. This has an excellent CRI of 98, which is very near the maximum CRI value.[65]

Molybdates are very interesting inorganic materials due to their use as luminescent materials, scintillators and in electrochemical and electrochromic devices. They are excellent potential RE doped phosphor hosts, as they intensify the spin and parity forbidden $[Xe]4f^n \leftrightarrow [Xe]4f^n$ transitions due to the overlap of the charge transfer band. $Eu_2Mo_4O_{15}$ has an external QY at room temperature of ~ 53.5% under excitation at 465 nm, and ~ 7.8% under excitation at 394 nm (during this process the excitation level is inside the band gap and therefore an energy loss), and above 300 K there is thermal quenching.[150]

1.4.6 Apatite-type silicate

Apatite-based silicates are potentially very attractive hosts for doping with RE ions, as they have excellent stability thanks to strong rigid Si-O bonds[79] coupled with chemical and structural flexibility with regard to accommodating guest ions.[80] Apatite-type materials in general are very versatile: they have been studied for applications including electrolytes for solid oxide fuel cells,[81–86] solid-state laser hosts,[87] nuclear waste immobilisation[88] and in biomedicine,[89–95] in addition to being used as phosphors.[96]

Apatite-type materials can be described with the general formula $A_{10}(BO_4)_6X_{2\pm\delta}$ (where A = Gd, La, Ca, Sr, ... is a large cation, B = Si, P, ... is a smaller cation and X = F, Cl, O, ... is an anion). They mostly crystallise in a hexagonal structure in space group $P6_3/m$, although some adopt monoclinic or triclinic structures.[97–103] The apatite structure can be described as a zeolite-like framework in which columns of face-sharing AO_6 trigonal prisms (shown as pink polyhedra in Figure 1.16) share corners with BO_4 tetrahedra (shown as blue polyhedra in Figure 1.16) to form channels running down the crystallographic c-axis. These channels are filled with A_6O_2 constituents (purple spheres in Figure 1.16).

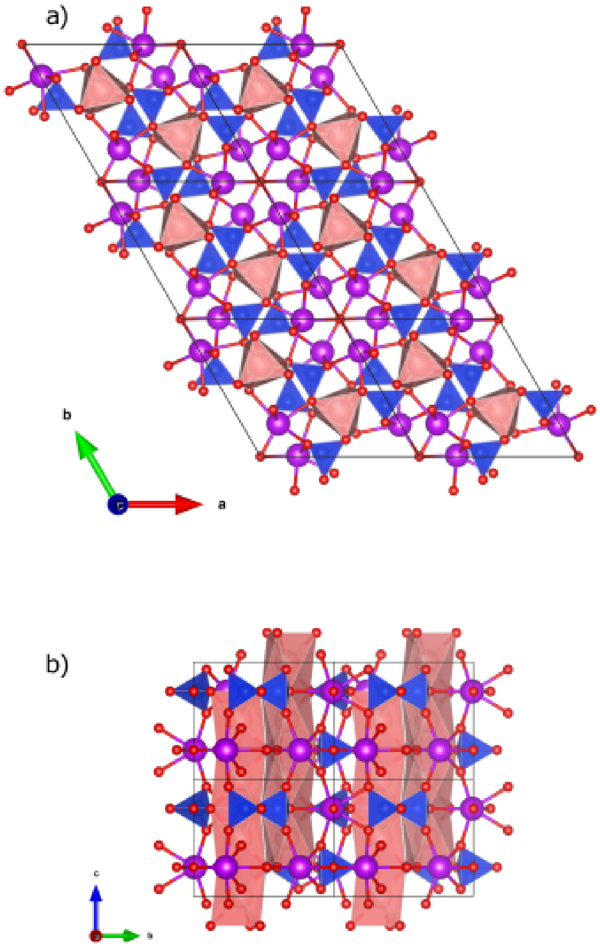

Figure 1.16: The structure shown here is hexagonal $Gd_{9.33}(SiO_4)_6O_2$, space group $P6_3/m$. GdO_6 trigonal prisms are illustrated in pink, SiO_4 tetrahedra in blue. The latter share corners to form channels filled with Gd_6O_2 units (purple and red spheres inside the polyhedral framework). 7-coordinate GdO_7 polyhedra have been excluded for clarity. Gd atoms remain as purple spheres. a) View along the c axis, and b) view along the a axis.[104]

In hexagonal apatites in space group $P6_3/m$, there are two crystallographically independent A-sites (shown in Figure 1.16, where Wyckoff site 4f is shown in pink and 6h in purple) onto which rare earth and transition metal ions can be doped. In triclinic apatites in space group P-1, the number of unique A-sites increases to five.[101] As the emission properties of luminescent ions occupying such sites can be influenced by their local environment, apatites offer extensive opportunities for tuning the luminescence.

In this project, the gadolinium silicate apatite, $Gd_{9.33}(SiO_4)_6O_2$, was chosen to be the host for the RE-doped phosphors. Gd^{3+} ions inside the apatite matrix can be used as sensitisers to allow the forbidden emissions of Dy^{3+} activators.[64] The $O^{2-} \rightarrow Gd^{3+}$, $O^{2-} \rightarrow Dy^{3+}$ charge transfer band and the *f-d* spin-allowed transition of Dy^{3+} is usually located in the near UV region.[10, 105–107] With this in mind, La^{3+} can be used as a sensitiser in some phosphors, although without energy levels separated in the visible range.[108]

1.5 Aims of the PhD project

The aim of this project was to design, synthesise and determine the structures and relevant optical properties of new luminescent inorganic silicate materials. Initially, silicates, which are known for their high chemical and thermal stability and abundance, were identified as suitable hosts for luminescent materials, as is discussed in section 1.4. My material design was guided by crystallochemical factors, such as the symmetry of the available crystallographic sites for the dopant ions and the polyhedral connectivity in the structure. Both factors are likely to affect the optical properties and hence the performance of materials as phosphors. The main aim is the development of single-phase phosphors for solid-state white lighting applications with improved light quality and a high energy conversion efficacy.

First, a series of potential UV-excited down-converting $Gd_{9.33}(SiO_4)_6O_2$ phosphor hosts was synthesised and then doped by Dy^{3+}, described in Chapter 3. Chapter 4 discusses green-emitting Tb^{3+}-doped phosphors. Chapter 5 reports the introduction of Eu^{3+} as a red component to achieve single phase white phosphors, obtaining Dy^{3+}, Eu^{3+}- and Tb^{3+}, Eu^{3+}-co-doped phosphors. Chapter 6 describes singly Eu^{3+}-doped phosphors to obtain red-emitting phosphors. In addition, the relationship between the CuO_4^{6-} chromophore environment and the optical properties of silicate NIR-emitters is described in Chapter 7.

1.6 References

[1] CIE, C. *Cambridge University Press Cambridge*, 1932.

[2] Schubert, E.F. and Kim, J.K. *Science*, 308(5726), 2005.

[3] George, N.C., Denault, K.A., and Seshadri, R. *Annual Review of Materials Research*, 43, 2013.

[4] Sharma, P., Khan, M., and Choubey, A., 2019.

[5] Nakamura, S., Mukai, T., and Senoh, M. *Applied Physics Letters*, 64(13), 1994.

[6] Pimputkar, S., Speck, J.S., DenBaars, S.P., and Nakamura, S. *Nature Photonics*, 3(4), 2009.

[7] Murata, H. *Light emitting diode lamp*, 1990.

[8] Ooi, E.N., Sun, X., Ooi, B., Ng, T.K., and Shen, C. *SPIE OPTO*, 10940, 2019.

[9] Peng, Y., Wang, S., Li, R., Li, H., Cheng, H., Chen, M., and Liu, S. *Applied Optics*, 55(18), 2016.

[10] Fan, M.H., Liu, S., Yang, K., Guo, J., Wang, J.X., Wang, X.H., Liu, Q., and Wei, B. *Ceramics International*, 46(5), 2020.

[11] Smet, P.F., Parmentier, A.B., and Poelman, D. *Journal of the Electrochemical Society*, 158(6), 2011.

[12] Mueller-Mach, R., Mueller, G., Krames, M.R., Hoppe, H.A., Stadler, F., Schnick, W., Juestel, T., and Schmidt, P. *Physica Status Solidi a-Applications and Materials Science*, 202(9), 2005.

[13] Xia, Z.G., Xu, Z.H., Chen, M.Y., and Liu, Q.L. *Dalton Transactions*, 45(28), 2016.

[14] Sheu, J.K., Chang, S.J., Kuo, C.H., Su, Y.K., Wu, L.W., Lin, Y.C., Lai, W.C., Tsai, J.M., Chi, G.C., and Wu, R.K. *IEEE Photonics Technology Letters*, 15(1), 2003.

[15] Xu, C. and Poduska, K.M. *Journal of Materials Science-Materials in Electronics*, 26(7), 2015.

[16] Bazzi, R., Flores, M.A., Louis, C., Lebbou, K., Zhang, W., Dujardin, C., Roux, S., Mercier, B., Ledoux, G., Bernstein, E., Perriat, P., and Tillement, O. *Journal of Colloid and Interface Science*, 273(1), 2004.

[17] Yazdan Mehr, M., Bahrami, A., van Driel, W.D., Fan, X.J., Davis, J.L., and Zhang, G.Q. *International Materials Reviews*, 65(2), 2020.

[18] Hawkes, P. *Advances in Electronics and Electron Physics*, Elsevier Science1990.

[19] Potter, R.M., Blank, J.M., and Addamiano, A. *Journal of Applied Physics*, 40(5), 1969.

[20] Edmond, J.A., Kong, H.S., and Carter, C.H. *Blue LEDs, UV photodiodes and high-temperature rectifiers in 6H–SiC*, Elsevier, Amsterdam1993.

[21] Zheludev, N. *Nature Photonics*, 1(4), 2007.

[22] Grimmeiss, H. and Scholz, H. *Physics Letters*, 8(4), 1964.

[23] Krames, M.R., Shchekin, O.B., Mueller-Mach, R., Mueller, G.O., Zhou, L., Harbers, G., and Craford, M.G. *Journal of Display Technology*, 3, 2007.

[24] Matsuoka, T. In *Inst. Phys. Conf. Ser.*, volume 106, 141.

[25] Akasaki, I. and Amano, H. *Journal of crystal growth*, 146(1-4), 1995.

[26] Narukawa, Y., Sano, M., Sakamoto, T., Yamada, T., and Mukai, T. *physica status solidi (a)*, 205(5), 2008.

[27] Kneissl, M., Kolbe, T., Chua, C., Kueller, V., Lobo, N., Stellmach, J., Knauer, A., Rodriguez, H., Einfeldt, S., Yang, Z., Johnson, N.M., and Weyers, M. *Semiconductor Science and Technology*, 26(1), 2010.

[28] Muramoto, Y., Kimura, M., and Nouda, S. *Semiconductor Science and Technology*, 29(8), 2014.

[29] Morita, D., Sano, M., Yamamoto, M., Murayama, T., Nagahama, S.i., and Mukai, T. *Japanese Journal of Applied Physics*, 41(Part 2, No. 12B), 2002.

[30] Fujioka, A., Asada, K., Yamada, H., Ohtsuka, T., Ogawa, T., Kosugi, T., Kishikawa, D., and Mukai, T. *Progress of high-power deep-ultraviolet LEDs*, volume 9363, SPIE2015.

[31] Ichikawa, M., Fujioka, A., Kosugi, T., Endo, S., Sagawa, H., Tamaki, H., Mukai, T., Uomoto, M., and Shimatsu, T. *Applied Physics Express*, 9(7), 2016.

[32] Takano, T., Mino, T., Sakai, J., Noguchi, N., Tsubaki, K., and Hirayama, H. *Applied Physics Express*, 10(3), 2017.

[33] Ren, Z., Lu, Y., Yao, H., Sun, H., Liao, C., Dai, J., Chen, C., Ryou, J., Yan, J., Wang, J., Li, J., and Li, X. *IEEE Photonics Journal*, 11(2), 2019.

[34] Ding, F., Fan, Y., Sun, Y., and Zhang, F. *Advanced Healthcare Materials*, 8(14), 2019.

[35] Hong, G., Lee, J.C., Robinson, J.T., Raaz, U., Xie, L., Huang, N.F., Cooke, J.P., and Dai, H. *Nature Medicine*, 18(12), 2012.

[36] Arras, J. and Bräse, S. *ChemPhotoChem*, 2(2), 2018.

[37] Zhang, F., He, X.W., Li, W.Y., and Zhang, Y.K. *Journal of Materials Chemistry*, 22(41), 2012.

[38] Xie, R. and Peng, X. *Journal of the American Chemical Society*, 131(30), 2009.

[39] Yong, K.T. *Nanotechnology*, 20(1), 2008.

[40] Saha, A.K., Sharma, P., Sohn, H.B., Ghosh, S., Das, R.K., Hebard, A.F., Zeng, H., Baligand, C., Walter, G.A., and Moudgil, B.M. *Journal of Materials Chemistry B*, 1(45), 2013.

[41] Singh, N., Charan, S., Sanjiv, K., Huang, S.H., Hsiao, Y.C., Kuo, C.W., Chien, F.C., Lee, T.C., and Chen, P. *Bioconjugate Chemistry*, 23(3), 2012.

[42] Maldiney, T., Bessière, A., Seguin, J., Teston, E., Sharma, S.K., Viana, B., Bos, A.J.J., Dorenbos, P., Bessodes, M., Gourier, D., Scherman, D., and Richard, C. *Nature Materials*, 13(4), 2014.

[43] le Masne de Chermont, Q., Chanéac, C., Seguin, J., Pellé, F., Maîtrejean, S., Jolivet, J.P., Gourier, D., Bessodes, M., and Scherman, D. *Proceedings of the National Academy of Sciences*, 104(22), 2007.

[44] Li, Y., Gecevicius, M., and Qiu, J. *Chemical Society Reviews*, 45(8), 2016.

[45] Pan, Z., Lu, Y.Y., and Liu, F. *Nature Materials*, 11(1), 2012.

[46] Li, Y., Li, Y.Y., Sharafudeen, K., Dong, G.P., Zhou, S.F., Ma, Z.J., Peng, M.Y., and Qiu, J.R. *Journal of Materials Chemistry C*, 2(11), 2014.

[47] Xu, J., Tanabe, S., Sontakke, A.D., and Ueda, J. *Applied Physics Letters*, 107(8), 2015.

[48] Xu, J., Murata, D., Ueda, J., and Tanabe, S. *Journal of Materials Chemistry C*, 4(47), 2016.

[49] Liu, F., Liang, Y., and Pan, Z. *Physical Review Letters*, 113(17), 2014.

[50] Accorsi, G., Verri, G., Acocella, A., Zerbetto, F., Lerario, G., Gigli, G., Saunders, D., and Billinge, R. *Chemical Communications*, 50(97), 2014.

[51] Chen, Y., Shang, M., Wu, X., and Feng, S. *CrystEngComm*, 16(24), 2014.

[52] Chen, Y., Kan, M., Sun, Q., and Jena, P. *The Journal of Physical Chemistry Letters*, 7(3), 2016.

[53] Pozza, G., Ajò, D., Chiari, G., De Zuane, F., and Favaro, M. *Journal of Cultural Heritage*, 1(4), 2000.

[54] Clark, M.G. and Burns, R.G. *Journal of the Chemical Society A: Inorganic, Physical, Theoretical*, (0), 1967.

[55] Luo, Y., Chen, Z., Hu, J., Xu, Z., Meng, Q., and Tang, D. *Physical Chemistry Chemical Physics*, 21(5), 2019.

[56] Albert, E.B., Cotton, F.A., and Hall, H., 1968.

[57] Halcrow, M.A. *Chemical Society Reviews*, 42(4), 2013.

[58] Cotton, F.A. and Wilkinson, G. *John Wiley*, 540, 1980.

[59] Misra, S.K. and Wang, C. *physica status solidi (b)*, 154(1), 1989.

[60] Hoffmann, S.K. and Goslar, J. *Journal of Solid State Chemistry*, 44(3), 1982.

[61] Bersuker, I. *The Jahn-Teller effect and vibronic interactions in modern chemistry*, Springer Science & Business Media2013.

[62] Omary, M.A. and Patterson, H.H. *Luminescence, Theory*, Academic Press, Oxford2017.

[63] Chambers, M.D. and Clarke, D.R. *Annual Review of Materials Research*, 39, 2009.

[64] Blasse, G. and Grabmaier, B. *Luminescent materials*, Springer Verlag1994.

[65] Ye, S., Xiao, F., Pan, Y.X., Ma, Y.Y., and Zhang, Q.Y. *Materials Science & Engineering R-Reports*, 71(1), 2010.

[66] Uitert, L.G.V. and Johnson, L.F. *The Journal of Chemical Physics*, 44(9), 1966.

[67] Miyakawa, T. and Dexter, D.L. *Physical Review B*, 1(7), 1970.

[68] Mills, I., Homann, T.C.K., Kallay, N., and Kuchitsu, K. *Comm. on Physicochem. Symbols, Terminol. and Units*, 1993.

[69] Armentrout, P. *Science*, 251(4990), 1991.

[70] Richardson, F.S. *Inorganic Chemistry*, 19(9), 1980.

[71] Hund, F. *Zeitschrift für Physik*, 33(1), 1925.

[72] Hund, F. *Z. Phys.*, 42, 1927.

[73] Shchekin, O.B., Schmidt, P.J., Jin, F.H., Lawrence, N., Vampola, K.J., Bechtel, H., Chamberlin, D.R., Mueller-Mach, R., and Mueller, G.O. *Physica Status Solidi-Rapid Research Letters*, 10(4), 2016.

[74] Blasse, G. *Physics Letters A*, 28(6), 1968.

[75] Bleijenberg, K.C. and Blasse, G. *Journal of Solid State Chemistry*, 28(3), 1979.

[76] Kim, Y.H., Arunkumar, P., Kim, B.Y., Unithrattil, S., Kim, E., Moon, S.H., Hyun, J.Y., Kim, K.H., Lee, D., and Lee, J.S. *Nature materials*, 16(5), 2017.

[77] de Oliveira, A.S., da Silva, B.H.S.T., Góes, M.S., Cuin, A., de Souza, H., de Oliveira, L.F.C., de Souza, G.P., Schiavon, M.A., and Ferrari, J.L. *Journal of Luminescence*, 227, 2020.

[78] Hoshina, T. *Journal of the Physical Society of Japan*, 48(4), 1980.

[79] Sun, Z.H., Wang, M.Q., Yang, Z., Liu, K.P., and Zhu, F.Y. *Journal of Solid State Chemistry*, 239, 2016.

[80] Waychunas, G.A. *Reviews in Mineralogy and Geochemistry*, 48(1), 2002.

[81] Islam, M.S., Tolchard, J.R., and Slater, P.R. *Chemical Communications*, (13), 2003.

[82] Sansom, J.E.H., Richings, D., and Slater, P.R. *Solid State Ionics*, 139(3-4), 2001.

[83] Sansom, J.E.H. and Slater, P.R. *The synthesis and conductivities of the apatite-type phases La(9.33)Si(6-x)Ge(x)O(26)*, volume 90-91 of *Solid State Phenomena Series*. 2003.

[84] Slater, P.R., Fagg, D.P., and Irvine, J.T.S. *Journal of Materials Chemistry*, 7(12), 1997.

[85] Slater, P.R. and Sansam, J.E.H. *The synthesis and characterisation of new apatite-type oxide ion conductors*, volume 90-91 of *Solid State Phenomena Series*. 2003.

[86] Slater, P.R., Sansom, J.E.H., and Tolchard, J.R. *Chemical Record*, 4(6), 2004.

[87] Gong, X., Lin, Y., Chen, Y., Huang, Z., Huang, Y., and Luo, Z. *Chemistry of Materials*, 17(5), 2005.

[88] Ravikumar, R., Gopal, B., and Jena, H. *Inorganic Chemistry*, 57(11), 2018.

[89] Inoue, M., Rodriguez, A.P., Nagai, N., Nagatsuka, H., LeGeros, R.Z., Tsujigiwa, H., Inoue, M., Kishimoto, E., and Takagi, S. *Journal of Biomaterials Applications*, 25(8), 2011.

[90] Tayton, E., Purcell, M., Aarvold, A., Smith, J.O., Briscoe, A., Kanczler, J.M., Shakesheff, K.M., Howdle, S.M., Dunlop, D.G., and Oreffo, R.O.C. *Journal of Biomedical Materials Research Part A*, 102(8), 2014.

[91] Srividya, S., Sridevi, G., Kumar, B.S., and Sastry, T.P. *Biocatalysis and Agricultural Biotechnology*, 15, 2018.

[92] Shi, Z., Huang, X., Cai, Y., Tang, R., and Yang, D. *Acta Biomaterialia*, 5(1), 2009.

[93] Porter, A.E., Patel, N., Skepper, J.N., Best, S.M., and Bonfield, W. *Biomaterials*, 24(25), 2003.

[94] Bulina, N.V., Chaikina, M.V., Prosanov, I.Y., Komarova, E.G., Sedelnikova, M.B., Sharkeev, Y.P., and Sheikin, V.V. *Materials Science and Engineering: C*, 92, 2018.

[95] Ke, X., Shu-Hua, T., Niu, N., and Peng, W. *Materials Research Express*, 5(11), 2018.

[96] Guo, Q., Liao, L., and Xia, Z. *Journal of Luminescence*, 145, 2014.

[97] An, T., Baikie, T., Wei, F., Pramana, S.S., Schreyer, M.K., Piltz, R.O., Shin, J.F., Wei, J., Slater, P.R., and White, T.J. *Chemistry of Materials*, 25(7), 2013.

[98] Peet, J.R., Chambers, M.S., Piovano, A., Johnson, M.R., and Evans, I.R. *Journal of Materials Chemistry A*, 6(12), 2018.

[99] Peet, J.R., Piovano, A., Johnson, M.R., and Evans, I.R. *Dalton Transactions*, 46(46), 2017.

[100] Tate, M.L., Fuller, C.A., Avdeev, M., Brand, H.E.A., McIntyre, G.J., and Evans, I.R. *Dalton Transactions*, 46(37), 2017.

[101] Tate, M.L., Blom, D.A., Avdeev, M., Brand, H.E.A., McIntyre, G.J., Vogt, T., and Evans, I.R. *Advanced Functional Materials*, 27(8), 2017.

[102] Chambers, M.S., Chater, P.A., Evans, I.R., and Evans, J.S.O. *Inorganic Chemistry*, 58(21), 2019.

[103] Hartnett, T.Q., Ayyasamy, M.V., and Balachandran, P.V. *MRS Communications*, 9(3), 2019.

[104] Latshaw, A.M., Hughey, K.D., Smith, M.D., Yeon, J., and zur Loye, H.C. *Inorganic Chemistry*, 54(3), 2015.

[105] Pang, M.L., Lin, J., Fu, J., Xing, R.B., Luo, C.X., and Han, Y.C. *Optical Materials*, 23(3-4), 2003.

[106] Wang, Y.H., Wen, Y., and Zhang, F. *Materials Research Bulletin*, 45(11), 2010.

[107] Tong, M., Liang, Y., Li, G., Xia, Z., Zhang, M., Yang, F., and Wang, Q. *Optical Materials*, 36(9), 2014.

[108] Shih, H.R., Tsai, M.T., Teoh, L.G., and Chang, Y.S. *Ceramics International*, 41(9, Part A), 2015.

[109] Alessandri, R., Zulfikri, H., Autschbach, J., and Bolvin, H. *Chemistry – A European Journal*, 24(21), 2018.

[110] Dodson, C.M. and Zia, R. *Physical Review B*, 86(12), 2012.

[111] Jorgensen, C.K. *Molecular Physics*, 5(3), 1962.

[112] Reisfeld, R. and Jorgensen, C. *Lasers and Excited States of Rare Earths, Springer Berlin Heidelberg*, 2012.

[113] Dorenbos, P. *Journal of Luminescence*, 91(1-2), 2000.

[114] Hatanaka, M. and Yabushita, S. *Mechanisms of f–f hypersensitive transition intensities of lanthanide trihalide molecules: a spin–orbit configuration interaction study*, Springer2016.

[115] Blasse, G. *Chapter 34 Chemistry and physics of R-activated phosphors*, volume 4, Elsevier1979.

[116] Kim, D.H., Ryu, J.H., and Cho, S.Y. *Applied Physics A*, 102(1), 2011.

[117] Binnemans, K. *Coordination Chemistry Reviews*, 295, 2015.

[118] Levy, P.M. and Copland, G.M. *Physical Review*, 180(2), 1969.

[119] Baur, F. and Jüstel, T. *Optical Materials: X*, 1, 2019.

[120] Bünzli, J.C.G. and Eliseeva, S.V. *Basics of Lanthanide Photophysics*, Springer Berlin Heidelberg, Berlin, Heidelberg2011.

[121] Judd, B.R. *Physical Review*, 127(3), 1962.

[122] Ofelt, G.S. *The Journal of Chemical Physics*, 37(3), 1962.

[123] Hehlen, M.P., Brik, M.G., and Krämer, K.W. *Journal of Luminescence*, 136, 2013.

[124] Ćirić, A., Stojadinović, S., Sekulić, M., and Dramićanin, M.D. *Journal of Luminescence*, 205, 2019.

[125] Dačanin, L., Lukić, S.R., Petrović, D.M., Nikolić, M., and Dramićanin, M.D. *Physica B: Condensed Matter*, 406(11), 2011.

[126] Menzer, G. *Zeitschrift Fur Kristallographie*, 69(3/4), 1928.

[127] Bachmann, V., Ronda, C., and Meijerink, A. *Chemistry of Materials*, 21(10), 2009.

[128] Liu, Y.F., Zhang, X., Hao, Z.D., Wang, X.J., and Zhang, J.H. *Chemical Communications*, 47(38), 2011.

[129] Qu, M., Zhang, X., Mi, X., Liu, Q., and Bai, Z. *Journal of Alloys and Compounds*, 828, 2020.

[130] Gupta, K.K., Som, S., and Lu, C.H. *Materials Research Express*, 6(12), 2020.

[131] Li, J., Wang, W., Liu, B., Duan, G., and Liu, Z. *Scientific Reports*, 10(1), 2020.

[132] Denault, K.A., Brgoch, J., Gaultois, M.W., Mikhailovsky, A., Petry, R., Winkler, H., DenBaars, S.P., and Seshadri, R. *Chemistry of Materials*, 26(7), 2014.

[133] Moretti, F., Vedda, A., Chiodini, N., Fasoli, M., Lauria, A., Jary, V., Kucerkova, R., Mihokova, E., Nale, A., and Nikl, M. *Journal of Luminescence*, 132(2), 2012.

[134] Fernandez-Carrion, A.J., Ocana, M., Garcia-Sevillano, J., Cantelar, E., and Becerro, A.I. *Journal of Physical Chemistry C*, 118(31), 2014.

[135] Smet, P.F., Korthout, K., Van Haecke, J.E., and Poelman, D. *Materials Science and Engineering B-Solid State Materials for Advanced Technology*, 146(1-3), 2008.

[136] Park, J.K., Lim, M.A., Choi, K.J., and Kim, C.H. *Journal of Materials Science*, 40(8), 2005.

[137] Lee, S.P., Chan, T.S., and Chen, T.M. *Acs Applied Materials & Interfaces*, 7(1), 2015.

[138] Lin, C.C., Xiao, Z.R., Guo, G.Y., Chan, T.S., and Liu, R.S. *Journal of the American Chemical Society*, 132(9), 2010.

[139] Wang, Z., Xia, Z., Molokeev, M.S., Atuchin, V.V., and Liu, Q. *Dalton Transactions*, 43(44), 2014.

[140] Sahu, M.K. and Mula, J. *Journal of the American Ceramic Society*, 102(10), 2019.

[141] Li, Y.Q., van Steen, J.E.J., van Krevel, J.W.H., Botty, G., Delsing, A.C.A., DiSalvo, F.J., de With, G., and Hintzen, H.T. *Journal of Alloys and Compounds*, 417(1-2), 2006.

[142] Xie, R.J., Hirosaki, N., Mitomo, M., Takahashi, K., and Sakuma, K. *Applied Physics Letters*, 88(10), 2006.

[143] Li, C., Wang, X.M., Yang, Z.P., and Jiao, H. *ACS Applied Electronic Materials*, 2(4), 2020.

[144] Yoshimura, F., Yamane, H., and Yamada, T. *Inorganic Chemistry*, 59(1), 2020.

[145] Meyer, J. and Tappe, F. *Advanced Optical Materials*, 3(4), 2015.

[146] Uheda, K., Hirosaki, N., Yamamoto, Y., Naito, A., Nakajima, T., and Yamamoto, H. *Electrochemical and Solid-State Letters*, 9(4), 2006.

[147] Zhang, Y., Li, G.G., Geng, D.L., Shang, M.M., Peng, C., and Lin, J. *Inorganic Chemistry*, 51(21), 2012.

[148] Im, W.B., Kim, Y.I., Fellows, N.N., Masui, H., Hirata, G., DenBaars, S.P., and Seshadri, R. *Applied Physics Letters*, 93(9), 2008.

[149] Setlur, A.A., Radkov, E.V., Henderson, C.S., Her, J.H., Srivastava, A.M., Karkada, N., Kishore, M.S., Kumar, N.P., Aesram, D., Deshpande, A., Kolodin, B., Grigorov, L.S., and Happek, U. *Chemistry of Materials*, 22(13), 2010.

[150] Janulevicius, M., Grigorjevaite, J., Merkininkaite, G., Sakirzanovas, S., and Katelnikovas, A. *Journal of Luminescence*, 179, 2016.

2 Experimental methods

2.1 Synthetic methods

2.1.1 Solid-state synthesis

The most widely used method to prepare solids is a solid-state reaction. This involves grinding and heating the powder reagents in crucibles (i.e. alumina, platinum, gold, graphite, etc depending on the temperature and reagents reactivity) for a given length of time. Although this technique is not very sophisticated, it is very effective. It uses high temperature to improve the rate of diffusion or mass transfer within, and between, solid particles. The reagent material is diffused, with ions substituting across a compositional gradient using vacant lattice and interstitial sites, while at the same time maintaining charge neutrality.[1]

In this method, stoichiometric quantities of reagents are weighed to within ± 0.0001 g and ground together using an agate mortar and pestle. The hygroscopic reagents are dried before being weighed to ensure accurate stoichiometric quantities. The well-homogenised powder is placed in alumina crucibles inside a furnace and heated to high temperature, re-homogenising and heating for different periods of time depending on the progress of the solid state reaction.

2.1.2 Single crystal growth

The floating-zone (FZ) method was originally developed by Pfann to purify germanium.[2] When this method is used for single crystal growth, a large quantity ($\sim$20 g) of a highly pure polycrystalline sample is synthesised using the solid-state synthesis method, pressed and sintered into feed and seed rods. The feed rod is aligned vertically on top of the seed rod and a moving heater (consisting of four halogen lamps) heats the rods until a molten zone is formed and the two rods are merged (see Figure 2.1). Specific rotational and translational rates are maintained and the molten material cools and crystallises as it moves to the end of the feed rod.

The first part of the crystal consists of a large number of crystallites oriented randomly. These are known as seed grains. The growth rates of the seed grains are different in certain directions. Different seed grains will overlap as the crystal is being grown and ultimately only one seed direction will remain forming the single crystal.

Various parameters need to be controlled to obtain a high quality single crystal:

1. Gas. Impurities can form in certain compounds due to the choice of gas. Fast gas flow can cause a steep temperature gradient below the 'molten zone'. High gas pressure causes a rapid drop of the temperature in the whole system so a more powerful lamp set must be used. The gas pressure in the furnace can also be manipulated when certain volatile elements are present, to avoid oxidising or reducing of the compound.

2. Rate of crystal growth. There are fewer defects in the crystal when a slower rate is used but this might be counter-productive and cause some of the material to evaporate, affecting the composition.

3. Rotation of the rods. The faster the rods rotate, the lower the possibility of favouring a certain seed orientation.

4. Density of the rods. If the rod is not dense enough the melt can form bubbles. When these bubbles burst a crystal with inconsistent width can be created, or there is even a risk of collapse. Pre-melting the rod can ensure high density but it can be disadvantageous if the material evaporates.

5. Lamp power. If the lamps are set to high power, the temperature gradient might be too high and cause cracking due to thermal and structural strain.

A Crystal FZ-T-10000-H-VIII-VPO-PC optical floating-zone furnace, manufactured by Crystal Systems Corporation was used for single crystal growth in this research. The FZ furnace is equipped with four 300 W halogen lamps, with controlled atmosphere gas and tunable independent rotation of both rods.

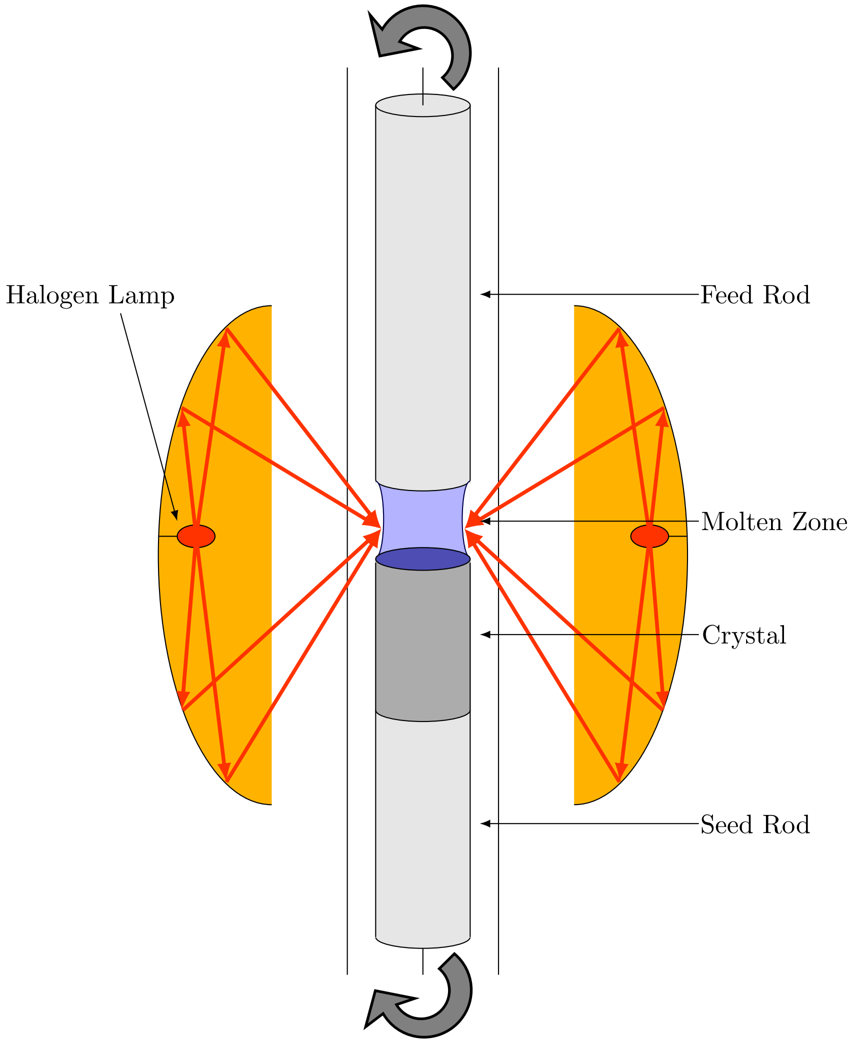

Figure 2.1: The floating-zone method.

2.2 X-Ray crystallography

2.2.1 Diffraction

X-ray diffraction is an analytical method widely used to characterise the structures of solids and to carry out phase analysis of crystalline materials. In this technique, a crystalline sample can act as a diffraction grating and diffract incoming radiation, resulting in both constructive and destructive interference.[3] This radiation needs to be of comparable size to the interatomic distances in the samples ($\sim$ 0.5 - 2.5 Å). Most of the radiation scattered is cancelled out due to the destructive interference. Constructive interference creates observable peaks in the diffraction pattern. This information is then used to produce a three-dimensional electron density distribution in the crystal. The direction of the diffraction depends on the size and shape of the unit cell of the material and the intensities of the diffracted waves depend on the kind and arrangement of atoms in the crystal structure.

Diffraction is an interference phenomenon but it can be considered as reflections from lattice planes, giving it an easier geometrical interpretation. The lattice planes are crystallographic planes characterised by the *hkl* Miller indices. Bragg's law describes the X-ray diffraction by using these planes in the crystal. If two parallel *hkl* scattering planes are separated by a distance of d_{hkl} (see Figure 2.2)[4] constructive interference will occur when the difference between the path lengths of the two beams is an integer number 'n' of wavelengths. This is described by Equations 2.1.

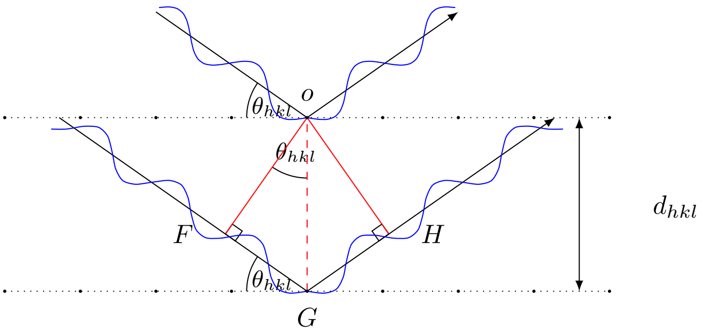

Figure 2.2: Derivation of Bragg's law.[4]

$$\begin{aligned} FG + GH =& n\lambda, \quad n = 1, 2, 3, ... && \text{(2.1a)} \\ sin(\theta_{hkl}) =& \frac{FG}{d_{hkl}} = \frac{GH}{d_{hkl}}, && \text{(2.1b)} \\ dsin(\theta_{hkl}) =& FG = GH, && \text{(2.1c)} \\ dsin(\theta_{hkl}) =& \frac{n\lambda}{2}, && \text{(2.1d)} \\ n\lambda =& 2dsin(\theta_{hkl}). && \text{(2.1e)} \end{aligned}$$

Hence, the position of each (*hkl*) reflection is expressed by Bragg's law as Equation 2.2

$$n\lambda = 2d_{hkl}sin(\theta_{hkl}), \tag{2.2}$$

where the spacing between the crystals planes, d_{hkl}, is related to the diffraction angle θ_{hkl} at which the reflections are observed when radiation with a wavelength λ is used.

The structure factor F_{hkl}, given by Equation 2.3, is a resultant of all waves scattered in the direction of the *hkl* reflection by the *n* atoms in the unit cell. This factor depends on the atomic scattering factor f_j and the position of each atom. The intensity observed in the diffraction pattern is proportional to —F—^{2} and is the sum of all scattered waves by individual atoms.[5]

$$F_{hkl} = \sum_{j=1}^{n} f_j e^{2\pi i(hx_j+ky_j+lz_j)}, \tag{2.3}$$

where f_j is the scattering factor of the jth atom with atomic fractional coordinates x_j, y_j and z_j. The atomic scattering factor (f) in Equation 2.3 varies linearly with the atomic number and decreases with increasing scattering angle θ_{hkl}.[3]

The observed intensity of the Bragg reflection, I_{hkl} is given by Equation 2.4.[6]

$$I_{hkl} = cL(2\theta)P(2\theta)A(2\theta)p_{hkl}|F_{hkl}|^2 \tag{2.4}$$

where F_{hkl} is the structure factor, c is the scale factor, L(2θ) is the Lorentz factor, P(2θ) is the polarisation factor, A(2θ) is the absorption, p_{hkl} is the multiplicity factor (number of symmetry equivalent reflections), θ is the Bragg angle. Thus, the structure factor is related to the observed intensities as shown by Equation 2.5.

$$I_{hkl} \propto |F_{hkl}|^2. \tag{2.5}$$

X-ray powder diffraction is a practical method to calculate the mean size of crystallites. Peak broadening can be attributed to size and strain of the crystallite.[7] The size contribution is given by Equation 2.6.[8]

$$\beta = \frac{\kappa\lambda}{L_{Vol} cos\theta}, \tag{2.6}$$

where β is the full width at half maximum, k is constant and L_{Vol} is the volume weighted mean column height. The volume weighted mean column height can be related to the average radius of a monodisperse spherical system using Equation 2.7.[9]

$$D_V = \frac{3R(1+c)^3}{2}, \tag{2.7}$$

where R is the average radius of the particles and c is defined by Equation 2.8.

$$c = \frac{\sigma_R^2}{R^2} \tag{2.8}$$

2.2.2 Single crystal and powder X-ray diffraction

In single-crystal X-ray diffraction (SCXRD), shown in Figure 2.3a, isolated individual spots arise from diffraction of X-rays by different planes of atoms within the crystal. This technique can measure the position and intensity of the *hkl* reflections, which can be used to determine the unit cell dimensions, the space group and precise atomic positions and derive the bond lengths, bond angles and details of site ordering.

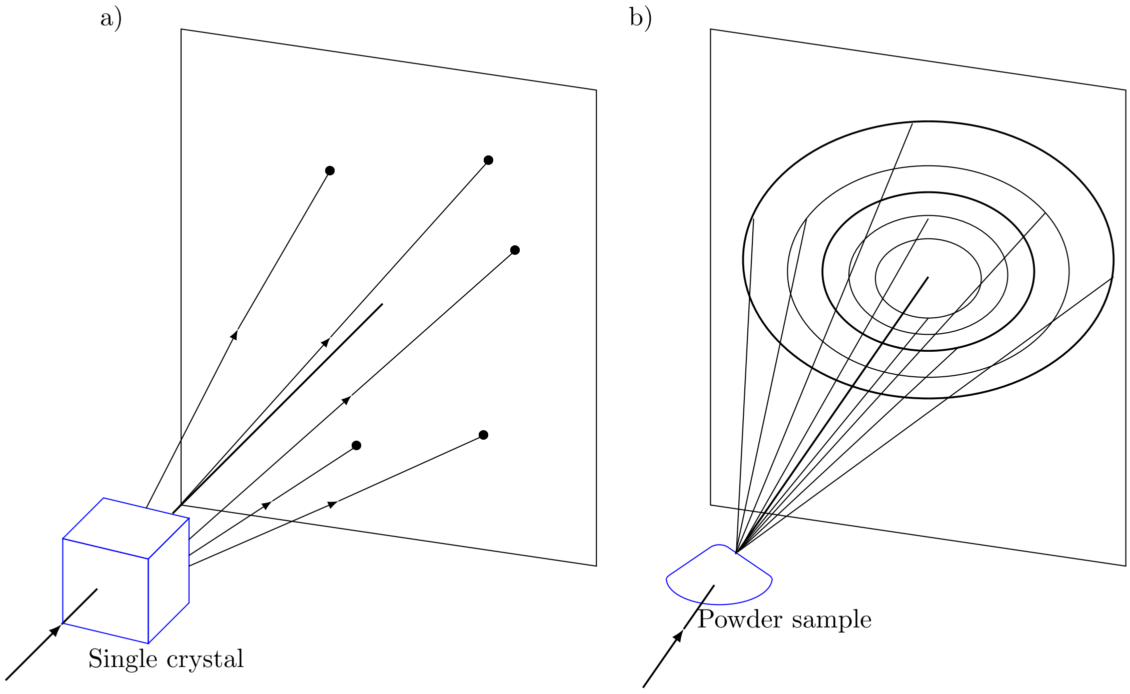

Figure 2.3: a) Single crystal and b) powder X-ray diffraction.[6]

Powder X-ray diffraction (PXRD) patterns, unlike SCXRD, produce cones of diffracted intensity in one dimension (shown in Figure 2.3b). This is due to the very large number of randomly oriented small crystals present in the powder. SCXRD is not always practical as growing single crystals can be difficult. PXRD is a better technique to use as a regular procedure, to identify the phase and purity level.

2.2.3 Instrumentation

Two Bruker AXS d8 Advance diffractometers (known in the group as d7 and d9) with the same setup were used for routine phase and Rietveld analysis. The X-ray sources for these diffractometers work at 40 kV and 40 mA using a Cu tube to provide $\mathrm{CuK}_{\alpha 1,2}$ radiation (λ=1.5406 Åand λ=1.5444 Å, respectively) and a Ni filter is used to remove K_β radiation. The diffractometers use a Lynx-eye detector and are operated by Diffrac+ XRD Commander software.[10]

The samples were ground using a pestle and mortar, passed through a 120 mesh sieve and placed on a silicon slide thinly covered in Vaseline. Both diffractometers operated using the same set-up: an aperture slit of 6 mm, flat plate configuration and variable divergence slits (v6), to avoid beam overspill at low angles, with 2θ scan range for each sample from 10 to 70, a step size of 0.02, a time per step of 0.5 and a scan time of 30 minutes at room temperature.

Variable temperature laboratory PXRD (VT-PXRD) was recorded in the Bruker AXS d8 Advance diffractometer using an Anton Parr HTK1200 high temperature furnace. The real temperature of the HTK1200 furnace was calibrated by collecting data for a standard sample, Al_2O_3, where the correction is

$$T_{real} = T_{set} + (aT_{set}^3 + bT_{set}^2 + cT_{set} + d), \tag{2.9}$$

where a = 1.61x10^{-7} K^{-2}, b = -5.86x10^{-4} K^{-1}, c = 0.565 and d = -134 K.

The samples were ground using a pestle and mortar, passed through the sieve onto an amorphous silica glass slide with a thin layer of vacuum grease and then mounted in an alumina sample holder inside the Anton-Paar furnace.

High quality powder x-ray diffraction patterns were recorded at the I11 beamline,[11] located at Diamond Light Source (DLS) Synchrotron (Figure 2.4) operatin with an energy range of 5-25 keV. Synchrotron radiation is emitted when charged particles travel at relativistic speed and are forced to change direction by a magnetic field. The detector is composed of five multi-crystal detectors (MAC), each with nine Si(111) analysing crystals.[12] Each sample was placed in a capillary and scanned with a 2θ range from 0 to 150 at room temperature. The beamline was used to collect high resolution powder diffraction on a small number of samples described in chapter 3, setting the energy at 15 keV with a calculated λ=0.82576 Å.

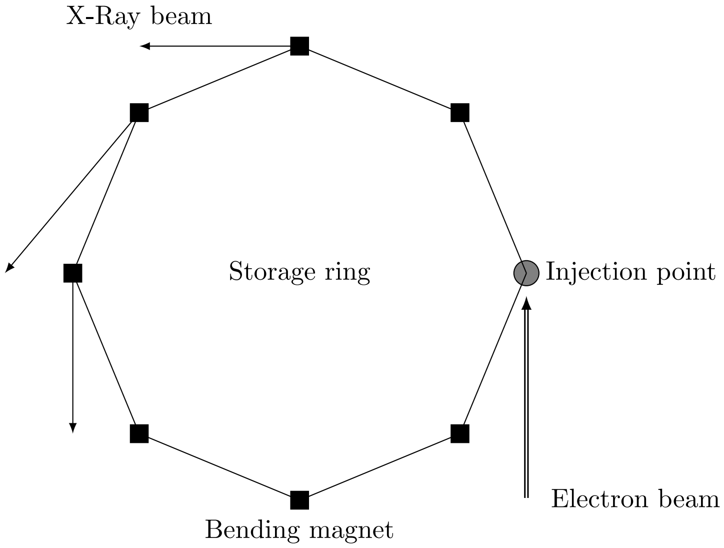

Figure 2.4: Diagram of a synchrotron, illustrating X-ray radiation output from bending magnets.[12]

The single crystals described in chapter 7 were examined with a Bruker D8 Venture diffractometer, which works at 50 kV and 35 mA, using MoK radiation λ=0.71073 Å and a Photon100 CMOS detector. Each crystal sample was selected based on its isotropic shape. Using oil, the sample was placed in a loop located in a brass holder set in a goniometer head. APEX3[13] software was used to centre the single crystal, collect and reduce data and identify the unit cell. The structure refinements were performed in Jana2006.[14]

2.2.4 Powder diffraction data analysis

Rietveld refinement[15] is one of the most widely used methods to analyse experimentally obtained powder diffraction patterns. In this method, least-squares refinements are performed in an iterative manner until the best fit is obtained between the experimental data and the calculated pattern based on the model of the crystal structure, diffraction optics effects, instrumental factors, lattice parameters, etc.[5] The aim of Rietveld refinement is to achieve the best least-squares fit to all the intensities given at each step in the diffraction patterns. The quantity minimised is the residual S_y given by Equation 2.10.

$$S_y = \sum_{j=1}^{n} w_j (y_j - y_{cj})^2, \tag{2.10}$$

where $w_j = \dfrac{1}{y_j}$, y_j is the observed intensity at the j-th step, y_{cj} is the calculated intensity at the j-th step and n is the number of data points.

The calculated intensities y_{cj} are the contributions from neighbouring Bragg reflections plus the background, and are given by Equation 2.11

$$y_{cj} = s \sum_{hkl} L_{hkl} |F_{hkl}|^2 \phi(2\theta_j - 2\theta_{hkl}) P_{hkl} A + y_{bj}, \tag{2.11}$$

where s is the scale factor, L_{hkl} includes the Lorentz, polarisation and multiplicity factors, ϕ is the reflection profile function, P_{hkl} is the preferred orientation function, A is the absorption factor, F_{hkl} is the structure factor and y_{bj} is the background intensity at the j-th step. Preferred orientation affects the relative intensities in a plane parallel to the sample surface.[7]

R_{wp} is the value that reflects the progress of the Rietveld refinement (Equation 2.12)

$$R_{wp} = \left[\frac{\sum_{j=1}^{n} w_j (y_j - y_{cj})^2}{\sum_{j=1}^{n} w_j (y_j)^2} \right]^{\frac{1}{2}} = \left[\frac{S_y}{\sum_{j=1}^{n} w_j (y_j)^2} \right]^{\frac{1}{2}}. \tag{2.12}$$

Another indicator of the refinement quality is the goodness of fit, S, given by Equation 2.13

$$S = \left[\frac{S_y}{(N-P)} \right]^{\frac{1}{2}} = \frac{R_{wp}}{R_e}, \tag{2.13}$$

with R_e being given by Equation 2.14

$$R_e = \left[\frac{(N-P)}{\sum_{j=1}^{n} w_j y_j} \right]^{\frac{1}{2}}, \tag{2.14}$$

where N is the number of observations and P is the number of parameters that can be refined.

The Rietvield refinements performed for the PXRD patterns presented in this thesis were analysed using a combination of jEdit and Topas Academic software.[16]

2.3 Optical measurements

2.3.1 Fundamentals

Fluorescence is a form of rapid decaying luminescence where spontaneous emission of radiation occurs within a few nanoseconds of the exciting radiation being extinguished.[17] Phosphors are fluorescent materials that normally convert high energy photons into lower energy visible wavelengths.[18]

A technique to analyse fluorescence in a sample is fluorescence spectroscopy, also called spectrofluorometry, where a beam of light hits the sample and excites the molecules to emit light, usually in the visible region.[19] This emission spectrum is the wavelength distribution of the emission at a set excitation wavelengths.

This technique also involves measurement of the absorption, with the fluorometer recording the relative emission of the sample at each excitation wavelength. The emission wavelength is set at a desired value by scanning the excitation wavelength.

There are three important events in fluorescence:

1. Excitation (absorption) of the activator by an incoming photon. This occurs in femtoseconds (10^{-15} seconds).
2. Vibrational relaxation of excited state electrons to the lowest energy level. This is a slower process and can be measured in picoseconds (10^{-12} seconds).
3. Return to the ground state and emission of a longer wavelength photon, this happens over a relatively long time period of nanoseconds (10^{-9} seconds).

The absorption and emission of a photon, or the intensities of vibronic transitions, are described by the Franck-Condon principle. This principle states that the absorption of a photon is practically instantaneous, as it involves the rearrangement of inertia-free ions. There are no changes in the nuclear coordinates during an electronic transition, hence the vibronic transitions are vertical as the transition is faster compared to the period of nuclear vibration. Figure 2.5 shows the Franck-Condon energy diagram, which represents the vibrational energy probability distribution among the various levels in the ground state and first excited state for a hypothetical system. The red arrow represent absorption, following a transition of the ground vibrational state to a high probability location. The orange arrow represent the non-radiative transition, when the photon relaxes from an excited state to a lower energy level. The yellow arrow represent emission, following a transition to the ground state. The emission spectra profile is the mirror image of the absorption spectra profile. This is known as the Kasha's rule inside the Franck-Condon principle, also known as the mirror symmetry absorption-emission. The Stokes shift is the difference between the highest peaks of this mirror image of absorption (the maxima of the lowest energy absorption band) and emission (highest energy fluorescence band) spectra.[18]

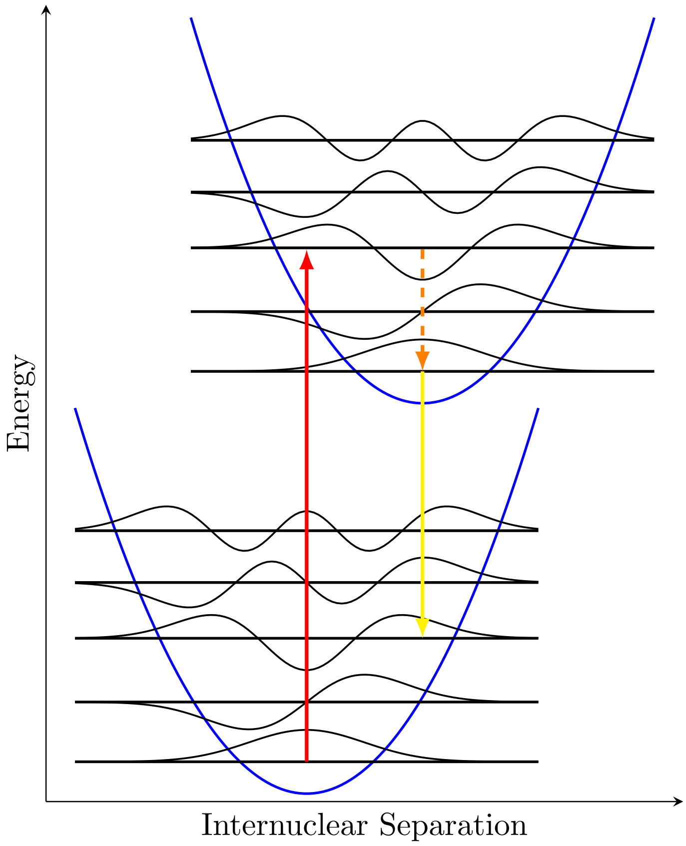

Figure 2.5: Franck-Condon energy diagram. Red arrow represent absorption. Orange arrow represent the non-radiative transition. Yellow arrow represent emission.[18]

2.3.2 Instrumentation

Fluorescence was measured using a Fluorolog-3 Horiba fluorometer, with a xenon flashlamp as the excitation source, and a Hamamatsu R928 photomultiplier tube for detection. Homogeneous, finely powdered samples of the materials were contained in a Spectralon® cup with a quartz cover slip, and placed inside a Quanta-ϕ F-3029 integrating sphere connected to the spectrometer via optical fibres.

The data-acquisition program integrated in the fluorometer is FluorEssence. This uses Origin software to analyse the raw data recorded by the fluorometer.

2.3.3 White-light characterisation

The human eye's response to light spans a region from 380 nm to 800 nm. The eye has four different types of photoreceptors: rod cells and red-, green-, and blue-sensitive cone cells. Recently a fifth type of photoreceptor has been discovered: the ganglion cells.[20] These regulate the human circadian (wake-sleep) rhythm, being 'blue-sky receptors' (460 nm to 500 nm), which is the reason why tunable CCT (from 6000 K to 20000 K at midday, decreasing to 2000 K at evening) is very important in lighting applications. Inappropriate lighting conditions have been proved to upset the body chemistry in mammals, leading to unfavourable health effects and in some cases creating dependence on sleep-inducing pharmaceuticals.[20]

Three reference stimuli, or tristimulus values, can be use to describe any colour. These real primary stimuli are set at $\lambda_R = 700.0$ nm for red, at $\lambda_G = 546.1$ nm for green and at $\lambda_B = 435.8$ nm for blue, as is shown in Figure 2.6(a). These colour-matching functions ($\bar{r}(\lambda)$, $\bar{g}(\lambda)$ and $\bar{b}(\lambda)$) are continuous and smooth, and one of the stimulus functions shows negative values, meaning that the colour is obtained by using one of the primaries to desaturate before a colour match between the other two colours.[21]

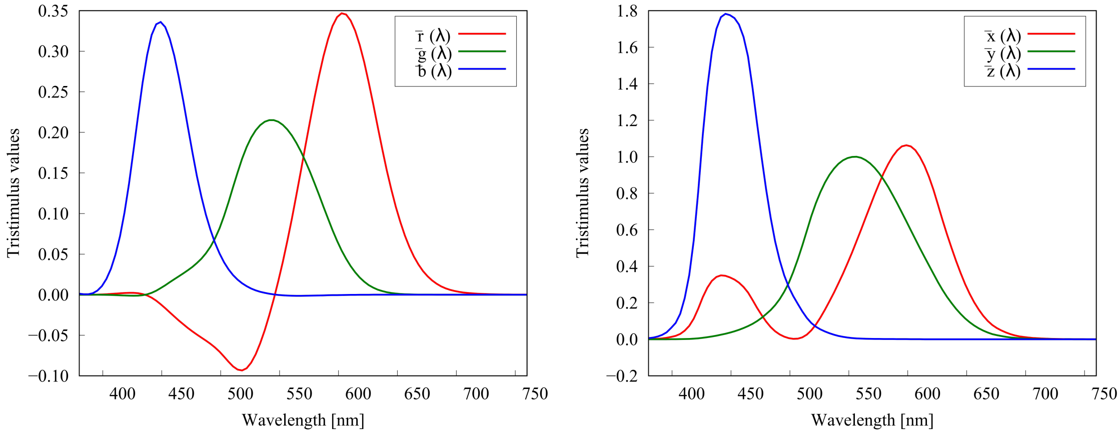

(a) Tristimulus values $\bar{r}(\lambda)$, $\bar{g}(\lambda)$ and $\bar{b}(\lambda)$. **(b)** Tristimulus values $\bar{x}(\lambda)$, $\bar{y}(\lambda)$ and $\bar{z}(\lambda)$.

Figure 2.6: Colour-matching functions.[21]

RGB tristimulus colour-matching functions are representations of the real primaries, but for easier colourimetric calculations the imaginary primaries **XYZ** were established as in Figure 2.6(b). This new colour-space has desirable properties:[22]

1) The new colour-matching functions $\bar{x}(\lambda)$, $\bar{y}(\lambda)$ and $\bar{z}(\lambda)$ are positive at every point, making it manageable to do the calculations.

2) The $\bar{y}(\lambda)$ colour-matching function represents the variation in brightness for the wavelength.

3) There is a fixed point of the equal-energy stimulus at colour coordinates $(\frac{1}{3},\frac{1}{3})$, which represents the white-light point.

4) The $\bar{z}(\lambda)$ colour-matching function can be set at zero after 650 nm.

In 1931, the Commission Internationale de l'Eclairage (CIE) standardised colorimetry for photopic (bright-light) vision. This involved the first quantitative measurements of the relation between the physical pure colours in the electromagnetic visible spectrum and the physiological perceived colours in human colour vision.

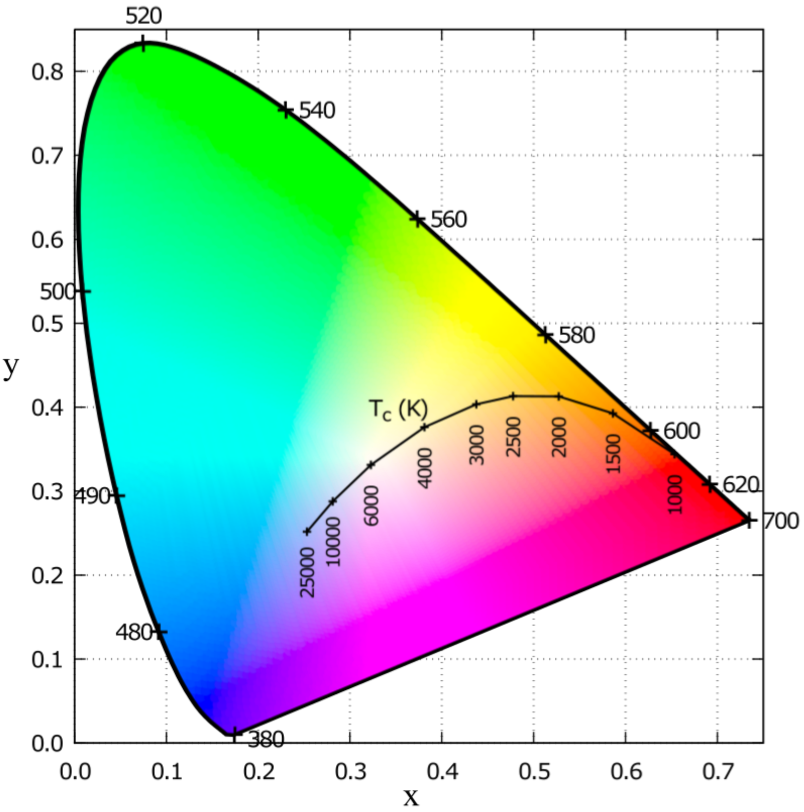

Figure 2.7: The 1931 CIE standard observer diagram.[23]

The colour coordinates for the 1931 CIE standard observer diagram[21, 23] were calculated using Equation 2.15

$$A = \int_{380nm}^{780nm} \Delta\lambda a_\lambda P(\lambda) d\lambda, \tag{2.15}$$

where A = X, Y, Z, are also known as imaginary primaries. The real primaries are the RGB tristimulus colour-matching functions (Figure 2.6), represented as a = x, y, z.

In the diagram in Figure 2.7, the locus outlining the coloured area is formed by monochromatic wavelengths and any colour in the visible spectrum can be represented by the x and y coordinates, where the colour-matching functions are related to the colour coordinates by the relations shown in Equation 2.16:

$$x = \frac{X}{X+Y+Z}, \qquad y = \frac{Y}{X+Y+Z}, \qquad z = \frac{Z}{X+Y+Z}. \tag{2.16}$$

The CIE diagram shows the Plankian locus with the emission colours of a black body characterised by an absolute scale temperature scale in kelvin (K) going from deep red at low temperatures through orange, yellow-white, white and finally blue-white at very high temperatures.

Considering this, any light source can be assigned a correlated colour temperature (CCT), which is the temperature of an ideal black body that is closest in shade to that of the light source (Figure 2.8). The CCT is calculated using the McCamy Equation 2.17:[24]

$$-449n^3 + 3525n^2 - 6823n + 5520.33, \tag{2.17}$$

where $n = \dfrac{x - 0.332}{y - 0.186}$.

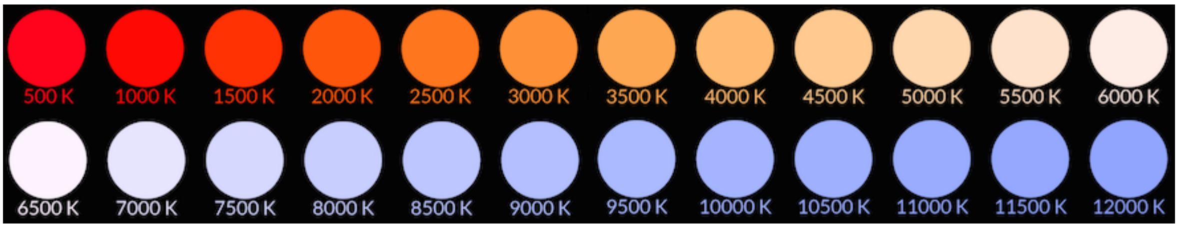

Figure 2.8: RGB components corresponding to the colour of a black body at different temperatures.

The colour-rendering index (CRI) is a standard method of characterising the quality of light by measuring the effect the light source has on the colour appearance of objects in comparison with their appearance under a reference source. In most practical cases, the light is incandescent lamp light or some phase of natural lighting. By definition, the maximum value of CRI is 100 (blackbody radiator). The CRI value is obtained by comparing the difference in the colour coordinates in the CIE of an object between when it is illuminated with the test source and when it is illuminated with a black body with the same CCT.

2.4 Scanning Electron Microscopy

2.4.1 Fundamentals

Electron microscopes can operate with a wavelength <1 Å, offering atomic resolution. The signal obtained can be directly transformed into an image by using a suitable lens. Scanning electron microscopy (SEM) uses a type of electron microscope where the sample is bombarded with electrons concentrated in a small probe (~20 Å). The secondary electrons are scattered back from the sample and are detected, thus obtaining an image of the surface. This image is commonly used to examine the morphology of the surface across the sample.[1]

Energy Dispersive X-ray Spectroscopy (EDX) is a technique that works together with SEM. In this technique the sample is bombarded with high energy electrons generating X-rays, which can be detected based in their wavelength or energy then allowing identification of the elements present in the sample.[17]

2.4.2 Instrumentation

A Hitachi SU-70 Field Emission Gun Scanning Electron Microscope (FEG SEM) was used to analyse the samples (Department of Physics, Durham). The samples were pressed into 8 mm diameter pellets, placed on carbon stickers attached to glass slides and coated with 30 nm of carbon or gold, depending on the charge build-up experienced by each sample. The FEG SEM was optimised to energies of 15 keV and 12 keV and calibrated with a cobalt chip.

2.4.3 Data Analysis

The data were recorded with Aztec software from Oxford Instruments plc.[25] Each measurement had a process time of 4 s, an acquisition time of 8 s, a scan size of 1024 resolution and dwell times of 9 μs and 11 μs, for around five different sites and fifteen spectra areas for each site per sample.

Further analysis was applied to the data (reported in % atomic) obtained from the software:

1) The average for each site, with standard deviation for each value.
2) Fixing the nominal oxygen content and scaling the % atomic of the other elements, with standard deviation for each value.
3) Calculation of the % atomic of the oxygen content by doing a charge balance of all the elements in each sample, with standard deviation for each value.

X-ray maps from the full frames showing the spatial distribution of all the elements in the specimen were recorded. The final images were shown as layered images, where the colours for each element are overlaid on the electron image. These overlaid images can identify a single phase when the distribution of the elements is even.

2.5 References

[1] Cheetham, A. and Day, P. *Solid state chemistry techniques. Clarendon, Oxford*, 1987.

[2] Pfann, W.G. *JOM*, 4(7):747–753, 1952.

[3] Cranswick, L.M., Le Bail, A., Madsen, I., Fitch, A., Allmann, R., Giacovazzo, C., Altomare, A., Cockcroft, J.K., Caliandro, R., and Norby, P. *Powder Diffraction: Theory and Practice, Royal Society of Chemistry*, 2008.

[4] Snyder, R., Bish, D., and Post, J. *Reviews in mineralogy*, 20, 1989.

[5] Young, R. *Introduction to the Rietveld method, The Rietveld Method*, 5:1–38, 1993.

[6] Cullity, B.D. *Elements of X-ray Diffraction, Addison-Wesley Publishing*, 1956.

[7] Coelho, A. *TOPAS-Academic is available at http://topas-academic. net.*

[8] Scherrer, P. *Kolloidchemie Ein Lehrbuch, Springer*, 1912.

[9] Balzar, D., Audebrand, N., Daymond, M.R., Fitch, A., Hewat, A., Langford, J.I., Le Bail, A., Louer, D., Masson, O., McCowan, C.N., Popa, N.C., Stephens, P.W., and Toby, B.H. *Journal of Applied Crystallography*, 37(6), 2004.

[10] Bruker AXS, K. *Diffrac+ XRD Commander v2.3: Software for Controlling Bruker Diffractometers*, 2000.

[11] Pecharsky, V.K. and Zavalij, P.Y. *Fundamentals of powder diffraction and structural characterization of materials, Springer*, 69, 2009.

[12] Adamson, P., Lennie, A., Murray, C., Parker, J., Potter, J., Tang, C., Thompson, S.., and Yuan, F. (BLS-I11-MAN-001), 2015.

[13] Bruker, I. *SAINT V8. A*, 38, 2016.

[14] Petříček, V., Dušek, M., and Palatinus, L. *Zeitschrift für Kristallographie-Crystalline Materials*, 229(5):345–352, 2014.

[15] Rietveld, H.M. *Journal of Applied Crystallography*, 2:65–, 1969. Part 2.

[16] Coelho, A.A., Evans, J.S.O., Evans, I.R., Kern, A., and Parsons, S. *The TOPAS symbolic computation system, Powder Diffraction*, 26(4):S22, 2011.

[17] Atkins, P. and dePaula, J. *Physical Chemistry, Oxford University Press USA*, 2006.

[18] Atkins, P., Overton, T., Rourke, J., Weller, M., and Armstrong, F. *Shriver and Atkins' inorganic chemistry, Oxford University Press USA*, 2010.

[19] Mehta, A. *Analytical Chemistry*, 2013.

[20] Schubert, E.F. and Kim, J.K. *Science*, 308(5726):1274–1278, 2005.

[21] Fairman, H.S., Brill, M.H., and Hemmendinger, H. *Color Research & Application*, 22(1):11–23, 1997.

[22] Judd, D.B. and Wyszecki, G. *Color in business, science, and industry, John Wiley & Sons*, 1975.

[23] CIE, C. *Commission internationale de l'eclairage proceedings, Cambridge University Press Cambridge*, 1932.

[24] McCamy, C.S. *Color Research and Application*, 17(2):142–144, 1992.

[25] Tubney Woods, Abingdon, O.O.Q.U.A.R.R. *AZTEC® (2289391), Oxford Instruments plc*, 2014.

3 New warm white-emitting Dy^{3+}-containing phosphors based on apatite-type $Gd_{9.33}(SiO_4)_6O_2$

3.1 Introduction

Traditional incandescent lamps are limited by the maximum temperature the filament can reach. Their efficiency is compromised by the dominance of invisible infrared emission (heat). As a result, research into white light-emitting diodes (w-LEDs) has been pursued by scientists worldwide, due to their high efficiency, environmental friendliness and design flexibility, aiming to replace all the other generations of lighting technology. The most widely available commercial w-LED is a combination of a blue LED (InGaN) with a yellow-emitting phosphor (YAG:Ce) in which a mixture of the blue and yellow can produce white light.[1]

An alternative way to obtain w-LEDs is by using single-phase rare earth (RE) doped luminescent materials combined with a UV LED. RE^{3+} ions play an important role in solid-state lighting, owing to their emissions in different spectral regions resulting from their $4f$-$4f$ or $5d$-$4f$ transitions.[2] However, the excitation spectrum of Dy^{3+} ions only includes narrow $4f$-$4f$ transition lines, as the charge transfer band and $4f^9$-$4f^8 5d^1$ are located in a lower region (< 220 nm). Therefore, Dy^{3+} cannot be directly excited with UV light.[3] During these transitions the host does not significantly influence the excitation and emission energies of Dy^{3+}, which therefore can be predicted using the Dieke diagram (shown in Figure 3.1).[2, 4]

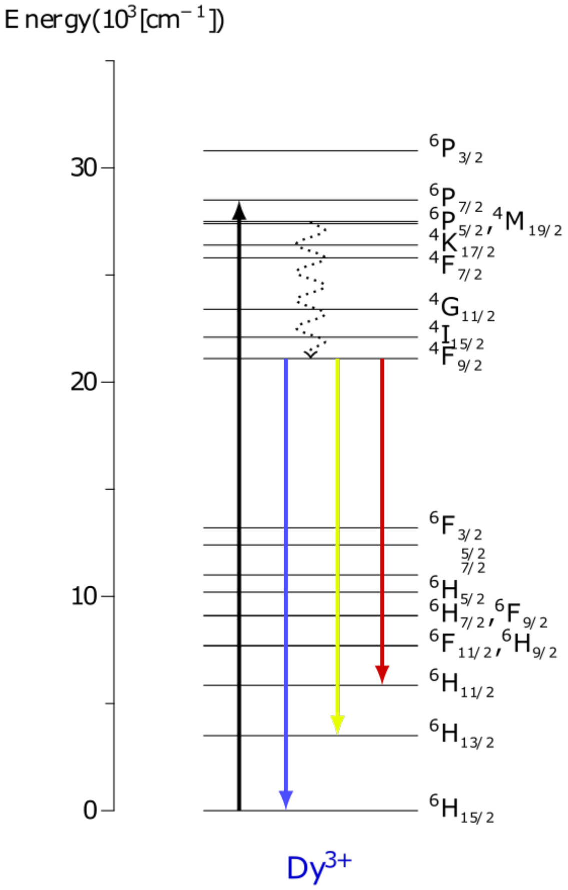

Figure 3.1: Energy-level diagram for Dy^{3+} ion showing the relevant transitions.[4]

In the visible region, Dy^{3+} ions present three emission bands:[5]

- a blue band at 480 nm, arising from the spin-allowed magnetic dipole (MD) $^4F_{9/2} \rightarrow {}^6H_{15/2}$ transition;

- a yellow band at 575 nm, arising from the hypersensitive (ΔL=2, ΔJ=2) $^4F_{9/2} \rightarrow ^6H_{13/2}$ transition. This spin-forbidden electric dipole (ED) transition is the only *f-f* emission transition observed at this wavelength region;
- a red band at 670 nm, arising from the weak electric dipole $^4F_{9/2} \rightarrow ^6H_{11/2}$ transition.

An adequate yellow-to-blue (Y/B) ratio, $^4F_{9/2} \rightarrow ^6H_{13/2}$ / $^4F_{9/2} \rightarrow ^6H_{15/2}$, can be achieved by changing the Dy^{3+} content (% atomic). The net result can then be adjusted to obtain emission in the white light (WL) region.[6, 7] Furthermore, the hypersensitive transition varies most obviously with the environment around the Dy^{3+} ions. If Dy^{3+} occupies an inversion symmetry site in the crystal structure, the MD transition is the dominant one and it can ultimately produce 'cold' (CCT > 5500 K) to 'neutral' (CCT around 3500–4500 K) white light. On the contrary, if Dy^{3+} is not located at an inversion centre, the ED transition is dominant, giving 'warm' yellowish-white light (CCT < 3500 K).[5] Consequently, the host selection is an important part of the development of phosphors, where for warm light a structure without an inversion centre.

An increasing number of phosphors have been reported in the literature whose chromaticity coordinates fall near two specific points: CIE 1931 standard whitepoint (WP) at (1/3, 1/3) and daylight at (0.31271, 0.32902). Selected illustrative examples are given below and summarised in Table 3.1. These have been chosen as they are Dy^{3+}-doped oxide hosts with emission in the white region, ranging from cold through warm to yellowish white light.

White-light	
Compound	Colour coordinates
$Ca_2Gd_8(SiO_4)_6O_2$:xDy^{3+} (x = 0.1-0.5)[8–10]	(0.331, 0.337)
$KBaY_{0.95}Si_2O_7$:0.05Dy^{3+}[11]	(0.3286, 0.3302)
Cold light	
Compound	Colour coordinates
$CaMoO_4$:xDy^{3+}[12]	(0.31,0.32)
$BaMgSiO_4$[13]	(0.3305, 0.3512)
$Sr_2Gd_8(SiO_4)_6O_2$:0.01Dy^{3+}[14]	(0.325, 0.355)
$Y_6Ba_4(SiO_4)_6F_2$[15]	Daylight
$Ca_2Pb_3(PO_4)_3Cl$:Dy^{3+}[16]	(0.302,0.291)
δ-$Gd_2Si_2O_7$:0.01Dy^{3+}[6]	(0.30,0.33)
$Ca_9La(PO_4)_5(SiO_4)Cl_2$:x$Dy^{3+}$[17]	Cold to white
$Ca(Bi_{0.95}Dy_{0.05})_2B_2O_7$[18]	(0.30,0.34)
$Bi_4Si_3O_{12}$:Dy^{3+}[19]	(0.294, 0.338) to (0.339, 0.377)
$Ca_2ZnSi_2O_7$:Dy^{3+}[20]	Deep blue
$Sr_4Ca(PO_4)_2SiO_4$[21]	(0.2837, 0.2838)
$SrAl_2Si_2O_8$:xDy^{3+}[22]	Light blue
$CaBi_{1.93}B_2O_7$:0.07Dy^{3+}[23]	(0.226, 0.228)
Warm light	
Compound	Colour coordinates
$Ca_9La_{1-x}(PO_4)_5(SiO_4)F_2$:x$Dy^{3+}$[24]	(0.311, 0.313) to (0.358, 0.366)
$Gd_2Ti_2O_7$:Dy^{3+}[25]	(0.375, 0.458)
YVO_4:Dy^{3+}[26]	Yellow
$Ca_4Y_6O(SiO_4)_6$:7%Dy^{3+}[27]	(0.354,0.373)
$Ba_2Y_3(SiO_4)_3F$:Dy^{3+}[28]	Yellowish-white
$Li_2Gd_4(WO_4)_7$:xDy^{3+}[29]	(0.4205,0.4602)
$Mg_2Zn(PO_4)_2$:2%Dy^{3+}[30]	(0.38,0.41)
$LaBO_3$:Dy^{3+}[31]	(0.425,0.445) to (0.427,0.450)

Table 3.1: Summary of Dy^{3+}-doped phosphors.

For example, $Ca_2Gd_8(SiO_4)_6O_2$:xDy^{3+} (x = 0.1-0.5) has strong absorption at around 275 nm, and at its optimum doping level (x = 0.4) it emits very near the WL point, with chromaticity coordinates (0.331, 0.337).[8–10] Recently, $KBaY_{0.95}Si_2O_7$:0.05Dy^{3+} phosphor has been studied. It presents chromaticity coordinates (0.3286, 0.3302) when excited at 350 nm.[11]

When the strongest emission intensity is in the blue region, the phosphors fall in the cold white light region. For example, $CaMoO_4$:xDy^{3+} nanophosphor emits in the deep blue region for x = 0-0.05, with the exception of x = 0.03. The concentration quenching (maximum reached at x = 0.02) and the cross-relaxation process allow the phosphor doped at x = 0.03 to emit cold white light with colour coordinates (0.31, 0.32).[12]

The chromatic coordinates (0.3305, 0.3512) of $BaMgSiO_4$ indicate that this phosphor can generate cold white light when excited at 384 nm.[13] $Sr_2Gd_8(SiO_4)_6O_2$:0.01Dy^{3+} phosphor emits in the cold white light region with colour coordinates (0.325, 0.355).[14] $Y_6Ba_4(SiO_4)_6F_2$ apatite phosphor has been reported with CIE coordinates in the daylight region, under 350 nm excitation.[15]

Dy^{3+}-doped $Ca_2Pb_3(PO_4)_3Cl$ phosphor has been reported to have a stronger magnetic dipole than electric dipole transition. This is caused by the Dy^{3+} ions occupying a high symmetry site. Therefore, the blue emission intensity is stronger than the yellow emission intensity, resulting in colour coordinates within the blue light region, (0.302, 0.291).[16]

δ-$Gd_2Si_2O_7$:0.01Dy^{3+} phosphor has been reported to show emission within the ideal white light region. However, the chromaticity coordinates are (0.30, 0.33),[6] so this should be considered the cold white light region, rather than ideal. The Dy^{3+} ions are located at a site with no inversion centre. This allows forced electric dipole transition. The activator is at a non-centrosymmetric site, giving a dominant blue band in the emission spectrum.

$Ca_9La(PO_4)_5(SiO_4)Cl_2$:x$Dy^{3+}$ gives tuneable white light going from cold white light to daylight, with coordinates near the WP region.[17] When efficiently excited by 349 nm irradiation $Ca(Bi_{0.95}Dy_{0.05})_2B_2O_7$ can emit blueish white light with CIE coordinates (0.30, 0.34).[18] $Bi_4Si_3O_{12}$:Dy^{3+} phosphor goes from daylight (0.294, 0.338) to warm (0.339, 0.377) light under 254 nm UV light excitation.[19]

There are a few extreme cases were the blue emission is completely outside the white light region, making the phosphors blue-emitters. $Ca_2ZnSi_2O_7$:Dy^{3+} phosphor presents emission in the deep blue region and concentration quenching due to the dipole-dipole interaction of the neighbouring Dy^{3+} ions.[20]

The colour coordinates of $Sr_4Ca(PO_4)_2SiO_4$ phosphor are (0.2837, 0.2838) when it is excited at 348 nm.[21] $SrAl_2Si_2O_8$:xDy^{3+} phosphor produces light-blue light with CCT ranging from 9562 K to 11730 K.[22] $CaBi_{1.93}B_2O_7$:0.07Dy^{3+} is another phosphor showing a bluish white emission, with colour coordinates (0.226, 0.228), when excited under 349 nm UV light.[23] The strong dominance of the blue band may be due to the Bi $^{3+}$ ions being another fluorescent centre,[32] which was not taken into consideration.

These cold white light emitters are not ideal for residential applications. The human eye photoreceptor of blue light regulates the human circadian (wake-sleep) rhythm, which is why the use of blue or even cold light is not advised for certain lighting applications. Inappropriate lighting conditions have been proved to upset the body chemistry of mammals, leading to unfavourable health effects and in some cases a dependence on sleep-inducing pharmaceuticals.[33] Even daylight emission, which is present in some of the above-mentioned phosphors, is not ideal for some applications as a very bright light inside the house at night is undesirable. For this reason, there has been much research on warm white light emitters.

$Ca_9La_{1-x}(PO_4)_5(SiO_4)F_2$:x$Dy^{3+}$ phosphor can go from cold (0.311, 0.313) to warm (0.358, 0.366) light by changing the Dy^{3+} doping level.[24] When excited in the UV region, $Gd_2Ti_2O_7$:Dy^{3+} pyrochlore nanomaterial emits white light with chromaticity coordinates near the WP, (0.324, 0.337). Conversely, when it is excited with blue light the colour coordinates for this phosphor are (0.375, 0.458) making it a deep yellow emitter.[25]

The synthesis process has been proved to be important. For instance, Dy^{3+}-doped YVO_4 phosphor has been reported to emit yellow light under 223 nm excitation when synthesised via a combustion process. After further heat treatment (around 1100 °C) of the material obtained, a considerable shift towards the white region was reported. It was shown that the extra heating increased the particle size and in consequence the grain boundary effect was avoided and the luminous efficiency increased.[26]

Apatite-type $Ca_4Y_6O(SiO_4)_6$ Dy^{3+}-doped phosphor is reported to emit in the warm white light region under 346 nm excitation. Its temperature dependence photoluminescence has been studied to inspect thermal stability. It was found that the phosphor shifts towards a deeper yellow light region at higher temperatures. At room temperature, colour coordinates (0.33,0.339) were recorded for $Ca_4Y_6O(SiO_4)_6$:7% Dy^{3+} phosphor, while at 300 °C (double the LED working temperature) the coordinates were (0.354,0.373).[27]

Dy^{3+}-doped $Ba_2Y_3(SiO_4)_3F$ material has been shown to have CCT < 5000 K, making it a phosphor for warm light applications.[28] $Li_2Gd_4(WO_4)_7$:xDy^{3+} phosphor has deep yellow emission with colour coordinates (0.4205,0.4602) when excited at 352 nm, and concentration quenching of $x = 0.04$ has been reported.[29] The CIE coordinates of 2 at. % Dy^{3+}-activated $Mg_2Zn(PO_4)_2$ fall within the yellowish-white light region, with colour coordinates(0.38,0.41).[30] Single phase $LaBO_3$:Dy^{3+} phosphors show colour coordinates that range from (0.425,0.445) to (0.427,0.450), corresponding to a light-yellow to yellow colour.[31]

The environment around the Dy^{3+} site is important and can be used to understand the optical properties of certain phosphors resulting from the hypersensitive transition. $A_3B(PO_4)_2{:}Dy^{3+}$ (where A= Na, K and B = Y, La) phosphors have been reported to be white light emitting materials. From the luminescence intensity, the relative luminescence intensity between the blue and yellow emission bands and stark splitting, it was concluded that the environment of the Dy^{3+} ions had higher symmetry in the $Na_3B(PO_4)_2$ than in the $K_3B(PO_4)_2$ (B = Y, La) host.[34]

White-light emitting $CaMoO_4{:}Dy^{3+}$ nanophosphors codoped with K^+ to charge compensate without creating defects (*i.e.* interstitial O^{2-}) can increase the luminescence intensity. The charge neutrality needs three Ca^{2+} ions to substitute two Dy^{3+} ions, while the charge compensation for the codoped compound only needs two Ca^{2+} ions to introduce one Dy^{3+} and one K^+ ion.[12] $SrMoO_4{:}Dy^{3+}$ phosphors used Na^+ ions to compensate the charge of the substitution of Sr^{2+} by Dy^{3+}, showing an increase in the emission intensity.[35] It has been reported that introducing La^{3+} as co-doping into the white-emitting $NaSrVO_4{:}Dy^{3+}$ phosphor improves its optical performance, increasing quantum efficiency and fluorescence decay.[36]

Figure 3.2 shows the energy-level diagram (derived from the Dieke diagram[37]) with the interaction between the Russell-Saunders coupling states of Gd^{3+} and Dy^{3+}. After UV irradiation, the Gd^{3+} sensitiser is excited from the ground $^8S_{7/2}$ state to the $^6P_{7/2}$ or ^6I_J states as anticipated. It can then populate excited states at a similar energy level of nearby Dy^{3+} ions by energy transfer, which relax to the $^4F_{9/2}$ state. The system goes from $^4F_{9/2}$ state to lower available states. This radiative decay permits transitions to $^6H_{15/2}$, $^6H_{13/2}$ and $^6H_{11/2}$, corresponding to blue, yellow and red bands respectively.

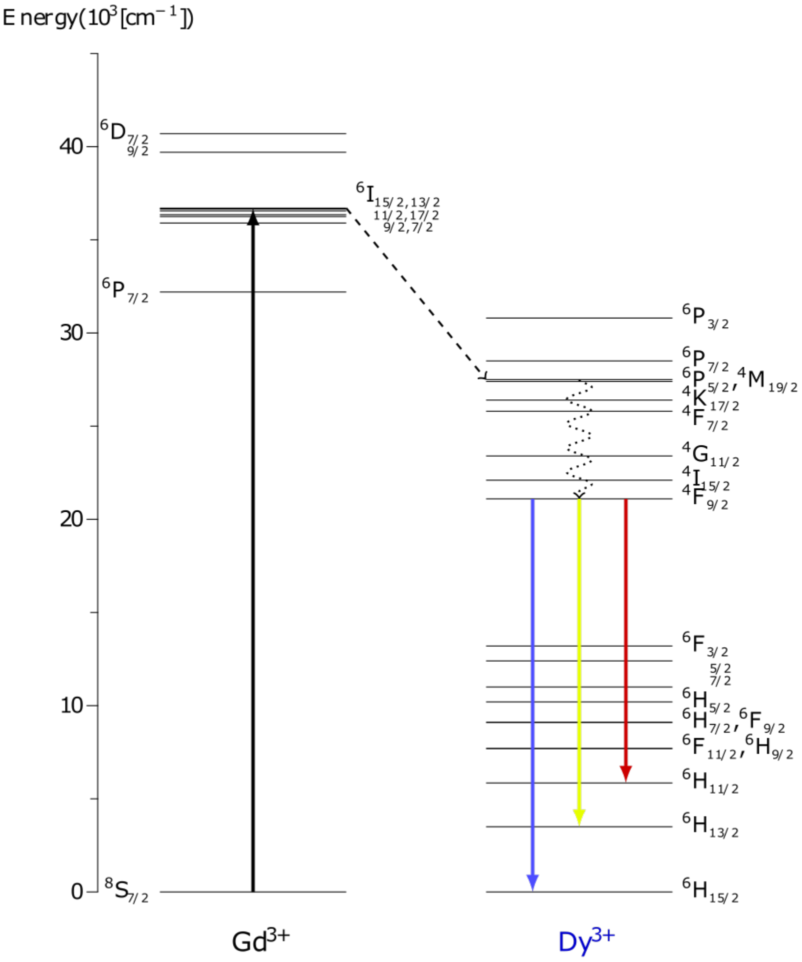

Figure 3.2: Energy-level diagrams for Gd^{3+} and Dy^{3+} ions showing the relevant transitions in the system.[4]

The first part of this chapter describes the compounds prepared as new potential phosphor hosts (series highlighted in Table 3.2, using as a host the gadolinium silicate apatite described in section 1.4.6).

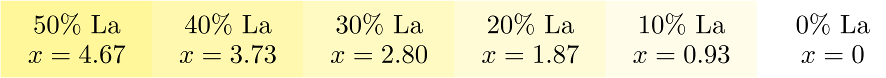

50% La $x = 4.67$	40% La $x = 3.73$	30% La $x = 2.80$	20% La $x = 1.87$	10% La $x = 0.93$	0% La $x = 0$

Table 3.2: La^{3+} content in the $Gd_{9.33-x}La_x(SiO_4)_6O_2$ host material.

The compounds described in the second part of this chapter are the $Gd_{9.33-x}Dy_x(SiO_4)_6O_2$ and $Gd_{4.67-\frac{x}{2}}La_{4.67-\frac{x}{2}}Dy_x(SiO_4)_6O_2$ (x = 0.05, 0.09 and 0.19) phosphor series, as highlighted in Table 3.3.

50% La					0% La
0.5% Dy $x = 0.05$					0.5% Dy $x = 0.05$
1.0% Dy $x = 0.09$					1.0% Dy $x = 0.09$
2.0% Dy $x = 0.19$					2.0% Dy $x = 0.19$

Table 3.3: The different doping levels for the $Gd_{4.67-\frac{x}{2}}La_{4.67-\frac{x}{2}}Dy_x(SiO_4)_6O_2$ and $Gd_{9.33-x}Dy_x(SiO_4)_6O_2$ phosphor series.

The structural model used for fitting all powder diffraction data presented in this chapter collected on the La^{3+} substituted and Dy^{3+}-doped $Gd_{9.33}(SiO_4)_6O_2$ materials is shown in Table 3.4, where the Gd^{3+} sites are being substituted with La^{3+}, Dy^{3+} or both. In each case, La^{3+} and Dy^{3+} were distributed on the two crystallographically independent A-sites: A1 (Wyckoff site 4f) and A2 (Wyckoff site 6h). A1 site is partially occupied and A2 site is fully occupied.

Site	Wyckoff Site	x	y	z	Occupancy	Total
A1(Gd)	4f	1/3	2/3	-0.00044	0.8333	3.3332
A2(Gd)	6h	0.23978	0.00813	1/4	1.0	6
Si1	6h	0.3708	0.3981	1/4	1.0	6
O1	6h	0.1216	0.5249	1/4	1.0	6
O2	6h	0.4839	0.3147	1/4	1.0	6
O3	12i	0.2490	0.3394	0.0642	1.0	12
O4	2a	0.0000	0.0000	1/4	1.0	2

Table 3.4: Crystallographic data for $Gd_{9.33}(SiO_4)_6O_2$ apatite.[38]

3.2 Experimental details

3.2.1 Sample preparation

Solid state synthesis was carried out to prepare polycrystalline samples in the $Gd_{9.33-x}La_x(SiO_4)_6O_2$ (x = 0, 0.93, 1.87, 2.8, 3.73 and 4.67) host series and $Gd_{4.67-\frac{x}{2}}La_{4.67-\frac{x}{2}}Dy_x(SiO_4)_6O_2$ and $Gd_{9.33-x}Dy_x(SiO_4)_6O_2$ (x = 0.05, 0.09 and 0.19) phosphor series. The stoichiometric equations for the reaction to obtain pure single-phase host compounds are given by Equation 3.1.

$$6SiO_2 + (\frac{9.33-x}{2})Gd_2O_3 + \frac{x}{2}La_2O_3 \rightarrow Gd_{9.33-x}La_x(SiO_4)_6O_2. \tag{3.1}$$

The stoichiometric amounts for the reactions carried out to obtain the Dy^{3+}-doped target compounds are given by Equations 3.2a and b.

$$6SiO_2 + (\frac{9.33-x}{4})La_2O_3 + (\frac{9.33-x}{4})Gd_2O_3 + \frac{x}{2}Dy_2O_3 \rightarrow Gd_{4.67-\frac{x}{2}}La_{4.67-\frac{x}{2}}Dy_x(SiO_4)_6O_2, \tag{3.2a}$$

$$6SiO_2 + (\frac{9.33-x}{2})Gd_2O_3 + \frac{x}{2}Dy_2O_3 \rightarrow Gd_{9.33-x}Dy_x(SiO_4)_6O_2. \tag{3.2b}$$

The details of the starting reagents used in these syntheses are shown in Table 3.5. To ensure their quality they were X-rayed prior to use.

Reagent	Supplier	Purity
Gd_2O_3	Sigma Aldrich	99.99%
La_2O_3	Sigma Aldrich	99.99%
Dy_2O_3	Sigma Aldrich	99.99%
SiO_2	Sigma Aldrich	99.99%

Table 3.5: Reagents used in these syntheses.

To prepare 2.0 g of each composition, the stoichiometric amounts of the reagents needed were weighed (with a precision of ±0.0001 g). As all these reagents are hygroscopic, there was an initial heating at 1200 °C for 12 hours, to eliminate any absorbed water. The reagents were then ground for 30 minutes and heated at 1400 °C with intermittent grinding for a total of up to 300 hours.

3.2.2 X-ray diffraction.

After each heating cycle, laboratory PXRD data were recorded following the data collection convention described in the section 2.2.3 to assess the progress of the solid-state reactions and product purity. The final recorded patterns were fitted using the initial structural model for $Gd_{9.33}(SiO_4)_6O_2$,[38] modified to reflect the composition of each sample. The refined parameters included the background, diffractometer zero point, pseudo-Voigt function peak shape, unit cell parameters and isotropic displacement parameters. All the PXRD data were analysed using Topas Academic software.[39]

3.2.3 Photoluminescence spectroscopy

A Horiba Fluorolog-3 fluorimeter was used for the optical measurements, with a xenon flashlamp as the excitation source, and a Hamamatsu R928 photomultiplier tube for detection. Homogeneous, finely powdered samples of the materials were contained in a Spectralon® cup with a quartz cover slip, and placed inside a Quanta-ϕ F-3029 integrating sphere, connected to the spectrometer via optical fibres. The data recorded was analysed as discussed in more detail in section 2.3.3.

Lifetime values were recorded by multichannel scaling following excitation with a pulsed xenon lamp. The light emitted was analysed at right angles to the excitation source, and detected using a Hamamatsu R928 photomultiplier tube, thermoelectrically cooled to -20 °C, after passing through a monochromator.

3.3 Results and discussion

3.3.1 New phosphor host materials based on apatite-type gadolinium silicate, $Gd_{9.33-x}La_x(SiO_4)_6O_2$

3.3.1.1 Structural characterisation: Powder X-Ray Diffraction

To confirm purity laboratory PXRD data were collected and fitted using the Rietveld method[39, 40] and the structural model in space group $P6_3/m$[38] (An example of an input file for these refinements can be found in Appendix A.3). Figure 3.3 shows the fits for the $Gd_{9.33-x}La_x(SiO_4)_6O_2$ (x = 0, 0.93, 1.87, 2.8, 3.73 and 4.67) host series, where the Refined parameters are presented in Appendix A.2. The fits confirm that highly crystalline $Gd_{9.33-x}La_x(SiO_4)_6O_2$ materials have been synthesised.

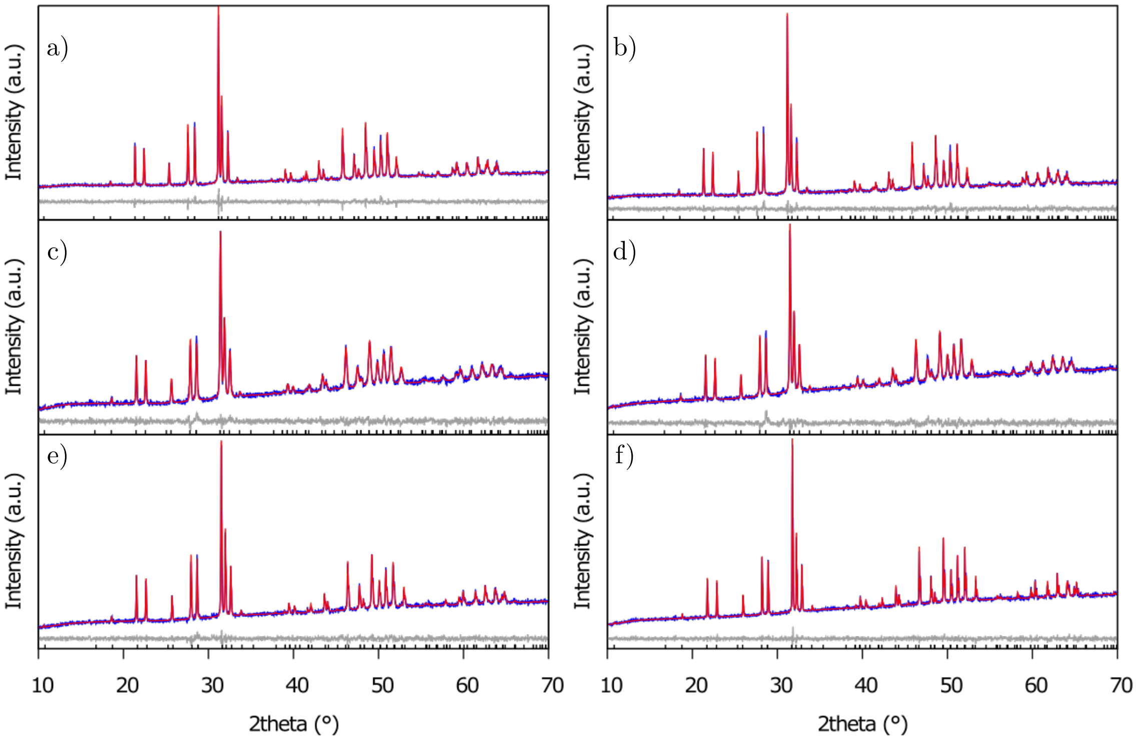

Figure 3.3: Rietveld fits of the laboratory PXRD data for $Gd_{9.33-x}La_x(SiO_4)_6O_2$. a) x = 4.67, R_{wp} = 3.914%. b) x = 3.73, R_{wp} = 3.725%. c) x = 2.80, R_{wp} = 3.491%. d) x = 1.87, R_{wp} = 3.148%. e) x = 0.93, R_{wp} = 2.969%. f) x = 0, R_{wp} = 2.773%.

High-quality PXRD were collected at the I11 beamline (Diamond Light Source synchrotron) to obtain high-resolution and better signal-to-noise PXRD patterns. 12-term polynomial background, zero point, pseudo-Voigt function peak shape, unit cell parameters, isotropic atomic displacement parameters for anions and cations and individual atomic coordinates for each site were refined for these compositions (An example of an input file for these refinements can be found in Appendix A.4). The synchrotron PXRD data show high purity levels for the first two hosts, as is shown in Figure 3.4 a) and b), and a small amount of Gd_2SiO_5 (which was not detectable in laboratory PXRD data) for the last four hosts, as is shown in Figure 3.4 c)-f). The fact that the Gd_2SiO_5 impurity was identified suggests that La^{3+} was incorporated into the apatite structure. The unit cell parameters refined, the R_{wp} and the amount of the second phase, if present, for the $Gd_{9.33-x}La_x(SiO_4)_6O_2$ hosts are given in Table 3.6.

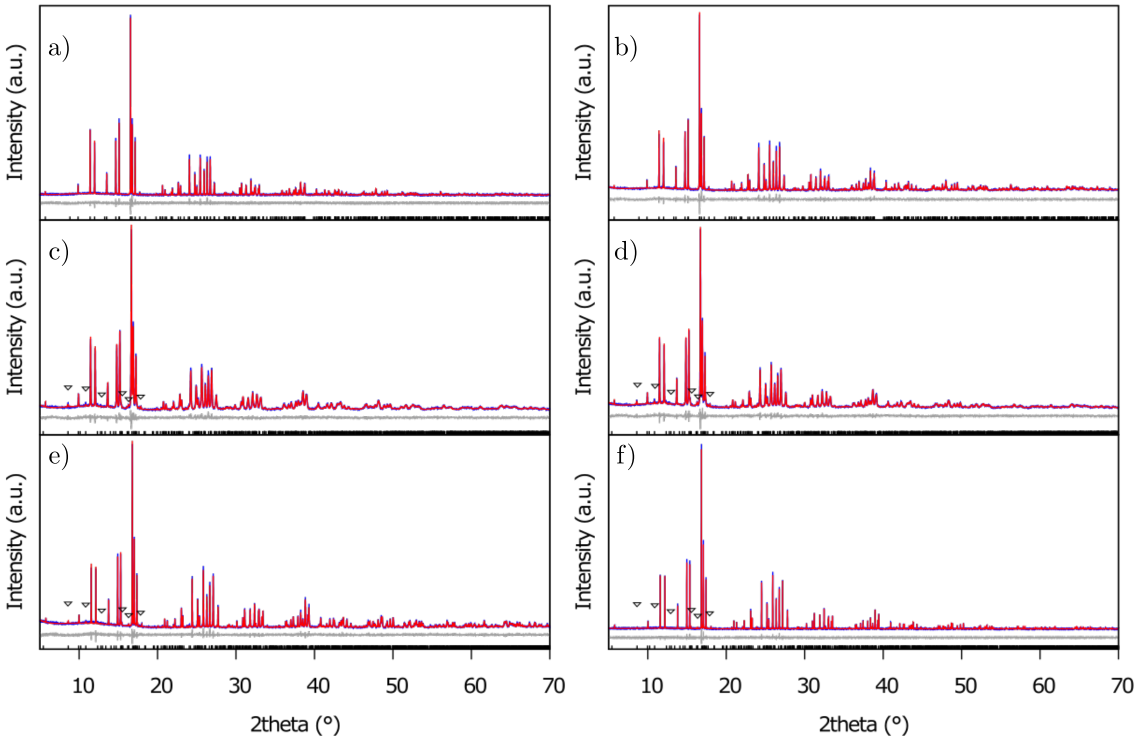

Figure 3.4: Rietveld refinement of the synchrotron PXRD patterns for $Gd_{9.33-x}La_x(SiO_4)_6O_2$. a) x = 4.67, R_{wp} = 11.01%. b) x = 3.73, R_{wp} = 10.83%. c) x = 2.80, R_{wp} = 9.16%. d) x = 1.87, R_{wp} = 9.24%. e) x = 0.09, R_{wp} = 11.26%. f) x = 0, R_{wp} = 10.06%. ∇ indicates the Gd_2SiO_5 impurity peaks.

x	a(Å)	b(Å)	V(Å^3)	R_{wp} (%)	Impurity
4.67	9.59669(3)	7.01439(3)	559.454(4)	11.01	No
3.73	9.57044(3)	6.97917(3)	553.603(5)	10.83	No
2.80	9.54178(9)	6.95206(8)	548.15(1)	9.16	5(2) wt% Gd_2SiO_5
1.87	9.51034(8)	6.92331(7)	542.3(1)	9.24	7(3) wt% Gd_2SiO_5
0.93	9.47619(4)	6.89575(4)	536.265(5)	11.26	3.7(2) wt% Gd_2SiO_5
0	9.441298(9)	6.870345(8)	530.362(1)	10.06	2.4(5) wt% Gd_2SiO_5

Table 3.6: Unit cell parameters for $Gd_{9.33-x}La_x(SiO_4)_6O_2$ (x = 0, 0.93, 1.87, 2.8, 3.73 and 4.67) hosts.

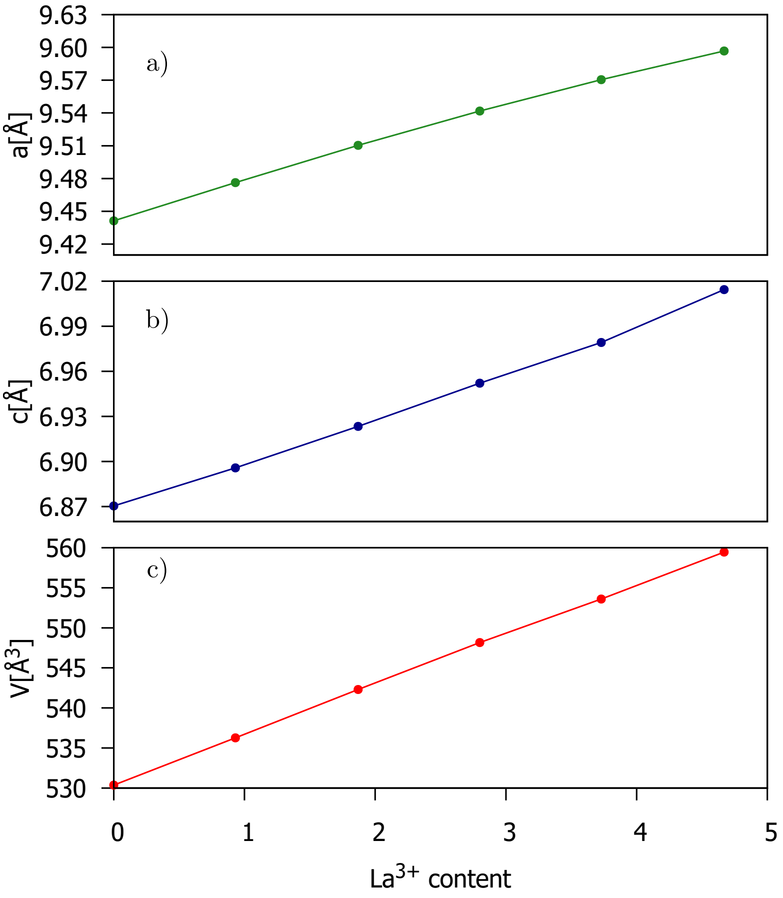

Figure 3.5: a) Lattice parameter a, b) lattice parameter c and c) unit cell volume V for $Gd_{9.33-x}La_x(SiO_4)_6O_2$ (x = 0, 0.93, 1.87, 2.8, 3.73 and 4.67) as a function of La^{3+} content (x).

Additional evidence of the incorporation of La^{3+} in the host structure can be found in the variation in the unit cell parameters. Figure 3.5 shows the relationship between the La^{3+} content and the lattice parameters for the synchrotron PXRD data.

The lattice parameter plots show linear behaviour dependent on the level of substitution of Gd^{3+} ions by La^{3+}. Vegard's law[41] can demonstrate, through the evolution of the unit cell parameters, that substitution has occurred. In this case, however, this behaviour is expected as the ionic radii[42] (coordination number 7) are 1.0 Å for Gd^{3+} and 1.1 Å for La^{3+}. Hence, if the La^{3+} ions are occupying the Gd^{3+} sites, following Vegard's law[41] an increase in the unit cell size is expected when the La^{3+} content increases. The average radius was calculated by Equation 3.3, the expected for the hosts series range from 1.00-1.05 Å.

$$\langle r \rangle = \sum_{RE=Gd,La,Dy} O_{RE} r_{RE}, \tag{3.3}$$

where O_{RE} is the occupancy and r_{RE} is the ionic radius of each atom.

3.3.2 New warm white-emitting phosphors based on apatite-type $Gd_{4.67-x}La_{4.67-x}(SiO_4)_6O_2$ and $Gd_{9.33-x}Dy_x(SiO_4)_6O_2$ doped with Dy^{3+}

3.3.2.1 Structural characterisation: Powder X-Ray Diffraction

Two Dy^{3+}-doped phosphor series were studied, the first one has half of the Gd sites substituted by La^{3+} and the second one has all the Gd sites fully occupied by Gd^{3+}. To confirm the purity of the $Gd_{4.67-\frac{x}{2}}La_{4.67-\frac{x}{2}}Dy_x(SiO_4)_6O_2$ and $Gd_{9.33-x}Dy_x(SiO_4)_6O_2$ (x = 0.05, 0.09 and 0.19) phosphors, the laboratory PXRD patterns were fitted using the Rietveld method and the structural model in space group $P6_3/m$.

All the data were analysed by Rietveld fitting.[39, 40] A 9-term polynomial background, zero point, Pseudo-Voigt peak shape function, unit cell parameters and isotropic atomic displacement parameters were refined. The Rietveld fits obtained shown in Figure 3.6 suggest that the six target Dy^{3+}-doped materials were obtained as single-phase products. Table 3.7 presents the refined unit cell parameters, the R_{wp} and the purity level. Figure 3.7 shows plots of the lattice parameters as a function of the doping level.

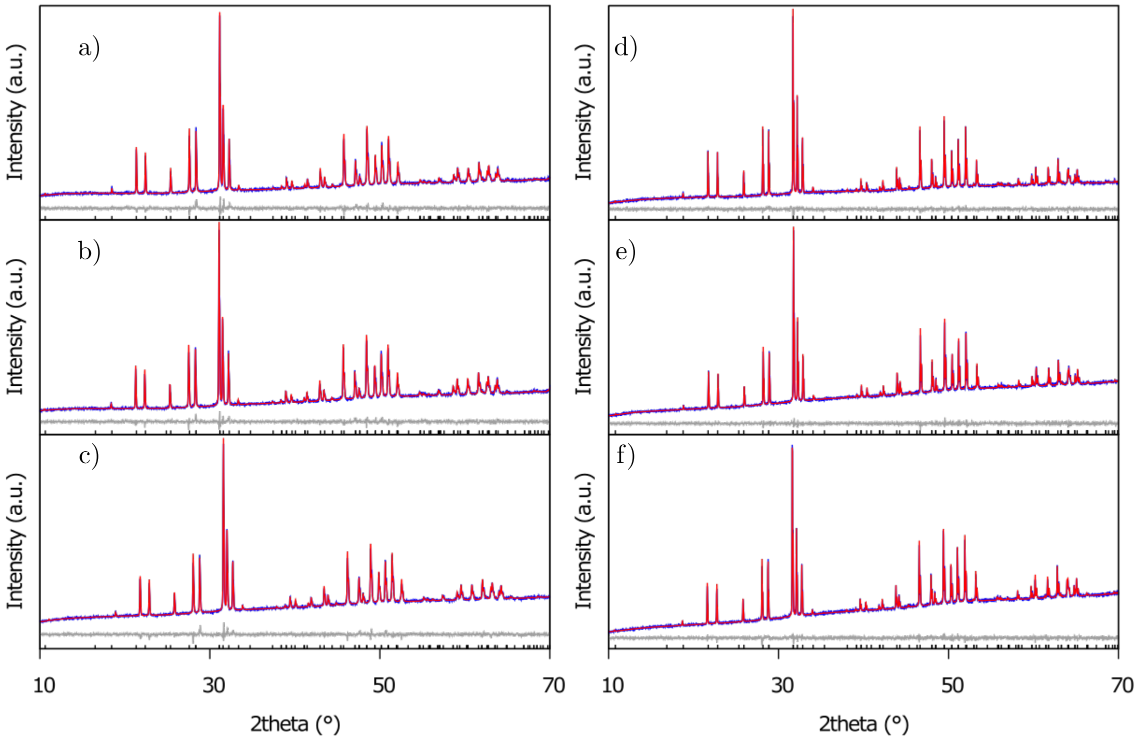

Figure 3.6: Rietveld fit of the laboratory PXRD data. $Gd_{4.67-\frac{x}{2}}La_{4.67-\frac{x}{2}}Dy_x(SiO_4)_6O_2$ a) x = 0.05, R_{wp} = 3.62%, b) x = 0.09, R_{wp} = 3.56%, and c) x = 0.19, R_{wp} = 3.69%. $Gd_{9.33-x}Dy_x(SiO_4)_6O_2$ d) x = 0.05, R_{wp} = 2.71%, e) x = 0.09, R_{wp} = 2.51%, and f) x = 0.19, R_{wp} = 2.45%.

$Gd_{4.67-\frac{x}{2}}La_{4.67-\frac{x}{2}}Dy_x(SiO_4)_6O_2$					
x	a (Å)	c (Å)	V (Å^3)	R_{wp} (%)	Impurity
0.05	9.6024(1)	7.0139(1)	560.08(2)	3.62	No
0.09	9.5994(1)	7.0092(1)	559.35(2)	3.56	No
0.19	9.6137(1)	7.0161(1)	561.57(2)	3.69	No
$Gd_{9.33-x}Dy_x(SiO_4)_6O_2$					
x	a (Å)	c (Å)	V (Å^3)	R_{wp}	Impurity
0.05	9.4511(1)	6.8754(1)	531.85(2)	2.71	No
0.09	9.44344(8)	6.8694(8)	530.53(1)	2.51	No
0.19	9.44004(7)	6.86735(8)	529.99(1)	2.45	No

Table 3.7: Unit cell parameters for $Gd_{4.67-\frac{x}{2}}La_{4.67-\frac{x}{2}}Dy_x(SiO_4)_6O_2$ and $Gd_{9.33-x}Dy_x(SiO_4)_6O_2$ (x = 0.05, 0.09 and 0.19) phosphors.

As discussed in the section 3.3.1.1, Vegard's law[41] can demonstrate, through the evolution of the unit cell parameters, that substitution has occurred. In this case, however, the ionic radii of the species replaced and the dopant are very similar. The ionic radii[42] (coordination number 7) are 1.0 Å for Gd^{3+}, 1.1 Å for La^{3+} and 0.97 Å for Dy^{3+}. It is expected for the $\mathrm{Gd}_{4.67-\frac{x}{2}}\mathrm{La}_{4.67-\frac{x}{2}}\mathrm{Dy}_x(\mathrm{SiO}_4)_6\mathrm{O}_2$ series a radius average (Equation 3.3) between 1.048-1.050 Å and for the $\mathrm{Gd}_{9.33-x}\mathrm{Dy}_x(\mathrm{SiO}_4)_6\mathrm{O}_2$ series an average between 0.999-1.000 Å. This means that the Dy-doping carried out here is unlikely to result in the clear changes of the unit cell parameters as a function of Dy content. As predicted, the lattice parameter plots (Figure 3.7) show a constant behaviour for different Dy^{3+} content in each series. The unit cell size is constant and does not depend on the Dy^{3+} doping level. However, there is a clear increase in the unit cell size between the series based on two different hosts.

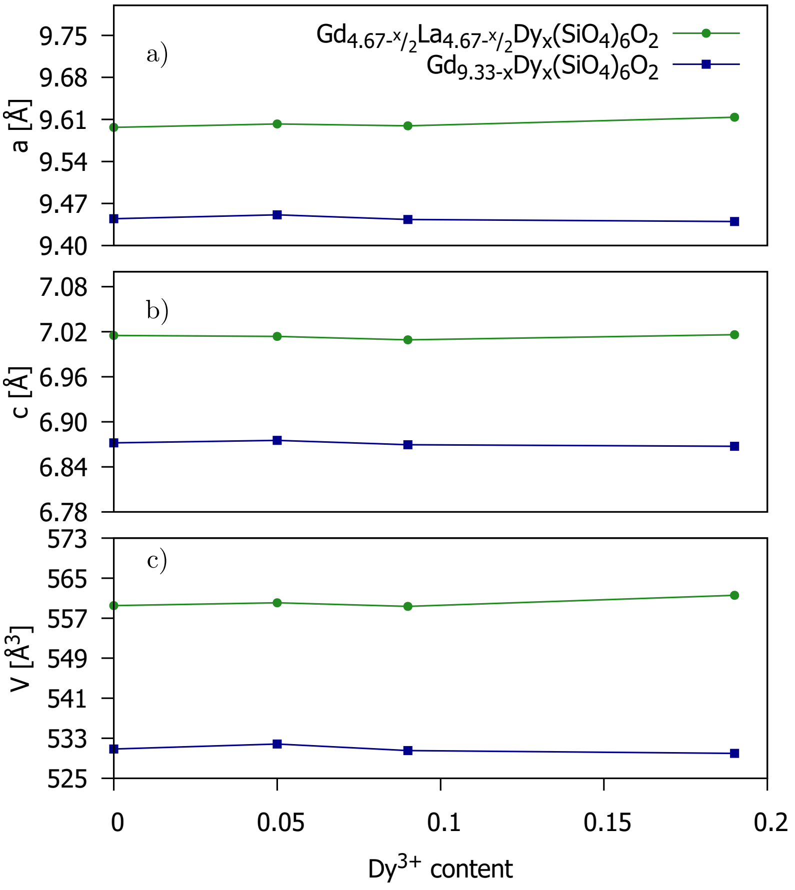

Figure 3.7: Lattice parameter a) a, b) c and c) unit cell volume V for $\mathrm{Gd}_{4.67-\frac{x}{2}}\mathrm{La}_{4.67-\frac{x}{2}}\mathrm{Dy}_x(\mathrm{SiO}_4)_6\mathrm{O}_2$ and $\mathrm{Gd}_{9.33-x}\mathrm{Dy}_x(\mathrm{SiO}_4)_6\mathrm{O}_2$ (x = 0.05, 0.09 and 0.19) as a function of Dy^{3+} content (x). The error bars are smaller than the data points.

3.3.2.2 Optical properties

The excitation spectra recorded for the $\mathrm{Gd}_{4.67-\frac{x}{2}}\mathrm{La}_{4.67-\frac{x}{2}}\mathrm{Dy}_x(\mathrm{SiO}_4)_6\mathrm{O}_2$ and $\mathrm{Gd}_{9.33-x}\mathrm{Dy}_x(\mathrm{SiO}_4)_6\mathrm{O}_2$ (x = 0.05, 0.09 and 0.19) materials, obtained at the 476 nm emission band of Dy^{3+}, are shown in Figure 3.8. The Dy^{3+} to O^{2-} charge transfer band is located at a lower wavelength, < 220 nm. Therefore, the dominant band at 275 nm belongs to the absorption of the Gd^{3+} sensitiser. The peaks representing the $\mathrm{Gd}^{3+} \rightarrow \mathrm{Dy}^{3+}$ energy transfer appear after excitation at 273 nm and 312 nm (red arrows in Figure 3.8). These excitation bands are attributed to the electronic transitions, $^8\mathrm{S}_{7/2} \rightarrow {}^6\mathrm{I}_{7/2-17/2}$ and $^8\mathrm{S}_{7/2} \rightarrow {}^6\mathrm{P}_{7/2-3/2}$, respectively (Figure 3.2). At lower energies, the peaks corresponding to the Dy^{3+} direct excitation are observed at 325, 350, 365, 386, 420 and 450 nm (black arrows in Figure 3.8), representing excitation of the Dy^{3+} ions from their ground $^6H_{15/2}$ state to the $^6P_{3/2}$, $^6P_{7/2}$, $^6P_{5/2}$, $^4F_{7/2}$, $^4G_{11/2}$ and $^4I_{15/2}$ excited states respectively (Figure 3.1).

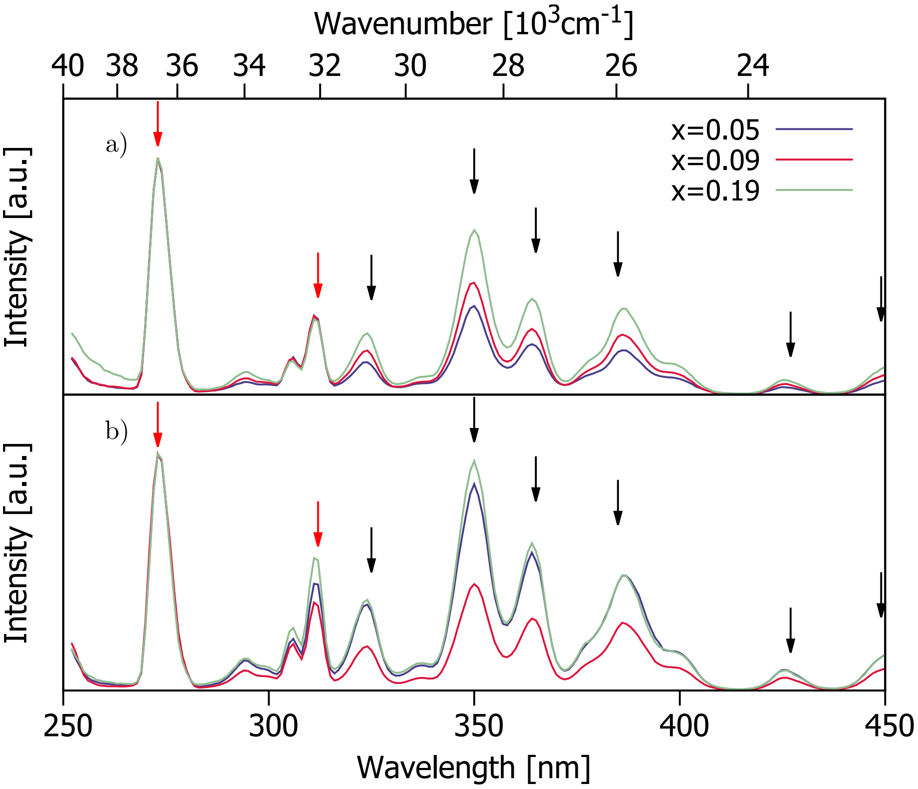

Figure 3.8: Excitation spectra of a) $Gd_{4.67-\frac{x}{2}}La_{4.67-\frac{x}{2}}Dy_x(SiO_4)_6O_2$, b) $Gd_{9.33-x}Dy_x(SiO_4)_6O_2$ materials, recorded at λ_{emi} =476 nm and normalised to the 273 nm peak. Red arrows show the Gd^{3+} excitation, indirectly populating the Dy^{3+}, and black arrows the direct Dy^{3+} excitation.

Figure 3.9 shows the emission spectra for the $Gd_{4.67-\frac{x}{2}}La_{4.67-\frac{x}{2}}Dy_x(SiO_4)_6O_2$ and $Gd_{9.33-x}Dy_x(SiO_4)_6O_2$ series, recorded upon excitation at 273 nm. The peaks detected are in the blue, yellow and red regions (green arrows, right to left, in Figure 3.9), corresponding to the $^4F_{9/2} \rightarrow {}^6H_{15/2}$, $^4F_{9/2} \rightarrow {}^6H_{13/2}$ and $^4F_{9/2} \rightarrow {}^6H_{11/2}$ transitions of the Dy^{3+} ions. The yellow emission peak is attributed to the $^4F_{9/2} \rightarrow {}^6H_{13/2}$ transition, a hypersensitive forced dipole transition, which is dependent on the symmetry of the site the activator ion occupies in the host. In these materials, the lack of inversion symmetry in the local environment of the Dy^{3+} ion is indicated by the yellow emission intensity, which is greater than the blue emission intensity. Similar behaviour has been reported for the warm white light emitting Dy^{3+}-doped Li_2MgZrO_4 phosphor, where the observed dominance of the yellow emission intensity over the blue has been used to prove that Dy^{3+} ions substitute Zr^{4+} on the low symmetry sites in the structure.[43]

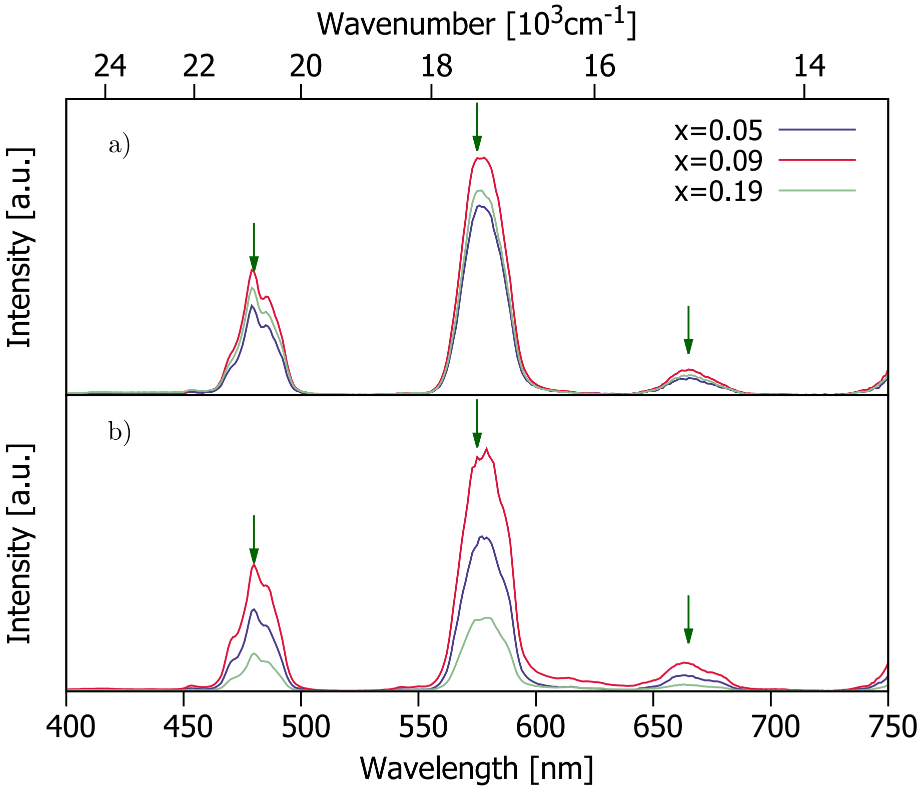

Figure 3.9: Emission spectra of a) $Gd_{4.67-\frac{x}{2}}La_{4.67-\frac{x}{2}}Dy_x(SiO_4)_6O_2$, b) $Gd_{9.33-x}Dy_x(SiO_4)_6O_2$, recorded at 273 nm. Green arrows show the Dy^{3+} emission.

The symmetry of the Dy^{3+} coordination environment is reflected in the ratio between the magnetic (blue region) and the electric (yellow region) dipole transitions, also known as the asymmetric or branching ratio.[25, 44] Figure 3.10 shows the blue/yellow (B/Y, $^4F_{9/2} \rightarrow ^6H_{15/2}/^4F_{9/2} \rightarrow ^6H_{13/2}$) intensity ratio as a function of the Dy^{3+} content, it shows a constant behaviour and indicates that the emission intensity in the yellow region remains roughly twice that of the intensity in the blue region. This behaviour was expected as the $^4F_{9/2} \rightarrow ^6H_{13/2}$ transition is a forced electric dipole transition allowed only for activator ions on low symmetry sites with no inversion centre,[26] which is the case for the Dy^{3+} ions in the materials prepared here.

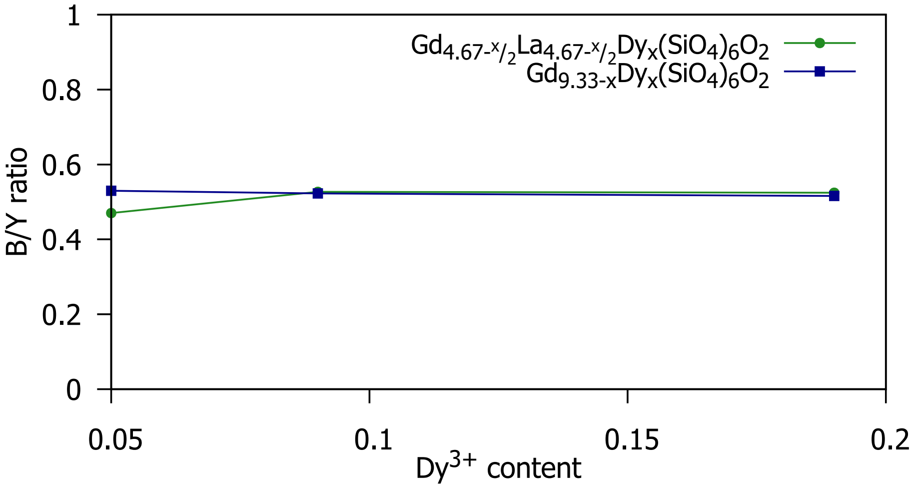

Figure 3.10: Blue/yellow emission intensity ratio as a function of Dy^{3+} content (x) in $Gd_{4.67-\frac{x}{2}}La_{4.67-\frac{x}{2}}Dy_x(SiO_4)_6O_2$ and $Gd_{9.33-x}Dy_x(SiO_4)_6O_2$, from data collected at 273 nm.

Table 3.8 shows the colour coordinates and the CCT obtained for the $Gd_{4.67-\frac{x}{2}}La_{4.67-\frac{x}{2}}Dy_x(SiO_4)_6O_2$ and $Gd_{9.33-x}Dy_x(SiO_4)_6O_2$ series. The CCT values range from 3200 to 3550 K, belonging to the warm white light region. As illustrated in the 1931 CIE diagram shown in Figure 3.11a (with a detailed zoom shown in Figure 3.11b), these phosphors exhibit primarily a warm white colour, tending towards the yellow. This is expected because of the weak emission intensity in the red region arising from the $^4F_{9/2} \rightarrow {}^6H_{11/2}$ transition. This B/Y intensity ratio has been seen in previous literature, where different Dy^{3+} doped phosphors fall inside the yellowish-white region of the colour range (examples shown in Figure 3.11), such as $ZnAl_2O_4$ phosphors with CIE coordinates (0.385, 0.409)[45] closer to the white region, Y_2O_2S with (0.45,0.52) close to the far yellow border[46] and Ca_2SnO_4:Dy^{3+} with (0.43, 0.46)[47] between these two regions and with similar coordinates to the $Gd_{4.67-\frac{x}{2}}La_{4.67-\frac{x}{2}}Dy_x(SiO_4)_6O_2$ and $Gd_{9.33-x}Dy_x(SiO_4)_6O_2$ phosphors.

$Gd_{4.67-\frac{x}{2}}La_{4.67-\frac{x}{2}}Dy_x(SiO_4)_6O_2$			
Dy content	Colour coordinates		CCT(K)
	x	y	
0.05	0.425	0.429	3397
0.09	0.418	0.423	3482
0.19	0.413	0.419	3545
$Gd_{9.33-x}Dy_x(SiO_4)_6O_2$			
Dy content	Colour coordinates		CCT(K)
	x	y	
0.05	0.424	0.422	3358
0.09	0.429	0.419	3252
0.19	0.432	0.421	3219

Table 3.8: The CIE coordinates and CCT values for the $Gd_{4.67-\frac{x}{2}}La_{4.67-\frac{x}{2}}Dy_x(SiO_4)_6O_2$ and $Gd_{9.33-x}Dy_x(SiO_4)_6O_2$ phosphors.

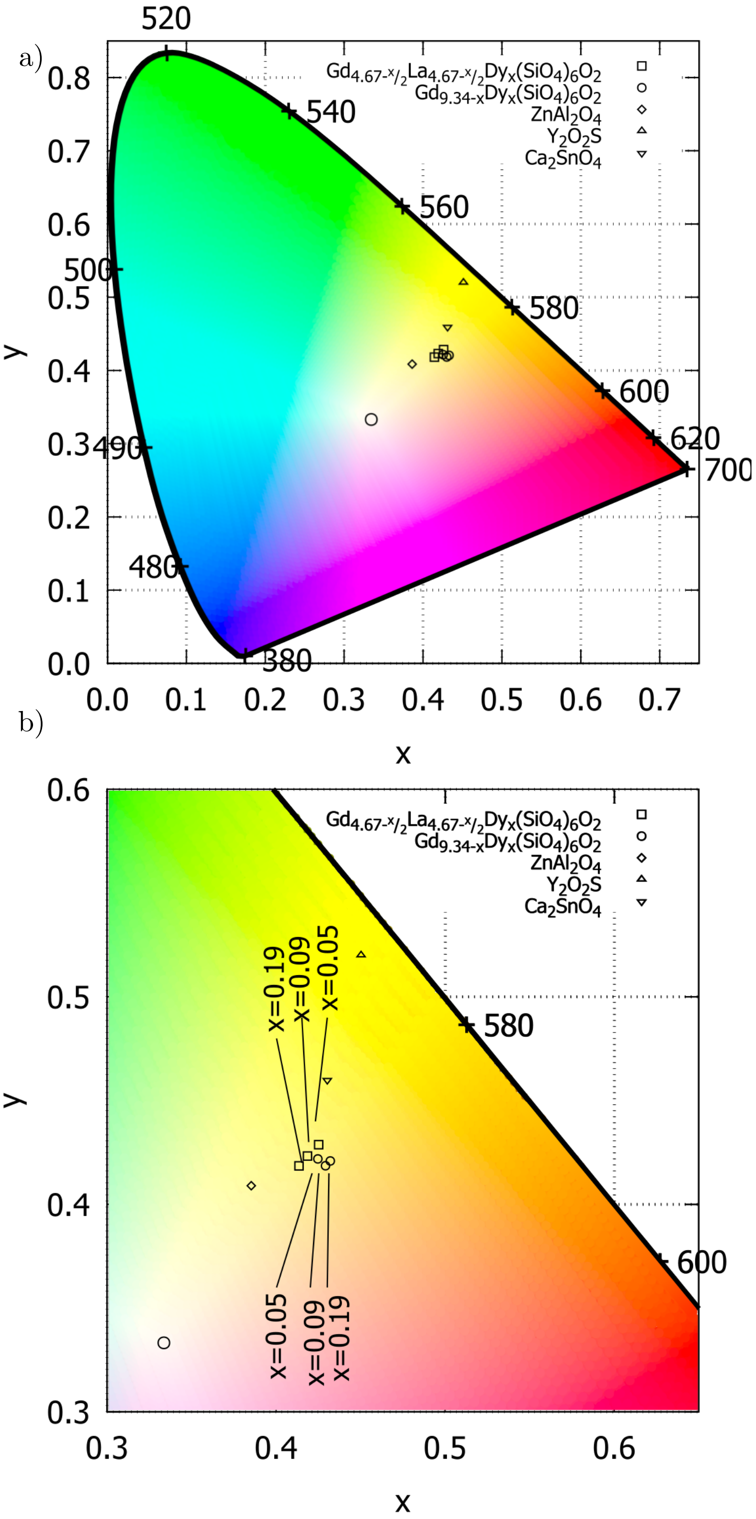

Figure 3.11: a) 1931 CIE chromaticity diagram showing the chromaticity coordinates at $\lambda_{exc} = 273$ nm for the $ZnAl_2O_4$:Dy^{3+},[45] Y_2O_2S:Dy^{3+},[46] Ca_2SnO_4:Dy^{3+},[47] $Gd_{4.67-\frac{x}{2}}La_{4.67-\frac{x}{2}}Dy_x(SiO_4)_6O_2$ and $Gd_{9.33-x}Dy_x(SiO_4)_6O_2$ series. b) Expansion of the pertinent CIE region for the hosts discussed.

3.3.2.3 Dy^{3+} temporal decay

The temporal decay of the Dy^{3+} emission was recorded for the $^4F_{9/2} \rightarrow ^6H_{15/2}$ and $^4F_{9/2} \rightarrow ^6H_{13/2}$ transitions under pulsed excitation at $\lambda_{exc} = 375$ nm. The curves (Figure 3.12) were fitted to a single exponential decay described in Equation 4.2 and the lifetime values obtained are summarised in Table 3.9.

$$I(t) = I_0 exp(-\frac{t}{\tau}), \tag{3.4}$$

where I(t) is the intensity at time t, I_0 the initial intensity, and τ is the lifetime.

$Gd_{4.67-\frac{x}{2}}La_{4.67-\frac{x}{2}}Dy_x(SiO_4)_6O_2$		
x	$^4F_{9/2} \rightarrow {}^6H_{15/2}$ transition (485 nm) τ(ms)	$^4F_{9/2} \rightarrow {}^6H_{13/2}$ transition (575 nm) τ(ms)
0.05	0.438(4)	0.487(3)
0.09	0.435(3)	0.437(3)
0.19	0.364(3)	0.355(2)
$Gd_{9.33-x}Dy_x(SiO_4)_6O_2$		
x	$^4F_{9/2} \rightarrow {}^6H_{15/2}$ transition (485 nm) τ(ms)	$^4F_{9/2} \rightarrow {}^6H_{13/2}$ transition (575 nm) τ(ms)
0.05	0.353(3)	0.351(3)
0.09	0.436(3)	0.436(3)
0.19	0.471(3)	0.469(3)

Table 3.9: Lifetime values obtained for the $Gd_{4.67-\frac{x}{2}}La_{4.67-\frac{x}{2}}Dy_x(SiO_4)_6O_2$ and $Gd_{9.33-x}Dy_x(SiO_4)_6O_2$ phosphors recorded after excitation at 375 nm.

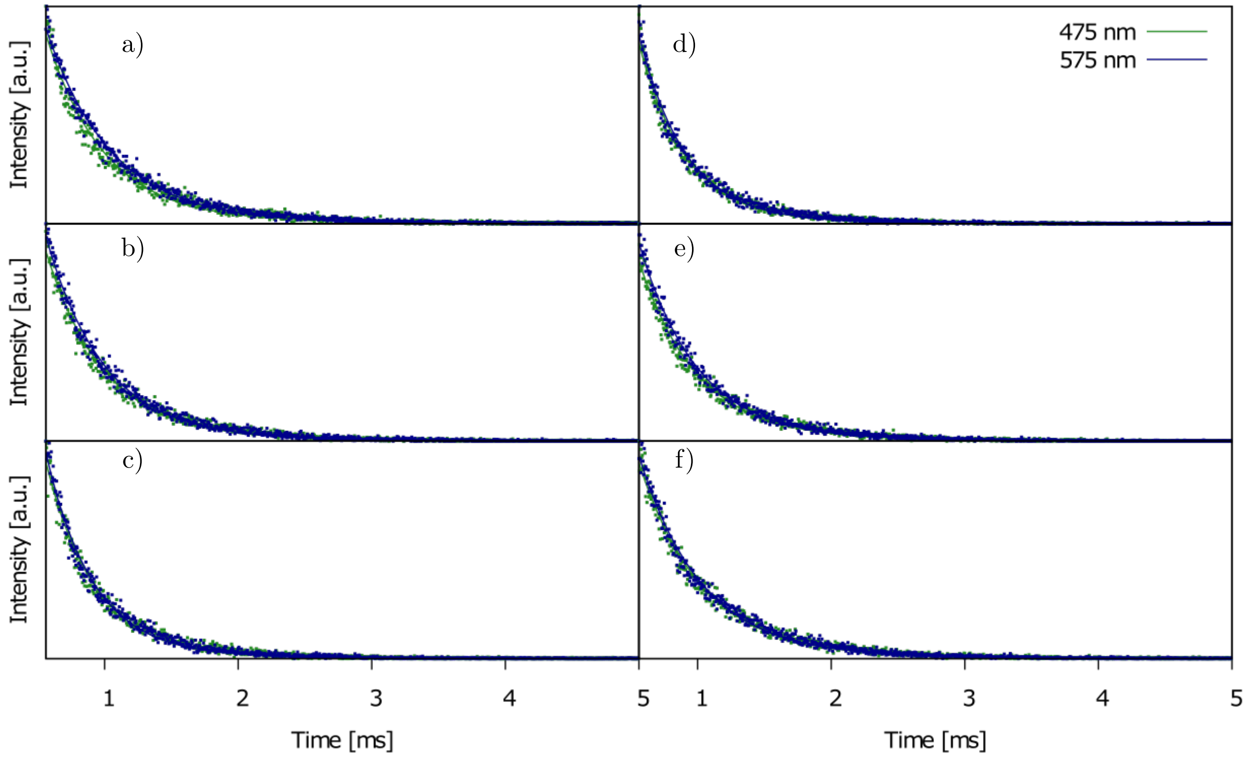

Figure 3.12: Fitted decay curves (solid line) of the experimental data (dots) of the $^4F_{9/2} \rightarrow {}^6H_{15/2}$ transition at 485 nm and the $^4F_{9/2} \rightarrow {}^6H_{13/2}$ transition at 575 nm for $Gd_{4.67-\frac{x}{2}}La_{4.67-\frac{x}{2}}Dy_x(SiO_4)_6O_2$ a) x = 0.05, b) x = 0.09 and c) x = 0.19, and $Gd_{9.33-x}Dy_x(SiO_4)_6O_2$ d) x = 0.05, e) x = 0.09 and f) x = 0.19 phosphors recorded after excitation at 375 nm.

In the literature, other apatite-type Dy^{3+} doped phosphors are $Sr_{3.94}Ca(PO_4)_2SiO_4$:0.04 Dy^{3+} and $Sr_{3.92}Li_{0.04}Ca(PO_4)_2SiO_4$:0.04 Dy^{3+}. Lifetime values at 574 nm emission ($^4F_{9/2} \rightarrow {}^6H_{15/2}$ transition) with 348 nm excitation of 0.475 ms and 0.531 ms respectively have been reported.[21] The decay values recorded for $Gd_{4.67-\frac{x}{2}}La_{4.67-\frac{x}{2}}Dy_x(SiO_4)_6O_2$ and $Gd_{9.33-x}Dy_x(SiO_4)_6O_2$ shown in Table 3.9 fall within the same range of values. The lifetime for the $^4F_{9/2} \rightarrow {}^6H_{13/2}$ transition is rarely presented in the literature.

The dependence of the lifetime on the Dy^{3+} content is shown in Figure 3.13. The lifetime for $Gd_{4.67-\frac{x}{2}}La_{4.67-\frac{x}{2}}Dy_x(SiO_4)_6O_2$ (blue data point in Figure 3.13) decreased slightly when increasing the Dy^{3+} content, suggesting concentration quenching. This can be explained as the higher the Dy^{3+} doping level, the more Dy^{3+} ions are within close proximity to other Dy^{3+}; allowing energy transfer between them (cross-relaxation mechanism, also known as self-quenching). At the same time, there is a lower quantity of sensitiser that can transfer energy to the Dy^{3+}.

On the other hand, it was observed that the lifetime trend is different for the $Gd_{9.33-x}Dy_x(SiO_4)_6O_2$ (x = 0.05, 0.09 and 0.19) phosphor series (red data points in Figure 3.13): as the Dy^{3+} content increases the lifetime increases as well. This may be an effect of the high Gd^{3+} content, allowing energy back-transfer from excited Dy^{3+} ions to repopulate the Gd^{3+} excited state.

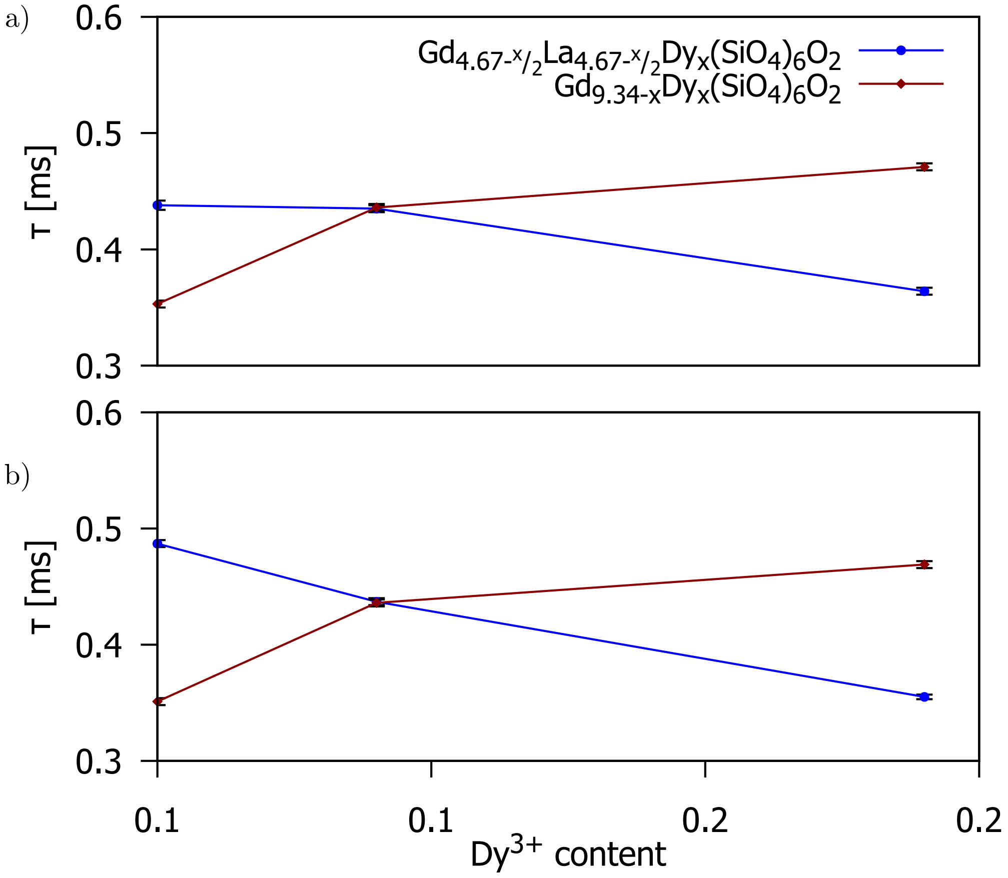

Figure 3.13: Lifetime values dependence Dy^{3+} content (x) for a) the $^4F_{9/2} \rightarrow {}^6H_{15/2}$ transition (485 nm) and b) the $^4F_{9/2} \rightarrow {}^6H_{13/2}$ transition (575 nm). Error given on the lifetime values is the standard deviation from the fitting.

3.4 Conclusions and future work

The series of new apatite-type silicate phosphor hosts $Gd_{9.33-x}La_x(SiO_4)_6O_2$ (x = 0, 0.93, 1.87, 2.80, 3.73 and 4.67) were synthesised and characterised by X-ray diffraction. The laboratory and synchrotron PXRD patterns demonstrated a good fit of the model structure of the $Gd_{9.33}(SiO_4)_6O_2$ apatite, suggesting that La^{3+} incorporation was successful. Additional evidence of this was observed in the lattice parameter plots, where a clear increase in the unit cell size was observed when the La^{3+} content was progressively increased from 0 to 4.67, allowing optimisation of substitution of La^{3+}. Thus, optimisation of different phosphor hosts based on gadolinium silicate apatite was shown to be possible.

Two different Dy^{3+}-doped apatite-type silicate single-phase phosphor series were synthesised and characterised by X-ray diffraction and optical measurements. Two related hosts, $Gd_{4.67-\frac{x}{2}}La_{4.67-\frac{x}{2}}Dy_x(SiO_4)_6O_2$ and $Gd_{9.33-x}Dy_x(SiO_4)_6O_2$, were doped systematically with Dy^{3+} (x = 0.05, 0.09 and 0.19) to obtain white-emitting phosphor. The 1931 CIE colour coordinates were calculated for each series, and the values inside the white light region, but in the warm white region, were obtained for all the materials. The chromaticity coordinates ranged from (0.413, 0.419) to (0.432, 0.421).

The emission decay curves of the samples were recorded under 375 nm pulsed light. These were fitted to determine the lifetime values, which ranged 0.351 to 0.487 ms, and the concentration quenching effects in the phosphors. The lifetime value suggests a concentration quenching for the $Gd_{4.67-\frac{x}{2}}La_{4.67-\frac{x}{2}}Dy_x(SiO_4)_6O_2$ phosphor with increasing Dy^{3+} content. This effect was not observed for the $Gd_{9.33-x}Dy_x(SiO_4)_6O_2$ (x = 0.05, 0.09 and 0.19) phosphor, which indicates the substitution of Gd^{3+} with La^{3+} caused to lower the quantity of sensitiser, hence less energy transfer $Gd^{3+} \rightarrow Dy^{3+}$. Based on this, it was demonstrated that the $Gd_{9.33}(SiO_4)_6O_2$ host is superior to its $Gd_{4.67}La_{4.67}(SiO_4)_6O_2$ counterpart.

A weak intensity of the red component in the Dy^{3+} emission was revealed as an obstacle to obtain a phosphor nearer to the white point in the 1931 CIE colour coordinates chart. At the same time, the B/Y ratio showed a higher intensity for the yellow emission intensity than for the blue emission intensity, creating a shift towards the yellow region in the chromaticity coordinates diagram. The ideal B/Y ratio to obtain the colour coordinates of the white light point could not be found.

Future work will be to find RE activators that emit in a more distributed emission in the visible spectra. Therefore, doped phosphors that emit with a balance of the integrated red, green and blue peaks.

3.5 References

[1] Nakamura, S., Mukai, T., and Senoh, M. *Applied Physics Letters*, 64(13), 1994.

[2] Jorgensen, C.K. *Molecular Physics*, 5(3), 1962.

[3] Dorenbos, P. *Journal of Luminescence*, 91(1-2), 2000.

[4] Dieke, G.H. and Crosswhite, H.M. *Applied Optics*, 2(7), 1963.

[5] Krupke, W.F. *Physical Review*, 145(1), 1966.

[6] Fernandez-Carrion, A.J., Ocana, M., Garcia-Sevillano, J., Cantelar, E., and Becerro, A.I. *Journal of Physical Chemistry C*, 118(31), 2014.

[7] Chuai, X.H., Zhang, H.J., Li, F.S., Lu, S.Z., Lin, J., Wang, S.B., and Kou, C.C. *Journal of Alloys and Compounds*, 334, 2002.

[8] Han, X.M., Lin, J., Li, Z., Qi, X.W., Li, M.Y., and Wang, X.Q. *Journal of Rare Earths*, 26(6), 2008.

[9] Wang, Y.H., Wen, Y., and Zhang, F. *Materials Research Bulletin*, 45(11), 2010.

[10] Pavitra, E., Raju, G.S.R., and Yu, J.S. *Ceramics International*, 39(6), 2013.

[11] Zhao, W.Y., Wen, H.X., Yang, X.D., and Qiao, X.J. *Materials Letters*, 261, 2020.

[12] Dutta, S., Som, S., and Sharma, S.K. *Dalton Transactions*, 42(26), 2013.

[13] Verma, B., Baghel, R.N., Bisen, D.P., Brahme, N., and Khare, A. *Journal of Alloys and Compounds*, 805, 2019.

[14] Rao, G.M., Raju, G.S.R., Hussain, S.K., Pavitra, E., Rao, P., and Yu, J.S. *New Journal of Chemistry*, 40(7), 2016.

[15] Sahu, P.K., Ramrakhiani, M., and Agrawal, S. *Journal of Fluorescence*, 29(5), 2019.

[16] Baig, N., Yadav, R.S., Dhoble, N.S., Barai, V.L., and Dhoble, S.J. *Journal of Luminescence*, 215, 2019.

[17] Liu, H., Liao, L., Guo, Q., Yang, D., and Mei, L. *Journal of Luminescence*, 181, 2017.

[18] Gao, Y., Li, Y.H., Sun, X.R., Jiang, P.F., Cong, R.H., and Yang, T. *Materials Research Bulletin*, 122, 2020.

[19] Zhang, L., Li, P., Zhao, A.K., Li, X., Tang, J., Zhang, F.B., Jia, G., and Zhang, C.M. *Journal of Alloys and Compounds*, 816, 2020.

[20] Mondal, K. and Manam, J. *Journal of Luminescence*, 195, 2018.

[21] Xu, D.D., Zhou, W., Zhang, Z., Li, S.J., and Wang, X.R. *Optical Materials*, 89, 2019.

[22] Yang, C., Li, X., Liu, Q.S., Li, G.Y., Zhang, X.Y., Bai, Z.H., Wang, X.C., and Mi, X.Y. *Journal of Materials Science-Materials in Electronics*, 31(2), 2020.

[23] Li, J.G., Yan, H.F., Liu, W.F., Yan, F.M., and Hu, J.Y. *Optoelectronics and Advanced Materials-Rapid Communications*, 11(3-4), 2017.

[24] Liu, H., Liao, L., Molokeev, M.S., Guo, Q., Zhang, Y., and Mei, L. *RSC Advances*, 6(29), 2016.

[25] Antic, Z., Kuzman, S., Dordevic, V., Dramicanin, M.D., and Thundat, T. *Luminescence*, 32(4), 2017.

[26] Do Han, S., Khatkar, S., Taxak, V., Sharma, G., and Kumar, D. *Materials Science and Engineering: B*, 129(1-3), 2006.

[27] Jiang, S., Luo, X., Liu, Y., Zhang, Y., Huang, C., Wang, Y., Luo, X., Xiang, G., Tang, X., Li, L., and Zhou, X. *Materials Research Bulletin*, 106, 2018.

[28] Deng, B., Chen, J., Liu, H., and Zhou, C.s. *Journal of Materials Science: Materials in Electronics*, 2019.

[29] Fan, M.H., Liu, S., Yang, K., Guo, J., Wang, J.X., Wang, X.H., Liu, Q., and Wei, B. *Ceramics International*, 46(5), 2020.

[30] Mahajan, R. and Prakash, R. *Journal of Materials Science-Materials in Electronics*, 31(5), 2020.

[31] Abaci, O.C.F., Mete, E., Esenturk, O., and Yilmaz, A. *Optical Materials*, 98, 2019.

[32] Blasse, G. and Bril, A. *The Journal of Chemical Physics*, 48(1), 1968.

[33] Schubert, E.F. and Kim, J.K. *Science*, 308(5726), 2005.

[34] Bedyal, A.K., Kunti, A.K., Kumar, V., and Swart, H.C. *Journal of Alloys and Compounds*, 806, 2019.

[35] Li, X., Guan, L., Sun, M.S., Liu, H.Y., Yang, Z.P., Guo, Q.L., and Fu, G.S. *Journal of Luminescence*, 131(5), 2011.

[36] Chen, M., Qiu, K.H., Zhang, P.C., Zhang, W.T., and Yin, Q. *Ceramics International*, 45(17), 2019.

[37] Reisfeld, R. and Jorgensen, C. *Lasers and Excited States of Rare Earths, Springer Berlin Heidelberg*, 2012.

[38] Latshaw, A.M., Hughey, K.D., Smith, M.D., Yeon, J., and zur Loye, H.C. *Inorganic Chemistry*, 54(3), 2015.

[39] Coelho, A.A., Evans, J.S.O., Evans, I.R., Kern, A., and Parsons, S. *Powder Diffraction*, 26(4), 2011.

[40] Rietveld, H.M. *Journal of Applied Crystallography*, 2, 1969.

[41] Vegard, L. *Zeitschrift für Physik*, 5(1), 1921.

[42] Shannon, R.D. *Acta crystallographica section A: crystal physics, diffraction, theoretical and general crystallography*, 32(5), 1976.

[43] Meena, M.L., Som, S., Singh, R.K., and Lu, C.F. *Polyhedron*, 177, 2020.

[44] Ilhan, M., Keskin, I.C., and Gultekin, S. *Journal of Electronic Materials*, 49(4), 2020.

[45] Prakash, R., Kumar, S., Mahajan, R., Khajuria, P., Kumar, V., Choudhary, R.J., and Phase, D.M. *Spectral Properties Of Dy3+ Doped ZnAl2O4 Phosphor*, volume 1953 of *AIP Conference Proceedings*. 2018.

[46] Som, S., Mitra, P., Kumar, V., Kumar, V., Terblans, J.J., Swart, H.C., and Sharma, S.K. *Dalton Transactions*, 43(26), 2014.

[47] Zhang, B.W., Shi, M.M., Zhang, D.Y., Guo, Y.Y., Chang, C.K., and Song, W.J. *Journal of Materials Science-Materials in Electronics*, 28(16), 2017.

4 Green-emitting phosphors: Tb^{3+}-doped $Gd_{9.33}(SiO_4)_6O_2$

4.1 Introduction

Colour tuneable luminescence in single-phase phosphors is receiving much attention due to their photoelectronic applications. New phosphors with different colour emissions have been developed in the effort to ultimately generate white lighting using high-efficiency multi-colour phosphors. YAG:Ce^{3+} phosphor under a specific current absorbs the emitted blue InGaN LED chip light and emits yellow light. Together with the blue light emitted by the LED, white luminescence is achieved. However, this system has a low colour rendering index (CRI, <75 out of 100) and a high correlated colour temperature (CCT) caused by a lack of the red component, limiting its application.[1] A strategy to overcome this drawback is to use a single high-energy UV-emitting LED to excite multiple RGB phosphors. A good phosphor candidate is needed to cover the green region in the visible spectrum.[2] The human eye's response to the yellow and green region is very strong. Consequently, narrow linewidths in the emission are not necessary for the luminous efficacy of radiation. However to obtain a "100% luminous efficacy of radiation", defined as 408 lm/W at a CRI of 90, the centre emission wavelength has to be 530 nm.[3]

The rare earth Tb^{3+} ion ($4f^8$ configuration) is an efficient activator of luminescent materials due to its emission in the visible region (λ_{max} = 544 nm) when it is excited in the UV region.[4] The sharp emission bands of Tb^{3+} ions arise from $4f$-$4f$ transitions. As the Dieke diagram[5, 6] in Figure 4.1 shows, Tb^{3+} ion emissions are related to $^5D_3 \rightarrow {}^7F_J$ transitions in the blue region and $^5D_4 \rightarrow {}^7F_J$ transitions in the green region (J = 6,5,4,3,2). The colour can be tuned towards the blue or the green region by adjusting the Tb^{3+} doping content.[7] The phosphors present deeper green emission colour with higher Tb^{3+} content level, before reaching concentration quenching.

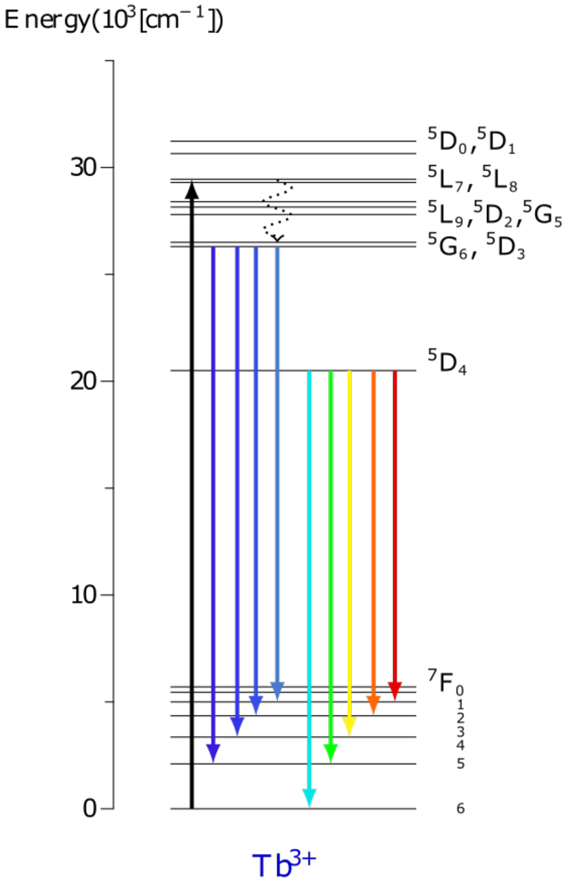

Figure 4.1: Tb^{3+} ion energy-level diagram showing the relevant transitions in the system.[5]

In the last few years, Tb^{3+} doped phosphors have been reported in the literature to have a lifetime in the millisecond region due to the forbidden *f*-*f* transition in the Tb^{3+} ions. Examples of relevant results are given below and summarised in Table 4.1. These have been selected as they are Tb^{3+}-doped oxide hosts that emit in the light green or deep green regions or can be tuned from blue to green.

Compound	Colour coordinates
Y_2SiO_5:Ce^{3+},Tb^{3+}[8]	(0.177, 0.122) to (0.335, 0.08)
$Ca_2Pb_3(PO_4)_3Cl$:Tb^{3+}[9]	(0.218, 0.578)
$Ba_2La_{2.85}Tb_{0.15}(SiO_4)_3F$[10]	(0.2908, 0.5282)
$LiTb_9(SiO_4)_6O_2$[11]	(0.241, 0.6460)
$Sr_{3.5}Y_{6.5}O_2(PO_4)_{1.5}(SiO_4)_{4.5}$:$Eu^{2+}$,$Tb^{3+}$[12]	(0.2723, 0.3766) to (0.2812, 0.4537)
$Ba_4La_6(SiO_4)_6Cl_2$:0.3 Tb^{3+}[13]	(0.37, 0.61)
$Ca_2RE_{7.88}Tb_{0.12}(SiO_4)_6O_2$ (RE = Y or La)[14]	(0.2137, 0.329) to (0.260, 0.565)
$La_{9.33}(SiO_4)_6O_2$:7% Tb^{3+}[15]	(0.2675, 0.5802)
$Ca_2La_8(SiO_4)_6O_2$:xTb^{3+}[16]	(0.30,0.51) to (0.30,0.58)
$Ca_3La_6(SiO_4)_6$:Ce^{3+}, Tb^{3+}[17]	(0.19, 0.10) to (0.33, 0.56)
$Ca_3La_6(SiO_4)_6$:0.5 Tb^{3+}[17]	(0.35, 0.55)

Table 4.1: Summary of Tb^{3+}-doped phosphors.

For example, $Ca_{2-x}Nb_2O_7$:xTb^{3+} (x = 0.01-0.1) has been found to emit in the deep green region when excited at 310 nm, with colour coordinates varying from (0.2203, 0.4140) to (0.2339, 0.5148).[18] $BaAl_2Si_2O_8$:Bi^{3+},Tb^{3+} phosphors have been reported to produce green emission that can be tuned to deep green by increasing the Bi^{3+} doping level. The colour coordinates range from (0.2608, 0.4418) to (0.2674, 0.4670).[19] Photoluminescent examination of the Y_2O_3:Tb^{3+} phosphor reveals bright green phosphorescence when it is excited at 210 nm, with colour coordinates (0.268, 0.416).[20]

Phosphors that emit in the deeper green region have been reported, such as $SrAl_2Si_2O_8$:0.18Tb^{3+}, which has CIE coordinates (0.264, 0.516) and a CCT value of 7182 K when excited at 377 nm.[21] $Na_3La_{0.7}(PO_4)_2$:0.3Tb^{3+} phosphors show colour coordinates (0.2987, 0.5695) when excited at 378 nm UV.[22] The $YK_3B_6O_12$:Tb^{3+} phosphor presents a bright green colour with CIE coordinates (0.25,0.58) under UV lamp excitation.[23]

The possibility of tuning the chromaticity of the Tb^{3+} emission solely by changing the Tb^{3+} doping content has been researched. An example is Tb^{3+}-doped δ-$Gd_2Si_2O_7$, which can be tuned from blue to green in the CIE diagram of colour coordinates when the doping level is changed from 0.5 to 5.0 at. %.[24] Tb^{3+} doped phosphors have been reported to be blue to deep green tuneable emitters. Oxyborates are good hosts for green-emitting phosphors, such as $Ca_4TbO(BO_3)_3$, which shows no concentration quenching and outstanding luminescent properties with a performance 200% better than the commercially available $LaPO_4$:Tb.[25]

$Sr_8ZnSc(PO_4)_7$ phosphor can be tuned from blue to green with colour coordinates that range from (0.205, 0.186) to (0.245, 0.411) when excited at 370 nm. Furthermore, this phosphor presents an increase in stable $^5D_3 \rightarrow {}^7F_J$ emissions of Tb^{3+} due to a trap mechanism that moves electrons to the conduction band, helped by heat.[26]

The blue to light turquoise phosphor $Na_2Y_{2-x}B_2O_7$:0.02Ce^{3+}, zTb^{3+},0.02Eu^{3+} (z =0, 0.03, 0.05, 0.1, 0.15 and 0.2) has been synthesised and studied to optimise its emission by tuning the ratio between Ce^{3+} and Eu^{3+}, indicating that it is a good candidate for n-UV white LEDs.[27] Another phosphor studied in the presence of other RE ions is Y_2SiO_5:Ce^{3+},Tb^{3+} which can be tuned from blue to green by changing the Tb^{3+} doping level, with colour coordinates from (0.177, 0.122) to (0.335, 0.08).[8]

Recently, the apatite structure has been studied as an important compound for developing phosphor hosts. For instance, $Ca_2Pb_3(PO_4)_3Cl$:Tb^{3+} excited at 371 nm shows CIE coordinates (0.218, 0.578),[9] the apatite-type phosphor $Ba_2La_{2.85}Tb_{0.15}(SiO_4)_3F$ has colour coordinates (0.2908, 0.5282) when excited at 373 nm[10] and $LiTb_9(SiO_4)_6O_2$ emits with CIE coordinates (0.241, 0.6460) under UV irradiation at 254 nm. The site and occupancy of the rare earth has been calculated by theoretically calculating the crystal field effect. The 6h site was estimated to be in the high energy absorption band and the 4f site in the low energy absorption band.[11]

The phosphate-silicate oxyapatite $Sr_{3.5}Y_{6.5}O_2(PO_4)_{1.5}(SiO_4)_{4.5}$:$Eu^{2+}$,$Tb^{3+}$ is a green phosphor that can be tuned to a deeper green colour by changing the Tb^{3+} doping level. The variation in the colour coordinates has been calculated to be from (0.2723, 0.3766) to (0.2812, 0.4537) under 365 nm UV excitation.[12] Similarly, the chlorapatite $Ba_4La_6(SiO_4)_6Cl_2$:0.3 Tb^{3+} phosphor has been reported to be a green emitter with colour coordinates (0.37, 0.61) when excited at 376 nm.[13]

It has recently been discovered that rare earth metals with silicate oxyapatite hosts tolerate an unusually broad range of dopants, particularly in lanthanide sites.[28] One such phosphor that has been studied is $Ca_2RE_{7.88}Tb_{0.12}(SiO_4)_6O_2$ (RE = Y or La), which emits in the green and turquoise regions. The colour coordinates vary from (0.2137, 0.329) to (0.260, 0.565) when it is excited at 235 nm.[14]

$La_{9.33}(SiO_4)_6O_2$:7% Tb^{3+} microfibres can emit in the green region with chromaticity coordinates (0.2675, 0.5802) under UV excitation and can be used in field emission displays.[15] The emission of the phosphor $MgY_4Si_3O_{13}$:0.01%Tb^{3+} has colour coordinates (0.275, 0.484) under near-UV excitation at 355 nm.[29] The y value of the reported CIE coordinates for $Ca_2La_8(SiO_4)_6O_2$:xTb^{3+} change from 0.51 to 0.58 with increasing doping levels, while the x value remains at 0.30.[16]

$Ca_3La_6(SiO_4)_6$:Ce^{3+}, Tb^{3+} has a critical distance for energy transfer is 7.1 Å. It shows an energy transfer from Ce^{3+} to Tb^{3+} ions via dipole-dipole interaction. Under UV excitation this phosphor emits from purple-blue (0.19, 0.10) to green (0.33, 0.56) by increasing the Tb^{3+} content. The CIE coordinates for $Ca_3La_6(SiO_4)_6$:0.5 Tb^{3+} are (0.35, 0.55) when it is excited at 288 nm.[17]

The presence of a good suitable sensitiser is needed in a Tb^{3+}-doped phosphor to allow the forbidden f-f transitions. The Gd^{3+} ion could be a good prospect due its similar ionic radius, making Tb^{3+} a suitable substituent for Gd^{3+} sites. Furthermore, the Gd^{3+} ion has been researched due to the stability of its half-filled $4f^n$ shell-ground state. The absorption efficiency of Tb^{3+} is low in the n-UV region due the forbidden $4f$-$4f$ electric dipole transitions. Subsequently, broad-band excitation of $4f$-$5d$ transition ions transfers energy to the sharp line emission of $4f$-$4f$ transition ions, making it possible for the lowest excited state level (Figure 4.2), $^6P_{7/2}$, of the Gd^{3+} ions to stay in the UV region allowing transfer to the Tb^{3+} ions.[30]

The interaction between the Russell-Saunders coupling states of Gd^{3+} and Tb^{3+} is shown in Figure 4.2. The sensitiser Gd^{3+} is excited from its ground $^8S_{7/2}$ state to $^6P_{7/2}$ or ^6I_J states when it is excited with UV radiation. The energy transfer between Gd^{3+} and Tb^{3+} happens when the excited state of the Gd^{3+} populates excited states of similar energy of nearby Tb^{3+} ions. It can then relax to two different states, $^5D_3$ or $^5D_3$, going from these populated states to lower states. The $^5D_4$ state typically has a greater possibility of having four main radiative transitions to the ^7F_J (J = 6, 5, 4, 3) manifold, of which that to $^7F_5$ is invariably the most intense.

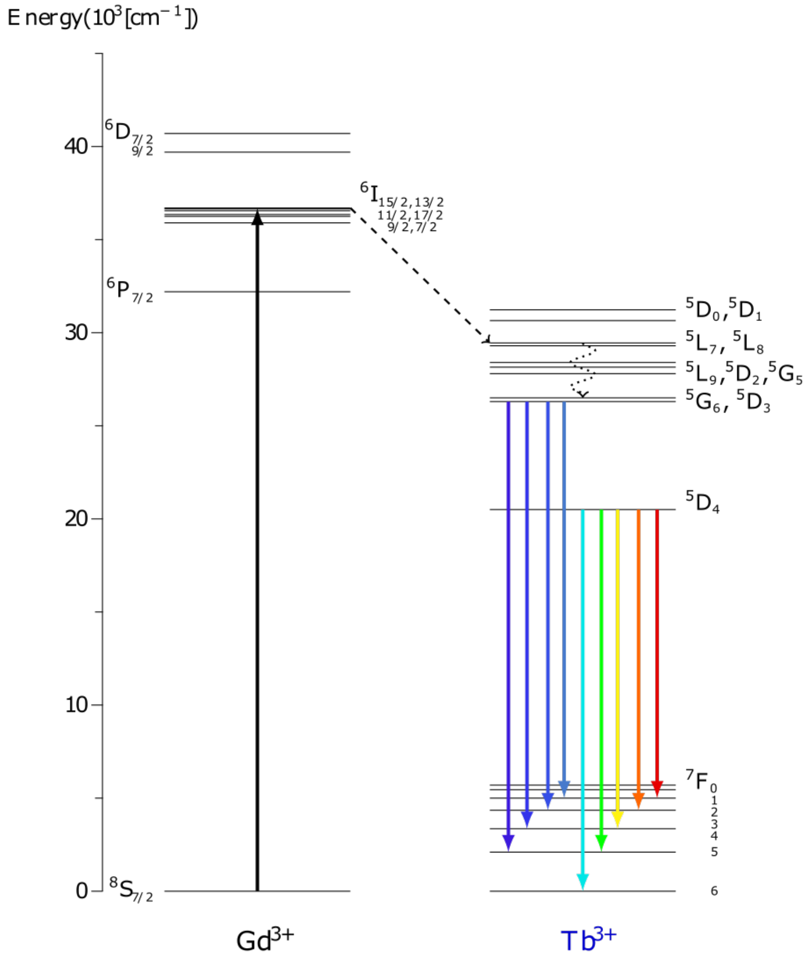

Figure 4.2: Energy-level diagrams for Gd^{3+} and Tb^{3+} ions showing the relevant transitions in the system.[5]

$Gd^{3+} \rightarrow Tb^{3+}$ energy transfer has been reported. $Ca_2Re_8(SiO_4)_6O_2$:Eu^{3+}/Tb^{3+} (Re = Y, La, Gd) compounds display a decrease in emission intensity and lifetime such as Gd >Y >La, proving the Gd compound to be a better host phosphor.[31] $KBaGd(WO_4)_3$:0.4 Tb^{3+} phosphors have a dominant emission peak at 550 nm under 250 nm excitation, making them potential candidates for green-emitting phosphors. These are exceptional materials. The shortest distance between adjacent Gd^{3+} ions is 3.95 Å. This is below the 5 Å necessary between the sensitiser and the activator for exchange interaction to take place. In addition, it is large enough to avoid high concentration quenching effects and to enhance the luminescent intensity of the doped Re^{3+} ions. The reported colour coordinates for $KBaGd(WO_4)_3$:Tb^{3+} phosphor are (0.334, 0.588) and (0.329, 0.596) under 250 nm and 378 nm irradiation, respectively.[32]

The compounds studied in this chapter are in the $Gd_{9.33-x}Tb_x(SiO_4)_6O_2$ (x = 0.07, 0.09 and 0.19) phosphor series, with doping levels as shown in Table 4.2. The structural model for the doped $Gd_{9.33}(SiO_4)_6O_2$ host is shown in Table 3.4 in Chapter 3. The doping goes to two crystallographically independent A-sites: A1 (Wyckoff site 4f) and A2 (Wyckoff site 6h).

0.8% Tb $x = 0.07$	1.0% Tb $x = 0.09$	2.0% Tb $x = 0.19$

Table 4.2: Schematic representation of the different doping levels for the $Gd_{9.33-x}Tb_x(SiO_4)_6O_2$ phosphor series.

4.2 Experimental details

4.2.1 Sample preparation

The green phosphor series was synthesised using the solid-state method. The stoichiometric amounts for the reaction to obtain pure single-phase Tb^{3+}-doped compounds are given by Equation 4.1.

$$6SiO_2 + \frac{(9.33 - x)}{2} Gd_2O_3 + \frac{x}{2} Tb_2O_3 \rightarrow Gd_{9.33-x} Tb_x (SiO_4)_6 O_2, \tag{4.1}$$

where x = 0.07, 0.09 and 0.19.

To check the purity of the starting reagents used in the synthesis of the target materials (details shown in Table 4.3), PXRD patterns were recorded following the data collection details described in section 2.2.3.

Reagent	Supplier	Purity
Gd_2O_3	Sigma Aldrich	99.99%
Tb_2O_3	Sigma Aldrich	99.99%
SiO_2	Sigma Aldrich	99.99%

Table 4.3: Reagents used in these syntheses.

All the samples were heated to 1200 °C for 12 hours prior to weighing to remove absorbed water or other species. Stoichiometric amounts of the reagents were weighed (with a precision of ±0.0001 g) to prepare 2.0 g of each composition. They were ground for around 30 minutes and heated at 1400 °C with intermittent grinding for a total of up to 300 h.

4.2.2 X-ray diffraction.

Between each heating cycle, the process of the solid-state reaction towards a pure material was monitored by recording laboratory PXRD data following the data collection details described in section 2.2.3. Once the product purity was proved, final recorded patterns were fitted using the appropriate modified structural model for $Gd_{9.33}(SiO_4)_6O_2$.[33] The variables refined included the background, diffractometer zero point, pseudo-Voigt function peak shape, unit cell parameters and isotropic atomic displacement parameters. All the PXRD data were analysed using Topas Academic software.[34]

4.2.3 Photoluminescence spectroscopy

A Horiba Fluorolog-3 fluorimeter was used for the optical measurements with a xenon flashlamp as the excitation source and a Hamamatsu R928 photomultiplier tube for detection. Homogeneous finely powdered samples of the materials were contained in a Spectralon® cup with a quartz cover slip and placed inside a Quanta-ϕ F-3029 integrating sphere connected to the spectrometer via optical fibres. The data recorded was analysed as discussed in more detail in section 2.3.3.

Lifetimes were recorded by multichannel scaling following excitation with a pulsed xenon lamp. The emitted light was analysed at right angles to the excitation source and detected using a Hamamatsu R928 photomultiplier tube thermoelectrically cooled to -20 °C after passage through a monochromator.

4.3 Results and discussion

4.3.1 Structural characterisation: Powder X-Ray Diffraction

The purity of the $Gd_{9.33-x}Tb_x(SiO_4)_6O_2$ phosphors was confirmed using laboratory PXRD. The PXRD patterns were fitted using the Rietveld method[34, 35] and the structural model in space group $P6_3/m$. The 9-term polynomial background, zero point, pseudo-Voigt function peak shape, unit cell parameters and isotropic atomic displacement parameters independently for each phase were refined. Figure 4.3 shows that all the $Gd_{9.33-x}Tb_x(SiO_4)_6O_2$ compounds produced a pure single-phase.

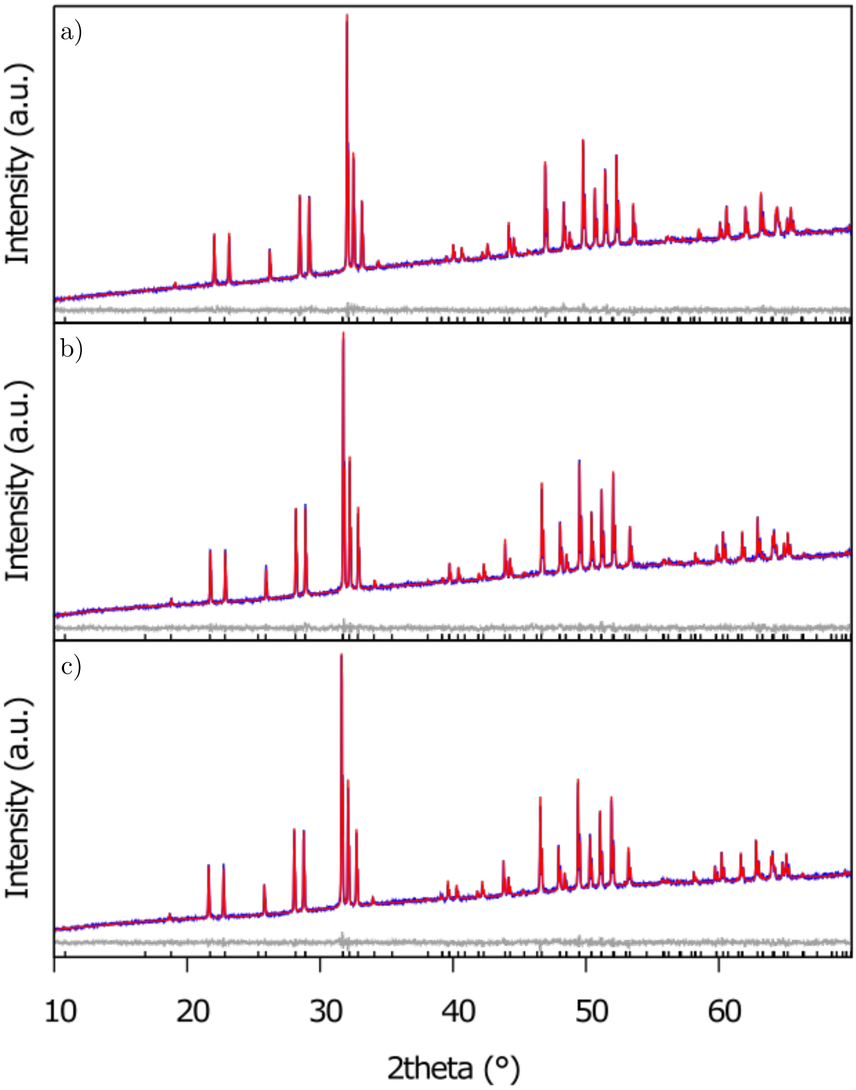

Figure 4.3: Rietveld fit of the laboratory PXRD data. $Gd_{9.33-x}Tb_x(SiO_4)_6O_2$: a) x = 0.07, R_{wp} = 1.95%, b) x = 0.09, R_{wp} = 2.00% and c) x = 0.19, R_{wp} = 2.08%.

The refined unit cell parameters, the R_{wp} and the purity level reached are presented in Table 4.4. Figure 4.4 presents the plots of the lattice parameters as a function of the doping level.

x	a (Å)	c (Å)	V (Å^3)	R_{wp} (%)	Impurity
0.07	9.45006(7)	6.87749(7)	531.900(9)	1.95	No
0.09	9.4418(7)	6.87262(7)	530.595(9)	2.00	No
0.19	9.43785(7)	6.86845(7)	529.83(1)	2.08	No

Table 4.4: Unit cell parameters for $Gd_{9.33-x}Tb_x(SiO_4)_6O_2$ phosphors.

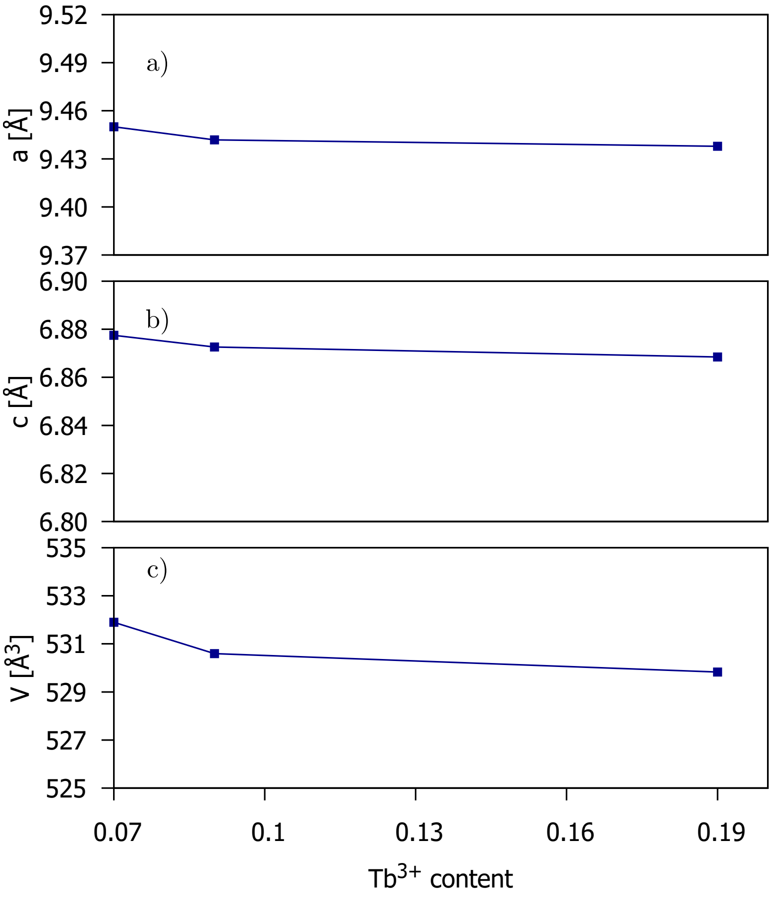

Figure 4.4: Lattice parameters of the a) a, b) c and c) unit cell volume V for $Gd_{9.33-x}Tb_x(SiO_4)_6O_2$ (x = 0.07, 0.09 and 0.19) as a function of Tb^{3+} content (x). The error bars are smaller than the data points.

Vegard's law[36] can be applied to confirm that the doping has been carried out successfully. The increase or decrease in the average of the ionic radii can track if the doping has gone into the desired site. In this case, the ionic radii (coordination number 7)[37] for Gd^{3+} is 1.0 Å and for Tb^{3+} is 0.98 Å. Therefore, the difference between the average ionic radii is very small. Nevertheless, a small decrease in the unit cell can be observed in Figure 4.4 as the Tb^{3+} content level increases. In addition, it was proved that the Gd^{3+} site is ideal to be doped by the Tb^{3+} ions due the similarity of the cationic radii.

4.3.2 Optical properties

Figure 4.5 shows the excitation spectra recorded at 476 nm for the Tb^{3+}-doped phosphors. The peaks representing the $Gd^{3+} \rightarrow Tb^{3+}$ energy transfer appear after excitation at 273 nm and 312 nm. These excitation bands are attributed to the electronic transitions represented in Figure 4.2, $^8S_{7/2} \rightarrow {}^6I_{7/2-17/2}$ and $^8S_{7/2} \rightarrow {}^6P_{7/2-3/2}$ respectively. The broad feature found between 330 nm and 420 nm is representative of the direct excitation of the Tb^{3+} ions (represented in Figure 4.1). This region is attributed to the spin-forbidden $4f^8$-$4f^75d^1$ transition of Tb^{3+}.[25]

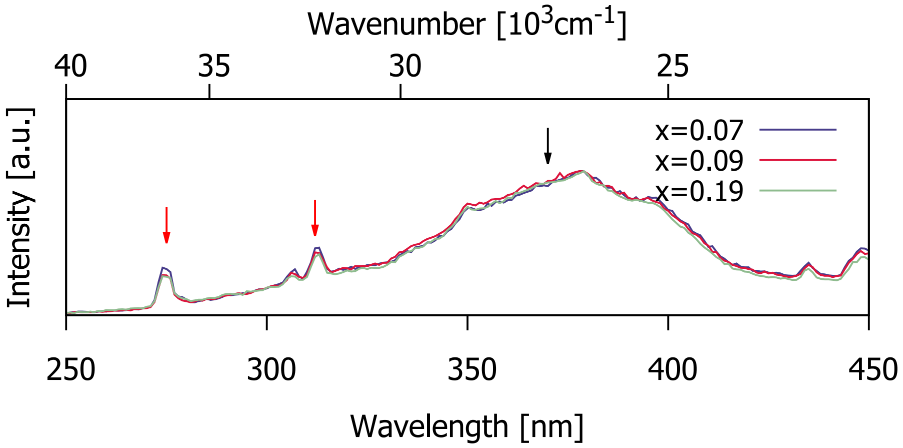

Figure 4.5: Excitation spectra of $Gd_{9.33-x}Tb_x(SiO_4)_6O_2$ materials recorded at λ_{emi} = 476 nm and normalised to the highest peak. The red arrows show the Gd^{3+} excitation indirectly populating the Tb^{3+} and the black arrows the direct Tb^{3+} excitation.

Figure 4.6 shows the emission spectra for the $Gd_{9.33-x}Tb_x(SiO_4)_6O_2$ (x = 0.07, 0.09 and 0.19) phosphor series recorded under excitation at 273 nm. The typical emission peaks can be observed at 488 nm, 545 nm, 586 nm and 615 nm and are attributed to $^5D_4 \rightarrow ^7F_J$ (J = 6, 5, 4, and 3 respectively) transitions from levels of $4f^8$ configuration of Tb^{3+}. Weak $^5D_3 \rightarrow ^7F_J$ (J = 5, 4, 3 and 2) transitions can also be observed at 413 nm, 436 nm, 456 nm and 469 nm respectively. Table 4.5 summarises the emission bands in the visible region for the Tb^{3+} ions.

Transition	Wavelength (nm)
$^5D_4 \rightarrow ^7F_6$	488
$^5D_4 \rightarrow ^7F_5$	545
$^5D_4 \rightarrow ^7F_4$	586
$^5D_4 \rightarrow ^7F_3$	615
$^5D_3 \rightarrow ^7F_5$	413
$^5D_3 \rightarrow ^7F_4$	436
$^5D_3 \rightarrow ^7F_3$	456
$^5D_3 \rightarrow ^7F_2$	469

Table 4.5: Emission bands present in the $Gd_{9.33-x}Tb_x(SiO_4)_6O_2$ phosphor series.

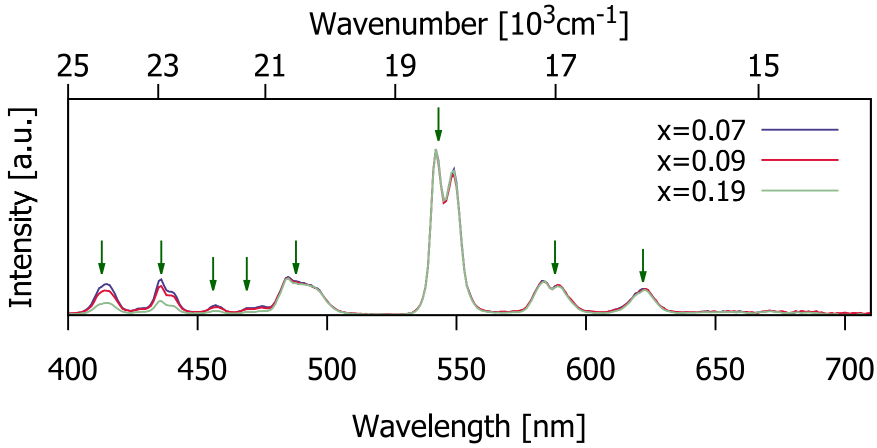

Figure 4.6: Emission spectra of $Gd_{9.33-x}Tb_x(SiO_4)_6O_2$: recorded at $\lambda_{exc} = 273$ nm and normalised to the 545 nm peak. Green arrows show the Tb^{3+} emission.

The emission spectra show a decrease in the blue emission intensity when the Tb^{3+} doping level increases, showing concentration quenching for the $^5D_3$-excited level transition. However, the green emission (545 nm) exhibits enhancement when the Tb^{3+} content increases.

For a "100% luminous efficacy of radiation", defined as 408 lm/W at a CRI of 90, the centre emission wavelength has to be 530 nm.[3] The $Gd_{9.33-x}Tb_x(SiO_4)_6O_2$ phosphor series present a very clear dominant green emission band at 545 nm with a FWMH of 13 nm. This dominant emission peak is found very near to the centre emission wavelength.

Figure 4.7 shows the blue to green ratio (B/G, $^5D_4 \rightarrow {}^7F_6/{}^5D_4 \rightarrow {}^7F_5$, found in Table 4.5) as a function of Tb^{3+} content. If the emission arises mainly from the $^5D_3$-excited level, the emission colour is blue; in contrast if the emission is mainly from the $^5D_4$-excited level, the emission colour is green. It has previously been observed that the Tb^{3+} concentration and the molecular vibrational energy of the host lattice are the main factors influencing the relative intensity between $^5D_4$ and $^5D_3$ emissions.[31]

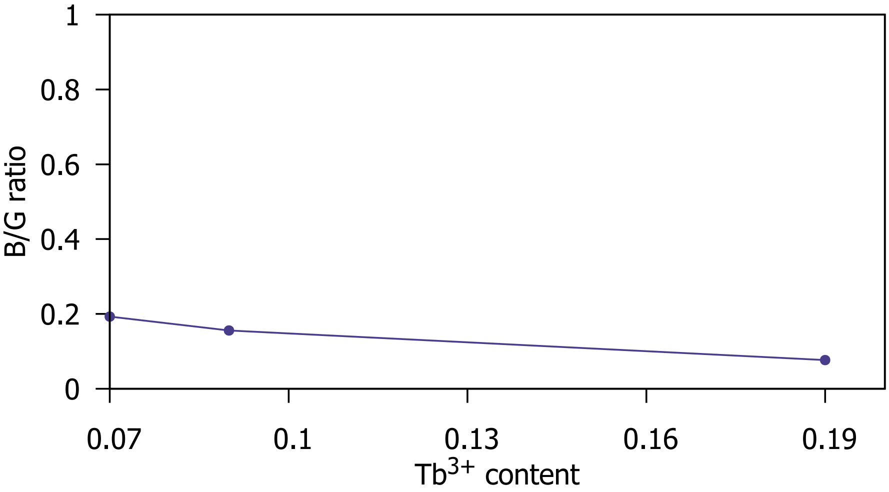

Figure 4.7: Blue/green emission intensity ratio as a function of Tb^{3+} content (x) in $Gd_{9.33-x}Tb_x(SiO_4)_6O_2$, from data collected at 273 nm.

Table 4.6 presents the chromaticity coordinates and the CCT obtained for the $Gd_{9.33-x}Tb_x(SiO_4)_6O_2$ series. These are illustrated in the 1931 CIE diagram in Figure 4.8a, with a detailed zoom shown in Figure 4.8b. $Gd_{9.33-x}Tb_x(SiO_4)_6O_2$ phosphors emit within the green region, tending towards the light green region. This is expected due to the dominant emission corresponding to transitions from the $^5D_4$-excited level. The high levels of Tb^{3+} provide concentration quenching for the blue emission, as is observed in Figure 4.6. The $Gd_{9.33-x}Tb_x(SiO_4)_6O_2$ (x = 0.07, 0.09 and 0.19) phosphor series is believed to produce within the blue region at lower Tb^{3+} content. In the same sense, with an increase in the Tb^{3+} content, the colour coordinates shifted towards a deeper green. The values are comparable to the CIE coordinates published in the literature for $Ca_3La_6(SiO_4)_6$:$0.5Tb^{3+}$ (0.35, 0.55) when excited at 288 nm (shown in Figure 4.8).[17]

Tb content	Colour coordinates		CCT(K)
	x	y	
0.07	0.3120	0.4623	6034
0.09	0.3171	0.4744	5881
0.19	0.3269	0.5218	5625

Table 4.6: CIE coordinates and CCT values for $Gd_{9.33-x}Tb_x(SiO_4)_6O_2$ phosphors.

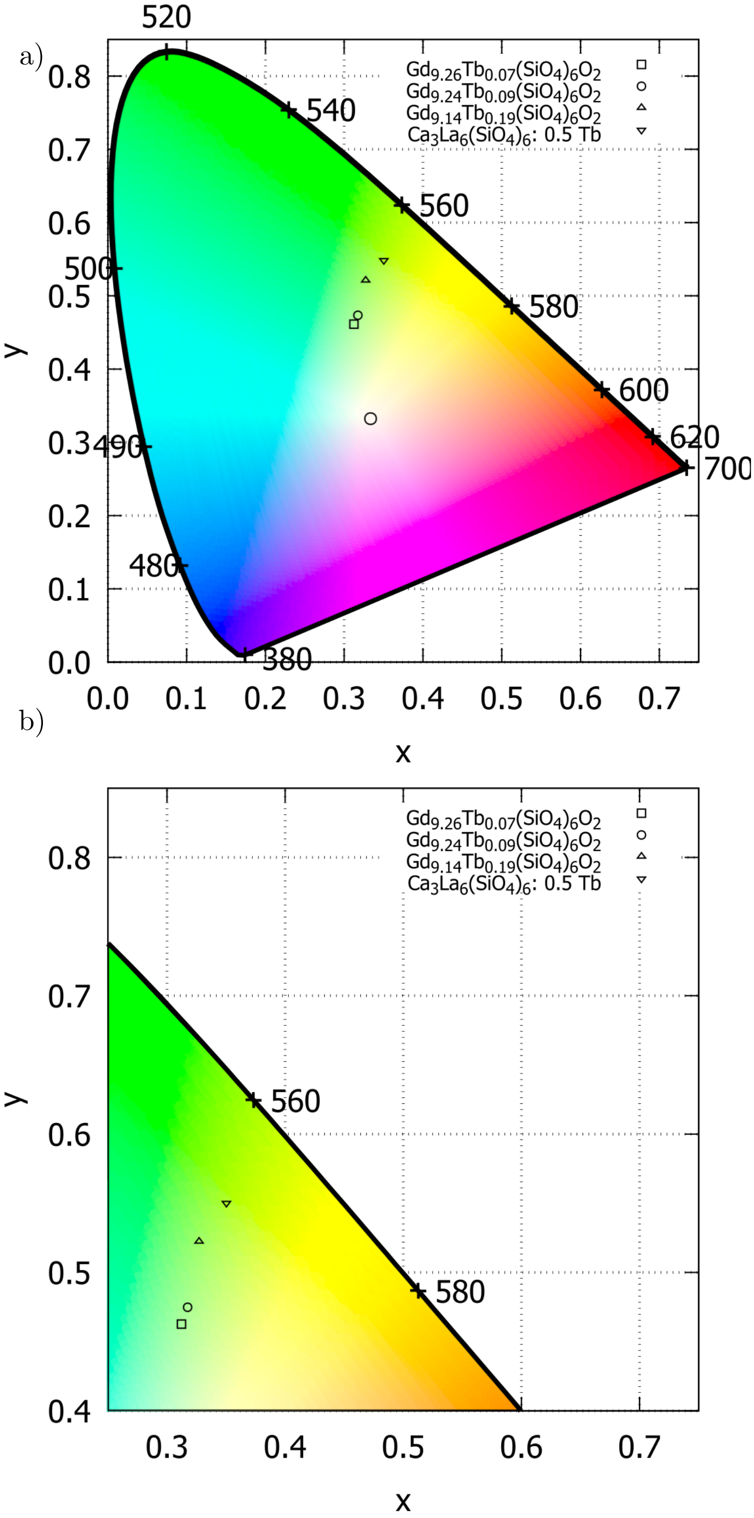

Figure 4.8: a) 1931 CIE chromaticity diagram showing the chromaticity coordinates at $\lambda_{exc} = 273$ nm for the $Gd_{9.33-x}Tb_x(SiO_4)_6O_2$ phosphor series. b) Expansion of the pertinent CIE region for the hosts discussed.

4.3.3 Tb^{3+} temporal decay

Figure 4.9 shows the fitted decay curves for the $^5D_4 \rightarrow ^7F_5$ and $^5D_4 \rightarrow ^7F_3$ transitions recorded under pulsed excitation at $\lambda_{exc} = 375$ nm. These decay curves were fitted with a single exponential decay described in Equation 4.2.

$$I(t) = I_0 exp(-\frac{t}{\tau}), \tag{4.2}$$

where I(t) is the intensity at time t, I_0 the initial intensity and τ is the lifetime.

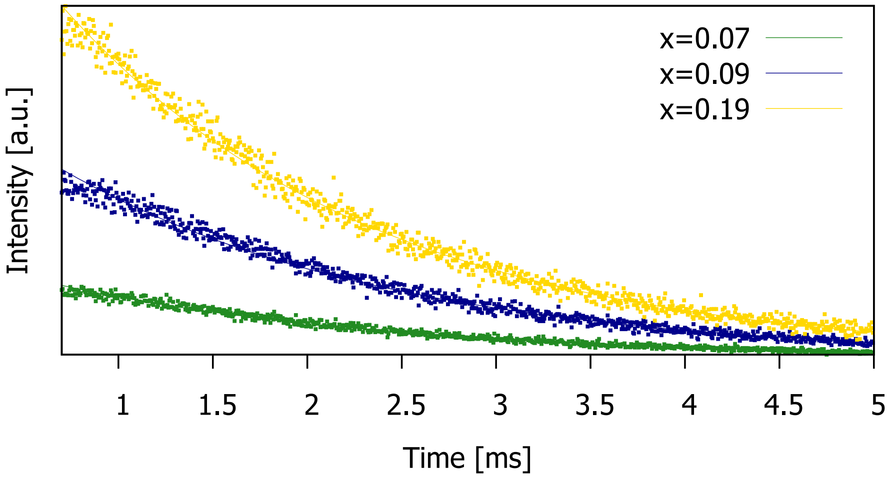

Figure 4.9: Fitted decay curves (solid line) of the experimental data (dots) of the $^5D_4 \rightarrow ^7F_5$ transition at 545 nm for $Gd_{9.33-x}Tb_x(SiO_4)_6O_2$ phosphors recorded after excitation at 375 nm.

The lifetime values calculated for the $Gd_{9.33-x}Tb_x(SiO_4)_6O_2$ phosphors are compiled in Table 4.7. The Tb^{3+} $^5D_4 \rightarrow ^7F_5$ transition lifetime values are in the order of 1.8 ms. These values are congruent with those published for $Ca_4La_{0.95}O(BO_3)_3$:0.05 Tb^{3+}[25] and $YK_3B_6O_{12}$:0.06Tb^{3+}[23] phosphors, with decay values of τ = 2.02 ms and τ = 1.68 ms respectively.

x	$^5D_4 \rightarrow ^7F_5$ transition (545 nm) τ(ms)
0.07	1.77(3)
0.09	1.75(2)
0.19	1.66(2)

Table 4.7: Lifetime values obtained for $Gd_{9.33-x}Tb_x(SiO_4)_6O_2$ phosphors recorded after excitation at 375 nm.

The lifetime values for $Gd_{9.33-x}Tb_x(SiO_4)_6O_2$ phosphors as a function of the Tb^{3+} content are shown in Figure 4.10. There is a small decrease in the $^5D_4 \rightarrow ^7F_5$ transition lifetime values with an increase in the doping. The Tb^{3+} decay became faster with higher doping concentration. Hence, the Gd^{3+} → Tb^{3+} energy transfer is much more efficient in high Tb^{3+} content phosphors.

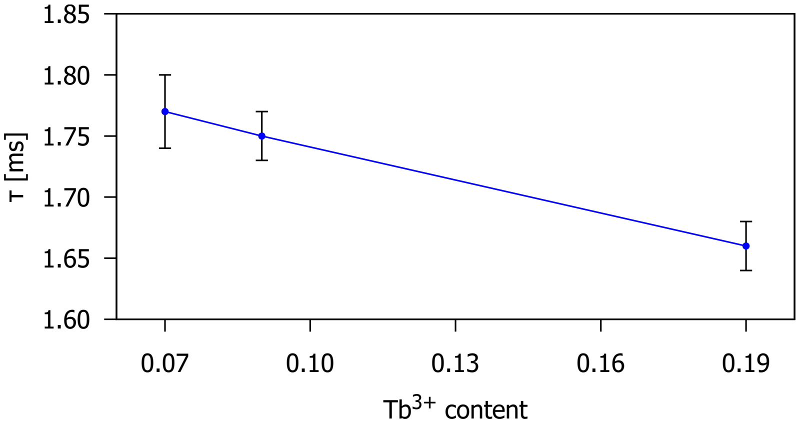

Figure 4.10: Lifetime values according to Tb^{3+} content (x) for the $^5D_4 \rightarrow ^7F_5$ transition (545 nm). The error given for the lifetime values is the standard deviation from the fitting.

4.4 Conclusions and future work

The Tb^{3+}-doped apatite-type silicate single-phase phosphor series were synthesised and characterised by powder x-ray diffraction and optical measurements.

The $Gd_{9.33-x}Tb_x(SiO_4)_6O_2$ phosphor was doped systematically (x = 0.07, 0.09 and 0.19). The phosphor series presented green emission colour. The dominant emission peak is found at 545 nm, which is close to the desirable green phosphor centre emission wavelength, required for the "100% luminous efficacy of radiation". The 1931 CIE colour coordinates confirmed the doping as right shifting was observed. The chromaticity coordinates obtained ranged from (0.3120, 0.4623) to (0.3269, 0.5218), identifying these phosphors as light green emitters shifting towards almost deep green when the doping level increases. At lower Tb^{3+} doping levels it is presumed to emit in the blue region. Hence, $Gd_{9.33-x}Tb_x(SiO_4)_6O_2$ phosphor is a blue to green tuneable phosphor. The chemical modification of the phosphor by increasing the Tb^{3+} content level allowed the reduction of the B/G ratio, consequently a desirable deeper green emitting phosphor.

The emission decay curves were also measured and fitted to determine the lifetimes. The lifetime value for the $^5D_4 \rightarrow ^7F_5$ transition (545 nm) is around 1.8 ms, which is an expected decay value for Tb^{3+} doped phosphors.

The shift in the colour coordinates and the lifetime values proved that the concentration quenching has not been reached. Future work should focus on doping the host with higher levels of Tb^{3+} to achieve a deeper green emitter, which was not possible in this project due to the length of time needed to synthesise the materials. In the same way, variable temperature analysis of the $Gd_{9.33-x}Tb_x(SiO_4)_6O_2$ green phosphors is needed to test their behaviour at LED working temperatures.

4.5 References

[1] Nakamura, S., Mukai, T., and Senoh, M. *Applied Physics Letters*, 64(13), 1994.

[2] Kim, Y.H., Viswanath, N.S.M., Unithrattil, S., Kim, H.J., and Im, W.B. *ECS Journal of Solid State Science and Technology*, 7(1), 2018.

[3] Phillips, J., Coltrin, M., Crawford, M., Fischer, A., Krames, M., Mueller-Mach, R., Mueller, G., Ohno, Y., Rohwer, L., Simmons, J., and Tsao, J. *Laser & Photonics Reviews*, 1(4), 2007.

[4] Zhou, B., Yang, W., Han, S., Sun, Q., and Liu, X. *Advanced Materials*, 27(40), 2015.

[5] Dieke, G.H. and Crosswhite, H.M. *Applied Optics*, 2(7), 1963.

[6] Jorgensen, C.K. *Molecular Physics*, 5(3), 1962.

[7] Xie, M., Tao, Y., Huang, Y., Liang, H., and Su, Q. *Inorganic chemistry*, 49(24), 2010.

[8] Zhang, X., Zhou, L., Pang, Q., Shi, J., and Gong, M. *The Journal of Physical Chemistry C*, 118(14), 2014.

[9] Baig, N., Yadav, R.S., Dhoble, N.S., Barai, V.L., and Dhoble, S.J. *Journal of Luminescence*, 215, 2019.

[10] Ma, X., Liao, L., Guo, Q., Liu, H., Zhou, T., and Mei, L. *RSC Advances*, 8(48), 2018.

[11] Kim, D., Park, D., Oh, N., Kim, J., Jeong, E.D., Kim, S.J., Kim, S., and Park, J.C. *Inorganic Chemistry*, 54(4), 2015.

[12] Liu, H.K., Zhang, Y.Y., Liao, L.B., and Xia, Z.G. *Journal of Luminescence*, 156, 2014.

[13] Guo, Q., Ma, X., Liao, L., Liu, H., Yang, D., Liu, N., and Mei, L. *Journal of Solid State Chemistry*, 280, 2019.

[14] Muresan, L.E., Perhaita, I., Prodan, D., and Borodi, G. *Journal of Alloys and Compounds*, 755, 2018.

[15] Peng, C., Shang, M.M., Li, G.G., Hou, Z.Y., Geng, D.L., and Lin, J. *Dalton Transactions*, 41(16), 2012.

[16] Shen, B., Wu, F., Zhang, Y., Xia, H., Chen, B., and Hu, J. *Journal of Alloys and Compounds*, 809, 2019.

[17] Lin, H.C., Yang, C.Y., Das, S., and Lu, C.H. *Journal of the American Ceramic Society*, 97(6), 2014.

[18] Xian, J.Q., Yi, S.P., Deng, Y.M., Zhang, L., Hu, X.X., and Wang, Y.H. *Physica B-Condensed Matter*, 483, 2016.

[19] Ma, P.C., Song, Y.H., Yuan, B., Sheng, Y., Xu, C.Y., Zou, H.F., and Zheng, K.Y. *Ceramics International*, 43(1), 2017.

[20] Jin, Y., Zhou, H.P., and Zhang, D.F. *Rare Metal Materials and Engineering*, 45(11), 2016.

[21] Yang, C., Li, X., Liu, Q.S., Li, G.Y., Zhang, X.Y., Bai, Z.H., Wang, X.C., and Mi, X.Y. *Journal of Materials Science-Materials in Electronics*, 31(2), 2020.

[22] Qin, D. and Tang, W.J. *Rsc Advances*, 7(5), 2017.

[23] Yang, L., Wan, Y.P., Huang, Y.L., Chen, C.L., and Seo, H.J. *Journal of Alloys and Compounds*, 684, 2016.

[24] Fernandez-Carrion, A.J., Ocana, M., Garcia-Sevillano, J., Cantelar, E., and Becerro, A.I. *Journal of Physical Chemistry C*, 118(31), 2014.

[25] Chen, Z., Chen, X.A., Huang, S.M., and Pan, Y.X. *Ceramics International*, 42(12), 2016.

[26] Chen, Y., Yu, B., Gou, J., and Liu, S.F. *Journal of Materials Chemistry C*, 6(40), 2018.

[27] Wen, D. and Shi, J. *Dalton Transactions*, 42(47), 2013.

[28] George, N.C., Denault, K.A., and Seshadri, R. *Annual Review of Materials Research*, 43, 2013.

[29] Wang, W.R., Jin, Y., Yan, S., Yang, Y.Q., Liu, Y.L., and Xiang, G.T. *Ceramics International*, 43(18), 2017.

[30] Blasse, G. and Grabmaier, B. *Luminescent materials*, Springer Verlag1994.

[31] Han, X.M., Lin, J., Zhou, H.L., Yu, M., Zhou, Y.H., and Pang, M.L. *Journal of Physics-Condensed Matter*, 16(15), 2004.

[32] Song, M., Zhao, W., Ran, W., Xue, J., Liu, Y., and Jeong, J.H. *Journal of Alloys and Compounds*, 803, 2019.

[33] Latshaw, A.M., Hughey, K.D., Smith, M.D., Yeon, J., and zur Loye, H.C. *Inorganic Chemistry*, 54(3), 2015.

[34] Coelho, A.A., Evans, J.S.O., Evans, I.R., Kern, A., and Parsons, S. *Powder Diffraction*, 26(4), 2011.

[35] Rietveld, H.M. *Journal of Applied Crystallography*, 2, 1969.

[36] Vegard, L. *Zeitschrift für Physik*, 5(1), 1921.

[37] Shannon, R.D. *Acta crystallographica section A: crystal physics, diffraction, theoretical and general crystallography*, 32(5), 1976.

5 Single-phase white-emitting phosphors based on apatite-type gadolinium silicate, $Gd_{9.33}(SiO_4)_6O_2$ doped with Dy^{3+}, Eu^{3+} and Tb^{3+}

5.1 Introduction

There continues to be an intense research effort to replace traditional lighting technology (e.g., incandescent, halogen, xenon and fluorescent light sources) with more energy-efficient devices. Solid-state white lighting (SSWL) devices based on inorganic semiconductors and inorganic phosphors have become viable alternatives to provide ambient lighting.[1] Apart from energy efficiency, SSWL can offer numerous other desirable features, such as robustness and longevity; fast switching times; controllable spectral power distribution and spatial distribution; polarisation properties; and the use of relatively benign materials. The Commission Internationale de l'Elcairage (CIE) defines 'white light' in terms of red, green and blue colour coordinates, x, y, and z respectively with white being the point at which $x = y = z = \frac{1}{3}$. Other parameters are also important. The correlated colour temperature (CCT) of a device refers to the temperature that would be necessary for incandescence to lead to the same perceived colour: white light has a CCT of around 6000 K, although lower values are often desirable for the 'warmer' white of typical ambient room lighting. Meanwhile, the colour-rendering index (CRI) describes how well the colour of objects is revealed relative to a reference source, with a maximum CRI of 100 for sunlight.[2–4]

A number of different strategies have been adopted to generate white light in a solid-state lighting device.[5] These are shown in Figure 1.4 in section 1.1.1.3. A combination of red, green and blue (RGB) LED emitters can be used but this device structure is complicated by the usually different characteristics of the emitters in response to, for example, temperature, voltage fluctuations and ageing. Related issues arise when a single high-energy UV-emitting LED is used to excite multiple RGB phosphors since the phosphors may have different degradation rates and so the resultant colour changes over time. A more attractive solution is potentially to use a UV excitation source in conjunction with a single-phase phosphor that incorporates discrete R, G and B-emitting centres.[6] Lanthanide(III) ions with emission bands in the visible have long been used as phosphors, for example Eu^{3+}-doped Y_2O_3 exploiting the hypersensitive $^5D_0 \rightarrow ^7F_2$ *f-f* transition at about 617 nm was the red phosphor used in almost all conventional colour TV screens. For solid-state lighting, much of the lanthanide-based research over the past 20 years has turned to materials that utilise the $4f$-$5d$ emission bands of Ce^{3+} and Eu^{2+}.[5] The relatively low ionisation energies of these ions lead to energetically accessible *f-d* excited states. Unlike *f-f* transitions, they are Laporte-allowed, with large oscillator strengths, short emission decay times and broad absorption bands, all properties that are desirable for SSL. Nevertheless, *f-f* excited states do offer some attractions, in particular their narrow line-like emission spectra can favour high colour purity.

The combination of red-emitting Eu^{3+} with other higher-energy-emitting Ln^{3+} ions within a single phase is a potentially attractive way to generate a white-light-emitting phosphor for coating onto a UV LED. For example, Dy^{3+} has emission bands in the blue (485 nm, $^4F_{9/2} \rightarrow ^6H_{15/2}$) and yellow (580 nm, $^4F_{9/2} \rightarrow ^6H_{13/2}$) regions to complement the red of Eu^{3+}, while Tb^{3+} has an intense band in the green region (545 nm, $^5D_4 \rightarrow ^7F_5$) and a weaker band in the blue (490 nm, $^5D_4 \rightarrow ^7F_6$). These principal bands may be accompanied in the solid state by some non-Kasha emission from higher-lying excited states if there is sufficient excitation energy to populate them. Incorporation of the Gd^{3+} ion is also of interest to sensitise such visibly emitting ions through energy transfer: its lowest-lying excited state $^6P_{7/2}$ has an energy of around 32000 cm^{-1} (corresponding to $\lambda = 312$ nm in the UV region). There are, of course, some drawbacks to this strategy. The Gd^{3+} absorptions are weak and require far-UV excitation sources, while the use of inter-ion energy transfer inevitably leads to intrinsic energy losses coupled with Stokes shift losses. With regard to excitation sources, however, far-UV sources are becoming more readily available with advances in LED technology.[7–10]

The approach of co-doping combinations of Eu^{3+} with Dy^{3+} and/or Tb^{3+} into a single-phase material requires careful consideration of the relative and absolute concentrations of the ions. Distance-dependent energy transfer processes can occur from higher-energy lanthanides to those with lower-lying excited states, strongly influencing the perceived colour and CIE coordinates, while elevated concentrations of any single Ln^{3+} can lead to self-quenching and loss of efficiency. The approach also requires a host of high chemical and thermal stability in order to avoid degradation under irradiation.

The silicate apatite structure has been a new object of study due to its ability to act as a sensitiser, by absorbing UV radiation and transferring it to an activator (RE dopant ions), making it a good host structure for luminescence.

More specifically, silicate apatites that contain lanthanides are known for having very good luminescent properties which are not affected by the environment (cations and anions) surrounding them.[11] If the X site is occupied by oxygen then the apatite is known as an oxyapatite structure. It belongs to the space group $P6_3/m$ (like most of the apatites). A very specific characteristic of this host lattice is that two different cation sites are present: 4 f and 6 h. These sites have been shown to be suitable for RE and transition metal ions. Therefore, silicate oxyapatites have been extensively investigated as phosphor hosts due to their very good physical and chemical stability, which results from their strong and rigid Si–O bonds.[12]

5.1.1 A brief survey of apatite-type silicate phosphors

The emission properties of phosphors can be strongly dependent on the environment around the activators. Apatites offer extensive opportunities for tuning the luminescence. This is illustrated by the range of emissions achieved in various apatite silicates.

The emission of $Ca_2Y_8(SiO_4)_6O_2{:}Bi^{3+}$ excited from 335 to 380 nm ranges from green-blue to blue.[12] $LiY_9(SiO_4)_6O_2{:}Ce^{3+}$ has been studied for its temperature-sensing properties. It has a tuneable emission from cyan to blue with changes of temperature and it shows temperature recycling with a reversible process from heating to cooling.[13] When excited with NUV light, $Ba_9Y_2(SiO_4)_6O_2{:}Ce^{3+}$ emits in the blue-green region with a QY of 60% at room temperature. When the temperature is increased to 500 K, it shows a red emission and its QY only decreases by 25%.[14] $Sr_2Y_8(SiO_4)_6O_2{:}Eu^{2+}/Eu^{3+}$ excited with a near ultraviolet (NUV) and blue light can emit in the green and orange region.[15]

The red-emitting $Sr_2Gd_8(SiO_4)_6O_2{:}xEu^{3+}$ phosphor has a constant decay rate of $\tau = 1.35$ ms when x is less than 3.0. This then decreases at high x, showing a high quenching concentration. The critical doping concentration is at x = 0.7075, with better chromaticity coordinates (at 0.646, 0.304) under NUV excitation than commercial phosphors.[16] $Ca_2Gd_8(SiO_4)_6O_2{:}Eu^{3+}$ is a red phosphor that has emission bands in 575-630 nm and features at 650 and 700 nm. It suffers thermal quenching, as it loses 99.5% of its intensity at 500 °C, but it shows excellent brightness at room temperature.[17]

$NaEu_9(SiO_4)_6O_2$, $Na_{1.5}Eu_{8.5}(SiO_4)_6OF$ and $Eu_{9.34}(SiO_4)_6O_2$ phosphors show maxima emission peaks at $\sim$ 607 nm and excitation peaks features from 350 nm to 425 nm, indicating a transition from the $4f^6$ configuration of the Eu^{3+} cation. Doping other luminescent cations onto the lanthanide site allows the luminescence to be tuned.[11]

The tuneable full-colour emitting $Ca_6Sc_4(SiO_4)_6{:}Ce^{3+}$ phosphor has been shown to have high emission intensity and high thermal stability, which is superior to YAG:Ce^{3+}. Following this, $Ca_{5.6}Mn_{0.4}Sc_{3.9}Ce_{0.1}Y_x(SiO_4)_6$ with x= 0.1 was discovered to have a very high CRI of 92 with a CCT of 6954 K, and x = 0.3 was discovered to have a very high CRI of 91 with a CCT of 5379 K.[18]

$LiLa_9(SiO_4)_6O_2{:}Ce^{3+}$ has two excitation bands at 355 and 380 nm and a broad emission peak with a maximum at $\sim$ 380 nm in the wavelength range 310 - 510 nm. The reported luminescence decay is 24 ns when the Ce^{3+} is on the 6h site monitored at 355 nm and 32 ns when the Ce^{3+} is on the 4f site monitored at 430 nm.[19] The $LiGd_9(SiO_4)_6O_2{:}Ce^{3+}$ emission curve can be fitted well with a sum of four Gaussian functions with bands at 369 and 396 nm when the Ce is in the 6h site and at 417 and 455 nm when it is in the 4f site, with an optimum doping at x = 0.07.[20]

Nanophosphors based on $Ca_2Gd_8(SiO_4)_6O_2{:}0.09Dy^{3+}$, xEu^{3+} (x = 0, 0.09, 0.19, 0.28) excited at 275 nm display blue, yellow and red emission bands so that a white-emitting phosphor can be achieved with the appropriate percentages of dopant ions.[21] According to the emission intensity, the phosphor showed a concentration quenching at Dy^{3+} doping levels > 1%.[22]

Cold-white emitting Dy^{3+}-doped $Sr_4Ca(PO_4)_2SiO_4$ phosphors incorporate Li^+, Na^+ or K^+ ions as charge compensation agents, enhancing the emission. Li^+-containing $Sr_4Ca(PO_4)_2SiO_4$ phosphor presented twice brighter emission in comparison with the $Sr_4Ca(PO_4)_2SiO_4$ phosphor.[23]

$Na_5Y_4(SiO_4)_4F{:}Eu^{2+},Tb^{3+},Eu^{3+}$ phosphors can be tuned from light blue to red, passing through white. The energy-transfer mechanism $Eu^{2+} \rightarrow Tb^{3+} \rightarrow Eu^{3+}$ was established.[24] Warm-white emitting $Ca_2Y_8(SiO_4)_6O_2$:Dy^{3+},Eu^{3+} materials shows tuneable emission from the blue to the red, passing the white region in the CIE diagram. When the phosphor reaches 100 °C the emission intensity decreases 9%, while at 150 °C the emission decrease 17% from the room temperature level. These phosphors have high thermal stability due to the rigidity of the apatite structure.[25]

The objectives of the work described here were twofold:

i) to prepare and structurally characterise single-phase phosphors based on the apatite-type silicate $Gd_{9.33}(SiO_4)_6O_2$ doped with combinations of Dy^{3+} and Eu^{3+} or Eu^{3+} and Tb^{3+};

ii) to investigate the emission properties of the materials under UV excitation, probing energy transfer from Gd^{3+} as a sensitisation pathway for the visible-emitting ions.

The compounds studied in this chapter are the white-emitting phosphor series highlighted in Tables 5.1 and 5.2.

0.02% Eu $x = 0.002$	0.05% Eu $x = 0.005$	0.1% Eu $x = 0.009$	0.2% Eu $x = 0.019$
0.5% Dy $y = 0.047$	0.5% Dy $y = 0.047$	0.5% Dy $y = 0.047$	0.5% Dy $y = 0.047$
1.0% Dy $y = 0.093$	1.0% Dy $y = 0.093$	1.0% Dy $y = 0.093$	1.0% Dy $y = 0.093$
2.0% Dy $y = 0.187$	2.0% Dy $y = 0.187$	2.0% Dy $y = 0.187$	2.0% Dy $y = 0.187$
3.0% Dy $y = 0.280$	3.0% Dy $y = 0.280$		

Table 5.1: Different doping levels of the $Gd_{9.33-x-y}Eu_xDy_y(SiO_4)_6O_2$ materials.

0.02% Eu $x = 0.002$	0.03% Eu $x = 0.003$	0.05% Eu $x = 0.005$	0.1% Eu $x = 0.009$	0.3% Eu $x = 0.028$	0.7% Eu $x = 0.065$
0.3% Tb $y = 0.028$	0.3% Tb $y = 0.028$	0.3% Tb $y = 0.028$			
0.4% Tb $y = 0.037$	0.4% Tb $y = 0.037$	0.4% Tb $y = 0.037$			
0.5% Tb $y = 0.047$	0.5% Tb $y = 0.047$	0.5% Tb $y = 0.047$	0.5% Tb $y = 0.047$	0.5% Tb $y = 0.047$	0.5% Tb $y = 0.047$
				0.8% Tb $y = 0.075$	0.8% Tb $y = 0.075$
				1.0% Tb $y = 0.093$	1.0% Tb $y = 0.093$

Table 5.2: Different doping levels of the $Gd_{9.33-x-y}Eu_xTb_y(SiO_4)_6O_2$ materials.

5.2 Experimental details

5.2.1 Sample preparation

All the samples were prepared using conventional solid-state synthesis. The reagents used were: Gd_2O_3 (Sigma Aldrich, 99.99%), SiO_2 (Sigma Aldrich, 99.99%), Dy_2O_3 (Sigma Aldrich, 99.99%), Tb_2O_3 (Sigma Aldrich, 99.99%) and Eu_2O_3 (Sigma Aldrich, 99.999%). The hygroscopic oxides were preheated to 1000 °C to expel absorbed water before weighing out the stoichiometric amounts. Typically, the samples were heated at 1400 °C with intermittent grinding for a total of up to 300 h.

5.2.2 X-ray diffraction.

To assess the progress of the solid-state reactions and product purity, laboratory powder X-ray diffraction (PXRD) patterns were recorded on a Bruker AXS d8 Advance diffractometer using $\mathrm{CuK}_{\alpha_{1,2}}$ radiation. The patterns were recorded in a 2θ range from 10°to 70°, using a step size of 0.021°and a step time of 0.5 s. The recorded patterns were fitted using the initial structural model of $\mathrm{Gd}_{9.33}(\mathrm{SiO}_4)_6\mathrm{O}_2$,[11] modified to reflect the composition of each sample. The $\mathrm{Gd}_{9.33}(\mathrm{SiO}_4)_6\mathrm{O}_2$ host was also characterised using a high-resolution powder diffraction beamline (I11) at Diamond Light Source, using a wavelength of λ=0.82576 Å. The sample was placed in a borosilicate glass capillary and data were collected in a 2θ range up to 150°, at room temperature. Typically, the parameters refined included the background, the diffractometer zero point, the peak shape (pseudo-Voigt function and an hkl-dependent peak shape[26] to model the anisotropic peak broadening where needed), unit cell parameters, isotropic displacement parameters (equated for anions and cations) and the atomic fractional coordinates for each site (for the synchrotron data only). All the PXRD data were analysed using Topas Academic software.[27]

5.2.3 Photoluminescence spectroscopy

A Horiba Fluorolog-3 fluorimeter was used for the optical measurements with a xenon flashlamp as the excitation source and a Hamamatsu R928 photomultiplier tube for detection. Homogeneous finely powdered samples of the materials were contained in a Spectralon® cup with a quartz cover slip, and placed inside a Quanta-ϕ F-3029 integrating sphere connected to the spectrometer via optical fibres. The data recorded was analysed as discussed in more detail in section 2.3.3.

Following excitation with a pulsed xenon lamp, lifetime values were recorded with multichannel scaling. After passing through a monochromator, the light emitted was analysed at right angles to the excitation source and detected using a Hamamatsu R928 photomultiplier tube thermoelectrically cooled to -20 °C.

5.3 Results and discussion

5.3.1 Characterisation of the $\mathrm{Gd}_{9.33}(\mathrm{SiO}_4)_6\mathrm{O}_2$ host

To confirm the purity of the $\mathrm{Gd}_{9.33}(\mathrm{SiO}_4)_6\mathrm{O}_2$ host, the synchrotron PXRD patterns were fitted using the Rietveld method and the structural model in space group $P6_3/m$. The analysis confirmed a highly crystalline and nearly pure product (Figure 5.1). The refined unit cell parameters were a = 9.441298(9) Å, c = 6.870345(8) Å and V = 530.362(1) Å^3. A small amount of $\mathrm{Gd}_2\mathrm{SiO}_5$ impurity (2.6(7)% by weight) was detected.

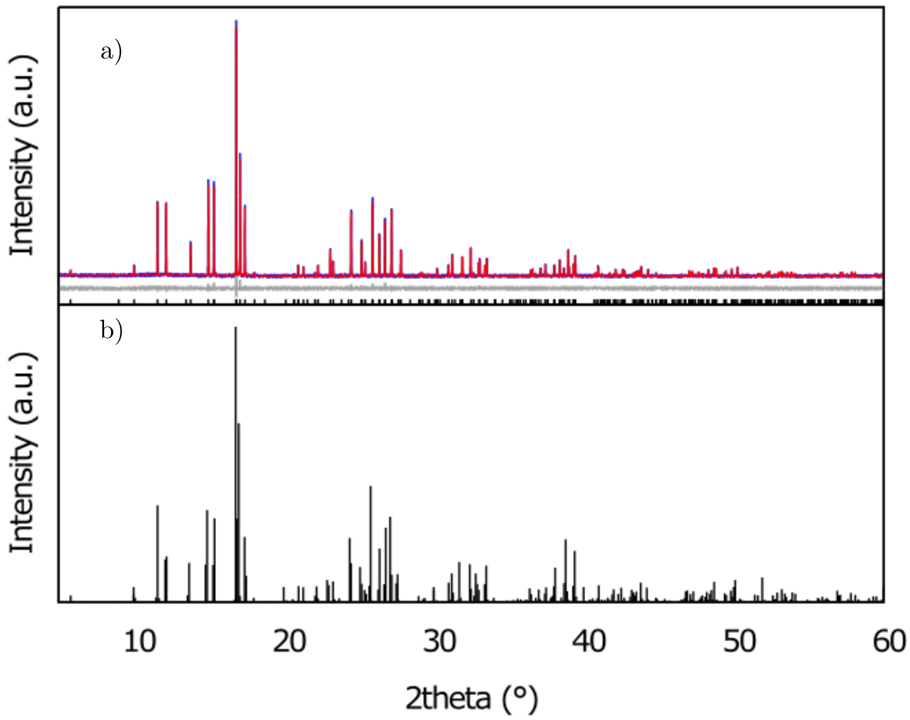

Figure 5.1: a) Rietveld fit of the synchrotron PXRD data for $Gd_{9.33}(SiO_4)_6O_2$. Rwp =9.94%. b) The corresponding PDF standard pattern.[11]

5.3.2 Phosphors incorporating dysprosium and europium: $Gd_{9.33-x-y}Eu_xDy_y(SiO_4)_6O_2$

5.3.2.1 Structure characterisation

In the first series of samples, $Gd_{9.33-x-y}Eu_xDy_y(SiO_4)_6O_2$, about 19 samples in total were prepared and characterised, and the 5 best-performing compositions in terms of colour coordinates near the white-light point are discussed here. These compositions along with their unit cell parameters are given in Table 5.3. The Rietveld fits of the PXRD data recorded for these materials showing single-phase products are given in Figure 5.2.

x	y	a(Å)	b(Å)	V(Å^3)	R$_{wp}$ (%)
0.002	0.093	9.44140(9)	6.86830(10)	530.22(1)	2.33
	0.187	9.44505(8)	6.86884(8)	530.67(1)	2.14
	0.280	9.4380(1)	6.8634(1)	529.46(1)	2.55
0.005	0.187	9.4387(1)	6.8730(1)	530.27(2)	2.67
	0.280	9.44244(8)	6.86654(8)	530.20(1)	2.25

Table 5.3: Unit cell parameters of the best-performing $Gd_{9.33-x-y}Eu_xDy_y(SiO_4)_6O_2$ (x=0.002: y=0.093, 0.187 and 0.280, and x= 0.005: y=0.187 and 0.280) phosphors.

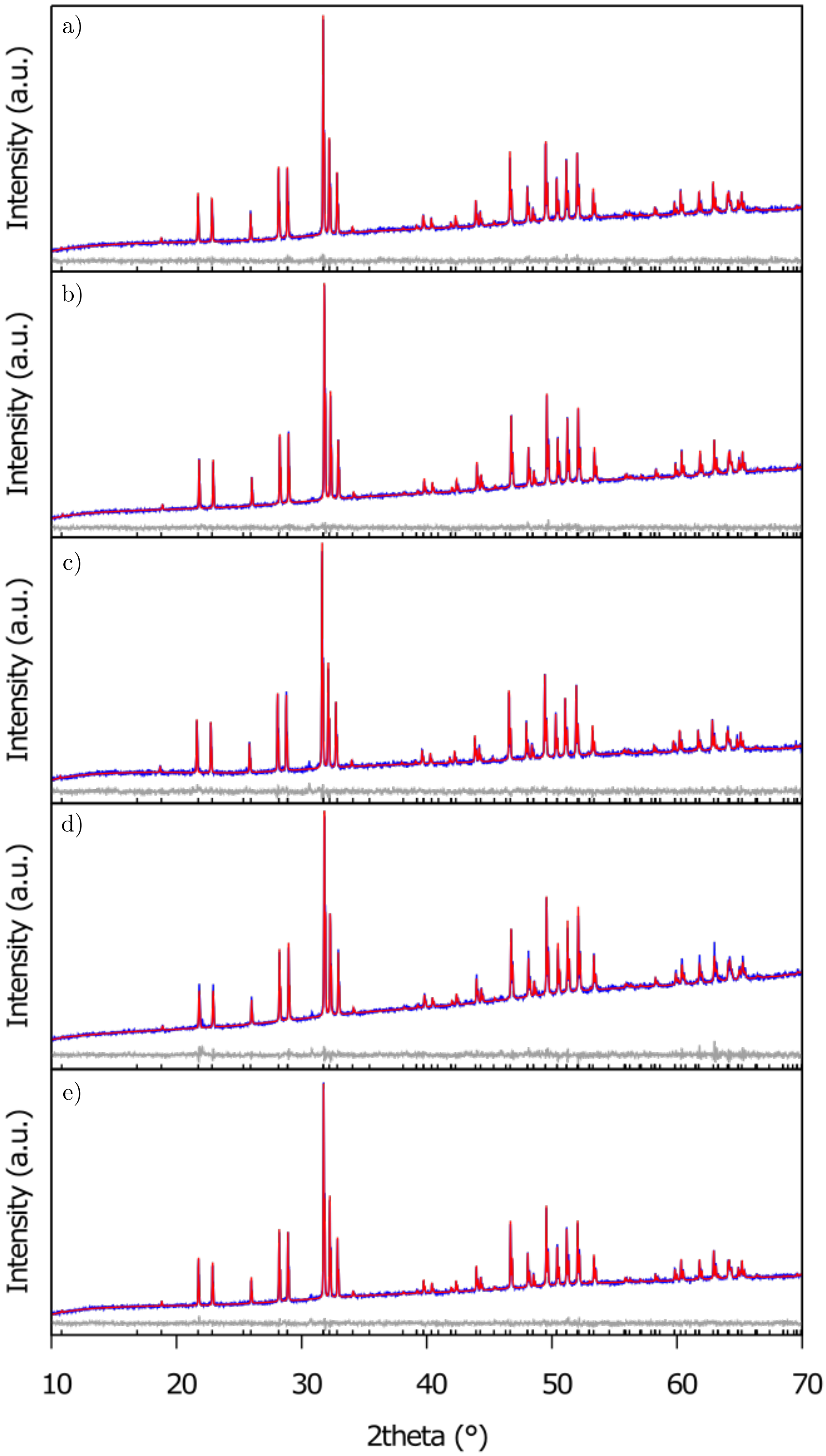

Figure 5.2: Rietveld fits of laboratory data for $Gd_{9.33-x-y}Eu_xDy_y(SiO_4)_6O_2$. x=0.002: a) y=0.093, b) y=0.187, c) y=0.280, and x= 0.005: d) y=0.187 and e) y=0.280.

5.3.2.2 Optical properties

The Russell-Saunders coupling states of Gd^{3+}, Dy^{3+} and Eu^{3+} are shown in the energy level diagram Figure 5.3. On irradiation in the UV region, excitation of the Gd^{3+} sensitiser from the ground $^8S_{7/2}$ state to the $^6P_{7/2}$ or ^6I_J states is anticipated. The excited $^6I_{7/2}$ state, for example, can then populate excited states of similar energy of nearby Dy^{3+} ions by energy transfer. These relax to the $^4F_{9/2}$ state. Radiative decay of the $^4F_{9/2}$ state gives blue, yellow and red emission bands (transitions to $^6H_{15/2}$, $^6H_{13/2}$ and $^6H_{11/2}$), but can also transfer energy to the $^5D_1$ state of any nearby Eu^{3+} ions. Relaxation of the $^5D_1$ state to the $^5D_0$ state is followed by emission to the ^7F_J manifold, of which the transitions to J = 1, 2 and 4 in the orange and red region are typically the most intense. Energy transfer from Gd^{3+} to higher-lying Eu^{3+} excited states is clearly also feasible without the involvement of Dy^{3+}.

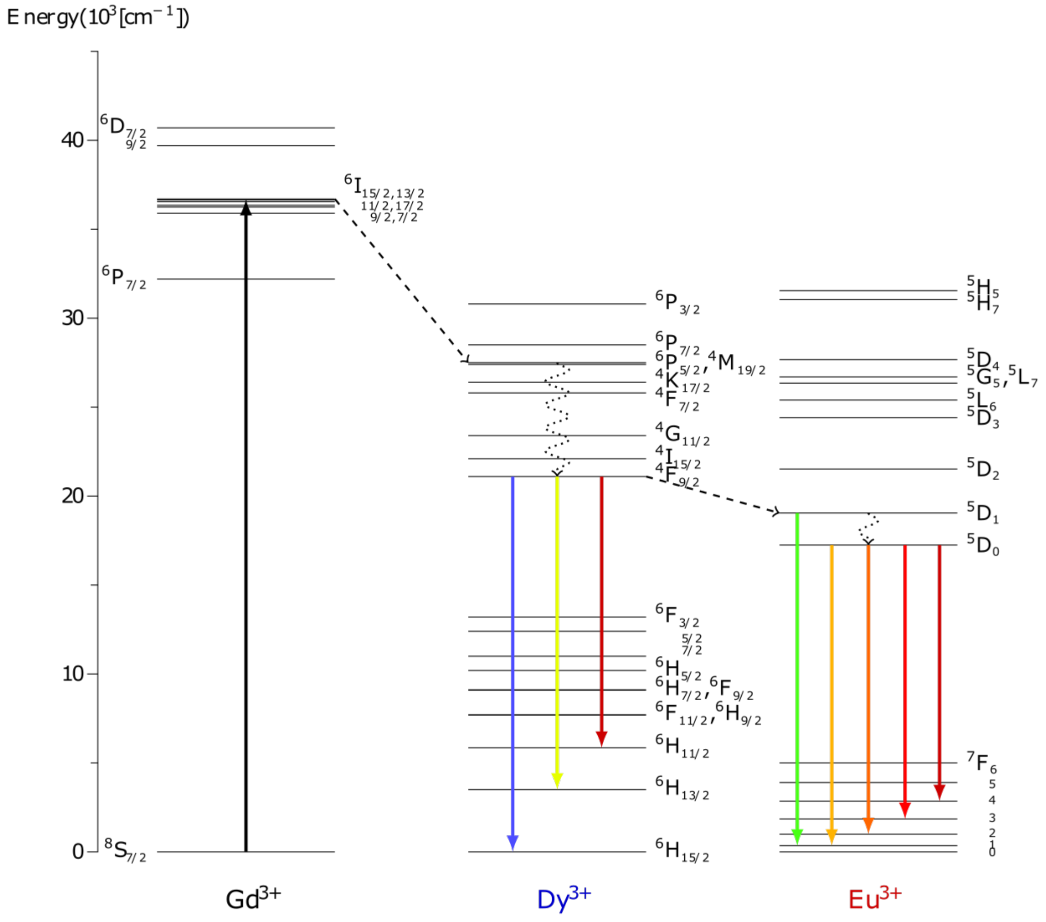

Figure 5.3: Energy-level diagrams for Gd^{3+}, Dy^{3+} and Eu^{3+} ions showing the relevant transitions in the system.

The excitation spectra recorded for the Dy^{3+}, Eu^{3+} co-doped materials registered at the 476 nm emission band of Dy^{3+} are shown in Figure 5.4. Bands due to the Gd^{3+} electronic transitions $^8S_{7/2} \rightarrow {}^6I_{13/2}$ and $^8S_{7/2} \rightarrow {}^6P_{7/2}$, indicative of absorption by Gd^{3+} followed by energy transfer to Dy^{3+}, appear at 273 nm and 312 nm respectively (Figure 5.3, red arrows in Figure 5.4). At lower energies, peaks corresponding to direct excitation of the Dy^{3+} from its ground $^6H_{15/2}$ state to the $^6P_{3/2}$, $^6P_{7/2}$, $^6P_{5/2}$, $^4F_{7/2}$ and $^4I_{15/2}$ excited states are observed at 325, 350, 365, 386 and 450 nm respectively (black arrows in Figure 5.4).

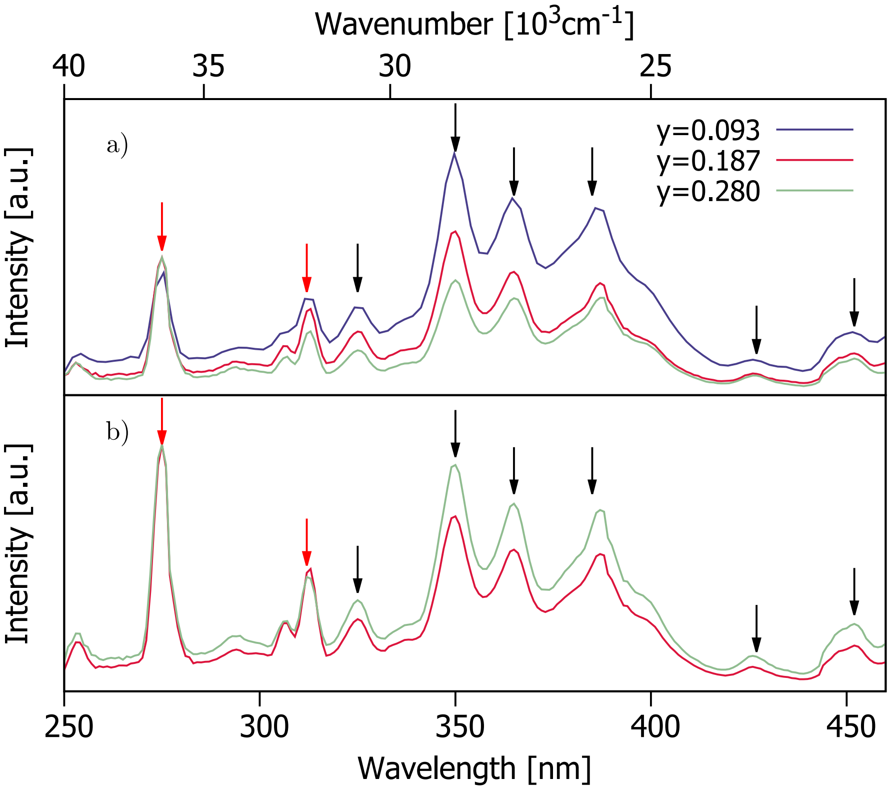

Figure 5.4: Excitation spectra of $Gd_{9.33-x-y}Eu_xDy_y(SiO_4)_6O_2$ materials recorded at λ_{emi}=476 nm and normalised to the 273 nm peak. For a) x=0.002 and b) x=0.005. Red arrows show the Gd^{3+} excitation indirectly populating the Dy^{3+} and black arrows the direct Dy^{3+} excitation.

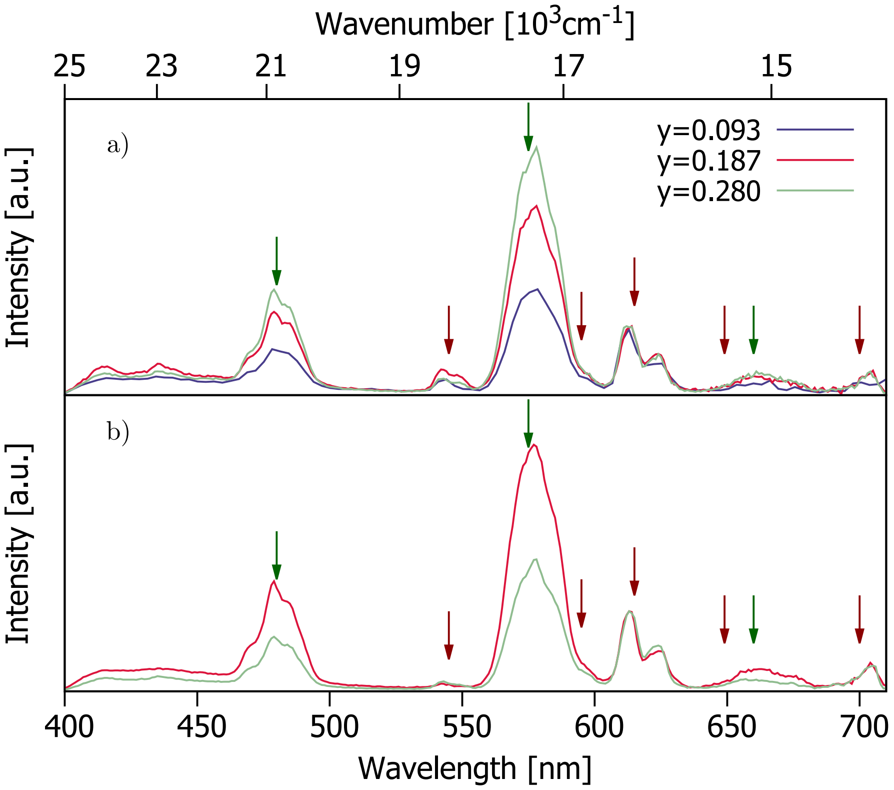

Figure 5.5: Emission spectra of $Gd_{9.33-x-y}Eu_xDy_y(SiO_4)_6O_2$ materials recorded at 273 nm and normalised in accordance with the Eu^{3+} peak in the 600 nm-640 nm range. For a) x=0.002 and b) x=0.005. Green arrows and red arrows show the Dy^{3+} emission and the Eu^{3+} emission respectively.

The emission spectra for the Dy^{3+}, Eu^{3+} co-doped series were recorded on excitation at 273 nm (Figure 5.5). The emission peaks observed are in the blue, yellow and red regions, corresponding to the $^4F_{9/2} \rightarrow {}^6H_{15/2}$, $^4F_{9/2} \rightarrow {}^6H_{13/2}$ and $^4F_{9/2} \rightarrow {}^6H_{11/2}$ transitions of Dy^{3+} (green arrows in Figure 5.5) and the $^5D_1 \rightarrow {}^7F_1$, $^5D_0 \rightarrow {}^7F_1$, $^5D_0 \rightarrow {}^7F_2$, $^5D_0 \rightarrow {}^7F_3$ and $^5D_0 \rightarrow {}^7F_4$ transitions of Eu^{3+} (red arrows in Figure 5.5).[28] Table 5.4 summarises the emission bands in the visible region for the Eu^{3+} ions.

Transition	Wavelength (nm)
$^5D_1 \rightarrow {}^7F_1$	545
$^5D_0 \rightarrow {}^7F_1$	585
$^5D_0 \rightarrow {}^7F_2$	615
$^5D_0 \rightarrow {}^7F_3$	655
$^5D_0 \rightarrow {}^7F_4$	700

Table 5.4: Emission bands present in the $Gd_{9.33-x-y}Eu_xB_y(SiO_4)_6O_2$ (B = Dy and Tb) phosphor series.

The colour coordinates obtained for this series of samples are shown in Figure 5.6a (with a more detailed zoom shown in Figure 5.6b). The compositions x=0.009 and x=0.019 are primarily red/orange emitters lacking a sufficient blue component for white light. The compositions which are the closest to the white point (the circle at x = y = 0.33 in Figure 5.6b) contain x=0.002 and y=0.093 or y=0.187 (upward-pointing triangles in Figure 5.6b). Table 5.5 shows the colour coordinates of the phosphors that lie within the white-light region of the 1931 CIE diagram.

Eu content	Dy content	Colour coordinates		CCT(K)
		x	y	
0.002	0.093	0.385	0.337	3538
	0.187	0.378	0.347	3830
	0.280	0.392	0.367	3621
0.005	0.187	0.393	0.360	3529
	0.280	0.412	0.355	3019

Table 5.5: CIE coordinates and CCTs for the best-performing $\mathrm{Gd_{9.33-x-y}Eu_xDy_y(SiO_4)_6O_2}$.

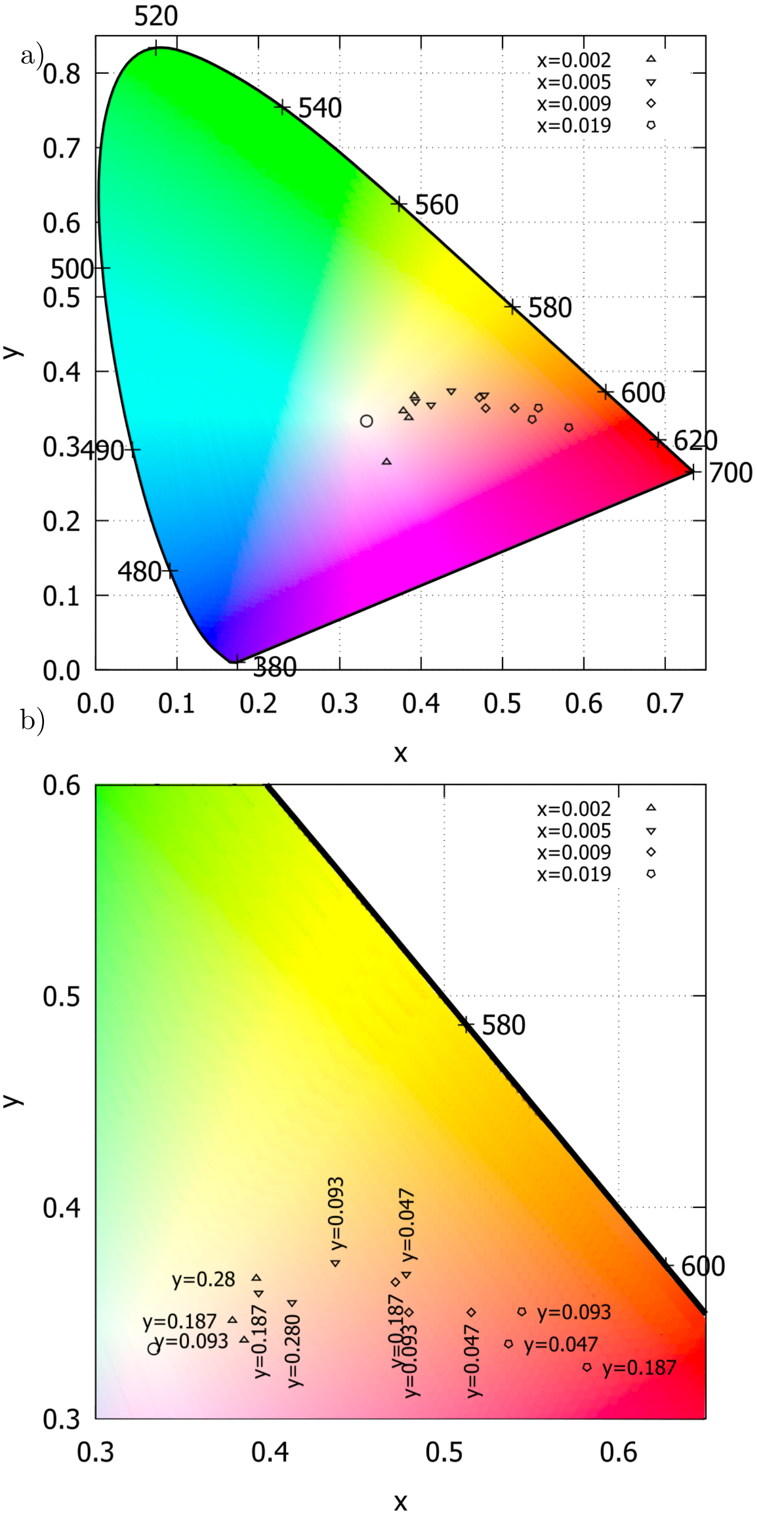

Figure 5.6: a) 1931 CIE chromaticity diagram showing the chromaticity coordinates at $\lambda_{exc} = 273$ nm for the Dy-doped host. b) Expansion of the pertinent CIE region for the hosts discussed.

The CCT values for these phosphors range from 3020 to 3830 K, showing that they emit warm hues inside the white region. Their properties suggest that they could be improved further by enhancing their blue/yellow emission ratio. Since Tb^{3+} ions emit in the blue and green,[29–32] it was decided to introduce them to prepare better-performing phosphors (see section 5.3.3).

5.3.2.3 Energy transfer, quenching and temporal decay

Figure 5.5a shows the variation in the relative intensity of Dy^{3+} and Eu^{3+} emissions with increasing Dy^{3+} content for a fixed Eu^{3+} content of x=0.002. The spectra are normalised to the $\Delta J = 2$ transition of Eu^{3+} at 615 nm. As might be expected, the Dy^{3+} emission is relatively more intense than the Eu^{3+} emission at higher Dy^{3+} content. On the other hand, in the x=0.005 samples there was proportionately less Dy^{3+} emission at the y=0.280 doping level than at the y=0.187, suggesting that a Dy^{3+} to Eu^{3+} energy transfer may be occurring. Excitation spectra registered at λ_{emi} = 615 nm, where only Eu^{3+} (but not Dy^{3+}) emits, show weak but defined features at 350 and 360 nm, well matching the excitation bands of Dy^{3+} (shown in Figure 5.7). This observation supports the notion that $Dy^{3+} \rightarrow Eu^{3+}$ energy transfer does occur.

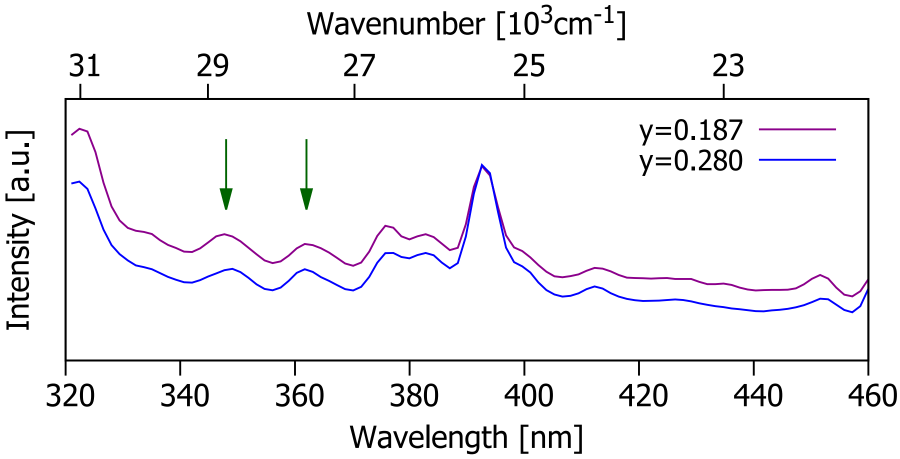

Figure 5.7: Excitation spectra of $Gd_{9.325-y}Eu_{0.005}Dy_y(SiO_4)_6O_2$ materials recorded at λ_{emi} =615 nm and normalised to the 390 nm peak. Green arrows show the Dy^{3+} excitation bands.

For each of the five materials in Table 5.6, the temporal decay of the Dy^{3+} emission was recorded for the $^4F_{9/2} \rightarrow ^6H_{15/2}$ and $^4F_{9/2} \rightarrow ^6H_{13/2}$ transitions under pulsed excitation at λ_{exc} = 375 nm, together with the Eu^{3+} emission for the $^5D_0 \rightarrow ^7F_2$ transition (Figure 5.8). The curves were fitted to an exponential decay of

$$I(t) = I_0 exp(-t/\tau), \quad (5.1)$$

where I_0 is the initial intensity, I(t) the intensity at time t, and τ is the lifetime. The variation in τ with the Dy^{3+} content is shown in Figure 5.9.

x	y	**Dysprosium emission**		**Europium emission**
		$^4F_{9/2} \rightarrow ^6H_{15/2}$ τ(ms)	$^4F_{9/2} \rightarrow ^6H_{13/2}$ τ(ms)	$^5D_0 \rightarrow ^7F_2$ τ(ms)
0.002	0.093	0.505(3)	0.479(3)	0.731(6)
	0.187	0.451(3)	0.429(2)	0.627(7)
	0.280	0.388(3)	0.370(3)	0.572(7)
0.005	0.187	0.445(3)	0.426(3)	0.662(7)
	0.280	0.379(3)	0.365(3)	0.700(7)

Table 5.6: Lifetimes obtained for the best-performing $Gd_{9.33-x-y}Eu_xDy_y(SiO_4)_6O_2$ phosphors recorded after excitation at 375 nm.

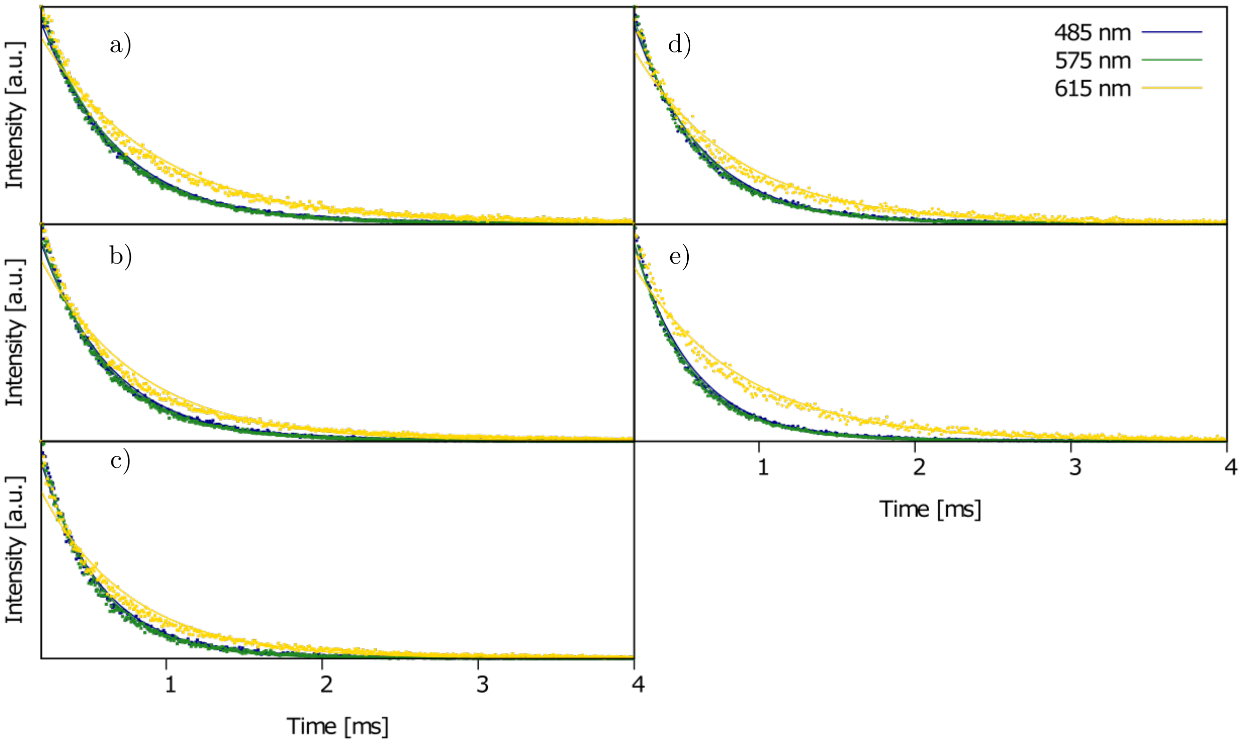

Figure 5.8: Decay curves fitted (solid line) of the experimental data (dots) of $^4F_{9/2} \rightarrow ^6H_{15/2}$ transition at 485 nm, $^4F_{9/2} \rightarrow ^6H_{13/2}$ transition at 575 nm and $^5D_0 \rightarrow ^7F_2$ transition at 615 nm for $Gd_{9.33-x-y}Eu_xDy_y(SiO_4)_6O_2$ phosphors with x=0.002: a) y=0.093, b) y=0.187 and c) y=0.280, and x=0.005: d) y=0.187 and e) y=0.280, recorded after excitation at 375 nm.

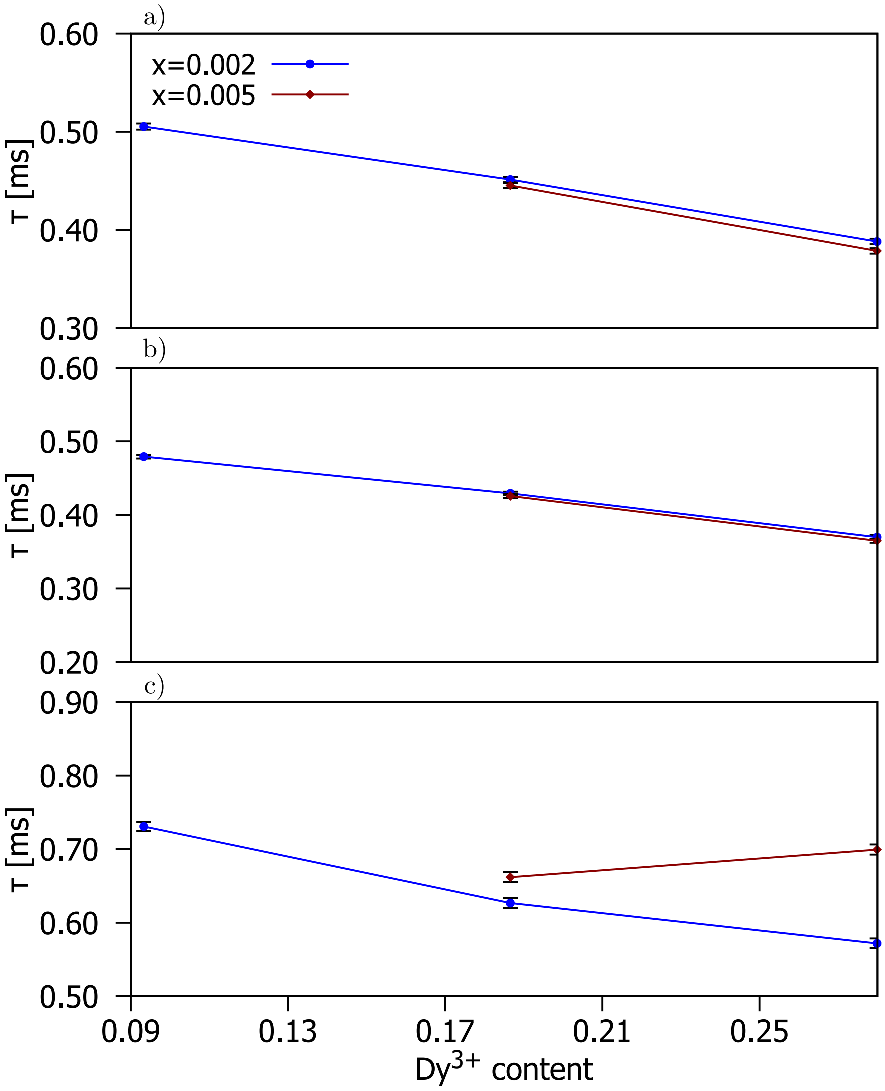

Figure 5.9: Average lifetime values dependence Dy3+ content for a) $^4F_{9/2} \rightarrow ^6H_{15/2}$ transition (485 nm), b) $^4F_{9/2} \rightarrow ^6H_{13/2}$ transition (575 nm) and c) $^5D_0 \rightarrow ^7F_2$ transition (615 nm).

From the lifetime values in Table 5.6, it can be seen that there is little variation in the Dy^{3+} lifetime, either with the Dy^{3+} doping level or with the Eu^{3+} content. The Dy^{3+} lifetimes in the samples with y=0.280 are a little shorter, below 0.4 ms, which could reflect energy transfer to Eu^{3+}, but the difference is larger than the experimental uncertainty on the value. Given the much higher Dy^{3+} relative to Eu^{3+} content, most Dy^{3+} ions will be isolated from Eu^{3+} in the structure, and so the observed Dy^{3+} decay will be dominated by emission from those ions that are not undergoing energy transfer to Eu^{3+}. Although back energy transfer from the excited Eu^{3+} ions to repopulate the Dy^{3+} excited state cannot be completely ruled out, the large energy gap of about 3800 cm^{-1} between the Eu^{3+} $^5D_0$ and the Dy^{3+} $^4F_{9/2}$ (compared to kT = 205 cm^{-1} at 295 K) renders it highly unlikely. The corresponding gap for the $^5D_1$ is smaller (around 2200 cm^{-1}) but the lifetime of this state will be shorter and hence back transfer similarly unlikely.

What is most striking, however, is that the Eu^{3+} lifetimes shown in Table 5.6 are all unequivocally shorter by a factor of about 2 than the Eu^{3+} lifetimes of the Tb,Eu co-doped phosphors (see Table 5.9). Apparently the $^5D_0$ excited state of the Eu^{3+} is quenched by Dy^{3+} ions. The much higher concentration of Dy^{3+} means that a high proportion of the Eu^{3+} ions are within close proximity to a Dy^{3+} ion, which can act as an acceptor of excited state energy through population of the ^6H_J (J =

13/2 – 5/2) and ^6F_J (J = 11/2 – 1/2) levels. The occurrence of such a process, hitherto little noted in the literature,[33, 34] suggests that the combination of Eu^{3+} and Dy^{3+} ions will be compromised and may not provide optimal emission efficiencies.

5.3.3 Phosphors incorporating terbium and europium: $Gd_{9.33}(SiO_4)_6O_2$:Tb^{3+}, Eu^{3+}

5.3.3.1 Structure characterisation

In order to further improve its properties, $Gd_{9.33}(SiO_4)_6O_2$ was co-doped with a combination of Tb^{3+} and Eu^{3+} ions. About 20 samples in total were prepared and characterised with different Eu^{3+} and Tb^{3+} contents, and the eight best-performing compositions with colour coordinates near to white light are discussed here. Their Rietveld fits and unit cell parameters are shown in Figure 5.10 and Table 5.7 respectively.

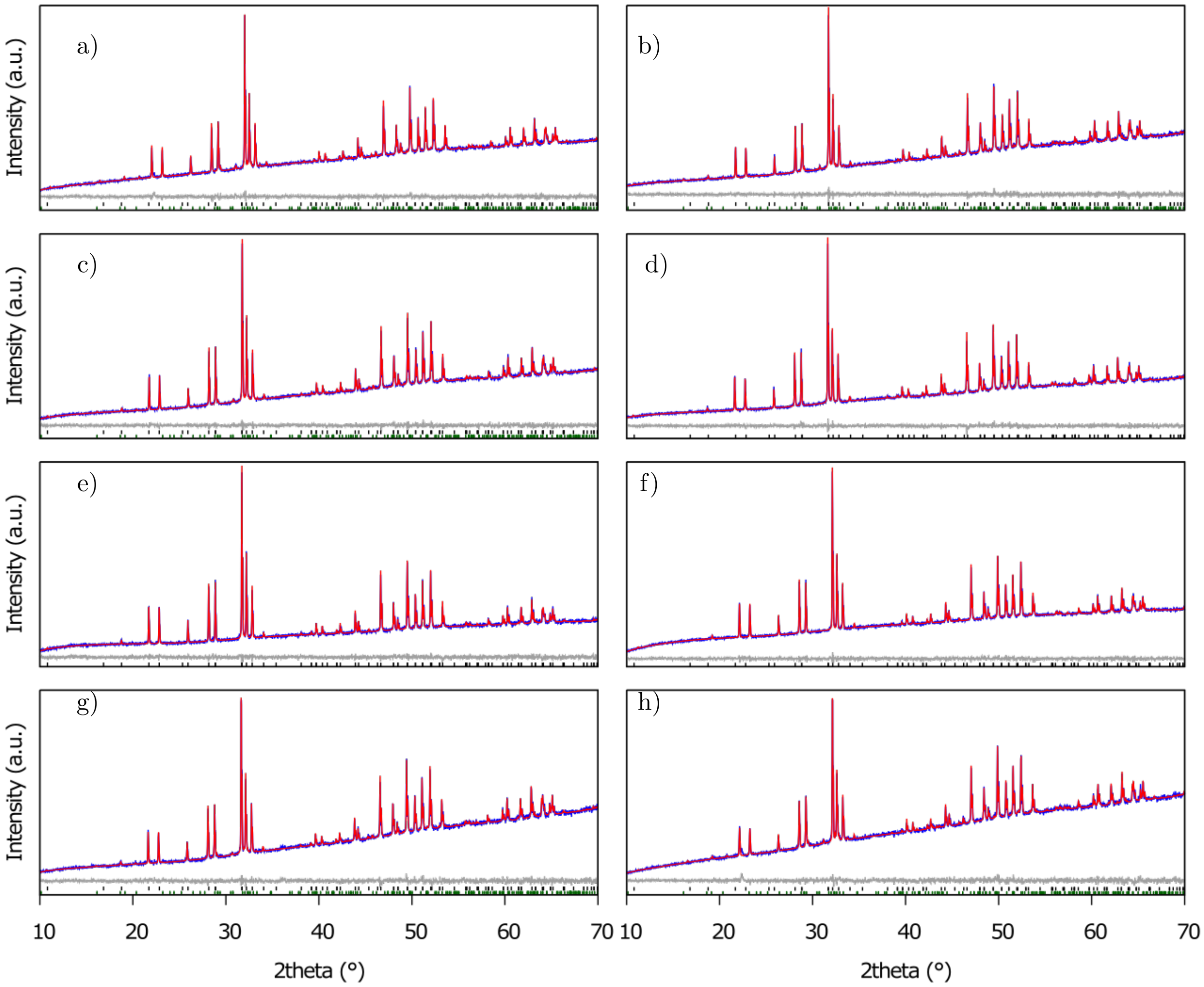

Figure 5.10: Rietveld refinements of laboratory data for $Gd_{9.33-x-y}Eu_yTb_y(SiO_4)_6O_2$. x=0.002: a) y=0.028, b) 0.037, c) 0.047, x=0.003: d) y=0.028, e) y=0.037, f) y=0.047, x=0.005: g) y=0.028, h) y=0.047.

x	y	a(Å)	b(Å)	V(Å^3)	R$_{wp}$ (%)	Gd_2SiO_5
0.002	0.028	9.44799(9)	6.87611(10)	531.56(1)	2.41	8.0(6) wt%
	0.037	9.43676(9)	6.87292(9)	530.05(1)	2.24	6.0(6) wt%
	0.047	9.44057(8)	6.87058(9)	530.30(1)	2.26	5.1(5) wt%
0.003	0.028	9.44201(8)	6.86741(8)	530.21(1)	2.09	n/a
	0.037	9.44195(9)	6.86903(9)	530.34(1)	2.31	n/a
	0.047	9.45422(9)	6.87583(9)	532.24(1)	2.23	n/a
0.005	0.047	9.439(1)	6.8697(1)	530.06(1)	2.23	4.4(7) wt%
	0.047	9.4505(1)	6.8808(1)	532.20(2)	2.49	8.3(7) wt%

Table 5.7: Unit cell parameters of the best-performing $Gd_{9.33-x-y}Eu_xTb_y(SiO_4)_6O_2$ phosphors.

5.3.3.2 Optical properties

The energy levels of pertinent excited states of Gd^{3+}, Tb^{3+} and Eu^{3+} are illustrated in Figure 5.11. The $^5D_3$ and $^5D_4$ states of Tb^{3+} can be populated indirectly via higher-lying excited states sensitised with Gd^{3+}. The Tb^{3+} $^5D_4$ state typically has four main radiative transitions to the ^7F_J (J = 6,5,4,3) manifold, of which that to $^7F_5$ is invariably the most intense. Alternatively, the Tb^{3+} $^5D_4$ state is energetically well-placed to undergo energy transfer to populate the $^5D_1$ or $^5D_0$ of nearby Eu^{3+} ions.[35]

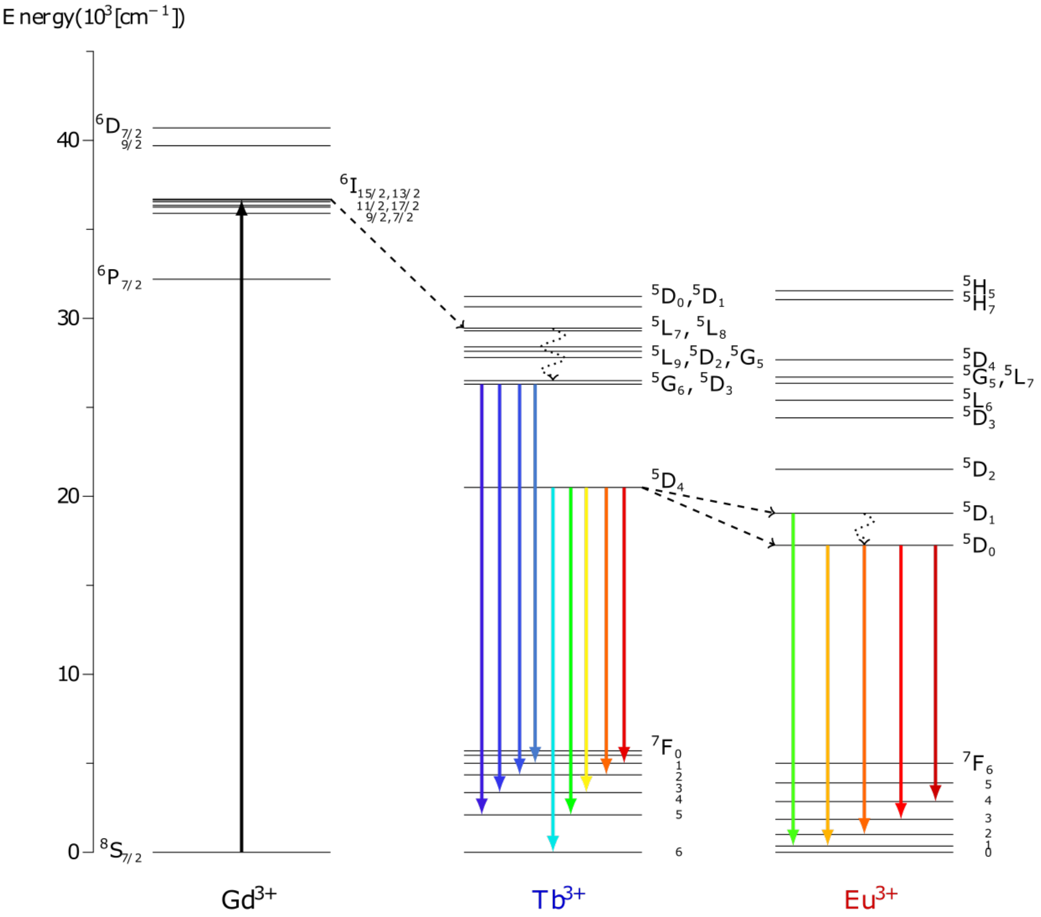

Figure 5.11: Energy-level diagrams for Gd^{3+}, Tb^{3+} and Eu^{3+} ions showing the relevant transitions in the system.

The excitation spectra registered at the emission maximum of Tb^{3+} (shown in Figure 5.12) display the $^8S_{7/2} \rightarrow {}^6I_{13/2}$ and $^8S_{7/2} \rightarrow {}^6P_{7/2}$ transitions of the Gd^{3+} at 273 nm and 312 nm, respectively, confirming the Gd-sensitised pathway to the terbium $^5D_4$ state. Direct excitation of Tb^{3+} is, of course, also possible, and accounts for the envelope of peaks in the 340-380 nm region.

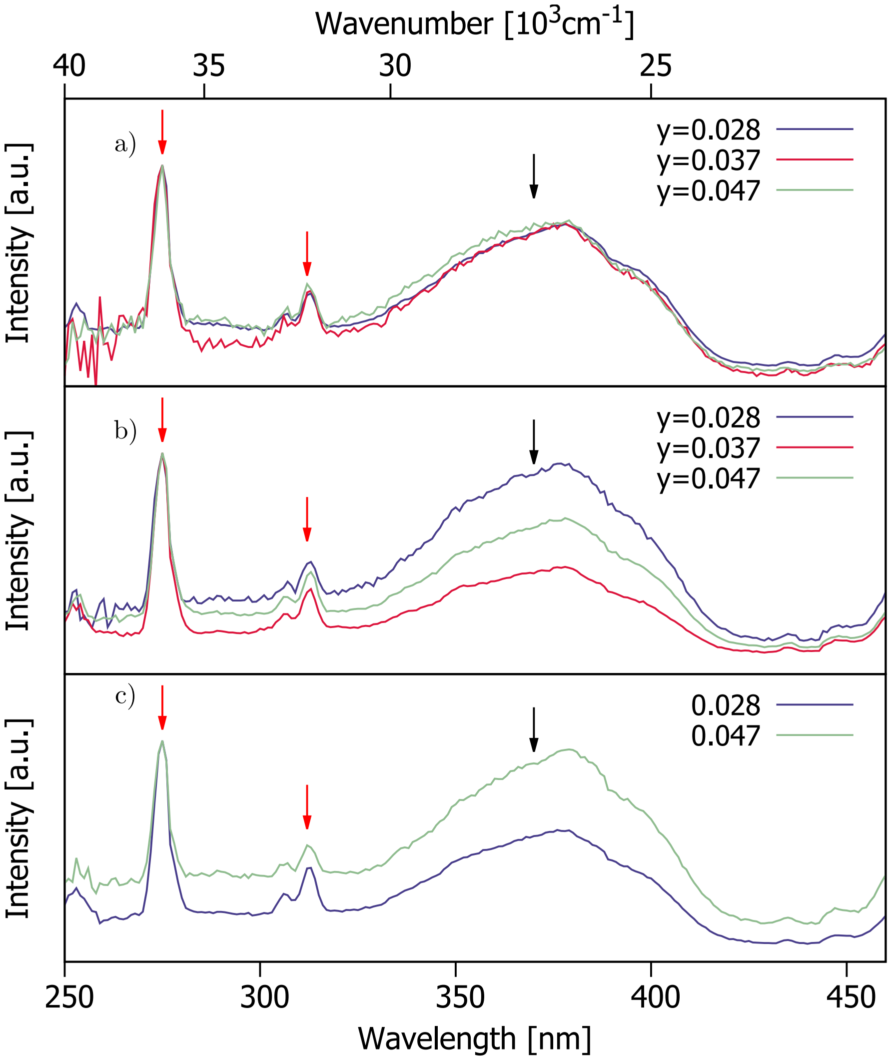

Figure 5.12: Excitation spectra of $Gd_{9.33-x-y}Eu_xTb_y(SiO_4)_6O_2$ materials recorded at $\lambda_{emi} = 476$ nm and normalised to the 273 nm peak. a) x=0.002, b) x=0.003 and c) x=0.005. Red arrows show the Gd^{3+} energy transfer and the black arrow the Tb^{3+} direct excitation.

The emission spectra recorded on excitation at 273 nm (Figure 5.13) show bands throughout the spectral region. The Tb^{3+} emissions (marked with green arrows) can be seen as intense peaks at 413 and 436 nm ($^5D_3 \rightarrow {}^7F_5$ and $^5D_3 \rightarrow {}^7F_4$ respectively), an envelope of bands in the 456-488 nm region ($^5D_3 \rightarrow {}^7F_3$, $^5D_3 \rightarrow {}^7F_2$ and $^5D_4 \rightarrow {}^7F_6$), a high-intensity peak at 543 nm ($^5D_4 \rightarrow {}^7F_5$), weak features at 583 nm ($^5D_4 \rightarrow {}^7F_4$) and a peak at 619 nm ($^5D_4 \rightarrow {}^7F_3$). The peaks originating from the Eu^{3+} ion emissions (marked with red arrows) are found at 565 nm, 615 nm, 650 nm and 695 nm, corresponding to the $^5D_1 \rightarrow {}^7F_1$, $^5D_0 \rightarrow {}^7F_2$, $^5D_0 \rightarrow {}^7F_3$ and $^5D_0 \rightarrow {}^7F_4$ transitions respectively. Table 4.5 and Table 5.4 summarises the emission bands in the visible region for the Tb^{3+} and Eu^{3+} ions.

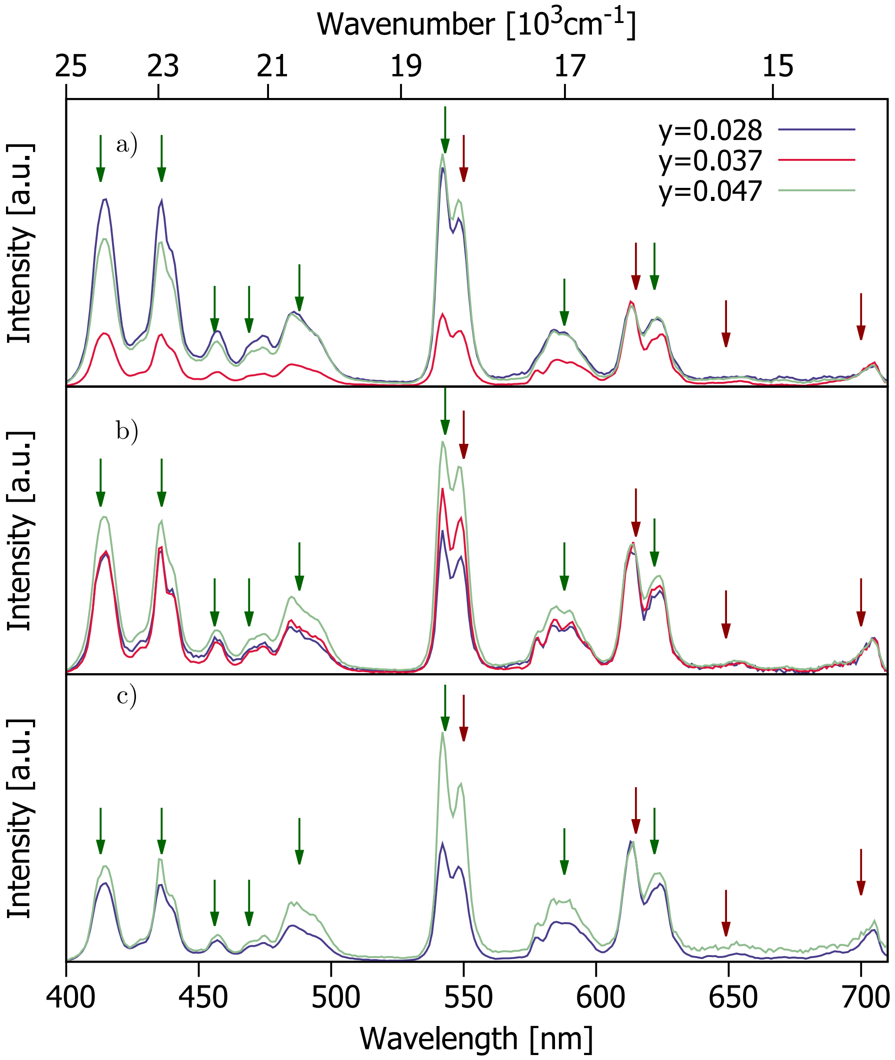

Figure 5.13: Emission spectra of $Gd_{9.33-x-y}Eu_xTb_y(SiO_4)_6O_2$ recorded at λ_{exc} = 273 nm and normalised to the Eu^{3+} $\Delta J = 2$ band. a) x=0.002, b) x=0.003 and c) x=0.005. Green and red arrows show the Tb^{3+} and Eu^{3+} emission bands respectively.

The colour coordinates obtained for the phosphors belonging to the $Gd_{9.33-x-y}Eu_xTb_y(SiO_4)_6O_2$ series are shown in Figure 5.14 and the CIE and CCT data are summarised in Table 5.8.

Eu content	Tb content	Colour coordinates		CCT(K)
		x	y	
0.002	0.028	0.301	0.302	7600
	0.037	0.387	0.328	3370
	0.047	0.308	0.331	6740
0.003	0.028	0.360	0.315	4210
	0.037	0.363	0.344	4300
	0.047	0.340	0.341	5190
0.005	0.028	0.388	0.341	3500
	0.047	0.354	0.350	4690

Table 5.8: The CIE coordinates and CCTs of the best-performing $Gd_{9.33-x-y}Eu_xTb_y(SiO_4)_6O_2$ phosphors.

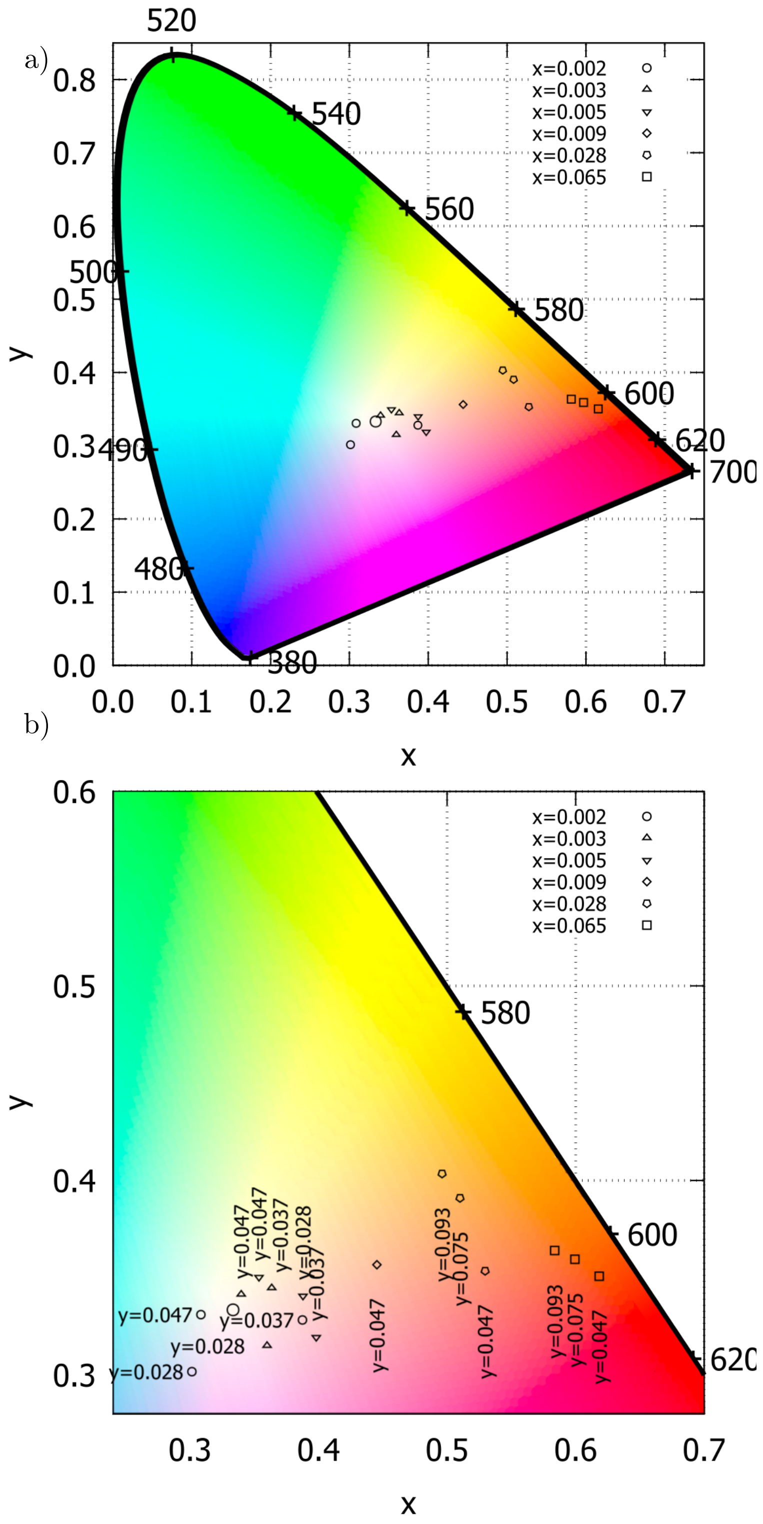

Figure 5.14: a) 1931 CIE chromaticity diagram showing the chromaticity coordinates at $\lambda_{exc} = 273$ nm of the Tb-doped host. b) Detailed diagram of the colour coordinates.

As can be seen from Table 5.8, the two best-performing phosphors are those containing y=0.047 together with x=0.003 and x=0.002, with colour coordinates very close to the ideal WL point: (0.340, 0.341) and (0.308, 0.331) respectively. The correlated colour temperatures of about 5200 K and 6700 K respectively are in the desirable warm white light region.

5.3.3.3 Energy transfer, quenching and temporal decay

Excitation spectra registered at $\lambda_{emi} = 615$ nm, where only Eu^{3+} (but not Tb^{3+}) emits, show weak but defined features at 350 and 362 nm, matching the excitation bands of Tb^{3+} (shown in Figure 5.15) well and suggesting the occurrence of at least some Tb^{3+} to Eu^{3+} energy transfer. Figure 5.16 shows the fitted decay curves for the Tb^{3+} ($^5D_4 \rightarrow {}^7F_5$) and Eu^{3+} ($^5D_0 \rightarrow {}^7F_2$) transitions recorded under pulsed excitation at $\lambda_{exc} = 375$ nm. The decay curves of these transitions can be fitted convincingly to a single exponential decay. The Tb^{3+} and Eu^{3+} lifetime values thus obtained are compiled in Table 5.9 and their variation with the Tb^{3+} content is shown in Figure 5.17.

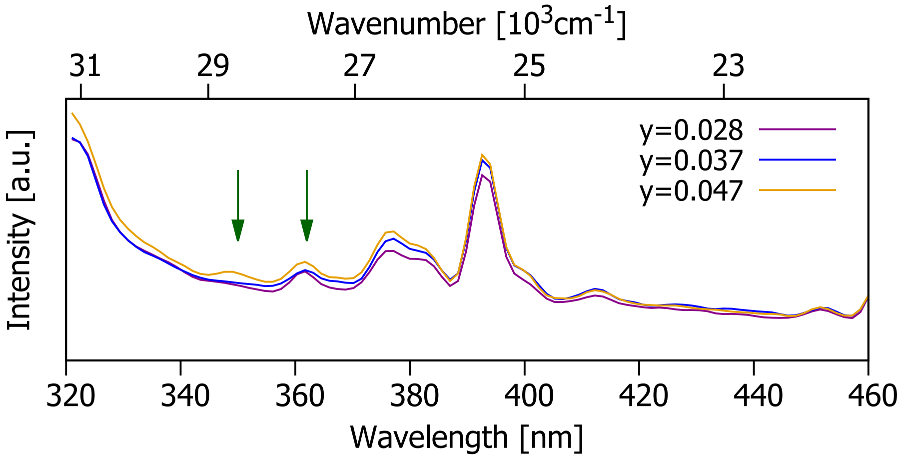

Figure 5.15: Excitation spectra of $Gd_{9.33-x-y}Eu_{0.003}Tb_y(SiO_4)_6O_2$ materials recorded at λ_{emi} =615 nm and normalised to the 390 nm peak. Green arrows show the Tb^{3+} excitation bands.

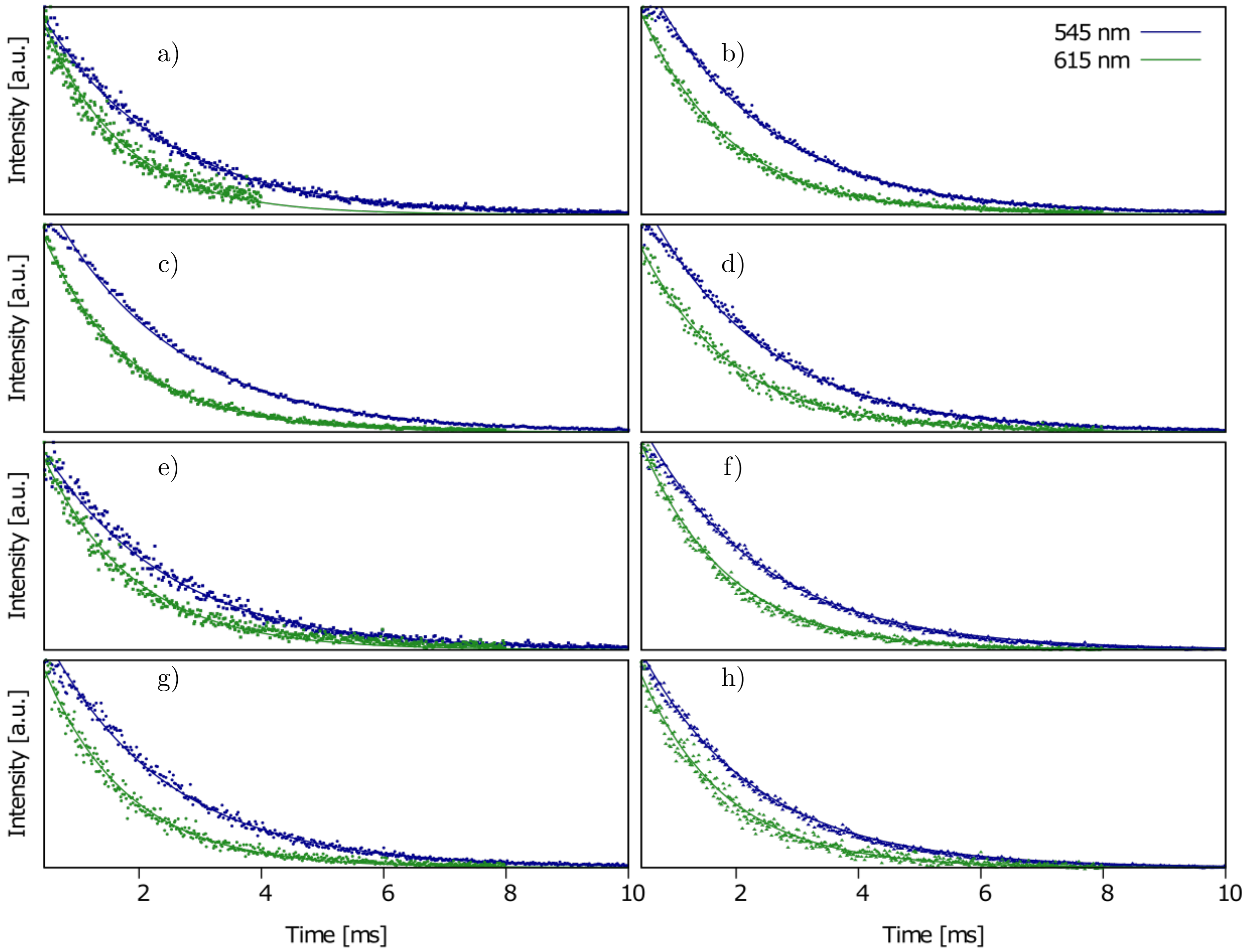

Figure 5.16: Fitted decay curves (solid line) of the experimental data (dots) of the $^5D_4 \rightarrow ^7F_5$ transition at 545 nm and the $^5D_0 \rightarrow ^7F_2$ transition at 615 nm for $Gd_{9.33-x-y}Eu_xTb_y(SiO_4)_6O_2$ recorded after excitation at 375 nm. For x=0.002: a) y=0.028, b) y=0.037 and c) y=0.047, x=0.003: d) y=0.028, e) y=0.037 and f) y=0.047, and x=0.005: g) y=0.028, h) y=0.047.

x	y	**Terbium emission**	**Europium emission**
		$^5D_4 \rightarrow ^7F_5$	$^5D_0 \rightarrow ^7F_2$
		τ(ms)	τ(ms)
0.002	0.028	1.98(1)	1.28(1)
	0.037	2.05(1)	1.402(6)
	0.047	2.05(2)	1.46(1)
0.003	0.028	1.97(1)	1.365(10)
	0.037	1.967(6)	1.449(7)
	0.047	1.953(9)	1.496(10)
0.005	0.028	1.975(6)	1.397(7)
	0.047	1.883(6)	1.39(1)

Table 5.9: Lifetime values obtained for the best-performing $Gd_{9.33-x-y}Eu_xTb_y(SiO_4)_6O_2$ phosphors recorded after excitation at 375 nm.

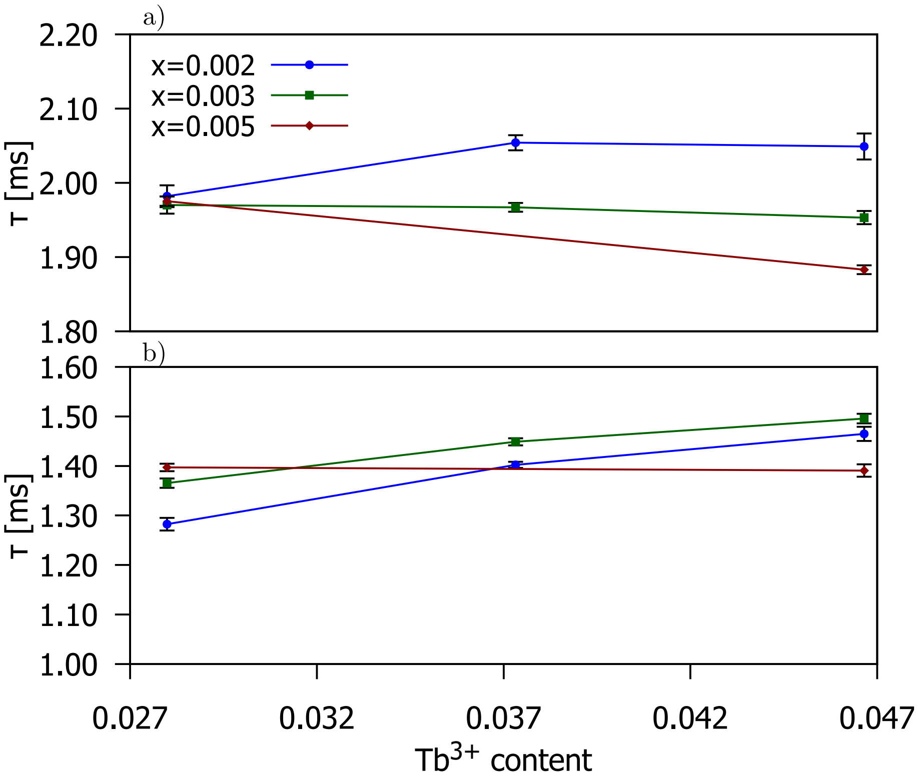

Figure 5.17: Variation in the lifetime values with the Tb^{3+} content for a) the $^5D_4 \rightarrow ^7F_5$ transition (545 nm), b) the $^5D_0 \rightarrow ^7F_2$ transition (615 nm).

There is no clear-cut evidence of significant variation in lifetimes with composition. At the low doping levels involved, the emission is probably dominated by Eu^{3+} and Tb^{3+} ions that are well isolated from one another by the host. The occurrence of Tb^{3+} to Eu^{3+} energy transfer would be expected to decrease the Tb^{3+} lifetime, but as most Tb^{3+} ions will not have nearby Eu^{3+} ions the observed emission decay appears unchanged on increasing from x=0.002 to x=0.005. It can be noted that the Eu^{3+} lifetimes are of the order of 1.5 ms, *i.e.* around double the value in Dy^{3+},Eu^{3+} co-doped systems. Terbium ions clearly do not act as quenchers of Eu^{3+} emission, in contrast to the Dy^{3+} ions in the previous systems, and this can be rationalised in terms of the poor match of the Eu^{3+} $^5D_0$ excited state energy with that of the Tb^{3+} ^7F_J levels.

5.4 Conclusions

Two series of new apatite-type silicate single-phase white-emitting phosphors were synthesised and characterised with powder x-ray diffraction and optical measurements. The $Gd_{9.33}(SiO_4)_6O_2$ host was systematically doped with Dy^{3+}, Tb^{3+} and Eu^{3+} to tune the emission to the white light region. The 1931 CIE colour coordinates were calculated for each series and the details of the phosphors that emit nearest to white light point have been given. The emission decay curves were also measured and fitted to determine the lifetimes and the concentration quenching effects in the phosphors.

Eight new phosphors came nearest to WL point. In terms of published work, the apatite $Gd_{9.33-x-y}Eu_xTb_y(SiO_4)_6O_2$, with x=0.003 and y=0.047, shows the best properties than any other apatite-based silicate phosphor, with colour coordinates of (0.340 0.341). The data show that a range of materials in the white light region can be accessed with CCT values ranging from 'warm white' (< 3500 K) through neutral (3500–4500 K) to 'daylight' > 5500 K). A comparison of the Eu^{3+} lifetimes in the Dy, Eu co-doped phosphors with those in the Tb, Eu-containing materials suggests quenching of the $^5D_0$ excited state of Eu^{3+} by the Dy^{3+} ions. This implies that the combination of Eu^{3+} and Dy^{3+} ions may not provide optimal efficiencies in phosphors, and that the combination of Eu^{3+} and Tb^{3+} is likely to be superior in optimising the emission properties.

5.5 Note

The work presented in this chapter was published in Journal of Materials Chemistry C:

Rodríguez-García, M. M.; Williams, J. A. G.; Evans, I. R., Single-phase white-emitting phosphors based on apatite-type gadolinium silicate, $Gd_{9.33}(SiO_4)_6O_2$ doped with Dy^{3+}, Eu^{3+} and Tb^{3+}. Journal of Materials Chemistry C 2019, 7 (25), 7779-7787.

5.6 References

[1] Ye, S., Xiao, F., Pan, Y.X., Ma, Y.Y., and Zhang, Q.Y. *Materials Science & Engineering R-Reports*, 71(1), 2010.

[2] Xia, Z.G., Xu, Z.H., Chen, M.Y., and Liu, Q.L. *Dalton Transactions*, 45(28), 2016.

[3] McKittrick, J., Hannah, M.E., Piquette, A., Han, J.K., Choi, J.I., Anc, M., Galvez, M., Lugauer, H., Talbot, J.B., and Mishra, K.C. *Ecs Journal of Solid State Science and Technology*, 2(2), 2013.

[4] Setlur, A., Lyons, R., Murphy, J., Kumar, N.P., and Kishore, M.S. *ECS Journal of Solid State Science and Technology*, 2(2), 2013.

[5] George, N.C., Denault, K.A., and Seshadri, R. *Annual Review of Materials Research*, 43, 2013.

[6] Schubert, E.F. and Kim, J.K. *Science*, 308(5726), 2005.

[7] Khan, M.A., Maeda, N., Jo, M., Akamatsu, Y., Tanabe, R., Yamada, Y., and Hirayama, H. *Journal of Materials Chemistry C*, 7(1), 2019.

[8] Kojima, K., Nagasawa, Y., Hirano, A., Ippommatsu, M., Honda, Y., Amano, H., Akasaki, I., and Chichibu, S.F. *Applied Physics Letters*, 114(1), 2019.

[9] Maeda, N., Jo, M., and Hirayama, H. *physica status solidi (a)*, 215(8), 2018.

[10] Takano, T., Mino, T., Sakai, J., Noguchi, N., Tsubaki, K., and Hirayama, H. *Applied Physics Express*, 10(3), 2017.

[11] Latshaw, A.M., Hughey, K.D., Smith, M.D., Yeon, J., and zur Loye, H.C. *Inorganic Chemistry*, 54(3), 2015.

[12] Sun, Z.H., Wang, M.Q., Yang, Z., Liu, K.P., and Zhu, F.Y. *Journal of Solid State Chemistry*, 239, 2016.

[13] Zhou, W.J., Pan, F.J., Zhou, L., Hou, D.J., Huang, Y., Tao, Y., and Liang, H.B. *Inorganic Chemistry*, 55(20), 2016.

[14] Brgoch, J., Borg, C.K.H., Denault, K.A., Mikhailovsky, A., DenBaars, S.P., and Seshadri, R. *Inorganic Chemistry*, 52(14), 2013.

[15] Sokolnicki, J. and Zych, E. *Journal of Luminescence*, 158, 2015.

[16] Liu, Y.W., Wang, Z.J., Zhong, J.P., Pan, F.J., Liang, H.B., and Xiao, Z.G. *Materials Letters*, 129, 2014.

[17] Chambers, M.D., Rousseve, P.A., and Clarke, D.R. *Journal of Luminescence*, 129(3), 2009.

[18] Liu, Y.F., Zhang, X., Hao, Z.D., Wang, X.J., and Zhang, J.H. *Chemical Communications*, 47(38), 2011.

[19] Xie, M.B., Zhu, G.X., Li, D.Y., and Pan, R.K. *Journal of Luminescence*, 181, 2017.

[20] Xie, M.B., Zhu, G.X., and Pan, R.K. *Journal of Physics and Chemistry of Solids*, 102, 2017.

[21] An, T., Baikie, T., Wei, F., Pramana, S.S., Schreyer, M.K., Piltz, R.O., Shin, J.F., Wei, J., Slater, P.R., and White, T.J. *Chemistry of Materials*, 25(7), 2013.

[22] Pavitra, E., Raju, G.S.R., and Yu, J.S. *Ceramics International*, 39(6):6319–6324, 2013.

[23] Xu, D.D., Zhou, W., Zhang, Z., Li, S.J., and Wang, X.R. *Optical Materials*, 89, 2019.

[24] Fang, Y., Tian, X., Liu, J., Zhang, Y., Liu, Y., Zhao, G., Zou, J., Vainos, N., and Hou, J. *Journal of Luminescence*, 207, 2019.

[25] de Oliveira, A.S., da Silva, B.H.S.T., Góes, M.S., Cuin, A., de Souza, H., de Oliveira, L.F.C., de Souza, G.P., Schiavon, M.A., and Ferrari, J.L. *Journal of Luminescence*, 227, 2020.

[26] Stephens, P. *Journal of Applied Crystallography*, 32(2), 1999.

[27] Coelho, A.A., Evans, J.S.O., Evans, I.R., Kern, A., and Parsons, S. *Powder Diffraction*, 26(4), 2011.

[28] Aull, B.F. and Jenssen, H.P. *Physical Review B*, 34(10), 1986.

[29] Chan, T.S., Liu, Y.M., and Liu, R.S. *Journal of Combinatorial Chemistry*, 10(6), 2008.

[30] Gameiro, C.G., da Silva, E.F., Alves, S., de Sa, G.F., and Santa-Cruz, P.A. *Journal of Alloys and Compounds*, 323, 2001.

[31] Lai, H., Bao, A., Yang, Y.M., Tao, Y.C., Yang, H., Zhang, Y., and Han, L.L. *Journal of Physical Chemistry C*, 112(1), 2008.

[32] Vandongen, A.M.A. *Journal of Non-Crystalline Solids*, 139(3), 1992.

[33] Kaczmarek, A.M., Ndagsi, D., and Van Deun, R. *Dalton Transactions*, 45(41), 2016.

[34] Dudar', S.S., Ermolaev, V.L., and Shablya, A.V. *Optics and Spectroscopy*, 102(4), 2007.

[35] Bao, G., Wong, K.L., Jin, D., and Tanner, P.A. *Light: Science & Applications*, 7(1), 2018.

6 Narrow-band red-emitting phosphors based on Eu^{3+}-doped $Gd_{9.33}(SiO_4)_6O_2$

6.1 Introduction

Traditional lighting is being replaced with more efficient and reliable devices such as white light emitting diodes (WLEDs). There is much interest in developing efficient solid-state white lighting to reduce world energy consumption. This involves several challenges, one of which is to produce red phosphors with high chemical and thermal stability, which at the same time have high quantum yield, hence are energy conversion efficient.

The colour-rendering index (CRI) is a measure of the truthfulness of the colour of an object under a certain light, where the maximum value is 100 for sunlight. The problem is that the higher the CRI, the lower the luminous efficacy, as the human visual response peaks at around 555 nm. For white lighting, the best possible balance between lighting quality and efficiency is a CRI of 90, where the luminous efficacy of radiation (LER) is 408 lm/W. Considering a linewidth of 1 nm, the centre emission wavelength for the red component that maximises efficiency is at 614 nm.[1–3]

For the yellow, green and blue components, where the human eye response is strong, narrow emission linewidths are not critical for efficiency. The blue component makes a low contribution to white light so it is not critical. On the other hand, the red component linewidth is critical and must be narrower than 20 nm in order to minimise spillover into deeper red, where the human visual response drops. The luminous efficacy percentage decreases with the linewidth by roughly 0.15%/nm.[4]

Trivalent rare earth elements are known to have emission bands in the visible spectrum. Eu^{3+} is one example and its hypersensitive $^5D_0 \rightarrow {}^7F_2$ (at around 619 nm) *f*-*f* transition is used to obtain emission at about 617 nm. The observed emission lines of Eu^{3+} correspond to its intraconfigurational transitions in the $[Xe]4f^6$ electron configuration. 119 ^{2S+1}L energy levels arise from this configuration due to Coulomb interaction between electrons. Spin-orbit coupling causes the energy levels to split into 295 J-levels, which split further into sublevels when subjected to a crystal field or any electric field. In the absence of a crystal field, each energy level consists of 2J+1 sublevels.[5] Of the seven possible $^5D_0 \rightarrow {}^7F_J$ transitions, $^5D_0 \rightarrow {}^7F_1$ (at around 593 nm) is the only transition with magnetic dipole character (parity-allowed). It is a transition allowed by the Laporte selection rule and has a weaker emission than the remaining six transitions of electric dipole character (parity-forbidden).[6] An overview of these transitions is given in Table 6.1.[5]

Transition	Dipole character	Range (nm)	Characteristic
$^5D_0 \rightarrow {}^7F_0$	ED	570–585	Only observed in C_n, C_{nv} and C_s
$^5D_0 \rightarrow {}^7F_1$	MD	585–600	Independent of environment
$^5D_0 \rightarrow {}^7F_2$	ED	610–630	Strongly dependent on environment
$^5D_0 \rightarrow {}^7F_3$	ED	640–660	Forbidden transition
$^5D_0 \rightarrow {}^7F_4$	ED	680–710	Intensity dependent on environment
$^5D_0 \rightarrow {}^7F_5$	ED	740–770	Forbidden transition
$^5D_0 \rightarrow {}^7F_6$	ED	810–840	Rarely measured and observed

Table 6.1: Summary of $^5D_0 \rightarrow {}^7F_J$ transitions observed in luminescence spectra of Eu^{3+}-doped phosphors.

The emission spectra of Eu^{3+} ions strongly depend on the symmetry of the site in the host lattice, which is why Eu^{3+} can be used as a spectral probe for the point symmetry of the doping site. If the Eu^{3+} is located on an inversion centre, the $^5D_0 \rightarrow {}^7F_1$ transition dominates the $^5D_0 \rightarrow {}^7F_2$ transition, resulting in bright orange luminescence.[7] $^5D_0$ level cannot be split, so the $^5D_0 \rightarrow {}^7F_J$ (J = 1, 2, 3, 4, 5, 6) transitions only depend on the ^7F_J splitting. The $^7F_0 \rightarrow {}^5D_0$ transition (at around 580 nm) can be used to determine the number of sites occupied by the Eu^{3+}. If more than one site is occupied by Eu^{3+} then the excitation and emission lines can overlap and therefore broaden. In the presence of a crystal field the 2J+1 sublevels (also called Stark sublevels) can be degenerate, depending on the point symmetry. The numbers of Stark sublevels for each value of J are given in Table 6.2.[8]

Site symmetry	Integer J						
	0	1	2	3	4	5	6
T, T_d, T_h, O, O_h	1	1	2	3	4	4	6
C_{3h}, D_{3h}, C_6, C_{6h}, C_{6v}, D_6, D_{6h}	1	2	3	5	6	7	9
C_3, S_6, C_{3v}, D_3, D_{3d}	1	2	3	5	6	7	9
C_4, S_4, C_{4h}, C_{4v}, D_4, D_{2d}, D_{4h}	1	3	4	5	7	8	10
C_1, C_S, C_2, C_{2h}, C_{2v}, D_2, D_{2h}	1	3	5	7	9	11	13

Table 6.2: Stark sublevels according to the site symmetry of the Eu^{3+} doping site.

Quantitative parameters which describe the *f*-*f* transitions of rare earth ions, such as transition probabilities, radiative lifetime, branching ratios, stimulated emission cross-section, among others, can be determined using the Judd–Ofelt analysis.[9, 10] The Eu^{3+} ion ($4f^6$ electron shell) has a very special characteristic: its magnetic dipole (MD) $^5D_0 \rightarrow {}^7F_1$ transition that has a dipole strength which is independent of the environment. Therefore, the dipole strength (D_{MD}) can be calculated and used as a reference for transitions originating from the $^5D_0$ level:[6, 11]

$$D_{MD} = 9.610^{-42} esu^2 cm^2 = 9.610^{-6} Debye^2, \tag{6.1}$$

where 1 esu = $N^{-5/2}$ cm.

The elements of the reduced matrix (U^λ) for electric dipole (ED) transitions originating from $^5D_0$ are zero, with the exception of levels $^7F_\lambda$ (λ = 2, 4, 6), where $U^2 = 0.0032$, $U^4 = 0.0023$ and $U^6 = 0.0002$.[12] The Judd-Ofelt parameters (Equation 6.2) can be calculated from the ratio of the integrated emission intensity arising from the $^5D_0 \rightarrow {}^7F_\lambda$ (λ = 2, 4, 6) and the MD $^5D_0 \rightarrow {}^7F_1$ transitions.[12]

$$\Omega_\lambda = \frac{D_{MD}\tilde{\nu}_1^3}{e^2\tilde{\nu}_\lambda^3 U^\lambda} \frac{9n_1^3}{n_\lambda(n_\lambda^2+2)^2} \frac{J_\lambda}{J_1}, \tag{6.2}$$

where Ω_λ are the Judd-Ofelt parameters, n is the refractive index, J_λ is the integrated intensity of the $^5D_0 \rightarrow {}^7F_\lambda$ transition and $\tilde{\nu}_\lambda$ is the average wavenumber of the transition to the $^7F_\lambda$ level.

The ratio of the radiative transition probabilities A_λ of the $^5D_0 \rightarrow {}^7F_\lambda$ (λ = 2, 4, 6) transitions to the A_1 of the $^5D_0 \rightarrow {}^7F_1$ can be expressed in terms of the ratio of the area S under the respective emission peaks is given by:[13]

$$\frac{A_\lambda(^5D_0 \rightarrow {}^7F_\lambda)}{A_1(^5D_0 \rightarrow {}^7F_1)} = \frac{S(^5D_0 \rightarrow {}^7F_\lambda)}{S(^5D_0 \rightarrow {}^7F_1)}, where \tag{6.3a}$$

$$A_1 = \frac{64\pi^4\tilde{\nu}_1^3}{3h} n_1^3 D_{MD}, \tag{6.3b}$$

$$A_\lambda = \frac{64\pi^4\tilde{\nu}_\lambda^3}{3h} \frac{n_\lambda(n_\lambda^2+2)^2}{9} D_{ED}^\lambda \tag{6.3c}$$

and h is the Planck constant (6.63×10^{-32} N cm).

The experimentally observed lifetime takes into account the radiative and non-radiative rates, and is obtained from the single exponential fit, Equation 6.4

$$I(t) = I_0 exp(\frac{-t}{\tau_{obs}}), \tag{6.4}$$

where I_0 is the initial intensity, I(t) the intensity at time t, and τ_{obs} is the experimentally observed lifetime.

The theoretical lifetime is obtained from the emission spectrum. The theoretical equation is an approximation of the radiative decay that can be calculated by means of the emission spectrum, as in Equation 6.5:[14]

$$\tau_{theo} = \frac{n_1^{-3}}{14.65} \frac{J_1}{J_T}, \tag{6.5}$$

where J_T is the total integrated intensity of the emission spectra. The branching ratios (Equation 6.6) can be used to predict the relative intensity of an emission originating from the $^5D_0$ level.

$$\beta_\lambda = \frac{J_\lambda}{J_T} \tag{6.6}$$

The intrinsic quantum yield, η, is the ratio of the number of photons emitted to the number of photons absorbed. This can be calculated from the direct observed lifetime and the lifetime calculated from the emission spectrum using Equation 6.7:

$$\eta = \frac{\tau_{obs}}{\tau_{exp}}. \tag{6.7}$$

In recent years, there has been significant emphasis on particularly the development of narrow-band red phosphors. Selected illustrative examples are given below and summarised in Table 6.3. Due to the nature of the $^5D_0 \rightarrow {}^7F_2$ transition, regardless of the symmetry of the doping site that Eu^{3+} is occupying there will always be splitting (as shown in Table 6.2), allowing a broadening of the emission peak and therefore making line red-emitting phosphors impossible.

Material	FWHM (nm)	λ_{emi} (nm)	Wyckoff sites (Site symmetries)	Splitting of $^5D_0 \rightarrow {}^7F_2$ emission peak
Y_2MoO_6:Eu^{3+}[15]	3	611	4e (C_2) and 8f (C_1)	5 peaks
Y_2SiO_5:Ce^{3+},Tb^{3+},Eu^{3+}[16]	5	612	8f (C_1)	5 peaks
Li_2SiN_2:Eu^{3+}[17]	7	612	8c (C_1)	5 peaks
$Sr_2(La_{1-x}Eu_x)_8(GeO_4)_6O_2$[18]	7	613	4f (C_3) and 6h (C_s)	3 and 5 peaks
$Ba_2La_{2.63}Tb_{0.15}Eu_{0.22}(SiO_4)_3F$[19]	10	616	4f (C_3) and 6h (C_s)	3 and 5 peaks
$Sr_3Gd_{0.9}Na(PO_4)_3F$:0.1 Eu^{3+}[20]	10	615	2d (C_3)	3 peaks
$Ba_2Gd_8(SiO_4)_6O_2$:Eu^{3+}[21]	10	615	4f (C_3) and 6h (C_s)	3 and 5 peaks
$Sr_5(PO_4)_{1.9}(SiO_4)_{0.95}$:Eu^{3+}[22]	14	614	4f (C_3) and 6h (C_s)	3 and 5 peaks
LiLaMg(W,Mo)O_6:Eu^{3+}[23]	15	615	4g (C_2)	5 peaks
$Ca_5(PO_4)_3F$:0.04 Eu^{3+}[24]	20	620	4f (C_3) and 6h (C_s)	3 and 5 peaks
$Sr_4La_6(SiO_4)_6F_2$:Eu^{3+}[25]	25	615	4f (C_3) and 6h (C_s)	3 and 5 peaks
$Sr_4La_6(SiO_4)_6C_{l2}$:Eu^{3+}[25]	25	615	4f (C_3) and 6h (C_s)	3 and 5 peaks
$Gd_2Mo_2O_9$:Eu^{3+}[7]	25	612	4a (C_3)	3 peaks
$La_2Mo_3O_{12}$:Eu^{3+}[7]	25	615	three 8f (C_1)	5 peaks
$La_2Mo_2O_9$:Eu^{3+}[7]	25	612	4a (C_3)	3 peaks
TiO_2:Eu^{3+}[26]	27	610	2a (D_{2h})	5 peaks

Table 6.3: Summary of narrow-band red phosphors.

The narrowest red phosphor reported is Y_2MoO_6:Eu^{3+}, which has a full width at half maximum (FWHM) of 3 nm at the dominant emission peak (at ~ 611 nm) when excited by near-UV (350 nm) or blue light (465 nm). The Eu^{3+} is located on two different Wyckoff sites (4e and 8f with site symmetries C_2 and C_1 respectively) with splitting into five for each site symmetry, creating multiple emission lines and some broadening.[15] Y_2SiO_5:0.01 Ce^{3+}, 0.50 Tb^{3+}, 0.01 Eu^{3+} is a near UV broadband-excited and narrow-line red phosphor. This phosphor emits at 612 nm with a FWHM of ~ 5 nm and its Wyckoff site 8f (with site symmetry C_1) splits the emission peak into five.[16]

Eu^{3+} occupies the Wyckoff sites 8c with site symmetry C_1 in Li_2SiN_2:Eu^{3+}, emitting at 612 nm and generating a splitting into three with a FWHM of 7 nm under near-UV radiation.[17] In $Sr_2(La_{1-x}Eu_x)_8(GeO_4)_6O_2$, two different Wyckoff sites 4f and 6h with site symmetries C_3 and C_S respectively are occupied, emitting at 613 nm and splitting into five when excited with near-UV radiation.[18] $Ba_2La_{2.63}Tb_{0.15}Eu_{0.22}(SiO_4)_3F$[19] phosphor (occupying two different Wyckoff sites 4f and

6h with site symmetry C_3 and C_S, and splitting into three and five respectively) emits at 616 nm, while $Sr_3Gd_{0.9}Na(PO_4)_3F$:0.1 Eu^{3+}[20] (occupying one Wyckoff site 2d with site symmetry C_3 and splitting into three) and $Ba_2Gd_8(SiO_4)_6O_2$:Eu^{3+}[21] (occupying two different Wyckoff site 4f and 6h with site symmetry C_3 and C_S, and splitting into three and five respectively) phosphors emit at 615 nm with a FWHM of $\sim$ 10 nm.

Red phosphors with FWHM >10 nm but that still are inside the narrow-band category are listed below. $Sr_5(PO_4)_{1.9}(SiO_4)_{0.95}$:$Eu^{3+}$ phosphor emits at 614 nm with a FWHM of 14 nm with Eu^{3+} occupying two sites (Wyckoff site 4f and 6h with site symmetries C_3 and C_S respectively), which splits the emission peak into three and five.[22] LiLaMg(W,Mo)O_6:Eu^{3+} emits at 615 nm (FWHM of 15 nm) with one site (Wyckoff site 4g with site symmetry C_2) splitting into five.[23] $Ca_5(PO_4)_3F$:0.04 Eu^{3+}[24] phosphor present its principal emission peak at 620 nm (FWHM of 20 nm) with two sites (Wyckoff sites 4f and 6h with site symmetries C_3 and C_S respectively) splitting into three and five each.

Phosphors with a linewidth wider than 20 nm have a penalty for their luminous efficiency. However, they are still known as narrow-band red phosphors. $Gd_2Mo_2O_9$:Eu^{3+} and $La_2Mo_2O_9$:Eu^{3+} phosphors (each with one Wyckoff site 4a occupied with site symmetry C_3 and splitting into three)[7] display an emission peak at 612 nm with FWHM of 25 nm, while $La_2Mo_3O_{12}$:Eu^{3+} (with a Wyckoff sites 8f occupied with site symmetry C_1 and splitting into five).[7] $Sr_4La_6(SiO_4)_6F_2$:Eu^{3+} and $Sr_4La_6(SiO_4)_6C_{l2}$:Eu^{3+} phosphors[25] emit at 615 nm with FWHM of 25 nm. The occupied Wyckoff sites 4f and 6h with a site symmetry C_3 and C_S respectively split into three and five each. TiO_2:Eu^{3+}[26] exhibits an emission at 610 nm with FWHM of 27 nm, with Eu^{3+} occupying only one Wyckoff site 2a with site symmetry D_{2h}, which splits into five.

The objective of the work presented in this chapter was to prepare and characterise a series of new narrow-band red phosphors based on apatite-type gadolinium silicate, $Gd_{9.33}(SiO_4)_6O_2$, a good potential host lattice for red phosphors. It can absorb energy efficiently in the near-UV region through the sensitiser Gd^{3+}. On account of its outstanding stability it has been already studied in white-emitting phosphors.[27] The red phosphor series studied are $Gd_{9.33-x}Eu_x(SiO_4)_6O_2$ (x = 0.03, 0.05, 0.07, 0.09, 0.19, 0.28, 0.47, 0.65, 0.93, 1.40 and 1.87) compounds, with doping levels as shown in Table 6.4. The doping goes to two crystallographically independent A-sites: A1 (Wyckoff site 4f) and A2 (Wyckoff site 6h). The structural model for the doped $Gd_{9.33}(SiO_4)_6O_2$ host is shown in Table 3.4 in Section 3.

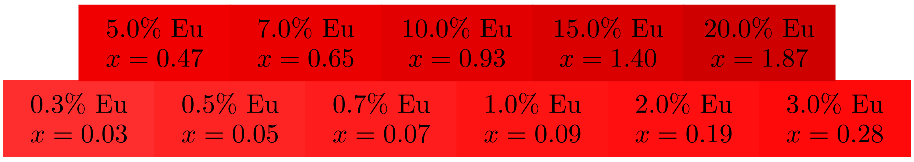

5.0% Eu $x = 0.47$	7.0% Eu $x = 0.65$	10.0% Eu $x = 0.93$	15.0% Eu $x = 1.40$	20.0% Eu $x = 1.87$	
0.3% Eu $x = 0.03$	0.5% Eu $x = 0.05$	0.7% Eu $x = 0.07$	1.0% Eu $x = 0.09$	2.0% Eu $x = 0.19$	3.0% Eu $x = 0.28$

Table 6.4: Schematic representation of the different doping levels for the $Gd_{9.33-x}Eu_x(SiO_4)_6O_2$ phosphor series.

6.2 Experimental details

6.2.1 Sample preparation

All the samples were prepared using conventional solid-state synthesis. The reagents used are listed in Table 6.5. The starting materials were dried at 1200 °C and PXRD patterns were recorded following the data collection details described in section 2.2.3 to check reagent quality prior to using them in the synthesis.

Reagent	Supplier	Purity
Gd_2O_3	Sigma Aldrich	99.99%
Eu_2O_3	Sigma Aldrich	99.99%
SiO_2	Sigma Aldrich	99.99%

Table 6.5: Reagents used in these syntheses.

The stoichiometric amounts of reagents used for the reaction to obtain single-phase Eu^{3+}-doped red phosphors are given by Equation 6.8.

$$6SiO_2 + \frac{(9.33-x)}{2}Gd_2O_3 + \frac{x}{2}Eu_2O_3 \rightarrow Gd_{9.33-x}Eu_x(SiO_4)_6O_2, \tag{6.8}$$

where x = 0.03, 0.05, 0.07, 0.09, 0.19, 0.28, 0.47, 0.65, 0.93, 1.40 and 1.87.

To prepare 2.0 grams of each composition, stoichiometric amounts of the reagents were weighed (with a precision of ±0.0001 g), then ground for around 30 minutes and heated in cycles with intermittent grinding, at 1400 °C for 100 hours and at 1500 °C for 200 h.

6.2.2 X-ray diffraction.

Laboratory PXRD patterns were recorded to check the purity of the samples between each heating cycle. The final recorded patterns were fitted using a modified structural model of $Gd_{9.33}(SiO_4)_6O_2$.[28] A Bruker AXS d8 Advance[29] diffractometer, using $CuK_{\alpha1,2}$ radiation, was used to record the patterns in a 2θ range from 10° to 70° using a step size of 0.02° and a step time of 1 s at room temperature. The refined variables included the background terms, diffractometer zero point, pseudo-Voigt peak shape function parameters, unit cell parameters and isotropic atomic displacement parameters for each phase. All PXRD data were analysed using Topas Academic software.[30]

For the variable temperature X-ray diffraction (VTXRD), a Bruker AXS d8 Advance diffractometer with $CuK_{\alpha1,2}$ radiation, a Lynxeye detector and an Anton Parr HTK1200 high temperature furnace were used. The patterns were recorded every 23.5 °C from 18 °C and 527 °C, with a previous heating and cooling cycle to eliminate any kind of moisture from the sample, in a 2θ range from 10° to 70° using a step size of 0.02° and a step time of 1 s. The refined variables included the background terms, diffractometer zero point, pseudo-Voigt peak shape function parameters, unit cell parameters and isotropic atomic displacement parameters for each pattern at each temperature.

6.2.3 Photoluminescence spectroscopy

A Horiba Fluorolog-3 fluorimeter was used for the optical measurements with a xenon flashlamp as the excitation source and a Hamamatsu R928 photomultiplier tube for detection. Homogeneous finely powdered samples of the materials were contained in a Spectralon® cup with a quartz cover slip and placed inside a Quanta-ϕ F-3029 integrating sphere connected to the spectrometer via optical fibres.

A Horiba Jobin-Yvon Fluorolog-3 Model FL3-221 spectrofluorometer system was used to collect the variable temperature emission spectra under excitation radiation from a 450 W xenon lamp using a (λ_{exc}= 320 nm). Homogeneous finely powdered samples of the materials were heated from room temperature to 475 °C.

Lifetime values were recorded by multichannel scaling following excitation with a pulsed xenon lamp. The emitted light was analysed at right angles to the excitation source and detected using a Hamamatsu R928 photomultiplier tube thermoelectrically cooled to -20 °C after passage through a monochromator.

The Judd-Ofelt parameters and derived quantities are calculated by JOES[12] software package.

6.3 Results and discussion

6.3.1 Structural characterisation and concentration quenching of $Gd_{9.33-x}Eu_x(SiO_4)_6O_2$ phosphor

6.3.1.1 Room temperature powder X-Ray diffraction

Figure 6.1 shows the Rietveld fits for the $Gd_{9.33-x}Eu_x(SiO_4)_6O_2$ (x = 0.03, 0.05, 0.07, 0.09, 0.19, 0.28, 0.47, 0.65, 0.93, 1.40 and 1.87) phosphor series. The patterns confirm highly crystalline $Gd_{9.33-x}Eu_x(SiO_4)_6O_2$ doped phases. A presence of small amounts of Gd_2SiO_5 (the peaks marked with ∇ in Figure 6.1, see Appendix A.5 for the detailed patterns) was detected. The refined weight percentage for the impurity phase in each sample is given in Table 6.6.

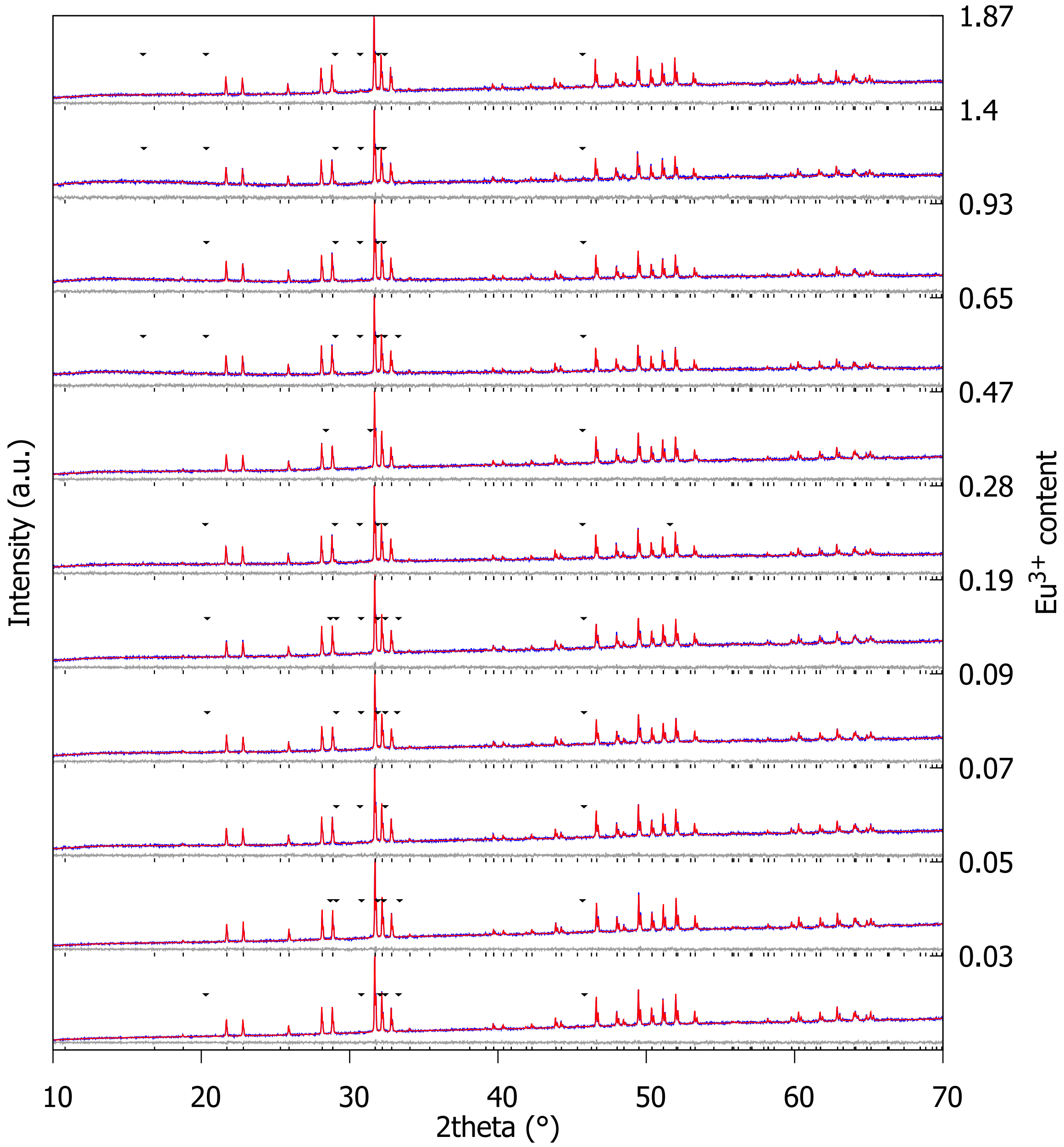

Figure 6.1: Rietveld fit of the laboratory PXRD data. $Gd_{9.33-x}$ $Eu_x(SiO_4)_6O_2$ (x = 0.03, 0.05, 0.07, 0.09, 0.19, 0.28, 0.47, 0.65, 0.93, 1.40 and 1.87).∇ indicates the Gd_2SiO_5 impurity peaks.

Table 6.6 presents the refined unit cell parameters, the R_{wp} and the purity level obtained from the Rietveld refinements. The lattice parameters as a function of Eu^{3+} content are shown in Figure 6.2. Considering that the ionic radii (CN = 7) are 1.00 Å for Gd^{3+} and 1.01 Å for Eu^{3+}, *i.e.* there is only 1% difference between the two radii of the two cations, no significant changes in the unit cell parameters are expected.

x	a (Å)	c (Å)	V (Å^3)	R$_{wp}$ (%)	Gd_2SiO_5(wt %)
0.03	9.44114(8)	6.869868(8)	530.31(1)	2.28	2.7(8)
0.05	9.4392(1)	6.8699(1)	530.09(2)	2.84	2.6(9)
0.07	9.44102(8)	6.86960(8)	530.27(1)	2.45	2(1)
0.09	9.4399(1)	6.8710(1)	530.26(2)	2.71	4.2(6)
0.19	9.4403(2)	6.8715(2)	530.34(2)	2.93	3.5(8)
0.28	9.4404(1)	6.8703(1)	530.25(2)	3.12	6.3(8)
0.47	9.4444(1)	6.8709(1)	530.76(2)	2.94	0.2(4)
0.65	9.4432(1)	6.8714(1)	530.65(2)	2.99	8(1)
0.93	9.4440(1)	6.8714(1)	530.75(2)	3.52	3.9(9)
1.40	9.4451(2)	6.8760(2)	531.23(3)	3.80	8(1)
1.87	9.4464(1)	6.8778(1)	531.51(2)	3.07	8.0(8)

Table 6.6: Unit cell parameters for $Gd_{9.33-x}$ $Eu_x(SiO_4)_6O_2$ phosphors.

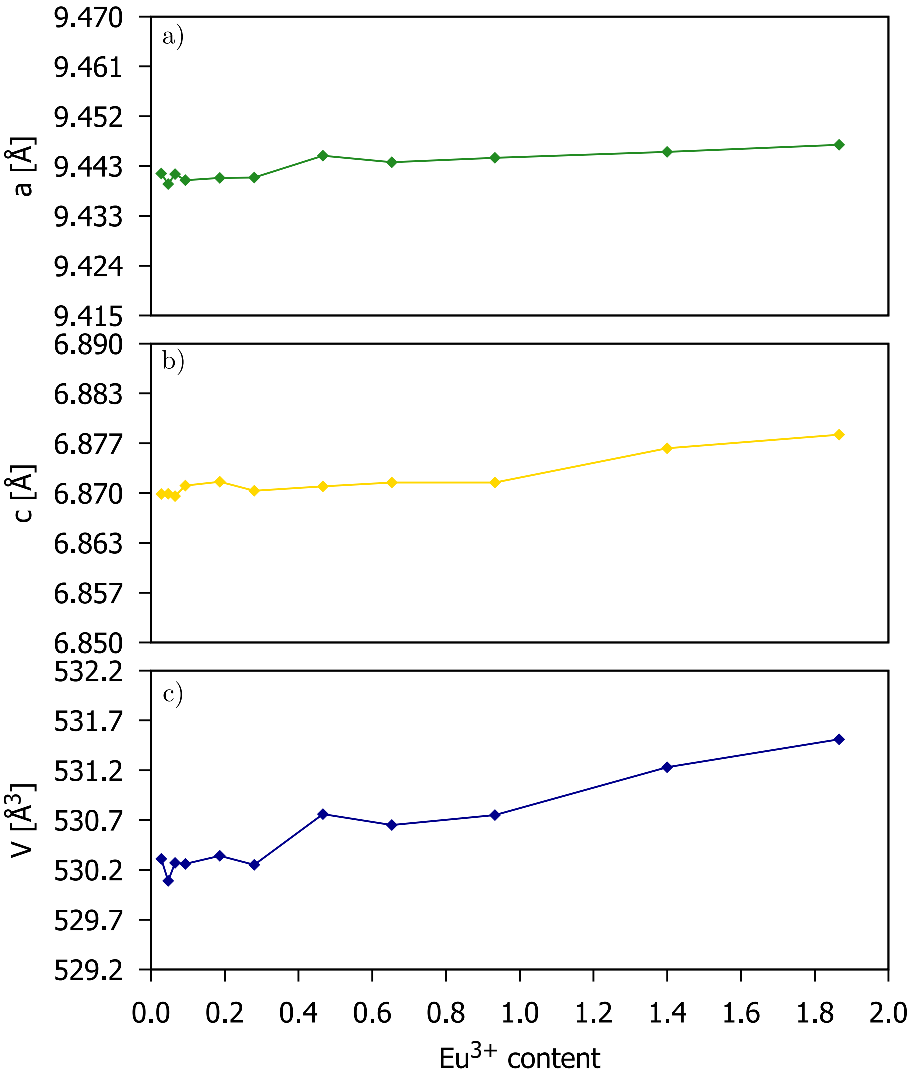

Figure 6.2: Lattice parameters of the a)a, b)c and c)unit cell volume V for $Gd_{9.33-x}$ $Eu_x(SiO_4)_6O_2$ (x = 0.03, 0.05, 0.07, 0.09, 0.19, 0.28, 0.47, 0.65, 0.93, 1.40 and 1.87) as a function of Eu^{3+} content. The error bars are smaller than the data points.

There are two crystallographically unique Gd sites in the apatite structure, A1 and A2, that the Eu^{3+} dopant can occupy. The distance between the sensitiser (Gd^{3+}) and the activators (Eu^{3+}) is important as cross-relaxation is possible. The critical distance for energy exchange can be calculated using Equation 6.9:[31, 32]

$$R_c = 2\left(\frac{3V}{4\pi x_c N}\right)^{1/3}, \tag{6.9}$$

where x_c is the critical concentration N and V is the number of cations in the unit cell and volume of the unit cell. The critical concentration is the activator content at which the emission intensity starts to decrease. As described in section 6.3.1.2, the concentration quenching was found to start at higher doping levels than x=0.93, then x_c = 0.93, N = 8 and V = 530.75, then the critical transfer distance is 5.140(6) Å. In general, when the critical distance is larger than 5 Å the mechanism of the non-radiative energy transfer is an electric multipolar interaction, mechanism responsible of concentration quenching.[21] The distance between the different Gd sites shown in Figure 6.3 ranges from 3.4 Å to 5.6

Å. Since the values are similar to the critical distance, there is a possibility of concentration quenching via the exchange interaction mechanism.

Figure 6.3 shows the connectivity between the different Gd^{3+} sites, labelled Gd1 (shown as pink polyhedra) and Gd2 (shown as purple polyhedra). Figure 6.3a shows the connectivity in the *ab* plane, where a $Gd1O_6$ trigonal prism shares all its 6 oxygen atoms with 7-coordinate $Gd2O_7$ polyhedra. Figure 6.3b shows the connectivity in the c-direction. The Gd1 sites are arranged in vertical chains formed by $Gd1O_6$ trigonal prisms, sharing top and bottom faces, connected by their 6 oxygen atoms with two other $Gd1O_6$ trigonal prisms. Figure 6.3c shows the Gd2 sites connected by two rings that share 2 oxygen atoms between the top and bottom layers. Each ring has three $Gd2O_7$ that share corners with a central oxygen atom.

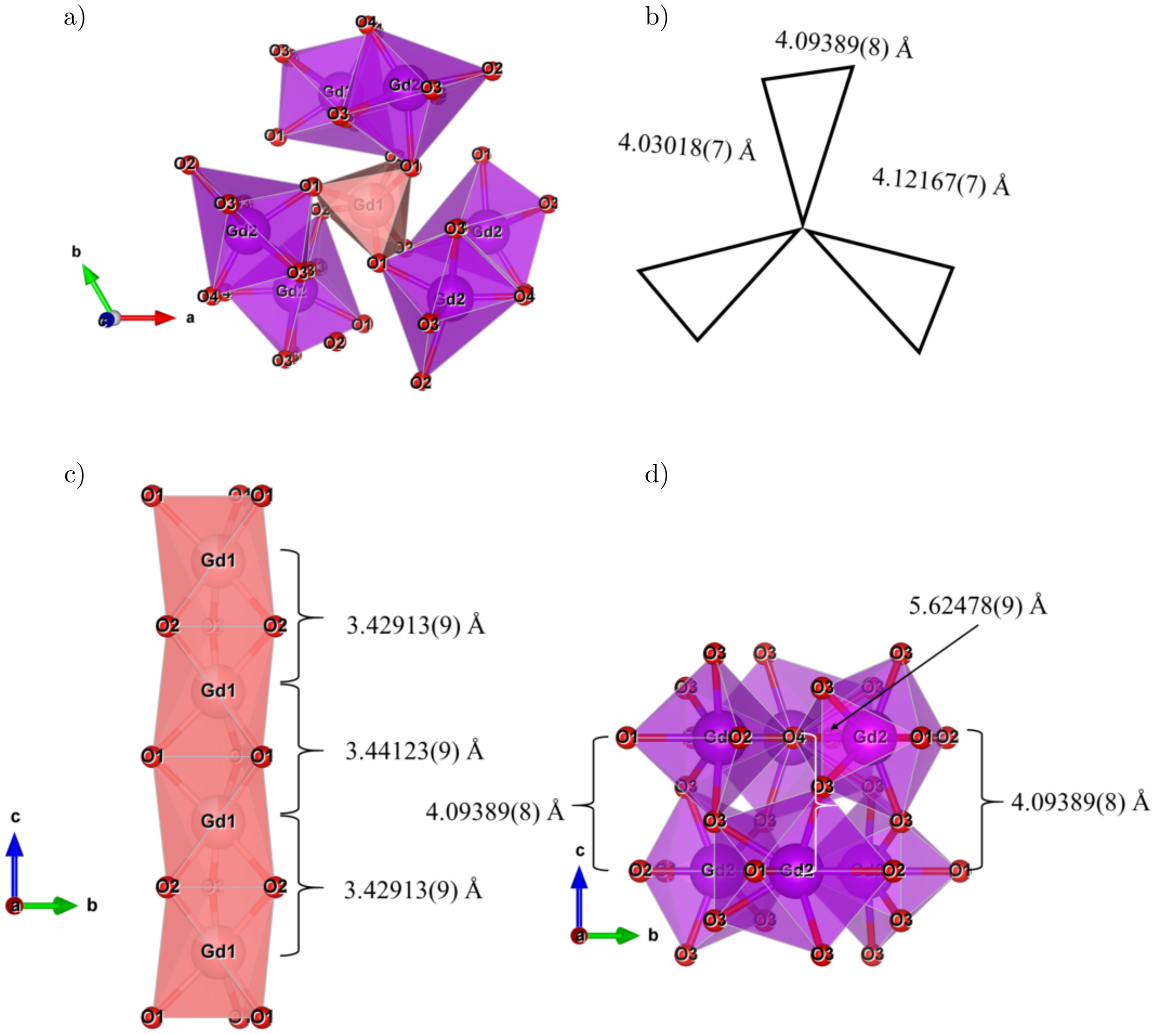

Figure 6.3: a) View of the *ab* plane, b) schematic of the *ab* plane, c) c-direction for Gd1 sites and d) c-direction for Gd2 sites for the $Gd_{9.33}(SiO_4)_6O_2$ structure.[28]

6.3.1.2 Concentration quenching and luminescence analysis

The energy level diagram shown in Figure 6.4 displays the interaction between the Russell-Saunders coupling states of Gd^{3+} and Eu^{3+}. Gd^{3+} ions when excited in the UV region contribute as sensitisers to the Eu^{3+} ions. Under UV radiation, a Gd^{3+} ion is excited from the ground $^8S_{7/2}$ state to the $^6P_{7/2}$ or ^6I_J states. Subsequently there is a possibility of an energy transfer to a nearby Eu^{3+} ion. Relaxation to the $^5D_0$ state is followed by emission to the ^7F_J manifold (J = 0, 1, 2, 3 and 4).

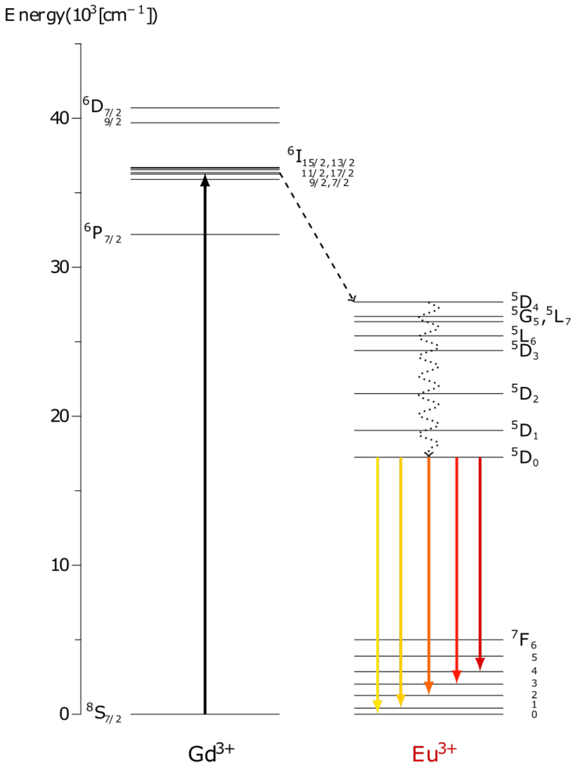

Figure 6.4: Energy-level diagrams for Gd^{3+} and Eu^{3+} ions showing the relevant transitions in Eu^{3+}-doped $Gd_{9.34}(SiO_4)_6O_2$ phosphors.

Figure 6.5 shows the emission spectra for $Gd_{9.33-x}Eu_x(SiO_4)_6O_2$ red phosphor recorded under excitation at 275 nm. The emission peaks observed are in the red region, corresponding to the $^5D_0 \rightarrow ^7F_0$, $^5D_0 \rightarrow ^7F_1$, $^5D_0 \rightarrow ^7F_2$, $^5D_0 \rightarrow ^7F_3$ and $^5D_0 \rightarrow ^7F_4$ transitions. As it is observed in the 614 nm peak, the Eu^{3+} is in non-centrosymmetric sites (Wyckoff sites 4f and 6h), allowing the hypersensitive $^5D_0 \rightarrow ^7F_2$ dominant transition. This attribute makes the gadolinium silicate apatite an optimum host for a red phosphor. For the emission peak at 614 nm, the FWHM is 7 nm, identifying it as a narrow-band red phosphor. The site symmetries of the Eu^{3+} atoms in the gadolinium silicate host are C_3 (4f) and C_S (6h). The expected splittings for the $^5D_0 \rightarrow ^7F_2$ transition are 3 and 5 for each site (as seen in Table 6.2), which are presented as broadening in Figure 6.5. However, $Gd_{9.33-x}Eu_x(SiO_4)_6O_2$ still satisfies the narrow-band red phosphor requirements.

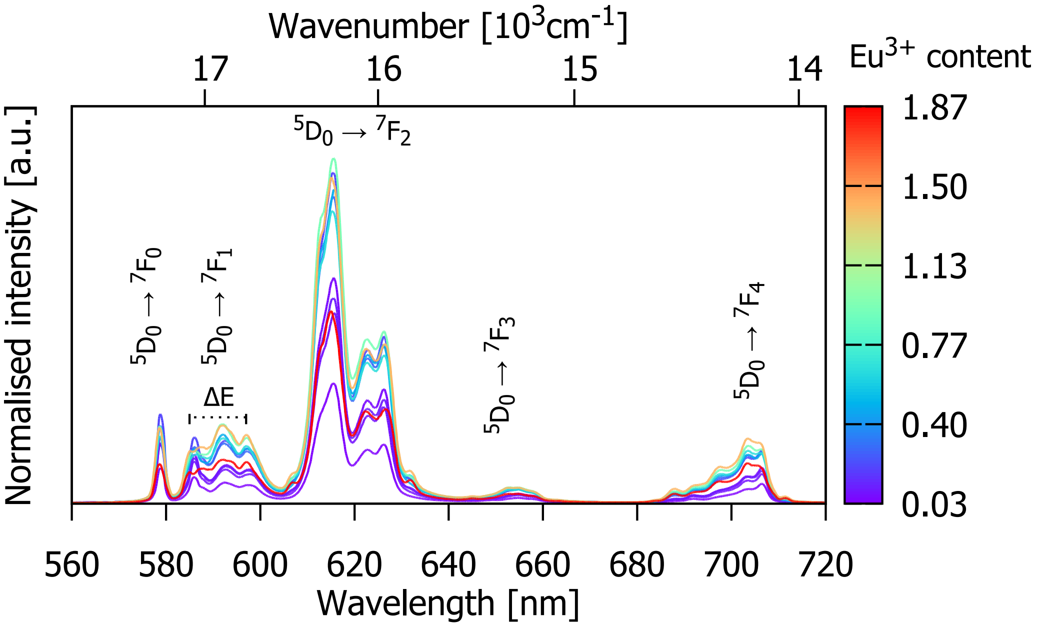

Figure 6.5: Room temperature emission spectra of $Gd_{9.33-x}$ $Eu_x(SiO_4)_6O_2$ (x = 0.03, 0.05, 0.07, 0.09, 0.19, 0.28, 0.47, 0.65, 0.93, 1.40 and 1.87) under 275 nm excitation. Maximum energy splitting of $^7F_1$ ΔE is labelled.

Figure 6.5 presents the emission spectra of all the $Gd_{9.33-x}$ $Eu_x(SiO_4)_6O_2$ (x = 0.03, 0.05, 0.07, 0.09, 0.19, 0.28, 0.47, 0.65, 0.93, 1.40 and 1.87) compounds. Five peaks can be observed centred at 577, 591, 614, 653 and 705 nm associated with $^5D_0 \rightarrow {}^7F_J$ (J = 0,1,2,3 and 4) spin-forbidden *f*–*f* transitions respectively. The dominant emission peak remains at around 614 nm.

Figure 6.6 shows the emission intensity arising from the $^5D_0 \rightarrow {}^7F_2$ for the $Gd_{9.33-x}$ $Eu_x(SiO_4)_6O_2$ (x = 0.03, 0.05, 0.07, 0.09, 0.19, 0.28, 0.47, 0.65, 0.93, 1.40 and 1.87) series as a function of the concentration of Eu^{3+}. It is clear that concentration quenching has been reached. The highest emission intensity detected was at a doping concentration x=0.93; after this the emission intensity decreases slightly for x=1.40, followed by an abrupt extreme drop of intensity for the material containing x=1.87. This demonstrated a better behaviour than the reported in the literature for $Sr_2(1-x)Eu_2xZnGe_2O_7$ phosphor, which has high emission intensity until the Eu^{3+} concentration reaches x=0.05.[33] And it exhibits even better performance than the obtained for $NaSrLa_{1-x}(MO_4)_3$ (M =Mo and W), where the highest emission intensity was found at x=0.008 and x=0.010 respectively.[34] High concentration quenching indicates a larger quantity of activators. which can potentially lead to a brighter phosphor.

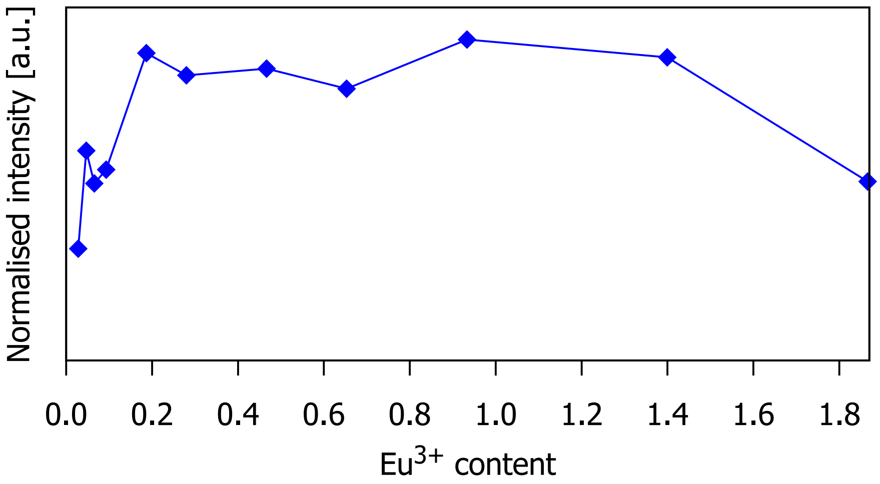

Figure 6.6: Room temperature emission spectra of $Gd_{9.33-x}$ $Eu_x(SiO_4)_6O_2$ (x = 0.03, 0.05, 0.07, 0.09, 0.19, 0.28, 0.47, 0.65, 0.93, 1.40 and 1.87) as a function of the Eu^{3+} concentration.

The lifetime values obtained from single exponential fitting are shown in Figure 6.7 as a function of the Eu^{3+} concentration. The values range from 1.05 to 1.35 ms, which is consistent with those published for Eu^{3+}-doped $Sr_2La_8(GeO_4)_6O_2$[18] and $Gd_{9.33-x-y}Eu_xTb_y(SiO_4)_6O_2$,[27] with decay values of τ = 0.9-1.3 ms and τ = 1.28-1.39 ms respectively. The lifetime value quenches for Eu^{3+} content above x=0.93, which is consistent to the observed behaviour in the emission (Figure 6.6). This can be attributed to an increase in the non-radiative energy transfer between Eu^{3+} ions due to their high concentration in the material. In the literature, the lifetime values reported for $BaLu_{2-x}Si_3O_{10}$:Eu^{3+} phosphors were found to drop from 2.024 to 1.538 ms when the x=0.002 and x=0.02 respectevily.[35]

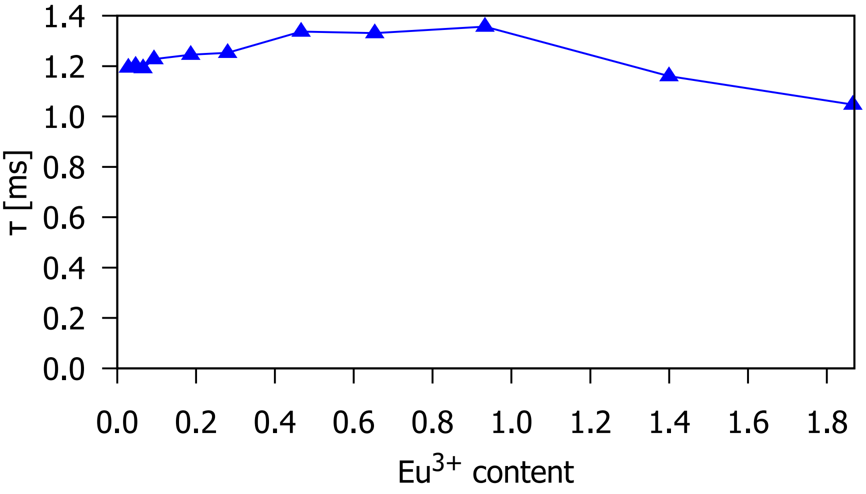

Figure 6.7: Lifetime values according to Eu^{3+} content for the $^5D_0 \rightarrow {}^7F_5$ transition (614 nm) for $Gd_{9.33-x}$ $Eu_x(SiO_4)_6O_2$ (x = 0.03, 0.05, 0.07, 0.09, 0.19, 0.28, 0.47, 0.65, 0.93, 1.40 and 1.87) materials.

6.3.1.3 Room temperature Judd-Ofelt analysis

The Judd-Ofelt theory allows quantitative analysis of the *f*-*f* transition of rare earth ions to give parameters such as Judd-Ofelt parameters, theoretical lifetime and intrinsic quantum yield.[9, 10] This was performed for $Gd_{9.33-x}Eu_x(SiO_4)_6O_2$ (x = 0.03, 0.05, 0.07, 0.09, 0.19, 0.28, 0.47, 0.65, 0.93, 1.40 and 1.87) phosphors. Figure 6.8 presents the Judd-Ofelt parameters Ω_2 and Ω_4 for the different concentration levels using a refractive index of 1.8.[36]

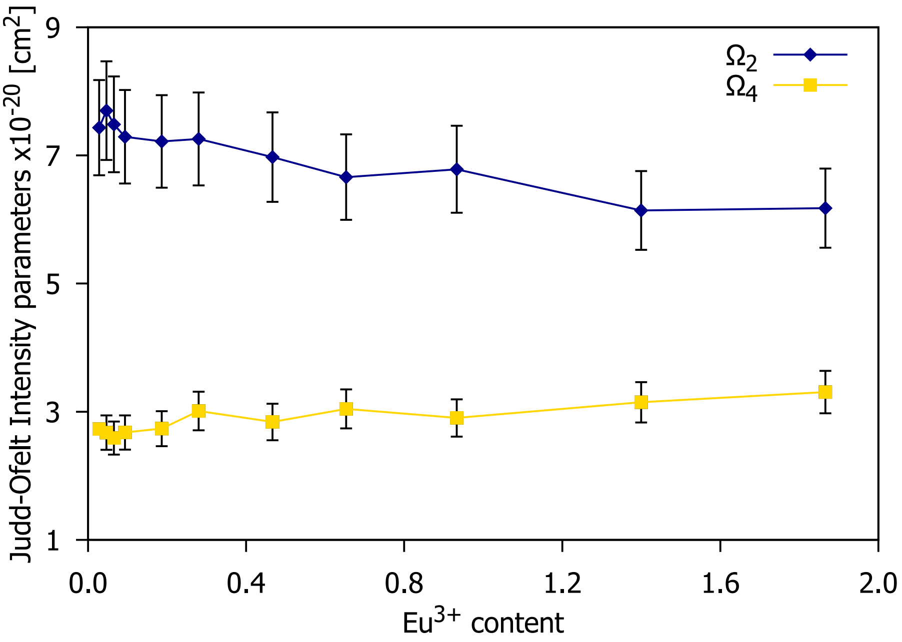

Figure 6.8: Judd-Ofelt intensity parameters estimated using Equation 6.2 from the emission spectra as a function of the Eu^{3+} concentration of the $Gd_{9.33-x}Eu_x(SiO_4)_6O_2$ (x = 0.03, 0.05, 0.07, 0.09, 0.19, 0.28, 0.47, 0.65, 0.93, 1.40 and 1.87) phosphors. Refractive index = 1.8.

Equation 6.2 shows that the Ω_2 parameter is dependent on the $^5D_0 \rightarrow {}^7F_2$ transition (dominant emission band at 614 nm). This parameter is strongly dependent on the refractive index. Materials with a high refractive index show a more intense hypersensitive transition.[37] Figure 6.8 shows that the Ω_2 value decreases when the doping content increases. The decrease in Ω_2 suggests a decrease in the average distortion of Eu^{3+} cation coordination polyhedra.[13] The available sites for the Eu^{3+} are 4f and 6h with C_3 and C_S symmetry respectively. The decrease of Ω_2 shown in Figure 6.8 suggests that the higher local symmetry site (C_3) is preferentially occupied at higher Eu^{3+} concentrations. This has been proposed for phosphors based on apatite structures, such as $A_2Y_8(SiO_4)_6O_2$ (A=Ca, Sr).[38] The values obtained range from 6.9(7) to 6.2(6) cm^{-1}, which is in accordance with the values reported in the literature for $Sr_{0.2}Ca_{9.65}Eu_{0.1}(PO_4)_6(OH)_2$[39] with $\Omega_2 = 6.68$ cm^{-1}, $Ca_{9.5}Eu_{0.5}(PO_4)_6(OH)_2$[40] with $\Omega_2 = 6.85$ cm^{-1} and $Sr_{9.95}Eu_{0.05}(PO_4)_6(OH)_2$[41] with $\Omega_2 = 6.83$ cm^{-1}.

The Ω_4 value is dependent on the $^5D_0 \rightarrow {}^7F_4$ transition (emission peak at 705 nm). This parameter is related to the viscosity and rigidity of the matrix. In Figure 6.8, Ω_4 experiences a small increase with an increase in the Eu^{3+} doping level. The values obtained range from 2.3(2) to 2.7(3) cm^{-1}. Ω_6 was not calculated as the emission arising from the $^5D_0 \rightarrow {}^7F_6$ transition is known to be weak. $\Omega_2 > \Omega_4$ demonstrates that covalence exists between the Eu^{3+} ion and the ligands and that there is asymmetry around the metal ion site.[13]

The observed lifetime was recorded following the data collection convention described in the section 6.2.3. The theoretical lifetime values were calculated using the total spontaneous emission rate. Figure 6.9 shows a comparison of these lifetime values as a function of the Eu^{3+} doping level. It is evident the theoretical lifetime has a systematic overestimation of $\sim$ 0.5 ms. However, the correlation between the observed lifetime and the theoretical lifetime approximation is observed up to x=0.93, where an increase in the lifetime values with higher doping levels is demonstrated. Furthermore, it is clear that after the concentration quenching was reached the Judd-Ofelt calculations overestimated the lifetime values.

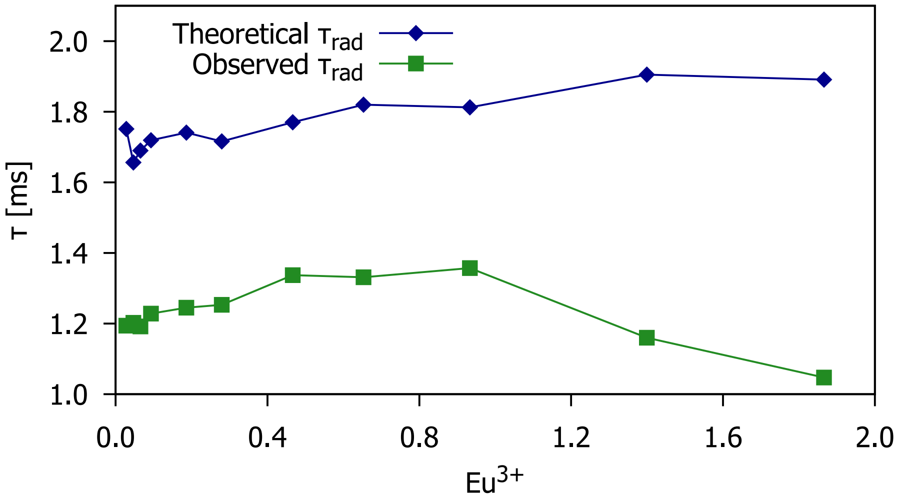

Figure 6.9: Lifetime values - theoretical (blue diamond)and observed (green square) - as a function of the Eu $^{3+}$ doping level for the $Gd_{9.33-x}Eu_x(SiO_4)_6O_2$ (x = 0.03, 0.05, 0.07, 0.09, 0.19, 0.28, 0.47, 0.65, 0.93, 1.40 and 1.87) phosphors.

The intrinsic quantum yield, η, was calculated for the $Gd_{9.33-x}Eu_x(SiO_4)_6O_2$ (x = 0.03, 0.05, 0.07, 0.09, 0.19, 0.28, 0.47, 0.65, 0.93, 1.40 and 1.87) phosphors. Table 6.7 presents the quantum yield values. This quantum yield is related to the efficiency of the sensitisation by the Gd^{3+}. The highest intrinsic quantum yield obtained for the $Gd_{9.33-x}Eu_x(SiO_4)_6O_2$ (x = 0.03, 0.05, 0.07, 0.09, 0.19, 0.28, 0.47, 0.65, 0.93, 1.40 and 1.87) phosphor series is for x=0.93, in accordance with the concentration quenching value. The values reported in the literature for apatite-type structures are comparable to the values obtained in Table 6.7, *e.g.* $\eta = 63\%$ for $Ca_{9.9}Eu_{0.1}(PO_4)_6(OH)_2$,[42] $\eta = 62\%$ for $Ca_{9.85}Eu_{0.1}(PO_4)_6F_2$[43] and $\eta = 66\%$ for $Ca_{9.95}Eu_{0.05}(PO_4)_6(OH)_2$.[40]

x	0.03	0.05	0.07	0.09	0.19	0.28	0.47	0.65	0.93	1.40	1.87
η (%)	68	73	71	71	72	73	75	73	75	61	55

Table 6.7: Quantum yield, η, for the $Gd_{9.33-x}Eu_x(SiO_4)_6O_2$ (x = 0.03, 0.05, 0.07, 0.09, 0.19, 0.28, 0.47, 0.65, 0.93, 1.40 and 1.87) phosphors. Refractive index = 1.8

6.3.2 Thermal stability of $Gd_{9.05}$ $Eu_{0.28}(SiO_4)_6O_2$ phosphor

6.3.2.1 Variable-temperature powder X-Ray diffraction

For a solid-state lighting application, the phosphors have to show thermal stability. The known LED working temperature is ~ 150 °C so the study of the phosphors at this temperature is important. The $Gd_{9.05}$ $Eu_{0.28}(SiO_4)_6O_2$ phosphor was chosen from the $Gd_{9.33-x}Eu_x(SiO_4)_6O_2$ (x = 0.03, 0.05, 0.07, 0.09, 0.19, 0.28, 0.47, 0.65, 0.93, 1.40 and 1.87) phosphor series to investigate the thermal structural and optical performance.

The laboratory variable temperature PXRD patterns (Figure 6.10) were recorded to investigate the thermal stability. The real temperature of the HTK1200 furnace was calibrated by collecting data for a standard sample, Al_2O_3, where the correction followed Equation 6.10.

$$T_{real} = T_{set} + (aT_{set}^3 + bT_{set}^2 + cT_{set} + d), \tag{6.10}$$

where a = 1.61 x 10^{-7} K^{-2}, b = 5.86 x 10^{-4} K^{-1}, c = 0.565 and d = 134 K.

Figure 6.10 shows a surface plot of the 42 diffraction patterns recorded. The $Gd_{9.05}$ $Eu_{0.28}(SiO_4)_6O_2$ phosphor exhibits a lack of phase transition and it was found to retain its crystallinity, demonstrating it can be used in applications that require high temperature environments, *e.g.* 150 °C, working LED temperature.

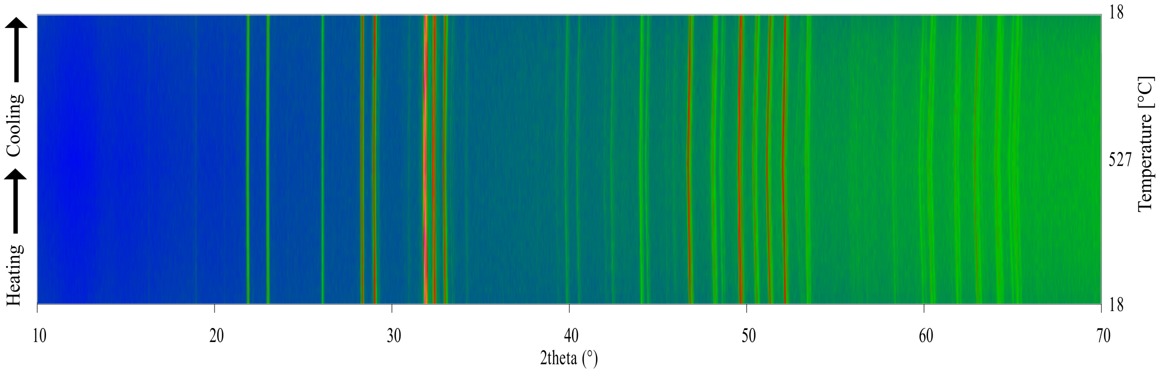

Figure 6.10: Variable-temperature laboratory PXRD patterns for the $Gd_{9.05}$ $Eu_{0.28}(SiO_4)_6O_2$ on warming and cooling between 18 °C and 527 °C. The artificial colour map shows intensity changes in the PXRD pattern.

Rietveld fitting of the different patterns was performed. The lattice parameters obtained are presented in Figure 6.11. The overlapping of the lattice parameters on heating and on cooling indicates a reversible process. The linear and volume thermal expansion coefficients were calculated using Equations 6.11.

$$\alpha_a = \frac{a_1 - a_0}{a_0(T_1 - T_0)}, \tag{6.11a}$$

$$\alpha_c = \frac{c_1 - c_0}{c_0(T_1 - T_0)}, \tag{6.11b}$$

$$\alpha_V = \frac{V_1 - V_0}{V_0(T_1 - T_0)}, \tag{6.11c}$$

where a_0, c_0 and V_0 are the initial unit cell parameters, a_1, c_1 and V_1 are the final unit cell parameters, T_0 is the initial temperature, T_1 is the final temperature at which the VT-PXRD patterns were taken.

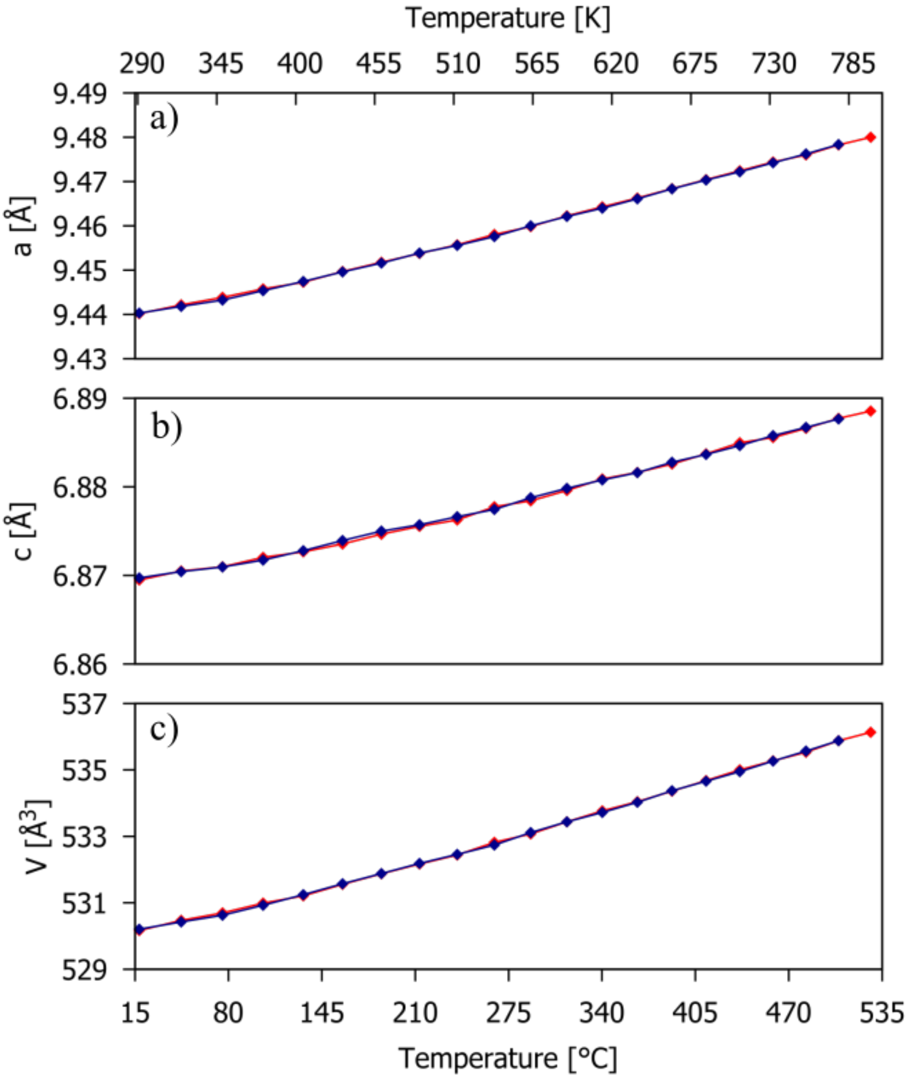

Figure 6.11: Unit cell parameters as a function of temperature obtained from the Rietveld fit for laboratory PXRD data on warming (red) and cooling (blue) recorded for $Gd_{9.05}$ $Eu_{0.28}(SiO_4)_6O_2$.

The thermal expansion coefficients obtained for the $Gd_{9.05}Eu_{0.28}(SiO_4)_6O_2$ red phosphor are presented in Table 6.8. The variation of the unit cell parameters with temperature for this sample shows normal positive thermal expansion.

		T_0	T_f	L_0 (Å)	L_f (Å)
α_a (C^{-1})	8.97(9)× 10^{-6}	30	500	9.4402(1)	9.4800(1)
α_c (C^{-1})	5.9(1)× 10^{-6}	30	500	6.8695(1)	6.8886(1)
α_V (C^{-1})	2.4(2)× 10^{-5}	30	500	530.17(2)	536.14(2)

Table 6.8: Thermal expansion coefficients for $Gd_{9.05}Eu_{0.28}(SiO_4)_6O_2$ phosphors.

6.3.2.2 Thermal quenching of $Gd_{9.05}$ $Eu_{0.28}(SiO_4)_6O_2$

For a solid-state lighting application, the phosphors have to show thermal stability. The known LED working temperature is ∼ 150 °C so determining the luminescence properties at this temperature is important. Figure 6.12 shows the emission spectra of $Gd_{9.05}$ $Eu_{0.28}(SiO_4)_6O_2$ recorded under 275 nm excitation. Broadening of the emission line is observed at room temperature, due to Eu^{3+} being located at two different crystallographic sites. Furthermore, broadening is also observed as the temperature increases. This is related to higher frequency lattice vibrations at higher temperatures. The $Gd_{9.05}$ $Eu_{0.28}(SiO_4)_6O_2$ phosphor was shown to have an excellent thermal behaviour (as determined in 6.3.2.1) due to the rigidity and stability of the host.

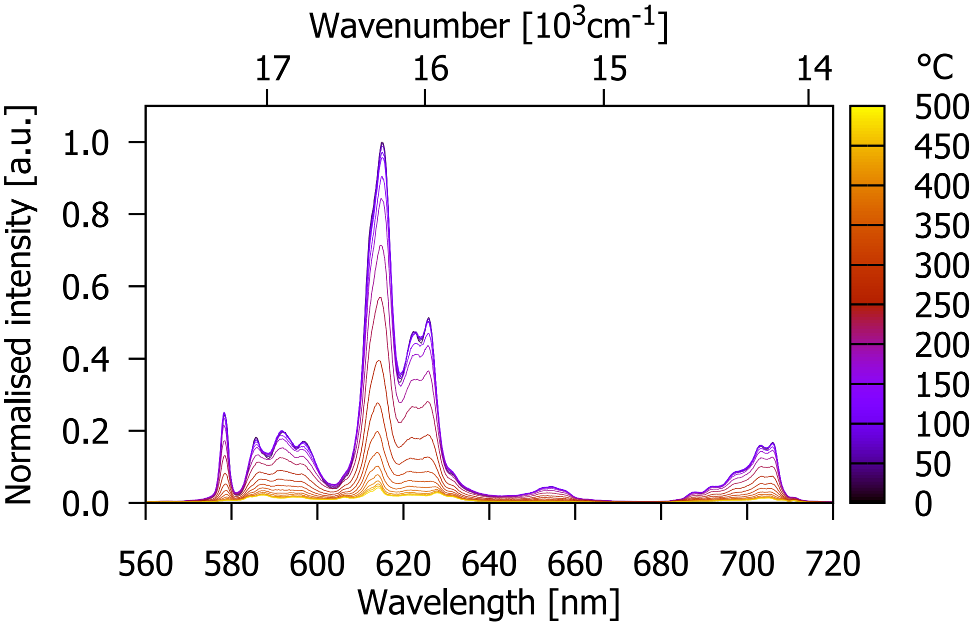

Figure 6.12: Temperature-dependent luminescence of the $Gd_{9.05}$ $Eu_{0.28}(SiO_4)_6O_2$ phosphor at λ_{exc} = 275 nm. Colour scale marks the temperature from 25 °C (purple) to 475 °C (yellow).

The normalised emission integrals obtained from the emission spectra are shown in Figure 6.13. The normalised emission integral only decreases by 10% at 150 °C (LED working temperature), in comparison to room temperature. Hence, the $Gd_{9.05}Eu_{0.28}(SiO_4)_6O_2$ phosphor presents good thermal quenching characteristics. This behaviour is proven to be superior to the reported in the literature for $NaSrEu(MoO_4)_3$ phosphor which retained 64.2% at 150 °C.[44]

The experimental data were fitted in order to extract the activation energy. The data were fitted with a single barrier quenching model, also known as Mott-Seitz model, in order to obtain the activation energy (ΔE_{MS}) of the thermal quenching process[45, 46] represented by Equation 6.12:

$$I_{MS}(T) = \frac{I_0}{1 + Bexp\left(-\frac{\Delta E_{MS}}{K_B T}\right)}, \tag{6.12}$$

where $I_{MS}(T)$ is the temperature-dependent emission integral and I_0 is the value of the emission integral at room temperature. ΔE_{MS} is the activation energy, k_B is the Boltzmann constant (8.617342×10^{-5} eV/K), B is the quenching frequency factor ($B = \frac{\tau_0}{\tau_{NR0}}$) and T is the temperature in K.

Nevertheless, the Mott-Seitz model is not justified for the case of lanthanide transitions, as it assumes a shift between configurational coordinates of the ground and excited level, which does not exist in trivalent REs. On the other hand, the multiphoton relaxation and charge transfer models are used for lanthanides. However, in the case of the Eu^{3+} the energy between the highest component of the $^7F_6$ and the lowest component of the first excited state $^5D_0$ is ~ 12500 cm^{-1}, making the multiphonon relaxation mechanism improbable for an Eu^{3+} silicate.[47, 48] The charge transfer model assumes the non-radiative relaxation via the crossing of the $^5D_0$ excited state and charge transfer band, where the thermal energy is used to rise to a higher energy through a non-radiative path. This model is described by Equation 6.13, where the phonon energy obtained represents the average energy of host phonons involved in the process.

$$I_{CT}(T) = \frac{I_0}{1 + \frac{B}{\sqrt{\frac{h\nu}{2k_B}coth\left(\frac{h\nu}{2k_BT}\right)}}exp\left(\frac{-2\Delta E_{CT}}{h\nu}tanh\left(\frac{h\nu}{2k_BT}\right)\right)}, \tag{6.13}$$

where I_{CT} is the temperature dependent emission integral, $I_0 = 1$ is the value of the emission integral at room temperature, $B = \kappa_{NR}/\kappa_R$ is the ratio of the non-radiative and radiative transition rates, ΔE_{CT} is the energy of the intersection between parabolas that represent the charge-transfer state and $^5D_0$ state in the configuration coordinate representation, k_B is the Boltzmann constant (8.617342×10^{-5} eV/K), and $h\nu$ is the average energy of the host phonons involved in the process.

ΔE is a way to quantify the thermal stability of the Eu^{3+} emission. The higher the value of ΔE is, the lower the probability of a non-radiation transition among the Eu^{3+} ions. From the charge transfer model fit (shown in Figure 6.13), the obtained ΔE_{CT} was 0.54(1) eV. The ΔE values found in the literature show that our phosphor is superior. ΔE is 0.412 eV for $Sr_4La_6(SiO_4)_6F_2$:Eu^{3+},[25] 0.481 eV for $Sr_4La_6(SiO_4)_6C_{l2}$:Eu^{3+},[25] 0.4(1) eV for $Eu_2Mo_4O_{15}$[46] and 0.84(4) eV for $Tb_2Mo_3O_{12}$:Eu^{3+}.[45] The last of these is a higher value than that of the $Gd_{9.05}Eu_{0.28}(SiO_4)_6O_2$ phosphor, which suggests this last compound is the one that decreases brightness as the temperature increases.

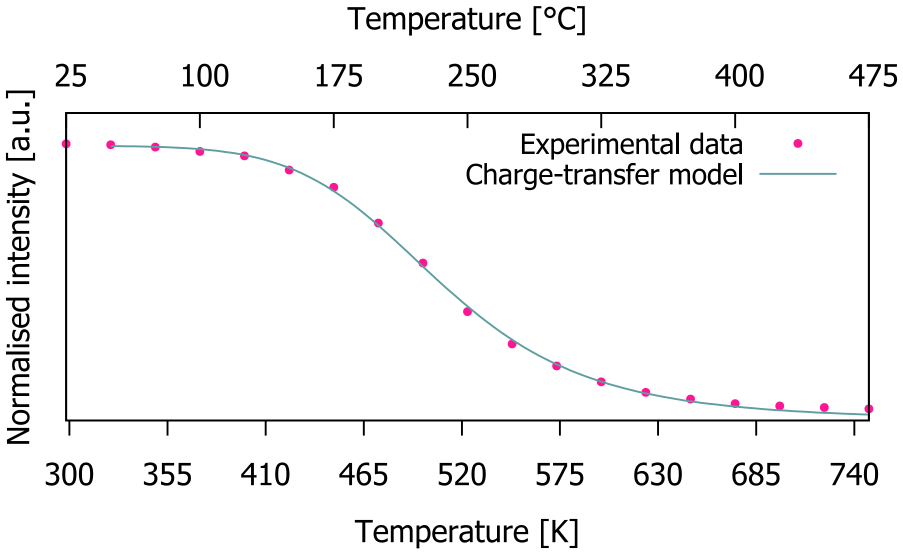

Figure 6.13: Change transfer model fit (solid line) for temperature-dependent emission integrals of the experimental data (dots) for the $Gd_{9.05}Eu_{0.28}(SiO_4)_6O_2$ phosphor.

6.3.2.3 Maximum energy splitting of $^7F_1$

The Stark components of the $^7F_1$ manifold are clearly visible in Figure 6.5. Figure 6.14 shows the maximum splitting ΔE values of the $^7F_1$ manifold as a function of temperature. The range of the values is 240-320 cm^{-1}, which is within the ranges reported in the literature, *e.g.* 307-323 cm^{-1} for $Eu_2Mo_3O_{12}$[45] and 350-374 cm^{-1} for $Y_{2-x}Lu_xO_3$:Eu^{3+}.[49]

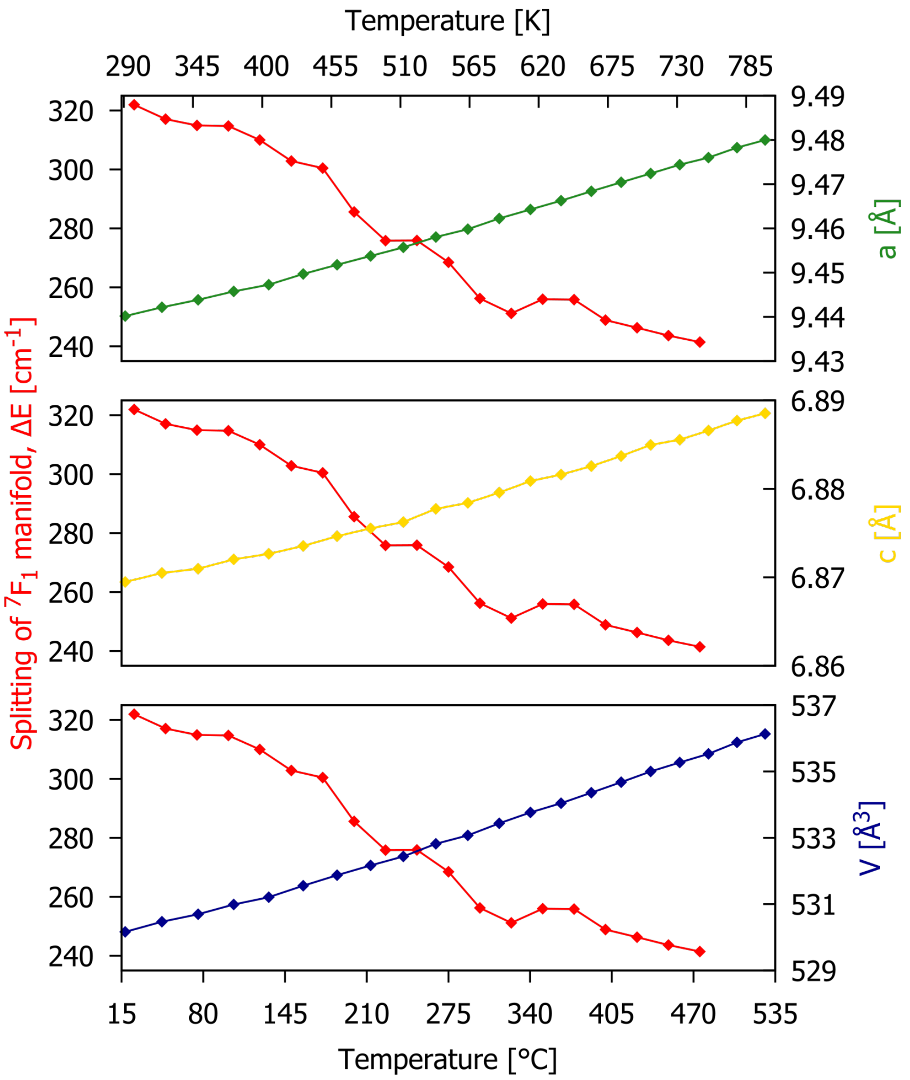

Figure 6.14: Maximum energy splitting of the $^7F_1$ manifold and lattice parameters as a function of temperature for the $Gd_{9.05}Eu_{0.28}(SiO_4)_6O_2$ phosphor.

The ΔE decreases as the temperature increases (from 320 cm^{-1} at 25 °C to 240 cm^{-1} at 475 °C). The splitting of the $^7F_1$ manifold (ΔE) is directly proportional to the intensity of the crystal field. The larger the crystal field, the larger ΔE. When temperature increases, the unit cell of the host material becomes larger (V is increasing) so the ligands are at larger distance from Eu^{3+} (thermal expansion, thermal expansion coefficients can be seen in Table 6.8) and the intensity of the crystal field decreases; the effect is manifested in smaller ΔE. This has also been observed in the $(Y_xLu_{1-x})_2O_3$:Eu^{3+} compound where ΔE decreases as the unit cell becomes larger, by increasing the doping level.[49]

6.3.2.4 Variable-temperature Judd-Ofelt analysis

Figure 6.15 presents the Judd-Ofelt parameters Ω_2 and Ω_4 for the $Gd_{9.05}Eu_{0.28}(SiO_4)_6O_2$ phosphor as a function of the temperature using a refractive index of 1.8. Table 6.9 presents the Ω_2 and Ω_4 values obtained for each temperature in 25 °C steps from 25 °C to 475 °C. It can be observed that the Ω_2 value stays constant up to 150 °C and then it decreases rapidly. This increase of the symmetry is related to the higher disorder presented for the structure at high temperature, hence the Eu^{3+} coordination polyhedra become more regular. This is manifested as a decrease of Ω_2. The Ω_4 parameter stays small and constant because the $Gd_{9.05}Eu_{0.28}(SiO_4)_6O_2$ structure is quite rigid and thermally stable (confirmed by VT-PXRD patterns shown in Figure 6.10), which is expected for the apatite structure, and ultimately the reason why this structure was chosen as a phosphor host. $\Omega_2 > \Omega_4$ behaviour is maintained.

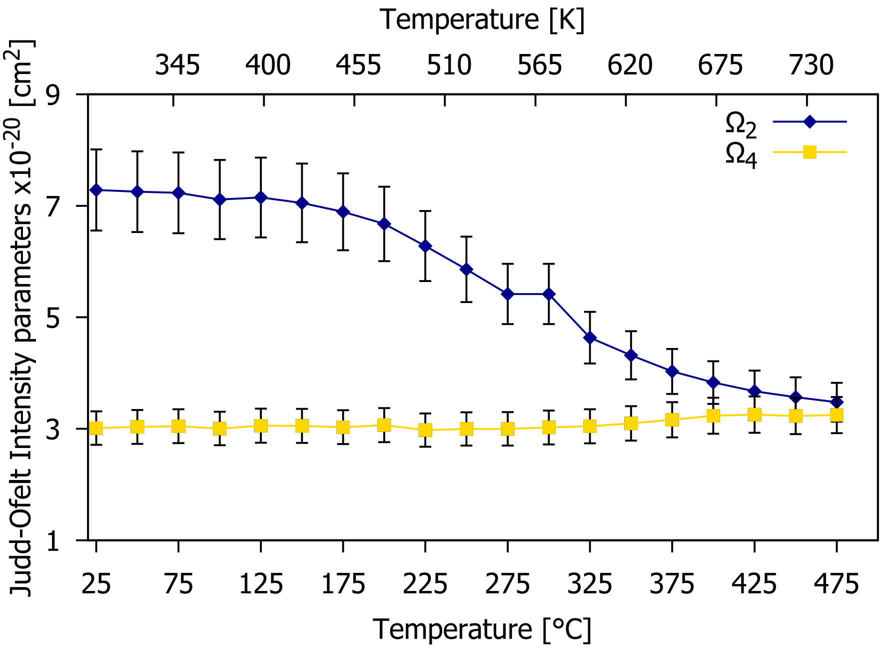

Figure 6.15: Temperature-dependent Judd-Ofelt intensity parameters estimated from the emission spectra of the $Gd_{9.05}Eu_{0.28}(SiO_4)_6O_2$ phosphor.

Figure 6.16 presents the radiative theoretical (calculated via the total spontaneous emission probability) lifetime values as a function of temperature. The theoretical τ_{rad} values are summarised in Table 6.9. τ_{rad} increases with increasing temperature. The Eu^{3+} temporal decay became faster at higher temperatures. This may be due to the $Gd^{3+} \rightarrow Eu^{3+}$ energy transfer occurring more efficiently as it is aided by the vibrational motion experienced at high temperatures.

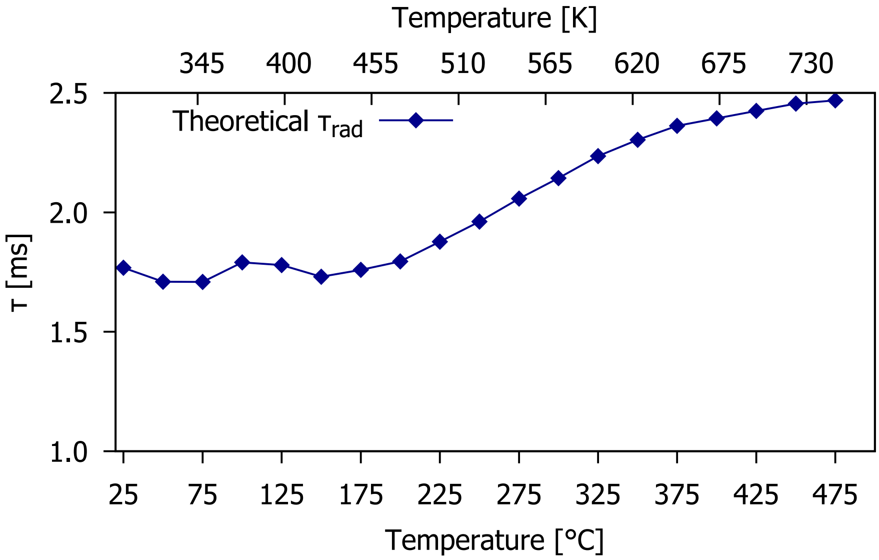

Figure 6.16: Temperature-dependent lifetime values for the $Gd_{9.05}Eu_{0.28}(SiO_4)_6O_2$ phosphor.

Table 6.9 shows the branching ratios (Equation 6.6, β_λ) for the $^5D_0 \rightarrow {}^7F_\lambda$ (λ = 1, 2 and 4) transitions. These values can be used to predict the relative intensity of an emission originating from the $^5D_0$ level. The branching ratio (relative contribution to the emission spectrum) for the $^5D_0 \rightarrow {}^7F_2$ emission transition is more than 67% at room temperature. Therefore, it is possible to have 67% of all decay processes result from MD emission ($^5D_0 \rightarrow {}^7F_2$).

Temperature (° C)	Ω_2 (cm^{-1})	Ω_4 (cm^{-1})	A_1 (s^{-1})	A_2 (s^{-1})	A_4 (s^{-1})	β_1 ratio	β_2 ratio	β_4 ratio	τ_{theo} (ms)
25	7.28	3.01	84.43	391.71	80.18	0.151	0.672	0.121	1.77
50	7.25	3.03	84.43	389.96	80.75	0.146	0.646	0.118	1.71
75	7.23	3.05	84.44	388.83	81.10	0.146	0.644	0.119	1.71
100	7.11	3.01	84.44	382.30	80.00	0.153	0.664	0.123	1.79
125	7.15	3.06	84.45	384.22	81.36	0.152	0.662	0.124	1.78
150	7.05	3.05	84.47	378.99	81.27	0.148	0.635	0.120	1.73
175	6.89	3.03	48.48	370.42	80.69	0.150	0.631	0.122	1.76
200	6.68	3.07	84.49	358.77	81.67	0.153	0.623	0.125	1.79
225	6.28	2.98	84.51	337.58	79.31	0.160	0.613	0.127	1.88
250	5.86	3.00	84.53	315.01	79.92	0.168	0.598	0.134	1.96
275	5.42	3.00	84.55	291.30	80.00	0.176	0.580	0.141	2.06
300	5.42	3.02	84.57	270.58	80.74	0.183	0.561	0.148	2.14
325	4.63	3.05	84.59	249.05	81.44	0.191	0.538	0.156	2.24
350	4.32	3.10	84.62	231.94	82.89	0.197	0.516	0.163	2.30
375	4.03	3.16	84.64	216.20	84.70	0.202	0.493	0.121	2.36
400	3.83	3.23	84.65	205.30	86.71	0.205	0.474	0.178	2.39
425	3.68	3.25	84.67	196.77	87.33	0.207	0.460	0.181	2.43
450	3.57	3.23	84.69	190.79	86.67	0.210	0.452	0.182	2.46
475	3.48	3.25	84.70	185.86	87.16	0.211	0.442	0.184	2.47

Table 6.9: Judd-Ofelt parameters, radiative transition possibilities of $^5D_0 \rightarrow {}^7F_\lambda$ (λ = 1, 2, 4) transitions, branching ratios, radiative theoretical and experimental lifetime values for the $Gd_{9.05}Eu_{0.28}(SiO_4)_6O_2$ phosphors at different temperatures.

6.4 Conclusions and future work

The narrow-band red phosphor series based on an apatite-type silicate host were synthesised and characterised by X-ray diffraction and optical measurements.

The $Gd_{9.33-x}Eu_x(SiO_4)_6O_2$ (x = 0.03, 0.05, 0.07, 0.09, 0.19, 0.28, 0.47, 0.65, 0.93, 1.40 and 1.87) phosphor was systematically doped. The connectivity between the sites occupied by the sensitiser (Gd^{3+}) and activator (Eu^{3+}) was studied to investigate the self-quenching probability. The critical distance was calculated to determine the non-radiative energy transfer mechanism. For the $Gd_{9.33-x}Eu_x(SiO_4)_6O_2$ series it was estimated to be 5.140(6) Å.

The lack of phase transitions and the reversible heating and cooling process was researched by the VT-PXRD pattern of the $Gd_{9.05}Eu_{0.28}(SiO_4)_6O_2$ compound. The thermal coefficients calculated confirmed normal positive thermal expansion.

The emission spectra at room temperature confirmed that the centre wavelength for the highest peak was at 614 nm, which is exactly the wavelength that maximises the efficiency of the red component for white lighting. In addition, the linewidth was calculated to be 7 nm for the 614 nm emission peak, which is within the critical 20 nm needed to avoid spillover into deeper red, where the human vision response drops. Therefore, the $Gd_{9.05}Eu_{0.28}(SiO_4)_6O_2$ compound series were confirmed to be narrow-band red phosphors.

The emission spectra for the different doping levels confirmed that concentration quenching was reached for doping levels higher than x=0.93. Future work should focus on doping the host with Eu^{3+} content 0.93>x<1.40 to know exactly at what doping level the emission intensity starts to drop. This was not possible in this project due to the length of time needed to synthesise the materials and laboratory time being reduced because of external conditions.

Temperature has a critical influence on the performance of LEDs. Variable temperature spectra were recorded to observe the behaviour of the phosphors at LED working temperature, ~150 °C. Thermal quenching was studied in depth for the $Gd_{9.05}Eu_{0.28}(SiO_4)_6O_2$ phosphor. The activation energy, ΔE_{CT}, was calculated to be 0.54(1) eV. Furthermore, the normalised emission integrals plotted as a function of temperature show a loss of only 10% at 150 °C.

The maximum energy splitting values for the $^7F_1$ manifold (ΔE) confirmed a direct relationship with the intensity of the crystal field. Judd-Ofelt intensity parameters for $Gd_{9.33-x}Eu_x(SiO_4)_6O_2$ (x = 0.03, 0.05, 0.07, 0.09, 0.19, 0.28, 0.47, 0.65, 0.93, 1.40 and 1.87) suggested a site selection for part of the Eu^{3+}. The decrease of the Ω_2 as a function of doping level determines an increase in symmetry around Eu^{3+}, hence a preference to occupy the 4f site (site symmetry C_3). The behaviour of the Ω_2 for the $Gd_{9.05}Eu_{0.28}(SiO_4)_6O_2$ compound at different temperatures demonstrated an increase in symmetry at high temperature.

6.5 Note

The work presented in this chapter is being prepared as manuscript:

Rodríguez-García, M.M., Williams, J. A. G. and Evans, I.R. Narrow-band red-emitting phosphors based on Eu^{3+}-doped $Gd_{9.33}(SiO_4)_6O_2$ (in preparation, 2020).

6.6 References

[1] Brodrick, J. *Solid-state Lighting R & D plan, Department of Energy, June*, 2016.

[2] Morgan Pattison, P., Hansen, M., and Tsao, J.Y. *Comptes Rendus Physique*, 19(3), 2018.

[3] Tsao, J.Y., Coltrin, M.E., Crawford, M.H., and Simmons, J.A. *Proceedings of the IEEE*, 98(7), 2010.

[4] Phillips, J., Coltrin, M., Crawford, M., Fischer, A., Krames, M., Mueller-Mach, R., Mueller, G., Ohno, Y., Rohwer, L., Simmons, J., and Tsao, J. *Laser & Photonics Reviews*, 1(4), 2007.

[5] Binnemans, K. *Coordination Chemistry Reviews*, 295, 2015.

[6] Görller-Walrand, C. and Binnemans, K. *Chapter 167 Spectral intensities of f-f transitions*, volume 25, Elsevier1998.

[7] Baur, F. and Jüstel, T. *Optical Materials: X*, 1, 2019.

[8] Bünzli, J.C.G. and Eliseeva, S.V. *Basics of Lanthanide Photophysics*, Springer Berlin Heidelberg, Berlin, Heidelberg2011.

[9] Judd, B.R. *Physical Review*, 127(3), 1962.

[10] Ofelt, G.S. *The Journal of Chemical Physics*, 37(3), 1962.

[11] Dačanin, L., Lukić, S.R., Petrović, D.M., Nikolić, M., and Dramićanin, M.D. *Physica B: Condensed Matter*, 406(11), 2011.

[12] Ćirić, A., Stojadinović, S., Sekulić, M., and Dramićanin, M.D. *Journal of Luminescence*, 205, 2019.

[13] Brik, M.G., Antic, Zcaron, eljka, M., Vukovic, K., and Dramicanin, M.D. *MATERIALS TRANSACTIONS*, 56(9), 2015.

[14] Werts, M.H.V., Jukes, R.T.F., and Verhoeven, J.W. *Physical Chemistry Chemical Physics*, 4(9), 2002.

[15] He, X., Bian, D., Wang, H., and Xu, J. *Luminescence*, 28(6), 2013.

[16] Zhang, X., Zhou, L., Pang, Q., Shi, J., and Gong, M. *The Journal of Physical Chemistry C*, 118(14), 2014.

[17] Ding, J., Li, Y., Wu, Q., Long, Q., Wang, C., and Wang, Y. *Journal of Materials Chemistry C*, 3(33), 2015.

[18] Li, Y.C., Chang, Y.H., Tsai, B.S., Chen, Y.C., and Lin, Y.F. *Journal of Alloys and Compounds*, 416(1-2), 2006.

[19] Ma, X., Liao, L., Guo, Q., Liu, H., Zhou, T., and Mei, L. *RSC Advances*, 8(48), 2018.

[20] Guo, N., Liang, Q., Li, S., Ouyang, R., and Lü, W. *Optical Materials*, 73, 2017.

[21] Liu, Y., Wang, Z., Zhong, J., Pan, F., Liang, H., and Xiao, Z. *Materials Letters*, 129, 2014.

[22] Roh, H.S., Lee, S., Caliskan, S., Yoon, C., and Lee, J.K. *Journal of Alloys and Compounds*, 772, 2019.

[23] Li, L., Chang, W., Chen, W., Feng, Z., Zhao, C., Jiang, P., Wang, Y., Zhou, X., and Suchocki, A. *Ceramics International*, 43(2), 2017.

[24] Fu, Z., Wang, X., Yang, Y., Wu, Z., Duan, D., and Fu, X. *Dalton Transactions*, 43(7), 2014.

[25] Shi, L., Zhao, S.w., Ying, Z., Han, Y.j., Li, M., Zhang, M.y., and Zhang, Z.w. *Journal of Materials Science: Materials in Electronics*, 30(2), 2019.

[26] Zhu, P., Zhu, H., Qin, W., Dantas, B.H., Sun, W., Tan, C.K., and Tansu, N. *Journal of Applied Physics*, 119(12), 2016.

[27] Rodríguez-García, M.M., Williams, J.A.G., and Evans, I.R. *Journal of Materials Chemistry C*, 2019.

[28] Latshaw, A.M., Hughey, K.D., Smith, M.D., Yeon, J., and zur Loye, H.C. *Inorganic Chemistry*, 54(3), 2015.

[29] Bruker AXS, K., 2000.

[30] Coelho, A.A., Evans, J.S.O., Evans, I.R., Kern, A., and Parsons, S. *Powder Diffraction*, 26(4), 2011.

[31] Dexter, D.L. *Journal of Chemical Physics*, 21(5), 1953.

[32] Blasse, G. *ENERGY TRANSFER IN OXIDIC PHOSPHORS*, volume 24. 1969.

[33] Chen, Y.L., Wang, J., and Wang, G.Q. *Optical Materials*, 106, 2020.

[34] Rajendran, M. and Vaidyanathan, S. *Journal of Alloys and Compounds*, 789, 2019.

[35] Annadurai, G., Devakumar, B., Sun, L., Guo, H., Wang, S., and Huang, X. *Journal of Luminescence*, 215, 2019.

[36] Batsanov, S.S., Ruchkin, E.D., and Poroshina, I.A. *Refractive Indices of Silicates and Germanates*, Springer2016.

[37] Auzel, F. *Journal of Alloys and Compounds*, 380(1), 2004.

[38] Jansen, T., Jüstel, T., Kirm, M., Mägi, H., Nagirnyi, V., Tõldsepp, E., Vielhauer, S., Khaidukov, N.M., and Makhov, V.N. *Journal of Luminescence*, 186, 2017.

[39] Sobierajska, P. and Wiglusz, R.J. *New Journal of Chemistry*, 43(37), 2019.

[40] Szyszka, K., Rewak-Soroczynska, J., Dorotkiewicz-Jach, A., Ledwa, K.A., Piecuch, A., Giersig, M., Drulis-Kawa, Z., and Wiglusz, R.J. *Journal of Inorganic Biochemistry*, 203, 2020.

[41] Zawisza, K. and Wiglusz, R.J. *Dalton Transactions*, 46(10), 2017.

[42] Wiglusz, R.J., Bednarkiewicz, A., Lukowiak, A., and Strek, W. *Spectroscopy Letters*, 43(5), 2010.

[43] Sobierajska, P., Pazik, R., Zawisza, K., Renaudin, G., Nedelec, J.M., and Wiglusz, R.J. *Crystengcomm*, 18(19), 2016.

[44] Rajendran, M. and Vaidyanathan, S. *Dalton Transactions*, 49(27), 2020.

[45] Baur, F., Glocker, F., and Jüstel, T. *Journal of Materials Chemistry C*, 3(9), 2015.

[46] Janulevicius, M., Grigorjevaite, J., Merkininkaite, G., Sakirzanovas, S., and Katelnikovas, A. *Journal of Luminescence*, 179, 2016.

[47] Nikolić, M.G., Jovanović, D.J., and Dramićanin, M.D. *Applied Optics*, 52(8), 2013.

[48] Dačanin, L.R., Lukić-Petrović, S.R., Petrović, D.M., Nikolić, M.G., and Dramićanin, M.D. *Journal of Luminescence*, 151, 2014.

[49] Antić, e., Krsmanović, R., Wojtowicz, M., Zych, E., Bártová, B., and Dramićanin, M.D. *Optical Materials*, 32(12), 2010.

7 Cu(II)-containing silicate near infrared (NIR) emitters: the relationship between the structural distortion within the CuO_4 chromophore and luminescence properties

7.1 Introduction

A number of mixed-metal silicates have been reported to exhibit near infra-red (NIR) emission, a property that can be exploited in many applications. For example, they can be used in biomedical imaging for early detection and diagnosis of diseases[1] using the NIR imaging window, which falls in the region of minimal tissue absorbance and autofluorescence between 650 nm and 1450 nm.[2, 3] Another possible use is in time-gated luminescence techniques, which rely on the use of luminophores with lifetime values thousands of times longer than those of prompt fluorescent dyes.[4, 5] Time-gated luminescence takes advantage of long-lived luminescent probes and time-delayed detection, giving a better signal-to-noise ratio. The detector is gated off during a resolving period while short-lived fluorescence fades, producing an autofluorescence-free spectrum and image.[6–9] Long-lived NIR emitters are suitable to be used in bioimaging with the NIR-emissive particles functioning as reporters of lifetime multiplexing and barcoding in cells.[10]

Calcium copper silicate, formula $CaCuSi_4O_{10}$, is an excellent NIR emitter. It is also known as Egyptian blue as it was the first synthetic pigment made in ancient Egypt[11–13] and one of the first luminescent pigments exploited for non-invasive wide-field imaging of artwork.[14] This material adopts the cuprorivaite structure type and has high chemical and thermal stability, as demonstrated by the lack of photo-bleaching and the presence of bright NIR luminescence in ancient artefacts.[15] Egyptian blue exhibits an exceptionally long-lived excited state, $\tau = 107$ μs, and the highest known room temperature photoluminescence quantum yield in the NIR region, around 10.5% with $\lambda_{max} = 910$ nm, which originates from d-d transition of divalent copper ions.[15]

There are several known pigments similar to Egyptian blue, including Han purple, Han blue ($BaCuSi_2O_6$ and $BaCuSi_4O_{10}$ respectively) and $SrCuSi_4O_{10}$. The optical properties of $BaCuSi_4O_{10}$ and $SrCuSi_4O_{10}$ have been reported in the literature. They have emissions associated with the $^2B_{2g} \rightarrow {}^2B_{1g}$ transition at 948 nm and 914 nm[16, 17] respectively. Hydrothermally prepared synthetic $BaCuSi_2O_6$[18] and $BaCuSi_4O_{10}$ microspheres and $SrCuSi_4O_{10}$ microparticles[19] are reported to have a luminescence decay value of 6.4 μs for $\lambda_{max} = 925$ nm, 33.3 μs for $\lambda_{max} = 977$ nm and 15.8 μs for $\lambda_{max} = 956$ nm respectively. Hydrothermally synthesised pigments tend to have larger surface areas and shorter decay times than their counterparts prepared by conventional solid state reactions. For $BaCuSi_2O_6$, $BaCuSi_4O_{10}$ and $SrCuSi_4O_{10}$ synthesised using the solid-state method, the lifetime values are 20 μs, 132μs and 149 μs.[20] Two other copper-containing silicates, $K_2CuSi_4O_{10}$ and $BaCu_2Si_2O_7$, have been studied in terms of their structural[21] and antiferromagnetic[22–26] properties respectively, but not yet for their potential properties as NIR emitters.

The luminescence properties of Egyptian Blue have been attributed to the presence of Cu(II) chromophores in a square planar environment within the structure (as shown in Figure 7.3).[27] However, no systematic structural investigation of the relationship between the Cu(II) coordination environment in Egyptian blue and similar materials and their luminescence properties has been reported. A detailed study of the relationship between the structural CuO_4^{6-} environment geometry and optical properties (emission, absorption and lifetime) is therefore needed to understand and optimise the copper silicate structure necessary for a long-lived NIR emitter.[15, 16, 28]

As mentioned above, there is interest in exploiting different types of NIR emitters in the bioassay and bioimaging industry. However, NIR fluorescent organic dyes tend to bleach and are therefore not suitable for long term imaging.[29, 30] In contrast, silicate nanomaterials have demonstrated excellent photophysical characteristics. For example, $CaCuSi_4O_{10}$ nanosheets[7] exhibit no bleaching and ultra-high brightness compared to other NIR-emitters. They are a highly versatile, bright, photostable and biocompatible NIR fluorescent material that have the potential for a wide range of bioimaging applications both in animal and plant systems.[31, 32] Novel NIR emitters have been studied as nanoparticles, which can be easily used in spectral multiplexing, where emitters can be excited at the same wave-length and distinguished by their different emission spectra, or even lifetimes.[4, 10]

In this work, four Cu(II)-containing silicate pigments, namely $CaCuSi_4O_{10}$, $BaCuSi_4O_{10}$, $K_2CuSi_4O_{10}$ and $BaCu_2Si_2O_7$, were synthesised in powder and single crystal form and a detailed study of the relationship between their structural and optical properties was carried out.

In addition, $K_2CuSi_4O_{10}$ nanoparticles were prepared following the exfoliation method to obtain nanosheets, which have previously been used to obtain $CaCuSi_4O_{10}$ nanoparticles[6] and their optical properties were investigated.

7.2 Experimental details

7.2.1 Sample preparation

Polycrystalline $CaCuSi_4O_{10}$, $BaCuSi_4O_{10}$ and $BaCu_2Si_2O_7$ were prepared using the standard solid-state reaction method. Stoichiometric amounts of $CaCO_3$ (0.00714 mol), SiO_2 (0.02857 mol) and CuO (0.00714 mol) for $CaCuSi_4O_{10}$ and $BaCO_3$ (0.00387 mol), SiO_2 (0.015468 mol) and CuO (0.00387 mol) for $BaCuSi_4O_{10}$ were ground with an agate mortar and pestle and heated and ground repeatedly for a total of about 56 hours at 1100 °C. $BaCu_2Si_2O_7$ was synthesised by ball milling stoichiometric amounts of $BaCO_3$ (0.00420 mol), SiO_2 (0.00839 mol) and CuO (0.00839 mol) in an agate milling medium with ethanol at 250 rpm for 1 hour, pressing the reagents into a rod and repeatedly calcining at 1015 °C for a total of about 140 hours with intermediate regrinding.

The preparation of polycrystalline $K_2CuSi_4O_{10}$ was based on synthesis of the $Na_{2-x}K_xCuSi_4O_{10}$ (x = 0, 0.5, 1) series.[33] A stoichiometric amount of CH_3CO_2K (0.00966 mol) was dissolved in H_2O (10 ml) and added to a stirred solution of $Cu(CH_3CO_2)_2$ (0.00483 mol) in CH_3CH_2OH (20 ml) while heating to 50 °C. The solution remained clear and pale blue in colour after adding $Si(OC_2H_5)_4$ and subsequently a drop of NH_4OH. The resulting solution was covered and left to stir overnight at room temperature, during which time the mixture gelled. The excess solvent and water were removed upon heating to obtain a bluish solid which was dried overnight in an oven at 90 °C. The dried solid was thoroughly ground with an agate mortar and pestle before being calcined for about 200 hours at 750 °C with intermittent grinding.

Single crystals of $CaCuSi_4O_{10}$ and $BaCuSi_4O_{10}$ were grown using the molten flux method. Stoichiometric samples were ground with 30 wt% of borax flux and calcined at 800 °C for 24 hours and then cooled down to 25 °C at a rate of 4 °C/hr. Attempts to grow $K_2CuSi_4O_{10}$ single crystals using this method were not successful.

Single crystals of $BaCu_2Si_2O_7$ were grown using the optical floating-zone (FZ) method. Around 20 g of pure $BaCu_2Si_2O_7$ powder was pressed into 2 rods of 6 mm diameter using a hydrostatic press at 50 MPa and sintered at 1015 °C for 52 h. Crystals were grown from the molten phase using an optical FZ furnace (Crystal Systems Corporation, FZ-T-10000-H-VIII-VPO-PC) equipped with four 300 W halogen lamps. The rods were mounted in the furnace and maintained in an oxygen atmosphere at approximately 0.6 MPa (flowing at 0.5 L/min). The feed rod started to melt at 45.8% power output and the crystal was grown at a rate of 5 mm/hr with counter-rotation of the rods at 20 rpm.

7.2.2 Exfoliation of $K_2CuSi_4O_{10}$

In the exfoliation process to obtain $K_2CuSi_4O_{10}$ nanoparticles, the as-prepared $K_2CuSi_4O_{10}$ material was delaminated following the exfoliation method.[6] A colloidal dispersion was obtained by stirring the bulk material for 4 weeks in 80 °C water. This dispersion was left to sediment for 24 hours, giving a milky pearlescent solution, which was decanted and filtered using a 25 nm Whatman Anodisk filter (Aldrich).

7.2.3 X-ray diffraction

To confirm the phase identity of the polycrystalline samples, laboratory powder X-ray diffraction (PXRD) patterns were recorded on a Bruker AXS d8 Advance diffractometer using $CuK_{\alpha1,2}$ radiation and a LynxEye detector, following the data collection convention described in section 2.2.3. Polycrystalline $K_2CuSi_4O_{10}$ was characterised using high-resolution powder diffraction beamline (I11) at Diamond Light Source with a wavelength of $\lambda = 0.82576$ Å. The sample was placed in a borosilicate glass capillary and data were collected in the 0° to 150° 2θ range at room temperature.

All the PXRD data were analysed with Rietveld refinements using Topas Academic software.[34, 35] The parameters refined included the background terms, zero point, peak shape (pseudo-Voigt function), preferred orientation, unit cell parameters and the overall isotropic atomic displacement parameters for all the atoms in the structure.

Single crystal X-ray diffraction data were collected at 120 K on a Bruker D8 Venture diffractometer using MoK$_\alpha$ radiation and a Photon100 CMOS detector. Samples with approximately isotropic shapes were selected and, using Fomblin oil, were placed in a 300 μm polymer loop located in a brass holder set in a goniometer head. APEX3[36] software was used to centre the single crystal, collect and reduce data and identify the unit cell. The structure refinements were performed in Jana2006.[37]

7.2.4 Photoluminescence spectroscopy

All the optical measurements were performed on samples placed in glass capillary tubes. Diffuse reflectance spectra were collected using a fibre optic probe,[38] a tungsten light source (Ocean Optics, HL-2000-HP) equipped with a temperature-balancing filter (Thor Labs) and a commercial CCD spectrometer (Ocean Optics, Maya2000-Pro). The spectra were referenced to the white Spectralon® standard. Emission spectra were collected using a custom-built system: a fibre-coupled diode laser (633 nm) was reflected from a long-pass filter (Semrock 633 nm RazorEdge) and focused onto the sample using a 10x reflective microscope objective. Fluorescence data were collected via the same objective and a long-pass filter which rejects any scattered excitation light. The transmitted light was collected via a fibre optic and analysed using a CCD/spectrograph (Ocean Optics, Maya2000-Pro). The spectral response of the optics and the spectrometer were corrected for using the output of a tungsten lamp (Ocean Optics, HL-2000-HP, 2900 K stated colour temperature).

Fluorescence lifetimes were measured using time-correlated single photon counting and collected using a customised system: excitation was provided by a pulsed 658 nm laser diode (Roithner LaserTechnik, RLT650-100MGE) with sub-10 μs pulses and a repetition rate of 100 Hz. Emission data were collected at 90° to the excitation and the emission wavelength of 950 nm was selected using a monochromator (Bentham, TM300) and measured using a single-photon-counting silicon avalanche photodiode (Perkin Elmer SPCM-AQR-13). Digitisation and data collection were achieved using a USB oscilloscope (National Instruments, USB-5133) sampling at 100 MS/s controlled using LabVIEW software (National Instruments).

7.2.5 Atomic Force Microscopy

$K_2CuSi_4O_{10}$ nanoparticles were dispersed in isopropanol at a concentration 0.01% (w/w). A Digital Instruments Nanoscope IV scanning probe microscope was used to record different sites in the wafer, obtaining the length and depth of the particles. The dispersed $K_2CuSi_4O_{10}$ nanoparticles were sonicated before being placed on a silica wafer.

7.2.6 Scanning Electron Microscopy

The $K_2CuSi_4O_{10}$ nanoparticles were scattered on a carbon stickers attached to a glass slide. Then it was coated with 30 nm of carbon. A Hitachi SU-70 Field Emission Gun Scanning Electron Microscope (FEG SEM) was used to analyse the samples (Department of Physics, Durham). The FEG SEM was optimised to an energy of 15 keV and calibrated with a cobalt chip.

7.3 Results and discussion

7.3.1 Structure characterisation

$CaCuSi_4O_{10}$[39] and $BaCuSi_4O_{10}$[40] crystallise in tetragonal space group $P4/ncc$, while $K_2CuSi_4O_{10}$ and $BaCu_2Si_2O_7$ adopt monoclinic space group $P2_1/m$[21] and orthorhombic space group $Pnma$[26, 41] respectively. The Rietveld fits to the PXRD data (Figure 7.1) confirm single-phase products suitable for the determination of optical properties. The unit cell parameters obtained from the refinements are presented in Table 7.1.

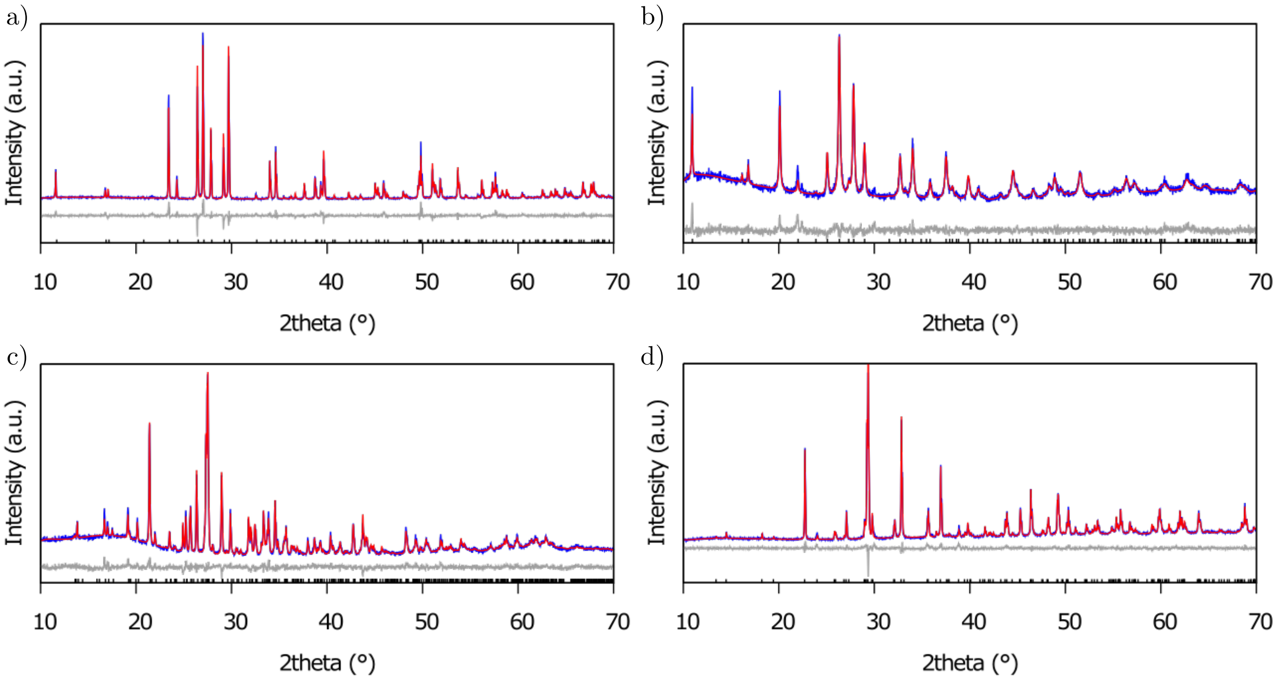

Figure 7.1: Rietveld fit of laboratory PXRD data for a) $CaCuSi_4O_{10}$, $R_{wp} = 6.49\%$, b) $BaCuSi_4O_{10}$, $R_{wp} = 4.20\%$, c) $K_2CuSi_4O_{10}$, $R_{wp} = 4.62\%$ and d) $BaCu_2Si_2O_7$, $R_{wp} = 4.26\%$.

Formula	a [Å]	b [Å]	c [Å]	β [°]	V [$Å^3$]
$CaCuSi_4O_{10}$	7.30137(7)	7.30137(7)	15.1291(2)	n/a	806.53(2)
$BaCuSi_4O_{10}$	7.4466(6)	7.4466(6)	16.137(2)	n/a	894.9(2)
$K_2CuSi_4O_{10}$	11.28391(5)	8.24929(4)	11.06834(5)	110.9179(4)	962.384(7)
$BaCu_2Si_2O_7$	6.86382(8)	13.1799(2)	6.9004(1)	n/a	624.24(1)

Table 7.1: Unit cell parameters for $CaCuSi_4O_{10}$, $BaCuSi_4O_{10}$, $K_2CuSi_4O_{10}$ and $BaCu_2Si_2O_7$ obtained from the PXRD.

In order to correlate the key structural details with the optical properties of these materials, structure determination from single crystals (shown in Figure 7.2) was carried out for $CaCuSi_4O_{10}$, $BaCuSi_4O_{10}$ and $BaCu_2Si_2O_7$. For $K_2CuSi_4O_{10}$, high resolution synchrotron PXRD data (pattern in Appendix A.6.3) were used instead, since single crystals could not be grown. The structural details are in Appendix A.6. The CuO_4^{6-} chromophore bonds and angles for the four materials are presented in Table 7.2.

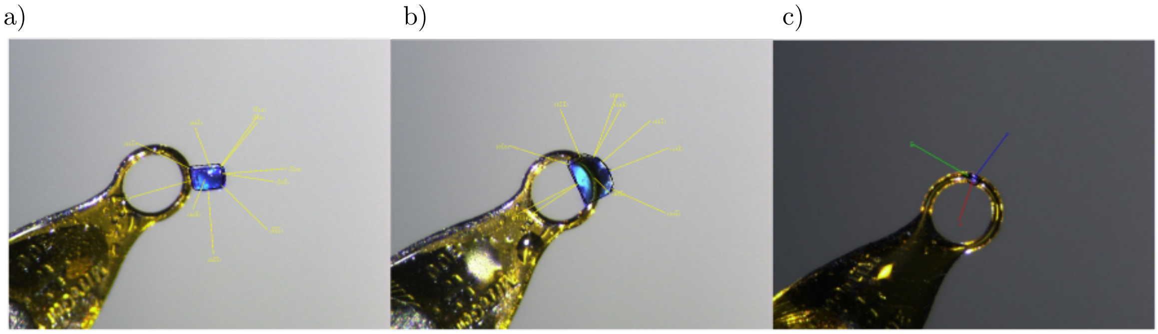

Figure 7.2: Image of the single crystals for a) $CaCuSi_4O_{10}$, b) $BaCuSi_4O_{10}$ and c) $BaCu_2Si_2O_7$.

Formula	$CaCuSi_4O_{10}$	$BaCuSi_4O_{10}$	$^*K_2CuSi_4O_{10}$	$BaCu_2Si_2O_7$
Cu-O Bond [Å]	1.925(1) ×4	1.924(3) ×4	1.948(6) 1.979(6) 1.946(6) 1.910(5)	1.922(2) 1.947(3) 1.963(3) 1.920(2)
O-Cu-O Adjacent angles [°]	89.9991(3) ×4	89.942(4) ×4	92.4(3) 88.5(3) 91.4(3) 87.8(3)	88.55(9) 93.65(9) 89.71(9) 91.09(9)
O-Cu-O Opposite angles [°]	180 ×2	176.4(1) ×2	170.3(3) 178.9(3)	167.65(5) 165.81(9)

Table 7.2: Bonds and angles of the different cuprosilicate pigments, from single crystals and high quality PXRD. *From powder data, obtained using high quality synchrotron PXRD.

In order to describe the distortion of the CuO_4^{6-} chromophore, a simple geometry index can be used.[42] This is defined by Equation 7.1:

$$\tau_4 = \frac{360° - (\alpha + \beta)}{141°}, \tag{7.1}$$

where α and β are the opposite angles in the four-coordinate environment. τ_4 is defined as zero for square planar geometry (as the opposite angles are 180°), while $0 < \tau_4 < 0.85$ describes a lower symmetry CuO_4^{6-} geometry. A limitation of the τ_4 index is that it does not differentiate between pyramid and seesaw geometry; instead it only approximately indicates the degree of distortion from square plane.

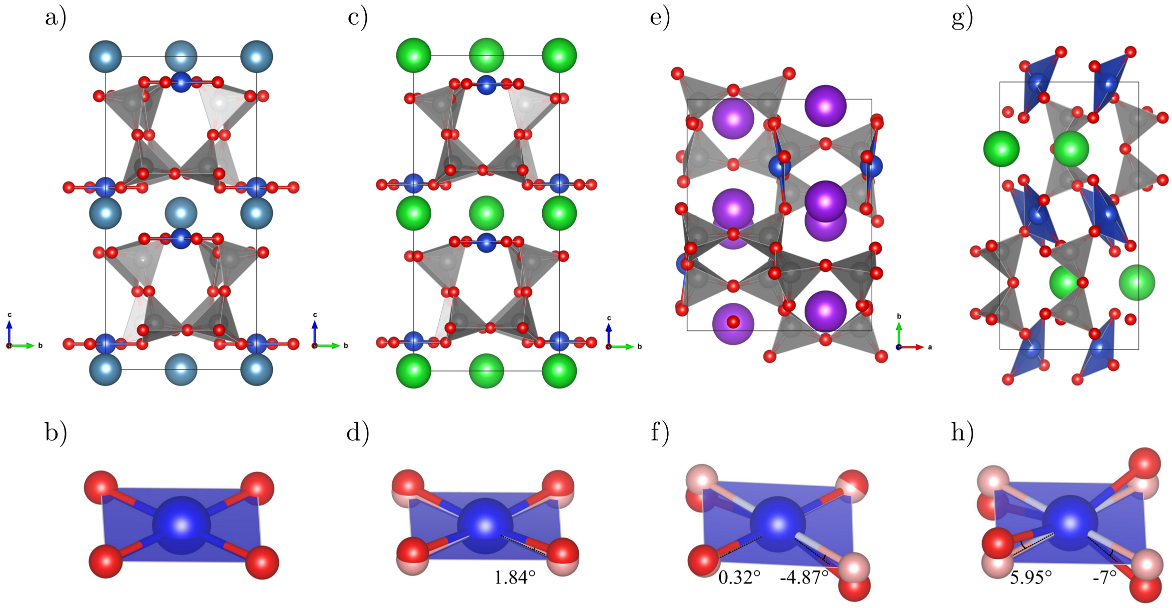

Figure 7.3: a) The tetragonal structure of $CaCuSi_4O_{10}$, space group $P4/ncc$. View along the a axis. b) View of CuO_4^{6-} in $CaCuSi_4O_{10}$, in a square planar environment. c) The tetragonal structure of $BaCuSi_4O_{10}$, space group $P4/ncc$. View along the a axis. d) View of CuO_4^{6-} in $BaCuSi_4O_{10}$, in a distorted square planar environment. e) The monoclinic structure of $K_2CuSi_4O_{10}$, space group $P2_1/m$. View along the a axis. f) View along the b axis of CuO_4^{6-} in $K_2CuSi_4O_{10}$, in a distorted square planar environment. g) The orthorhombic structure of $BaCu_2Si_2O_7$, space group $Pnma$. View along the c axis. h) View of CuO_4^{6-} in $BaCu_2Si_2O_7$, in a distorted square planar environment. Ca shown as light blue spheres, Ba as light green spheres, K as purple spheres, Cu as dark blue spheres, SiO_4^{4-} as grey tetrahedra and O as red spheres. CuO_4^{6-} in square plane corresponding to $CaCuSi_4O_{10}$ is shown in light pink and light blue for comparison of the distortion.

In $CaCuSi_4O_{10}$, the Cu(II) ion on the 4c Wyckoff site (site symmetry 4) is in a square planar CuO_4^{6-} environment ($\tau_4 = 0$), with four equidistant 1.925(2) Å Cu-O bonds, as shown in Figure 7.3b. The close similarity between the structures of Egyptian blue ($CaCuSi_4O_{10}$) and Han blue ($CaCuSi_4O_{10}$) is shown in Figure 7.3a and c. The SiO_4^{4-} tetrahedra share three corners with other adjacent SiO_4^{4-} tetrahedra and one corner with the CuO_4^{6-} square. The SiO_4^{4-} tetrahedra linked in this way form sheets parallel to the (ab) plane. In isostructural $BaCuSi_4O_{10}$, the Cu(II) is in the same Wyckoff site and the Cu-O bonds stay equidistant (1.924(3) Å) but there is a small distortion of the CuO_4^{6-} environment away from planar towards square pyramidal: the O-Cu-O angles between the nearest pairs of O atoms deform to 89.942(4)° and the opposite angle to 176.4(1)°, giving a distortion index with $\tau_4 = 0.052(1)$.

In the $K_2CuSi_4O_{10}$ structure (Figure 7.3e), the CuO_4^{6-} groups (with Cu(II) on the 4f Wyckoff site, with site symmetry 1) share two corners each to form 8-membered rings in the (ac) plane. These rings then link up by corner-sharing to form columns in the b-direction. The Cu-O bond lengths range from 1.910(5) to 1.979(6) Å, the O-Cu-O opposite angles range from 87.8(3)° to 92.4(3)° and the adjacent angles from 170.3(3)° to 178.9(3)°. The CuO_4^{6-} chromophore environment (Figure 7.3f) shows a distortion level of $\tau_4 = 0.077(3)$.

As is illustrated in Figure 7.3g, the $BaCu_2Si_2O_7$ structure contains SiO_4^{4-} tetrahedra sharing a corner with an adjacent SiO_4^{4-} tetrahedron, two corners with a CuO_4^{6-} group and a corner with two adjacent CuO_4^{6-} groups. Cu(II) is located on the 8d Wyckoff site, with site symmetry 1. The Cu-O bond lengths vary from 1.920(2) to 1.963(3) Å, the O-Cu-O adjacent angles range from 88.55(9)° to 93.65(9)° and the opposite angles from 165.81(9)° to 167.65(5)°. A large distortion of the CuO_4^{6-} group environment is shown in Figure 7.3h with $\tau_4 = 0.1882(7)$, the highest in the series.

7.3.2 NIR luminescence

Diffuse reflectance spectra (Figure 7.4a) were recorded for each material and the corresponding absorption spectra were calculated using the Kubelka-Munk model.[43]

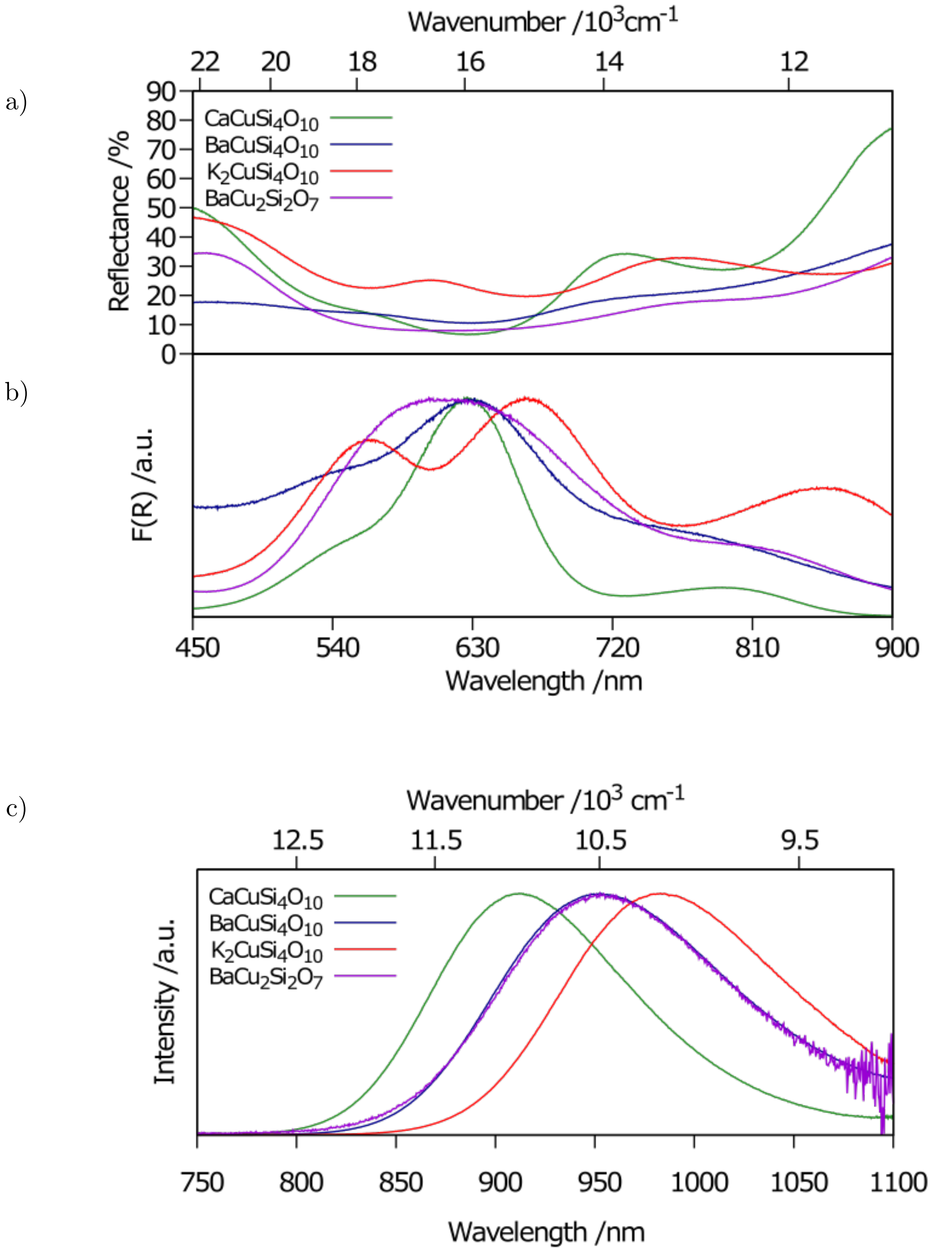

Figure 7.4: a) Diffuse reflectance, b) normalised absorption and c) emission spectra for $CaCuSi_4O_{10}$ (green), $BaCuSi_4O_{10}$ (blue), $K_2CuSi_4O_{10}$ (red) and $BaCuSi_2O_7$ (purple) powder samples.

To interpret the reflectance, the Kubelka-Munk function was applied to obtain the absorption spectrum, shown in Figure 7.4b. The absorption spectrum shows three peaks arising from three different electronic transitions (shown in Figure 7.5, details in Table 7.3. Figure 7.3 presents the symmetry of the Cu(II) environment for each sample.): $^2B_{1g} \rightarrow {}^2A_{1g}$, $^2B_{1g} \rightarrow {}^2E_g$ and $^2B_{1g} \rightarrow {}^2B_{2g}$ for the D_{4h} symmetry[12] and $^2A_1(x^2\text{-}y^2) \rightarrow {}^2A_1\ (z^2)$, $^2A_1\ (x^2\text{-}y^2) \rightarrow {}^2B_1$ (yz), $^2B_2$ (xz) and $^2A_1\ (x^2\text{-}y^2)$ $\rightarrow {}^2A_2$ (xy) for the C_{2v} symmetry.[44] These absorption peaks are attributed to the electric dipole $d \rightarrow d$ transitions in Cu(II) which are allowed by vibronic coupling. Figure 7.5 shows the energy diagram for the Cu(II) ion, obtained from the spectra collected in Figure 7.4. The ^2D free ion energy state of a Cu^{2+} ion is located in an octahedral (O_h) symmetry undergoes splitting into two sublevels, T_{2g} and

E_g, which then the geometry tetragonally distorts into two further sublevels for the D_{4h} symmetry: ^2E_g and $^2B_{2g}$; $^2A_{1g}$ and $^2B_{1g}$ respectively. For the C_{2v} symmetry, the O_h levels split into two sublevels T_{2g} and E_g and these split into three and two sublevels: $^2B_1(yz)$, $^2B_2(xz)$ and $^2A_2(xy)$; and $^2A_1(z^2)$ and $^2A_1(x^2\text{-}y^2)$ respectively. Levels $^2A_{1g}$ and $^2A_1$ (z^2) originate from the degenerate ground state E_g and are higher in energy by distortion than the ^2T_g levels, where the lowest energy absorption peak corresponds to the $^2B_{2g} \rightarrow {}^2B_{1g}$ and $^2A_2(xy) \rightarrow {}^2A_1(x^2\text{-}y^2)$ transitions respectively.

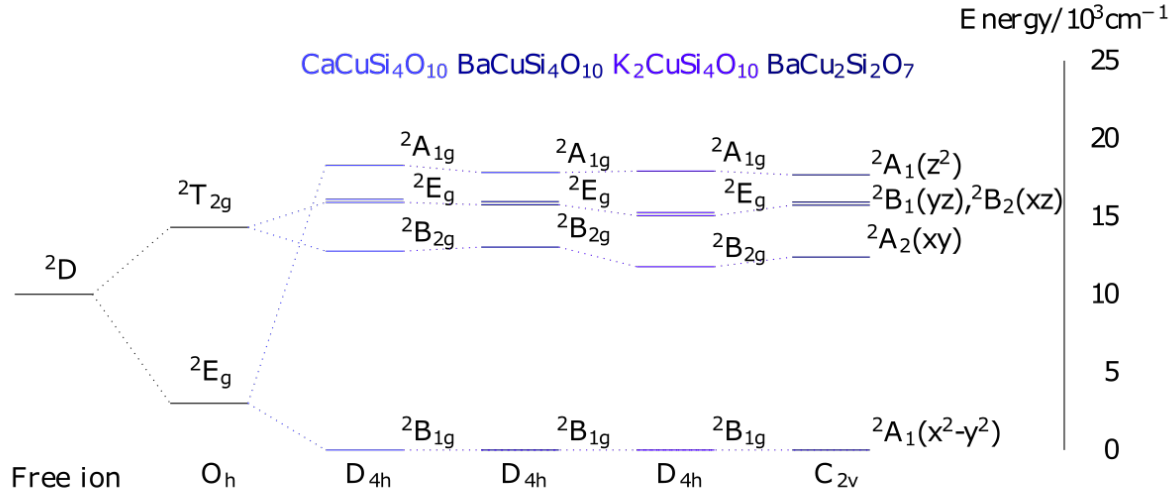

Figure 7.5: Simplified energy level diagram of Cu^{2+} ions in a D_{4h} and C_{2v} crystal field environment in $CaCuSi_4O_{10}$, $BaCuSi_4O_{10}$, $K_2CuSi_4O_{10}$ and $BaCu_2Si_2O_7$ lattices.

Formula	$^2A_{1g} \rightarrow {}^2B_{1g}$ [nm]	$^2E_g \rightarrow {}^2B_{1g}$ [nm]	$^2B_{2g} \rightarrow {}^2B_{1g}$ [nm]	λ_{max} [nm]
$CaCuSi_4O_{10}$	547(1)	628.8(3)	782.5(3)	912.0(4)
$BaCuSi_4O_{10}$	561(2)	635.01(7)	767(3)	953.0(5)
$K_2CuSi_4O_{10}$	558.2(1)	664.4(1)	849.4(2)	983.0(4)
Formula	$^2A_1$ $(z^2) \rightarrow$ $^2A_1$ $(x^2\text{-}y^2)$ [nm]	$^2B_1$ (yz),$^2B_2$ (xz) $\rightarrow$ $^2A_1$ $(x^2\text{-}y^2)$ [nm]	$^2A_2$ (xy) $\rightarrow$ $^2A_1$ $(x^2\text{-}y^2)$ [nm]	λ_{max} [nm]
$BaCu_2Si_2O_7$	565.8(2)	636.1(5)	807.3(3)	952.7(5)

Table 7.3: Key optical properties of the different cuprosilicate pigments, from powder samples. The error given on the values is the standard deviation from the fitting.

The absence of a broad absorption (Figure 7.4) with a blue component for the $CaCuSi_4O_{10}$, $BaCuSi_4O_{10}$ and $BaCu_2Si_2O_7$ materials causes the characteristic blue colour of cuprorivaite pigments. This has been reported for $CaCuSi_4O_{10}$ and $BaCuSi_4O_{10}$ pigments.[45] In contrast, the $K_2CuSi_4O_{10}$ compound shows broad absorption with a blue component, and is therefore lilac rather than blue. This is also observed in $BaCuSi_2O_6$[45] (known as Han purple).

The emission spectra are shown in Figure 7.4c. The emission maxima of $CaCuSi_4O_{10}$ is found at ~ 912 nm. For the emission peaks of $BaCuSi_4O_{10}$ (953nm), $K_2CuSi_4O_{10}$ (983 nm) and $BaCu_2Si_2O_7$ (953 nm) (the same as for $BaCuSi_4O_{10}$), red-shifts are observed.

The time-resolved photoluminescence for the $CaCuSi_4O_{10}$, $BaCuSi_4O_{10}$ and $K_2CuSi_4O_{10}$ was recorded under pulsed excitation at λ_{exc} = 658 nm. $BaCu_2Si_2O_7$ showed a very weak emission signal, which made it impossible to measure the lifetime. The decay curves (Figure 7.6) were fitted to a biexponential decay given by Equation 7.2:

$$I(t) = I_0 + I_1 exp\left(-\frac{t}{\tau_1}\right) + I_2 exp\left(-\frac{t}{\tau_2}\right), \tag{7.2}$$

where I(t) is the emission intensity as a function of time, I_0 is the initial intensity, I_i (i =1, 2) is the pre-exponential factor and τ_i (i =1, 2) the decay time. The weighted average decay time was calculated using the Equation 7.3:

$$\langle\tau\rangle = \frac{\tau_1^2 I_1 + \tau_2^2 I_2}{\tau_1 I_1 + \tau_2 I_2}. \tag{7.3}$$

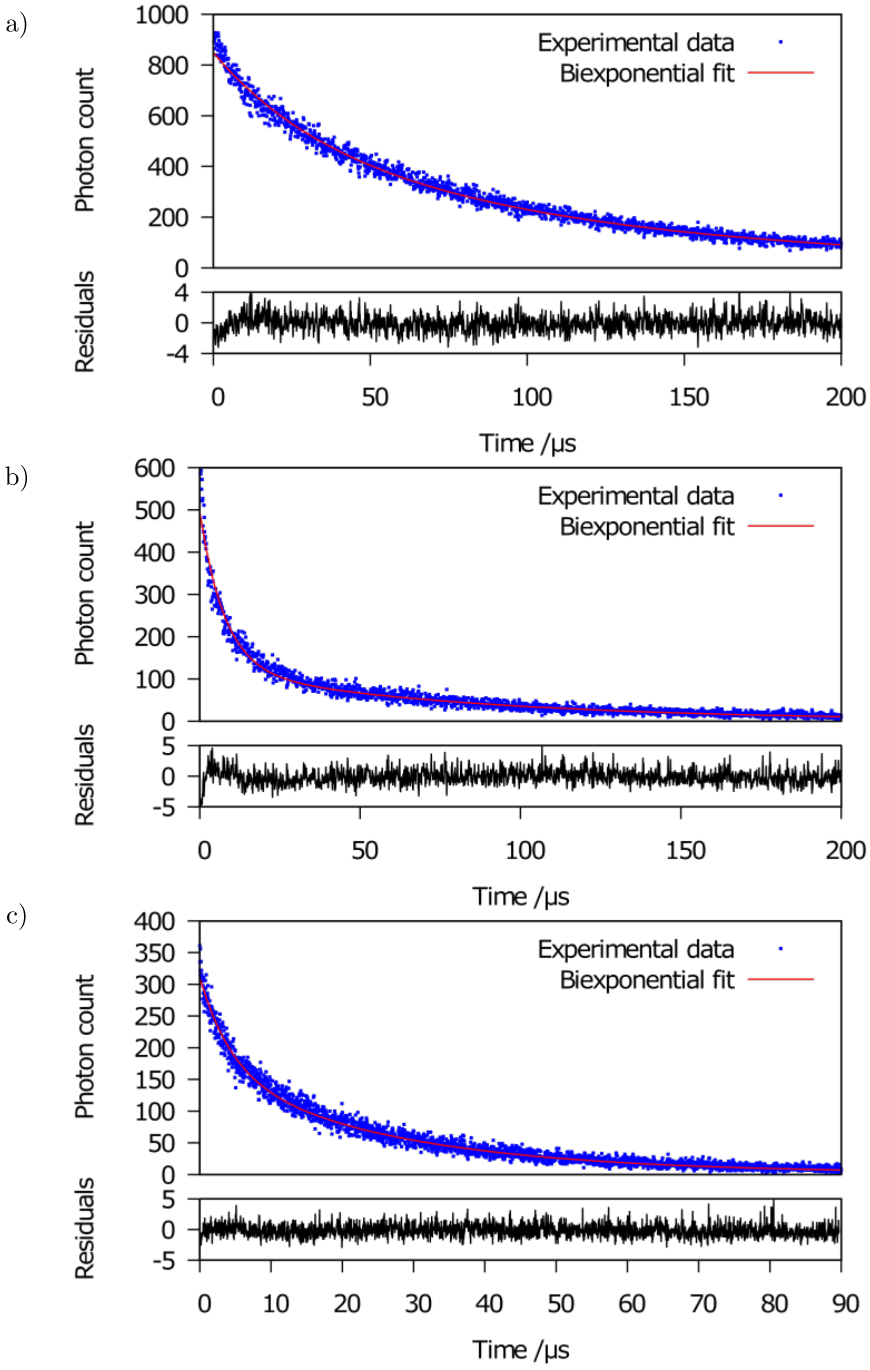

Figure 7.6: Fitted decay curves (solid red line) of the luminescence decay experimental data (blue dots) for a) $CaCuSi_4O_{10}$, b) $BaCuSi_4O_{10}$ and c) $K_2CuSi_4O_{10}$, recorded after excitation at 658 nm. The residuals are offset for clarity.

The fitted parameters obtained from the decay curve for each material are shown in Table 7.4. The goodness of fit (χ_R^2) of each fit and the residual curves evidence good quality fits, and the average lifetime value is found to be different for each compound. The lifetime values obtained for $CaCuSi_4O_{10}$ and $BaCuSi_4O_{10}$ are consistent with those reported in the literature (107 μs[15] and 33.3 μs[19] respectively). The lifetime value determined for $K_2CuSi_4O_{10}$ is shorter, at 23.1(5) ms.

Formula	I_0 [au]	I_1 [au]	τ_1 [μs]	I_2 [au]	τ_2 [μs]	$\langle\tau\rangle$ [μs]	χ^2_R
$CaCuSi_4O_{10}$	1.4(2)	504(8)	115(1)	343(8)	33(1)	102(1)	1.13
$BaCuSi_4O_{10}$	1.7(2)	201(6)	56(1)	587(6)	13.5(2)	38.6(9)	1.16
$K_2CuSi_4O_{10}$	2.0(4)	165(3)	26.0(5)	147(3)	4.4(2)	23.1(5)	1.03

Table 7.4: Fitted lifetime parameters of the different cuprosilicate pigments, from powder samples. The error given on the lifetime values is the standard deviation from the fitting.

The correlation between the level of distortion (τ_4) within the CuO_4 chromophore and the lifetime can be observed in Table 7.5. The lifetime value decreases with increasing distortion of the Cu(II) coordination environment away from ideal square planar geometry present in $CaCuSi_4O_{10}$. This could be due to bond elongation and distortion of the CuO_4^{6-} chromophore coordination environment, which causes a change in the symmetry from D_{4h} to C_{2v}. Similar behaviour has been observed in Pt(II)-containing compounds, where the square planar geometry is favourable to suppress the non-radiative decay processes and thus favours charge transfer transitions.[46]

Formula	Space group	Site symmetry	Lifetime [μs]	τ_4 [°]	Geometry
$CaCuSi_4O_{10}$	P4/ncc	4	102(1)	0	Square planar
$BaCuSi_4O_{10}$	P4/ncc	4	38.6(9)	0.052(1)	Square pyramid
$K_2CuSi_4O_{10}$	$P2_1/m$	1	23.1(5)	0.077(3)	Seesaw
$BaCu_2Si_2O_7$	Pnma	1	n/a	0.1882(7)	Seesaw

Table 7.5: Lifetime values and distortion analysis for the different cuprosilicate pigments.

7.3.3 $K_2CuSi_4O_{10}$ nanoparticles

7.3.3.1 Size and shape of $K_2CuSi_4O_{10}$ nanoparticles

The delamination process was done for the K2CuSi$_4$O$_{10}$ material, the filtered powder was further dried, obtaining a grey-lilac powder. This change in the tone of the initial colour is related to particle size, attributed to its dichroic properties (change in colour depending if the light is being scattered or transmitted).[6] The PXRD pattern collected from this sample (Figure 7.7) shows a high background and the broadening of the peaks, which by itself can be an indicator of decreased crystallite size. The sharpness of some peaks in the PXRD pattern show the presence of a mixture of nanoparticles and bulk material. These data were refined using a constant instrumental peak shape determined using CeO_2,[47] obtaining an estimated average particle size of the monodispersed spheres of 46(4) nm.

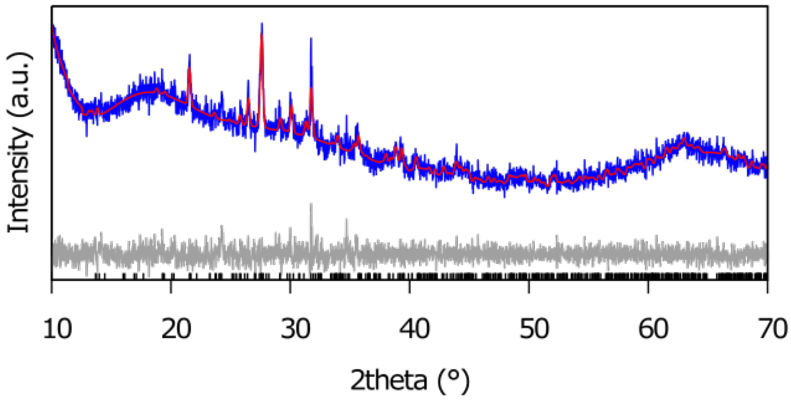

Figure 7.7: Rietveld fit of laboratory PXRD data for $K_2CuSi_4O_{10}$, Rwp = 3.33%.

Further particle size analysis was carried out using atomic force microscopy (AFM). Figure 7.8a) shows topographic images of two different sites with three different nanoparticles. For each site, the particles are indicated with blue, red and grey arrows. Figure 7.8b) shows the corresponding height profiles with the colours corresponding to the arrows. The thickness range of the nanoparticles (y-axis in Figure 7.8b) is from 2 nm to 5 nm and the lengths (x-axis in Figure 7.8b) range from 40 nm to 70 nm.

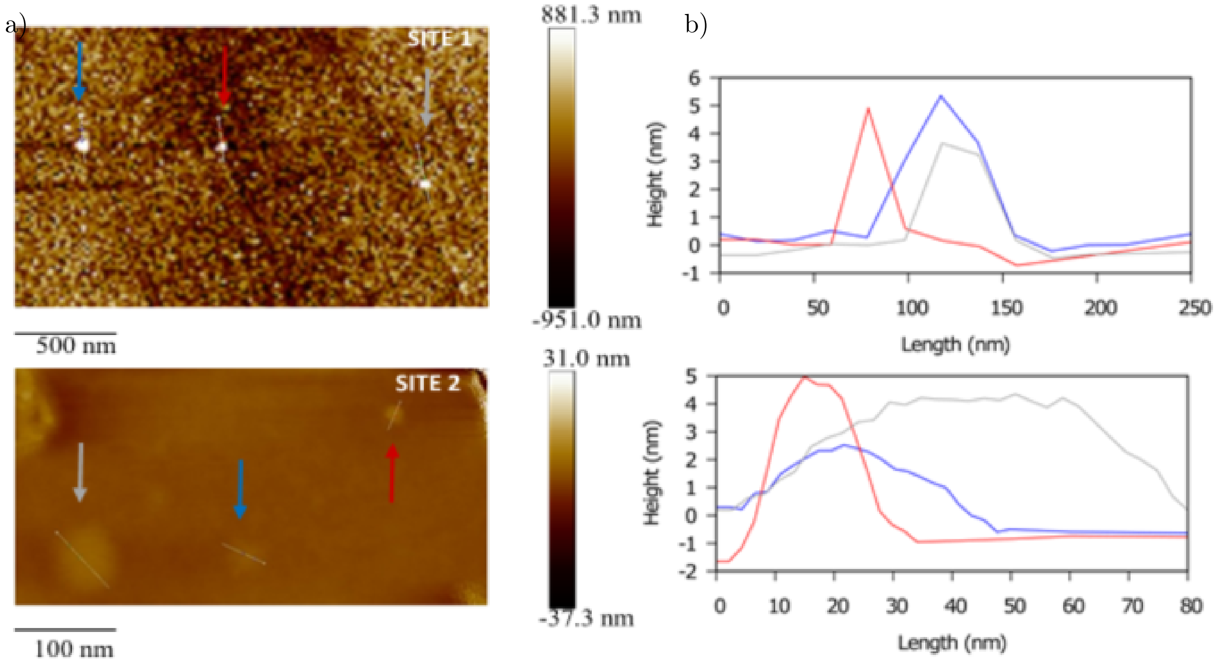

Figure 7.8: a) Topographic AFM image of $K_2CuSi_4O_{10}$ nanoparticles on two different sites (site 1 and site 2) and scales, and b) corresponding height profiles along the dotted lines in a).

Scanning electron microscopy (SEM) was performed on a carbon-coated powder sample in a vacuum using a Hitachi SU-70 FEG SEM. The SEM images of the bulk and nanoparticle samples are shown in Figure 7.9. The images show even spatial distribution of the different elements' colour mapping. Hence, an even distribution of elements in both cases was observed and no second phase was detected in either case. Figure 7.9b shows agglomerates of nanoparticles.

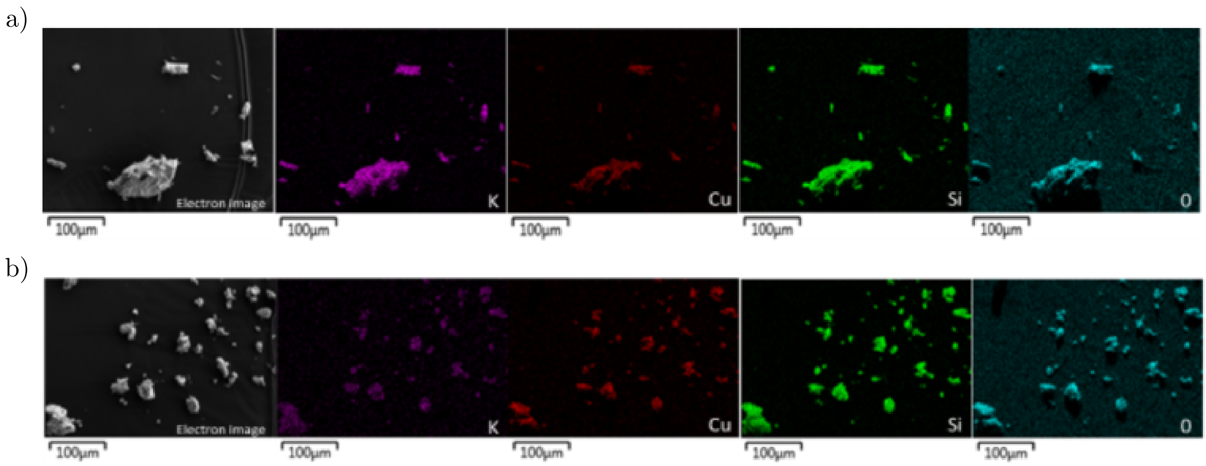

Figure 7.9: EDS-SEM map images of $K_2CuSi_4O_{10}$ a) bulk and b) nanoparticles. Element colour mapping: potassium is purple, copper is red, silicon is green and oxygen is blue

7.3.3.2 NIR fluorescence properties of $K_2CuSi_4O_{10}$ nanoparticles

The $K2CuSi_4O_{10}$ nanoparticles showed a substantially dimmed emission relative to the bulk material. This is in agreement with the behaviour reported for $CaCuSi_4O_{10}$ nanoparticles,[32] where the number of luminescent centres in a single layer, estimated using single particle fluorescence saturation, was 3.6 Cu^{2+} ions/nm^2.[31, 32]

The time-resolved photoluminescence was recorded on $K_2CuSi_4O_{10}$ nanoparticles for 0.8 ms, with a total of 200 data points under pulsed excitation at $\lambda_{exc} = 658$ nm. Figure 7.10 shows the fitted decay curve obtained. This was fitted to a biexponential decay given by Equation 7.2, where the average lifetime value is given by Equation 7.3. The lifetime value for the $K_2CuSi_4O_{10}$ nanoparticles is 16.9(3) μs. This is comparable to the 23.1(5)μs for the $K_2CuSi_4O_{10}$ bulk material. This conservation of the NIR emission properties in the nanoscale has been observed in $CaCuSi_4O_{10}$, where the nanoparticles presented a lifetime of $\sim$ 100 μs when the bulk material ranges from 100 μs to 142 μs.[32]

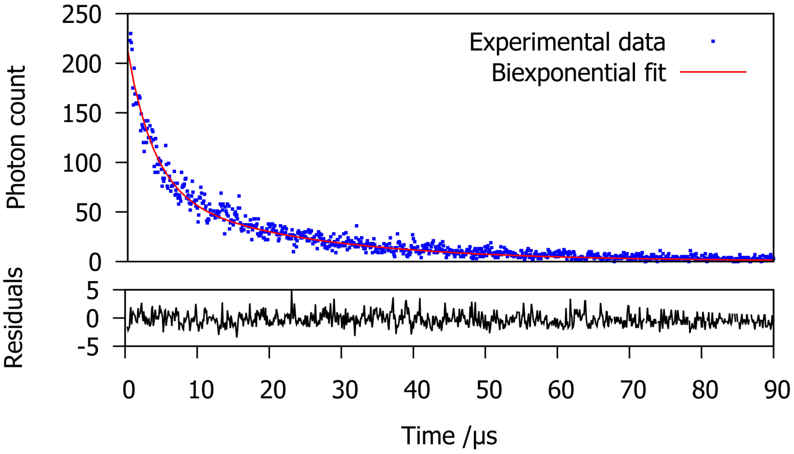

Figure 7.10: Fitted lifetime parameters of the different cuprosilicate pigments, from powder samples. The error given on the lifetime values is the standard deviation from the fitting. The goodness of fit $(\chi^2_R) = 3.08$.

7.4 Conclusions

$CaCuSi_4O_{10}$, $BaCuSi_4O_{10}$, $K_2CuSi_4O_{10}$ and $BaCu_2Si_2O_7$ were synthesised and characterised successfully. PXRD patterns analysed using Rietveld refinements demonstrated the quality of the polycrystalline materials prepared for optical measurements. Furthermore, $CaCuSi_4O_{10}$, $BaCuSi_4O_{10}$ and $BaCu_2Si_2O_7$ single crystals were grown, and high quality synchrotron PXRD data was collected for $K_2CuSi_4O_{10}$ to obtain precise structural information on each cuprosilicate pigment to investigate the Cu^{2+} square planar coordination environment and correlate this with the optical properties.

The optical properties were studied and a red-shift was observed in comparison to the Cu^{2+} square planar geometry of $CaCuSi_4O_{10}$. A strong correlation between distortion and lifetime was also found, where the lifetime value decreases with increasing distortion of the Cu(II) coordination environment away from ideal square planar geometry present in $CaCuSi_4O_{10}$. This correlation has been made for the first time for Cu(II)-containing compounds, necessary to achieve a better NIR emitter.

The $K_2CuSi_4O_{10}$ pigment was delaminated to form nanosheets successfully. This long-lived NIR emitter was shown to maintain its NIR optical properties at the nanoscale. Furthermore, demonstrating to be a potential candidate for use in bioimaging and as reporters of lifetime multiplexing and barcoding in cells[10] and forensics.[48]

7.5 Note

The work presented in this chapter is being prepared as a manuscript:

Rodríguez-García, M.M., Auckett, J. E., Markin, A., Beeby, A. and Evans, I.R. Cu(II)-containing silicate near infrared (NIR) emitters: the relationship between the structural distortion within the CuO_4 chromophore and luminescence properties (in preparation, 2020).

7.6 References

[1] Boppart, S.A., Oldenburg, A.L., Xu, C., and Marks, D.L. *Journal of biomedical optics*, 10(4), 2005.

[2] Pansare, V.J., Hejazi, S., Faenza, W.J., and Prud'homme, R.K. *Chemistry of materials*, 24(5), 2012.

[3] Verri, G. *Analytical and Bioanalytical Chemistry*, 394(4), 2009.

[4] Chen, Y.C. and Clegg, R.M. *Photosynthesis research*, 102(2-3), 2009.

[5] Connally, R. *Analytical Chemistry*, 83(12), 2011.

[6] Johnson-McDaniel, D., Barrett, C.A., Sharafi, A., and Salguero, T.T. *Journal of the American Chemical Society*, 135(5), 2013.

[7] Johnson-McDaniel, D. and Salguero, T.T. *Journal of visualized experiments: JoVE*, (86), 2014.

[8] E., C.R. and A., P.J. *Annals of the New York Academy of Sciences*, 1130(1), 2008.

[9] Zhang, L., Zheng, X., Deng, W., Lu, Y., Lechevallier, S., Ye, Z., Goldys, E.M., Dawes, J.M., Piper, J.A., and Yuan, J. *Scientific reports*, 4, 2014.

[10] Hoffmann, K., Behnke, T., Drescher, D., Kneipp, J., and Resch-Genger, U. *ACS Nano*, 7(8), 2013.

[11] Davy, H. *Philosophical Transactions of the Royal Society of London*, 105, 1815.

[12] Pozza, G., Ajò, D., Chiari, G., De Zuane, F., and Favaro, M. *Journal of Cultural Heritage*, 1(4), 2000.

[13] Mirti, P., Appolonia, L., Casoli, A., Ferrari, R.P., Laurenti, E., Amisano Canesi, A., and Chiari, G. *Spectrochimica Acta Part A: Molecular and Biomolecular Spectroscopy*, 51(3), 1995.

[14] Ganio, M., Salvant, J., Williams, J., Lee, L., Cossairt, O., and Walton, M. *Applied Physics A*, 121(3), 2015.

[15] Accorsi, G., Verri, G., Bolognesi, M., Armaroli, N., Clementi, C., Miliani, C., and Romani, A. *Chemical Communications*, 0(23), 2009.

[16] García-Fernández, P., Moreno, M., and Aramburu, J.A. *Inorganic chemistry*, 54(1), 2014.

[17] Borisov, S.M., Würth, C., Resch-Genger, U., and Klimant, I. *Analytical Chemistry*, 85(19), 2013.

[18] Chen, Y., Zhang, Y., and Feng, S. *Dyes and Pigments*, 105, 2014.

[19] Chen, Y., Shang, M., Wu, X., and Feng, S. *CrystEngComm*, 16(24), 2014.

[20] Berdahl, P., Boocock, S.K., Chan, G.C.Y., Chen, S.S., Levinson, R.M., and Zalich, M.A. *Journal of Applied Physics*, 123(19), 2018.

[21] Kawamura, K. and Iiyama, J. *Bulletin De Mineralogie*, 104(4), 1981.

[22] Tsukada, I., Sasago, Y., Uchinokura, K., Zheludev, A., Maslov, S., Shirane, G., Kakurai, K., and Ressouche, E. *Physical Review B*, 60(9), 1999.

[23] Poirier, M., Castonguay, M., Revcolevschi, A., and Dhalenne, G. *Physical Review B*, 66(5), 2002.

[24] Glazkov, V.N., Smirnov, A.I., Revcolevschi, A., and Dhalenne, G. *Physical Review B*, 72(10), 2005.

[25] Glazkov, V.N., Dhalenne, G., Revcolevschi, A., and Zheludev, A. *Journal of Physics: Condensed Matter*, 23(8), 2011.

[26] Yamada, T., Hiroi, Z., and Takano, M. *Journal of Solid State Chemistry*, 156(1), 2001.

[27] Chen, W., Shi, Y., Chen, Z., Sang, X., Zheng, S., Liu, X., and Qiu, J. *The Journal of Physical Chemistry C*, 119(35), 2015.

[28] Clark, M.G. and Burns, R.G. *Journal of the Chemical Society A: Inorganic, Physical, Theoretical*, (0), 1967.

[29] Carr, J.A., Franke, D., Caram, J.R., Perkinson, C.F., Saif, M., Askoxylakis, V., Datta, M., Fukumura, D., Jain, R.K., and Bawendi, M.G. *Proceedings of the National Academy of Sciences*, 115(17), 2018.

[30] Zhu, S., Yang, Q., Antaris, A.L., Yue, J., Ma, Z., Wang, H., Huang, W., Wan, H., Wang, J., and Diao, S. *Proceedings of the National Academy of Sciences*, 114(5), 2017.

[31] Selvaggio, G., Preiß, H., Chizhik, A., Nißler, R., Mann, F.A., Lv, Z., Oswald, T.A., Spreinat, A., Erpenbeck, L., Großhans, J., Giraldo, J.P., and Kruss, S. *bioRxiv*, 2019.

[32] Selvaggio, G., Chizhik, A., Nißler, R., Kuhlemann, l., Meyer, D., Vuong, L., Preiß, H., Herrmann, N., Mann, F.A., Lv, Z., Oswald, T.A., Spreinat, A., Erpenbeck, L., Großhans, J., Karius, V., Janshoff, A., Pablo Giraldo, J., and Kruss, S. *Nature Communications*, 11(1), 2020.

[33] Gupta, B., Saw, C.K., Kenny, M.E., and Harrington, B.A. *U.S. Patent 4,942,026*, 1990.

[34] Rietveld, H.M. *Journal of Applied Crystallography*, 2, 1969.

[35] Coelho, A.A., Evans, J.S.O., Evans, I.R., Kern, A., and Parsons, S. *Powder Diffraction*, 26(4), 2011.

[36] Bruker, I. *SAINT V8. A*, 38, 2016.

[37] Petříček, V., Dušek, M., and Palatinus, L. *Zeitschrift für Kristallographie-Crystalline Materials*, 229(5), 2014.

[38] Beeby, A., Garner, L., Howell, D., and Nicholson, C.E. *Journal of the Institute of Conservation*, 41(2), 2018.

[39] Pabst, A. *Acta Crystallographica*, 12(10), 1959.

[40] Chakoumakos, B.C., Fernandez-Baca, J.A., and Boatner, L.A. *Journal of Solid State Chemistry*, 103(1), 1993.

[41] Janczak, J., Kubiak, R., and Glowiak, T. *Acta Crystallographica Section C*, 46(8), 1990.

[42] Yang, L., Powell, D.R., and Houser, R.P. *Dalton Transactions*, (9), 2007.

[43] Kubelka, P. and Munk, F. *Z. Tech. Phys*, 12(593-601), 1931.

[44] Núñez, P., Ruiz-Morales, J.C., Lozano-Gorrín, A.D., Gili, P., Rodriguez, V.D., González-Platas, J., Barriuso, T., and Rodríguez, F. *Dalton Transactions*, (2), 2004.

[45] García-Fernández, P., Moreno, M., and Aramburu, J.A. *Journal of Chemical Education*, 93(1), 2016.

[46] Luo, Y., Chen, Z., Hu, J., Xu, Z., Meng, Q., and Tang, D. *Physical Chemistry Chemical Physics*, 21(5), 2019.

[47] Balzar, D., Audebrand, N., Daymond, M., Fitch, A., Hewat, A., Langford, J., Le Bail, A., Louër, D., Masson, O., and McCowan, C.N. *Journal of Applied Crystallography*, 37(6), 2004.

[48] Errington, B., Lawson, G., Lewis, S.W., and Smith, G.D. *Dyes and Pigments*, 132, 2016.

8 Overall conclusions and future work

During this PhD project, a total of 107 new silicate materials were synthesised and structurally and optically characterised. The phosphors were obtained by systematically doping a host material with different RE activators (Dy^{3+}, Tb^{3+}, Eu^{3+}) and by designing the chromophore coordination environment. The phosphors obtained emit in a range of colours: from yellowish white light, to tuneable blue to green light, to white light, to red light and NIR emission. Specifically:

Chapter 3 New warm white-emitting Dy^{3+}-containing phosphors based on apatite-type $Gd_{9.33}(SiO_4)_6O_2$. The $Gd_{9.33-x}(SiO_4)_6O_2$:x% La series was prepared and studied in order to optimise the different phosphor hosts based on gadolinium silicate apatite. Gd^{3+} was progressively substituted with La^{3+} from 0% to 50%. In order to select the best host for the white-emitting phosphors two different series – $Gd_{4.67-\frac{x}{2}}La_{4.67-\frac{x}{2}}(SiO_4)_6O_2$ and $Gd_{9.33-x}(SiO_4)_6O_2$ – were synthesised and doped systematically with Dy^{3+} (x = 0.5, 1.0 and 2.0%). The replacement of Gd^{3+} with La^{3+} decreased the quantity of sensitiser, hence less energy transfer $Gd^{3+} \rightarrow Dy^{3+}$.

The lifetime value showed concentration quenching for the $Gd_{4.67}La_{4.67}(SiO_4)_6O_2$, this effect was not observed for its counterpart. This demonstrated that the $Gd_{9.33}(SiO_4)_6O_2$ host had superior properties. The phosphors obtained emit in the yellowish white light region. The relative intensities of the blue emission band arising from the $^4F_{9/2} \rightarrow ^6H_{15/2}$ transition, the yellow emission band arising from the $^4F_{9/2} \rightarrow ^6H_{13/2}$ transition and the red emission band arising from the $^4F_{9/2} \rightarrow ^6H_{11/2}$ transition are such that the B/Y ratio in conjunction with the weak red component was insufficient to produce white light closer to the ideal (0.33,0.33) colour coordinates. As established in the aims of this project, the synthesis and characterisation of Dy^{3+}-doped phosphors was achieved. Furthermore, the feasibility of doping the gadolinium silicate apatite was proven.

Future work should therefore target another RE activator that emits in the red region to balance the RGB integrated emission peaks. Another approach can be to increase the Dy^{3+} concentration (>2 at. %) or change the host with a centrosymmetric site to one that allow the needed B/Y ratio to obtain white light. Furthermore, the stability of Gd_2SiO_5 should be studied, to avoid the formation of this impurity during the synthesis of the gadolinium silicate apatite.

Chapter 4 Green-emitting phosphors: Tb^{3+}-doped $Gd_{9.33}(SiO_4)_6O_2$. Colour tuneable Tb^{3+}-doped apatite-type silicate phosphors were synthesised and studied. Increasing the Tb^{3+} content level allowed to shift from a blue-emitting phosphor to a desirable green-emitting phosphor, consequently reducing the B/G ratio. The colour coordinates ranged from (0.3120,0.4623) to (0.3269,0.5218).

Future work should focus on doping the host with higher levels (>2 at. %) of Tb^{3+} to achieve a deeper green emitter and to reach the concentration quenching. Another important project could involve study compounds with low Tb^{3+} content (<0.5 at. %) to obtain a blue phosphor. In addition, substituting some of the Gd^{3+} ions by another ion to work as a sensitiser and achieve a brighter phosphor. Further work could involve studying the optical properties on variable temperature. The study of the morphology is also of great interest, as the brightness of the material is correlated to the surface of the material.

Chapter 5 Single-phase white-emitting phosphors based on apatite-type gadolinium silicate, $Gd_{9.33}(SiO_4)_6O_2$ doped with Dy^{3+}, Eu^{3+} and Tb^{3+}. Single-phase phosphors based on the apatite-type silicate $Gd_{9.33}(SiO_4)_6O_2$ doped with combinations of Dy^{3+} and Eu^{3+} or Eu^{3+} and Tb^{3+} were developed. Eight of the novel phosphors came nearer to the WL point. At least one, co-doped 0.5% Tb, 0.03% Eu shows better properties than any other apatite-based silicate phosphor in the literature, with colour coordinates (0.340 0.341).

As established in the aims of the project, this chapter shows the results of the development of white-emitting phosphors. Ultimately, this chapter was the culmination of the study of singly doped gadolinium silicate apatite, with Dy^{3+} (Chapter 3), Tb^{3+} (Chapter 4) and Eu^{3+} (Chapter 6), to observe their optical properties and the behaviour at different doping levels.

Future work should focus on this composition and investigate the temperature-dependent emission spectra to determine its behaviour at LED working temperatures ($\sim$ 150 °C). The growth of single crystals of the best performing phosphors is of high importance to observe the optical properties and facilitate the future commercial applications. As stated in the aims of this research, the developing of a novel single-phase white-emitting phosphors was done. Further work could involve fabricating the LED device: UV LED chip with this gadolinium silicate apatite phosphor.

Chapter 6 Narrow-band red-emitting phosphors based on Eu^{3+}-doped $Gd_{9.33}(SiO_4)_6O_2$. A series of new narrow-band red phosphors based on apatite-type gadolinium silicate was synthesised. $Gd_{9.33-x}(SiO_4)_6O_2$:x% Eu^{3+} (x = 0.3, 0.5, 0.7, 1.0, 2.0, 3.0, 5.0, 7.0, 10.0, 15.0 and 20.0) materials demonstrated outstanding chemical and thermal stability. The emission spectra at room temperature confirmed that the centre wavelength of the highest peak was 614 nm, which is exactly the wavelength that maximises the efficiency of the red component of white lighting. In addition, the linewidth of the 614 nm emission peak was 7 nm , which is within the critical 20 nm needed to avoid spillover into deeper red, where the human vision response drops. The concentration quenching was reached for doping levels higher than 10%. Variable-temperature spectra were recorded to report the behaviour of the phosphors at LED working temperature, ~150 °C, where only a loss of 10% was observed.

The work presented in this chapter is the round off, where the aims were accomplish. A complete study of the structural and optical analysis at room temperature and at LED working temperatures was achieved. Future work should focus on growing single crystals to monitor the Eu^{3+} coordination environment at high temperatures or to use Raman spectroscopy to determine the vibrational modes. Further work could involve the fabrication of the LED: combination of blue (463 nm), green (530 nm) and this red phosphor (614 nm) with a UV LED chip.

Chapter 7 Cu(II)-containing silicate near infrared (NIR) emitters: the relationship between the structural distortion within the CuO_4 chromophore and luminescence properties. Four Cu(II)-containing silicate pigments – $CaCuSi_4O_{10}$, $BaCuSi_4O_{10}$, $K_2CuSi_4O_{10}$ and $BaCuSi_2O_7$ – were synthesised. A detailed study of the relationship between their structural and optical properties was concluded. A connection between the CuO_4^{6-} chromophore environment and the lifetime value of the NIR emitter was established.

The PXRD of the $K_2CuSi_4O_{10}$ nanoparticles shows high background, further work could involve investigate the source of this amorphous background. In addition, the use of another technique to obtain size distribution, such as Dynamic Light Scattering, in the $K_2CuSi_4O_{10}$ nanoparticles could benefit this work. To study the morphology and size of the nanoparticles is needed the use of a high resolution technique such as transmission electron microscopy(resolution 0.1 nm). Future work should target novel materials that contain Cu(II) in a square planar environment, such as $ACuSi_4O_{10}$ (A = Mg, Sr) or $B_2CuSi_4O_{10}$ (B = Na, Rb, Cs).

A Appendix

A.1 Publications

- Rodríguez-García, M. M.; Williams, J. A. G.; Evans, I. R., Single-phase white-emitting phosphors based on apatite-type gadolinium silicate, $Gd_{9.33}(SiO_4)_6O_2$ doped with Dy^{3+}, Eu^{3+} and Tb^{3+}. Journal of Materials Chemistry C 2019, 7 (25), 7779-7787.
- Rodríguez-García, M.M., Williams, J. A. G. and Evans, I.R. Narrow-band red-emitting phosphors based on Eu^{3+}-doped $Gd_{9.33}(SiO_4)_6O_2$ (in preparation, 2020).
- Rodríguez-García, M.M., Auckett, J. E., Markin, A., Beeby, A. and Evans, I.R. Cu(II)-containing silicate near infrared (NIR) emitters: the relationship between the structural distortion within the CuO_4 chromophore and luminescence properties (in preparation, 2020).

A.2 Laboratory PXRD refined parameters

x	a(Å)	b(Å)	V(Å^3)	R$_{wp}$ (%)
4.67	9.5987(1)	7.0166(1)	559.86(2)	3.48
3.73	9.5694(3)	6.9783(2)	553.41(4)	3.23
2.80	9.5417(6)	6.9513(5)	548.09(8)	2.96
1.87	9.5126(4)	6.9244(3)	542.64(5)	2.92
0.93	9.4744(2)	6.8942(2)	535.94(3)	2.58
0	9.4446(1)	6.8721(1)	530.87(2)	2.76

Table I: Unit cell parameters for $Gd_{9.33-x}La_x(SiO_4)_6O_2$ (x = 0, 0.93, 1.87, 2.8, 3.73 and 4.67) hosts from laboratory PXRD.

A.3 Laboratory PXRD pattern refinement input file

```
'-------------------------------------------------------------
'Input File for simple Rietveld Refinement
'-------------------------------------------------------------
r_wp 2.57749895 r_exp 2.33577487 r_p 2.02492791 r_wp_dash 19.3423649 r_p_dash
32.3078434 r_exp_dash 17.5283912 weighted_Durbin_Watson 1.84766488 gof 1.10348775
'-------------------------------------------------------------
'General information about refinement here
'Remove comments as required
'-------------------------------------------------------------
iters 100000
chi2_convergence_criteria 0.001
do_errors
'-------------------------------------------------------------
'Information on datafile etc here
'Check that default weighting is appropriate for your data
'-------------------------------------------------------------
xdd d7_10220.raw
x_calculation_step = Yobs_dx_at(Xo); convolution_step 4
bkg @ 1711.67616`_1.24561171 613.491611`_2.07485517 -33.3358154`_1.96177067
-12.7360171`_1.88863088 -14.8496957`_1.83556102 20.4854367`_1.77311971
-11.15225`_1.75306435 11.932452`_1.69753178 -4.17728655`_1.69361379
-10.455453`_1.63900778 5.48535392`_1.67915924 5.90848316`_1.54563215
2.85346174`_1.53274757 -6.53740691`_1.38466271 3.78031857`_1.35864132
'd8 Lynx Eye Cu Ka1/a2 2 line emission
LP_Factor(!th2_monochromator, 0)
CuKa2(0.0001)
```

```
Zero_Error(zero, 0.05362`_0.00070)
Variable_Divergence_Intensity
'------------------------------------------------------------------
'Information on structure
'Type in phase/space group/cell etc
'Comment in/out sections as needed
'------------------------------------------------------------------
str
phase_name "Gd9.34(SiO4)6O2"
a lpa 9.444148`_0.000102
b lpa 9.444148`_0.000102
c lpc 6.871772`_0.000110
al 90.
be 90.
ga 120.
volume 530.793`_0.014
space_group "P63/m"
site Gd1 num_posns 4 x !xGd1=1/3; y !yGd1=2/3; z !zGd1 -0.00044 occ Gd+3 0.8333
beq bval 1.54671`_0.08731
site Gd2 num_posns 6 x !xGd2 0.23978 y !yGd2 0.00813 z !zGd2 0.25 occ Gd+3 1.0 beq
bval 1.54671`_0.08731
site Si1 num_posns 6 x !xSi1 0.3708 y !ySi1 0.3981 z !zSi1 0.25 occ Si+4 1 beq
bval 1.54671`_0.08731
site O1 num_posns 6 x !xO1 0.1216 y !yO1 0.5249 z !zO1 0.25 occ O-2 1 beq bval
1.54671`_0.08731
site O2 num_posns 6 x !xO2 0.4839 y !yO2 0.3147 z !zO2 0.25 occ O-2 1 beq bval
1.54671`_0.08731
site O3 num_posns 12 x !xO3 0.2490 y !yO3 0.3394 z !zO3 0.0642 occ O-2 1 beq bval
1.54671`_0.08731
site O4 num_posns 2 x !xO4 0.0000 y !yO4 0.0000 z !zO4 0.25 occ O-2 1 beq bval
1.54671`_0.08731
scale @ 0.000120788025`_1.04e-006
r_bragg 0.78303769
TCHZ_Peak_Type(pku,-0.00452`_0.00403,pkv, 0.00618`_0.00319,pkw,
-0.00289`_0.00060,!pkz, 0.0000,pky, 0.09493`_0.00317,!pkx, 0.0000)
Simple_Axial_Model(axial, 5.44688`_0.21949)
Phase_Density_g_on_cm3( 6.41996`_0.00017)
Rietveld_Plot(MMRG014.xyd)
Rietveld_Tics_2th(MMRG014.2th)
```

A.4 Synchrotron PXRD pattern refinement input file

```
'------------------------------------------------------------------
'Input File for Rietveld Refinement of I11 data
'------------------------------------------------------------------
r_wp 9.94012078 r_exp 5.72159518 r_p 7.63920359 r_wp_dash 16.3824254 r_p_dash
15.3832656 r_exp_dash 9.42982566 weighted_Durbin_Watson 1.18960986 gof 1.73729886
iters 100000
'#define write_out
chi2_convergence_criteria 0.001
'continue_after_convergence
'randomize_on_errors
do_errors
xdd 576275-mac-001_reb_0003.xye
start_X 5
finish_X 110
x_calculation_step = Yobs_dx_at(Xo); convolution_step 4
```

```
bkg @ 98.2833815`_0.144776489 -78.2503572`_0.218752136 38.3017321`_0.194292833
-14.3636589`_0.176307822 5.67845815`_0.173317747 1.97885057`_0.167728
-6.52576561`_0.166341457 8.56457104`_0.160049204 -5.47535682`_0.157002839
1.80764826`_0.149977457 7.65280771`_0.148775455 -11.3215531`_0.138923223
10.7138968`_0.136475224 -8.51376343`_0.118622133 6.18878964`_0.111968536
'lambda derived on peak shape derived on 574646-mac-001_offline.xye on
21/4/2017.xye by John 2016
'Si zero was -1.69258/1000 degrees
lam ymin_on_ymax 0.00001 la 1.0 lo 0.8257653_8.44468382e-008 lh 0.1
LP_Factor( 90) 'change the LP correction or lh value if required
prm zero -1.11808`_0.02154 th2_offset = (zero/1000);:  -0.00111808`_2.15410741e-005
str
phase_name "Gd9.34(SiO4)6O2"
a lpa1 9.441298`_0.000009
b lpa1 9.441298`_0.000009
c lpc1 6.870345`_0.000008
al 90.
be 90.
ga 120.
'volume vol1 530.362_0.001
space_group "P63/m"
site Gd1 num_posns 4 x !xGd1=1/3; y !yGd1=2/3; z zGd1 -0.00061`_0.00018 occ Gd+3
0.8333 beq bval1 1.07664`_0.04240
site Gd2 num_posns 6 x xGd2 0.24021`_0.00005 y yGd2 0.00804`_0.00007 z !zGd2=1/4;
occ Gd+3 1.0 beq bval2 0.61837`_0.04103
site Si1 num_posns 6 x xSi1 0.37198`_0.00025 y ySi1 0.39963`_0.00025 z !zSi1=1/4;
occ Si+4 1 beq bval3 0.68338`_0.05630
site O1 num_posns 6 x xO1 0.12438`_0.00063 y yO1 0.52775`_0.00064 z !zO1=1/4; occ
O-2 1 beq bval4 1.13928`_0.06301
site O2 num_posns 6 x xO2 0.48512`_0.00061 y yO2 0.31889`_0.00063 z !zO2=1/4; occ
O-2 1 beq bval4 1.13928`_0.06301
site O3 num_posns 12 x xO3 0.25145`_0.00039 y yO3 0.33997`_0.00038 z zO3
0.06755`_0.00047 occ O-2 1 beq bval4 1.13928`_0.06301
site O4 num_posns 2 x !xO4 0.0000 y !yO4 0.0000 z !zO4=1/4; occ O-2 1 beq bval4
1.13928`_0.06301
scale @ 5.62227287e-005`_1.137e-005
r_bragg 2.27582202
Phase_Density_g_on_cm3( 6.42517`_0.00001)
MVW( 2052.143,vol 530.362`_0.001,percent1 97.355`_0.739)
Stephens_hexagonal
(
etac, 0.90176`_0.04415 min 0 max 1,
s400c, 0.70795`_0.06385,
s004c, 2.16482`_0.19747,
s202c, 2.83937`_0.26221
)
'Rietveld_Plot(MMRG014.xyd)
'Rietveld_Tics_2th(MMRG014_1.2th)
' CS_G(sizeG1, 655.29905_9.11660)
' Strain_G(strainG1, 0.05560_0.00030)
' CS_L(sizeL1, 974.94503_9.79237)
' LVol_FWHM_CS_G_L(1, 4479.52093_4079.72544, 0.89, 5415.54388_6363.98805, csgc,
9999.96879_20999.08714_LIMIT_MIN_0.3, cslc, 9960.99055_2130.93012_LIMIT_MAX_10000)
' e0_from_Strain( 0.00007_0.00000, sgc, 0.00523_0.00224_LIMIT_MIN_0.0001, slc,
0.02956_0.00052)
'
str
```

```
phase_name "Gd2SiO5"
a lpa2 9.134246`_0.000238
b lpb2 7.059829`_0.000189
c lpc2 6.749166`_0.000180
al 90.
be lpbe 107.52000`_0.00227
ga 90.
'volume 419.908_0.042
space_group "P121/c1"
site Gd1 x 0.11453 y 0.14600 z 0.41628 occ Gd+3 1 beq bval5 0.50204`_0.11237
site Gd2 x 0.52458 y 0.62451 z 0.23428 occ Gd+3 1 beq bval5 0.50204`_0.11237
site Si1 x 0.2020 y 0.5876 z 0.4598 occ Si+4 1 beq bval5 0.50204`_0.11237
site O1 x 0.2032 y 0.4302 z 0.6453 occ O-2 1 beq bval5 0.50204`_0.11237
site O2 x 0.1317 y 0.4587 z 0.2520 occ O-2 1 beq bval5 0.50204`_0.11237
site O3 x 0.3839 y 0.6361 z 0.5059 occ O-2 1 beq bval5 0.50204`_0.11237
site O4 x 0.0941 y 0.7681 z 0.4507 occ O-2 1 beq bval5 0.50204`_0.11237
site O5 x 0.3837 y 0.3782 z 0.0487 occ O-2 1 beq bval5 0.50204`_0.11237
scale @ 2.36976313e-006`_4.833e-007
r_bragg 4.82738015
Phase_Density_g_on_cm3( 6.76289`_0.00032)
'CS_G(sizeG2, 483.07016_81.92146_LIMIT_MIN_0.3)
Strain_G(strainG2, 0.15082`_0.00271)
'LVol_FWHM_CS_G_L(1, 4489.50742_2730.67638, 0.89, 5424.90489_4230.06584, csgc,
10000.00000_13854.33845, cslc, 9999.98933_2023.80745)
'e0_from_Strain( 0.00007_0.00002, sgc, 0.00010_0.05869_LIMIT_MIN_0.0001, slc,
0.03165_0.00047)
MVW( 1690.330,volume2 415.039`_0.020,percent2 2.645`_0.739)
' Rietveld_Tics_2th(MMRG014_2.2th)
'{{{ overall instrumental peak shape etc for each str
for strs {
'peak shape derived on 574646-mac-001_offline.xye on 21/4/2017
'This is a fixed instrumental profile
'Just use size/strain on your sample
TCHZ_Peak_Type(!pku,-0.00072_0.00002,!pkv, -0.00008_0.00001,!pkw,
-0.00080_0.00002,!pkz, 0.00087_0.00002,!pky, 0.01490_0.00011,!pkx, 0.00175_0.00002)
Simple_Axial_Model(!axial, 2.12938_0.00228)
prm !packing_density 0.6 min 0.1 max 1.0 'typically 0.2 to 0.5
prm !capdia 0.5 'capillary diameter in mm
prm !linab = Get(mixture_MAC) Get(mixture_density_g_on_cm3);:  436.86158`_0.25388
'in cm-1
prm muR = (capdia/20)*linab*packing_density;:  6.55292`_0.00381
Cylindrical_I_Correction(ab3s, 1.04478`_0.13299)
}
'}}}
#ifdef write_out
out "Lattice_Parameters.txt" append
Out_String(MMRG014_05)
Out(lpa1, " %4.6f", " %1.6f")
Out(lpc1, " %6.6f", " %1.6f")
Out(vol, " %6.6f", " %1.6f")
Out(Get (gof), " %6.6f")
Out(Get (r_wp), " %6.6f\n")
#endif
```

A.5 Detailed Rietveld fit of Eu^{3+}-doped phosphors

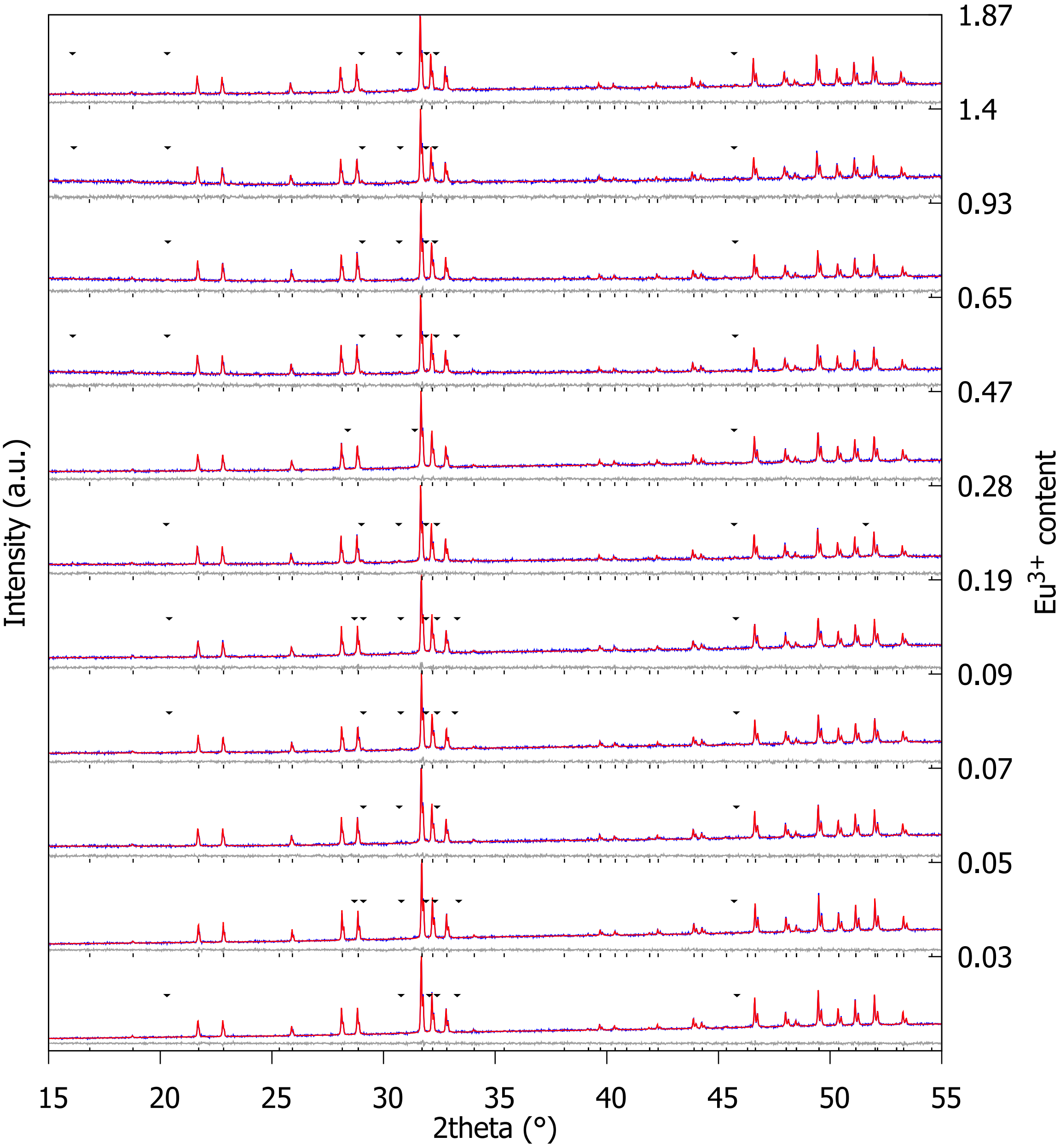

Figure A.1: Rietveld fit of the laboratory PXRD data. $Gd_{9.33-x}$ $Eu_x(SiO_4)_6O_2$ (x = 0.03, 0.05, 0.07, 0.09, 0.19, 0.28, 0.47, 0.65, 0.93, 1.40 and 1.87).∇ indicates the Gd_2SiO_5 impurity peaks.

A.6 Crystallographic details for the NIR emitters

A.6.1 CaCuSi$_4$O$_{10}$

Space Group	$P4/ncc$
Lattice parameters	$a = b = 7.3001(5)$ Å, $c = 15.0983(2)$ Å
Volume	804.6104(1) Å^3
Radiation wavelength	0.71073 Å
Temperature	120 K
Number of reflections collected	12456
Number of unique reflections	682
Number of parameters refined	26
R(all)	2.33
wR(all)	3.17
GOF(obs)	2.41
GOF(all)	2.31

Site	Atom	x	y	z	Occ	U$_{iso}$ (Å^2)
Cu1	Cu	0.5	0	0.08141(2)	1	0.00254(9)
Ca1	Ca	0	0	0	1	0.00355(12)
Si1	Si	0.17687(5)	0.25281(6)	0.14695(3)	1	0.00267(12)
O1	O	0.25710(14)	0.10266(15)	0.08191(7)	1	0.0046(2)
O2	O	0.25222(16)	0.45756(15)	0.12598(6)	1	0.0057(2)
O3	O	0.21163(15)	0.21163(15)	0.25	1	0.0090(3)

A.6.2 BaCuSi$_4$O$_{10}$

Space Group	$P4/ncc$
Lattice parameters	$a = b = 7.4392(3)$ Å, $c = 16.1056(1)$ Å
Volume	891.3112(5) Å^3
Radiation wavelength	0.71073 Å
Temperature	120 K
Number of reflections collected	13679
Number of unique reflections	756
Number of parameters refined	26
R(all)	2.86
wR(all)	4.43
GOF(obs)	3.33
GOF(all)	3.17

Site	Atom	x	y	z	Occ	U$_{iso}$ (Å^2)
Ba1	Ba	0	0	0	1	0.00753(12)
Cu1	Cu	0.5	0	0.09404(5)	1	0.00582(16)
Si1	Si	-0.23184(10)	0.31129(11)	0.15414(5)	1	0.0061(2)
O1	O	-0.2743(4)	0.2743(4)	0.25	1	0.0194(8)
O2	O	-0.0265(3)	0.2513(3)	0.13637(13)	1	0.0111(4)
O3	O	0.2805(3)	0.1366(3)	0.09023(12)	1	0.0126(4)

A.6.3 $\mathbf{K_2CuSi_4O_{10}}$

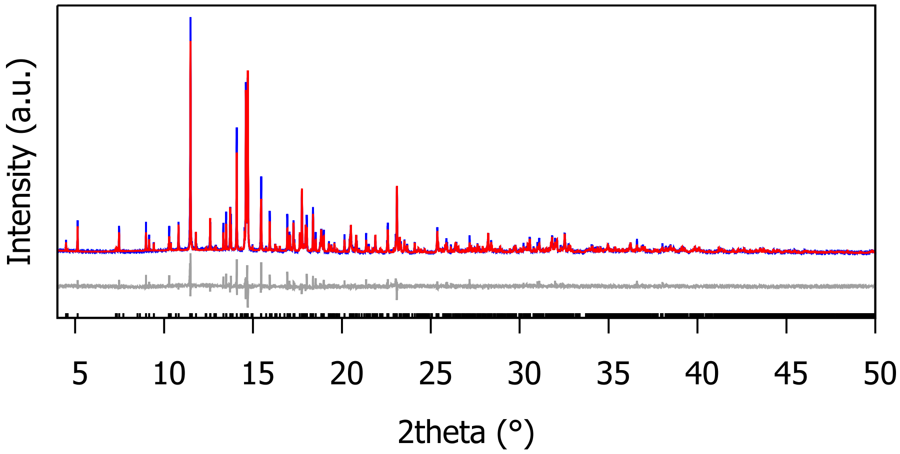

Figure A.2: Rietveld fit of synchrotron PXRD data for $K_2CuSi_4O_{10}$, $R_{wp} = 11.42\%$.

Space Group	$P2_1m$
Lattice parameters	$a = 11.28391(5)$ Å, $b = 8.24929(4)$ Å, $c = 11.06834(5)$ Å $\beta = 110.9179(4)°$
Volume	962.384(7) Å^3
Radiation wavelength	0.82576 Å
Range (2θ)	4-150°
R_{wp}	11.42

Site	Atom	x	y	z	Occ	U_{iso} (Å^2)
Cu1	Cu	0.2125(1)	0.4979(2)	0.2892(1)	1	1.27(9)
K1	K	0.0264(3)	0.25	0.0292(3)	1	1.27(9)
K2	K	0.0549(9)	0.25	0.4417(3)	1	1.27(9)
K3	K	0.4561(3)	0.25	0.5244(3)	1	1.27(9)
K4	K	0.4157(3)	0.25	0.9169(3)	1	1.27(9)
Si1	Si	0.2498(3)	0.5640(3)	0.0154(3)	1	1.27(9)
Si2	Si	0.4643(3)	0.4429(4)	0.2291(3)	1	1.27(9)
Si3	Si	0.2581(3)	0.5557(4)	0.5951(3)	1	1.27(9)
Si4	Si	0.0902(3)	0.4389(4)	0.7484(3)	1	1.27(9)
O1	O	0.4572(7)	0.25	0.1928(7)	1	0.83(9)
O2	O	0.2647(7)	0.75	0.5829(7)	1	0.83(9)
O3	O	0.0723(7)	0.25	0.7179(7)	1	0.83(9)
O4	O	0.2320(7)	0.75	0.9618(7)	1	0.83(9)
O5	O	0.4062(5)	0.5273(6)	0.0903(5)	1	0.83(9)
O6	O	0.1757(4)	0.5291(6)	0.1049(5)	1	0.83(9)
O7	O	0.0278(5)	0.4741(7)	0.2486(5)	1	0.83(9)
O8	O	0.3907(4)	0.4818(6)	0.3250(5)	1	0.83(9)
O9	O	0.2465(5)	0.4691(6)	0.4730(5)	1	0.83(9)
O10	O	0.1444(4)	0.5194(6)	0.6437(5)	1	0.83(9)
O11	O	0.3893(5)	0.5001(7)	0.7117(4)	1	0.83(9)
O12	O	0.2046(5)	0.4478(6)	0.8892(5)	1	0.83(9)

A.6.4 $BaCu_2Si_2O_7$

Space Group	*Pnma*
Lattice parameters	a = 6.8449(4) Å, b = 13.1606(8) Å, c = 6.8845(4) Å
Volume	620.18(6) Å^3
Radiation wavelength	0.71073 Å
Temperature	120 K
Number of reflections collected	10334
Number of unique reflections	1070
Number of parameters refined	41
R(all)	2.39
wR(all)	2.28
GOF(obs)	1.44
GOF(all)	1.38

Site	Atom	x	y	z	Occ	U_{iso} (Å^2)
Ba1	Ba	-0.01255(3)	0.25	0.04402(3)	1	0.00339(7)
Cu1	Cu	0.22197(5)	0.00412(2)	0.20620(5)	1	0.00266(9)
Si1	Si	0.00233(9)	0.13396(6)	-0.47291(11)	1	0.00208(19)
O1	O	0.3277(3)	0.13349(13)	0.1305(3)	1	0.0044(4)
O2	O	0.1819(3)	0.05881(14)	0.4660(3)	1	0.0033(4)
O3	O	-0.0592(3)	0.11229(14)	-0.2516(3)	1	0.0042(4)
O4	O	-0.4034(4)	0.25	-0.0156(4)	1	0.0037(5)